Postnatal Development of the Action Potential Waveform in Cortical Neurons: A Biophysical Perspective

Felicity Heloise Inkpen

A dissertation submitted to The University of Bristol in accordance with the requirements for award of the degree of Doctor of Philosophy in the Faculty of Life Sciences

School of Physiology, Pharmacology and Neuroscience

October 2018

50000 words

Abstract

As the new-born brain grows and matures, the neurons within migrate, form synapses, and assemble into functional networks, all whilst changing in morphology and adapting to function. The first two weeks of life are a particularly dynamic period, with the adaptations in electrical properties and activity underpinned by the composition and biophysical properties of the neuronal membrane. The action potential (AP) is the foundation of neuronal communication, being the primary indicator of neuronal activity, the progenitor of neurotransmitter release and synaptogenesis, implicated in the formation of neuronal networks, and controlling gene expression. Changes to the AP waveform over maturation are therefore simultaneously indicative of the underlying biophysics and influential to neuronal structure and function. Even subtle changes to the AP waveform can contain a wealth of information, but thorough biophysical characterisation of the AP waveform with neuronal development has remained elusive. Such characterisation requires a combination of established experimental techniques, as well as carefully optimised models to elucidate the underlying membrane properties, ion channel populations and neuronal conductances that give the observed dynamics their particular development-dependent shape.

By fitting computational conductance-based Hodgkin-Huxley models to electrophysiological data, the underlying biophysics can be illuminated. But, with multiple and developmentally-dynamic parameters to consider, accurate and fast optimisation techniques are needed. Voltage-based fitting methods can produce complex parameter error landscapes with local or narrow minima, requiring computationally expensive algorithms to return the maximal conductances associated with various channels. By instead algebraically solving the expressions for the ion channel gating variables and computing the difference between passive and active neuronal currents, parameter optimisation can be reduced to a simple linear sum of currents. The minimisation of the residual of this sum can be presented graphically for the different maximal conductances of the Hodgkin-Huxley model in multidimensional yet simple parameter landscapes that allow for intuitive interpretation and fast model optimisation.

Via the combination of current-clamp whole-cell electrophysiology, dye-filling and confocal imaging, the biophysical characteristics of regular-spiking excitatory neurons in the somatosensory cortex of neonatal mice aged between 3 and 11 postnatal days were investigated. The experimental protocols used facilitated consideration of the development of ion channel populations, membrane thickness, cell morphology and gap junctions when painting a picture of neuronal biophysics.

This work demonstrates that postnatal neuronal development is correlated with large increases in the height and speed of APs. Passive membrane dynamics are observed to mature, with analysis via a two-compartment model of exponential decay revealing a developmentally dependent fast passive current sink in some cells. Further to this, these passive dynamics are manipulated to reveal surface area predictions that correlate with morphological observations. A surprising diversity of neuronal morphologies is found within the layer IV barrel cortex, along with evidence of gap junction coupling between neurons, with potential implications for development-dependent regulation of neural networks. Mathematical models, built on artificial data sets and optimised for multiple parameters via residual current minimisation, demonstrate better robustness to noise than models optimised via voltage-comparison methods. Resultant multiple-channel neuron models can be used to provide a probe of the biophysical heterogeneity of maturing neuronal populations.

The combination of electrophysiological, computational and imaging techniques allows us to make biophysically complex predictions of neuronal development, to produce a picture of the changing biophysical nature of these excitatory neurons as they approach maturity, and to elucidate the dynamics that drive maturation of neuronal excitability.

Author’s declaration

I declare that the work in this dissertation was carried out in accordance with the requirements of the University's Regulations and Code of Practice for Research Degree Programmes and that it has not been submitted for any other academic award. Except where indicated by specific reference in the text, the work is the candidate's own work. Work done in collaboration with, or with the assistance of, others, is indicated as such. Any views expressed in the dissertation are those of the author.

SIGNED: ..... DATE:.....

This thesis is dedicated to the memory of

Irene Sharrock Inkpen, 3rd September 1927 – 19th March 2018,

and

Norman Geoffrey Inkpen, 2nd May 1928 – 14th June 2018

Who could not be apart.

Acknowledgements

No Doctorate of Philosophy is a solo endeavour; the contents of this thesis were only possible due to the advice, help and support of the following people:

To my supervisors, Dr Michael Ashby and Dr Nathan Lepora, thank you for your direction, encouragement, instruction, and for the many inspirational conversations. Thank you to Dr Lucia Marucci and Dr James Hodge for your advice and many helpful suggestions. I would also like to thank the network of academics who have been instrumental to this research project, in particular the Neural Dynamics programme directors and students. I am, of course, very thankful for the funding provided by the Wellcome Trust via the University of Bristol Neural Dynamics Program, without which this project would not be possible.

This PhD would absolutely not have been completed without the invaluable advice and support of the postdoctoral researchers that I had the pleasure of working with over the past four years. In particular, I would like to thank Dr Sarah Hulme for her early pep talks, Dr Aleks Domanski for many illuminating scientific conversations and confidence-boosting chats, but I would especially like to thank Dr Jon Witton for his endless supply of help and advice, and for his support and friendship in the most difficult moments of this PhD.

To the other members of the Ashby Lab, Juan Agullo Campello, Eleanor Conole, Christine Cross, Daniela Franchini, James Johnson, Rob Lees, Soraya Mefta, and Lasani Wijetunge, I extend my sincere thanks for the comradery, friendship and laughter. Working with this group of fantastic young scientists has been an absolute pleasure.

I would like to thank Dr Sarah Harris of the University of Leeds for taking on the role of academic mentor at-a-distance and providing me with advice and reassurance in moments of self-doubt. To my friends in Bristol and beyond who have endured this PhD with me, I extend my thanks for being endlessly forgiving of my lateness or absence at social events, and for ceaselessly believing in my ability as a scientist (at times contrary to all available evidence). In particular, I would like to thank Dr Ceri-Wyn Thomas and Dr James Verdon for their advice, encouragement and support.

To my parents, Andy and Una Inkpen, thank you for your warm words of encouragement and unfaltering belief in me. Your expectation that I always be best version of myself has been a driving force in my life, as has your example of determination. Finally, I would like to thank my two best friends, Dr Claire Mitchell and Dr Lara Small. Without the unconditional and unfaltering love and support of these two amazing women I would not have been able to complete this PhD.

Contents

List of Figures

1. Introduction

2. Methods

3. Active Dynamics

4. Passive Dynamics

5. Gap Junctions and Morphology

6. The Effect of Neurobiotin on Spiking Properties

7. Multi-parameter Optimisation of Conductance-Based Hodgkin-Huxley Models

List of Abbreviations

ACSF	-	Artificial cerebral spinal fluid
AHP	-	After hyperpolarisation
AIS	-	Axonal initial segment
ANOVA	-	Analysis of variance
AP	-	Action potential
C	-	Capacitance
Ca	-	Calcium
DAPI	-	4′,6-diamidino-2-phenylindole
GJCC	-	Gap junction coupled cells
gK	-	Fast potassium conductance
gL	-	Leak conductance
gM	-	Slow potassium conductance
gNa	-	Sodium conductance
HC	-	Holding current
K	-	Potassium
Na	-	Sodium
NB	-	Neurobiotin
P	-	Postnatal day
PBS	-	Phosphate buffered saline
PD	-	Passive dynamics
PFA	-	Paraformaldehyde
RMS	-	Root mean squared
SEM	-	Standard error of the mean
Vm	-	Membrane potential

1 Introduction

How do cortical neurons go from immature unconnected cells, to functional, mature, efficient units, integrating sensory information and determining behaviour? A biophysical approach, observing a neuron as a balance of inputs and outputs controlled through the combined action of different features, can improve upon our understanding of neuronal development. The biophysical underpinning of development that determines the trajectory of maturation in cortical neurons remains an area of contention, and is the subject of this thesis.

When considering the biophysics of developing cortical neurons, where better to start than with the most fundamental unit of brain activity and neuronal communication: the action potential. Often regarded as simply a binary unit of activity, the action potential contains information within its height, width, waveform, timing, and the frequency at which it is fired. This information, once transmitted to other maturing neurons, informs further development, triggering gene transcription, protein expression and the initiation of plasticity mechanisms (Khazipov and Luhmann 2006, Valiullina, Akhmetshina et al. 2016). This adaptation of biophysical properties, particularly over the dynamic first two postnatal weeks, is reflected in the changing waveform of the action potential. When combined with observations of changing neuronal morphology, and with the intrinsic and passive dynamics of the cell – features that affect spiking activity – the forces that drive a cell towards maturity and function can be elucidated.

As development is investigated, more subtle questions can be asked. Is development a gradual process, or are there critical periods when biophysical properties of the neurons fundamentally change? Through a combination of electrophysiology and microscopy a picture of the neuron as a dynamic, biophysical unit with inputs and outputs, can begin to be understood. However, a repertoire of experimental techniques alone is limited in scope for both comprehension of the developing neuron, and for making predictions, due to the interdependencies of developmental processes. The combination of experimental techniques and computational models can therefore be used to illuminate the primary drivers of neuronal development, and their corresponding relationships.

Though evidence of developmental changes to the action potential (AP) waveform in cortical neurons have been reported previously, observation and characterisation of how these changes present themselves, and how they influence other developmental processes, remains a gap in

the developmental neuroscience literature. Additionally, the synergy of different developmental changes – individual cell growth, formation of ion channels, formation of neuronal networks –to provide optimum behaviour, has been discussed previously by theoreticians and computational neuroscientists, but experimental application of these interdependent relationships remains elusive, partly due to the overwhelming complexity of such a problem. Suggestions of 'tuning' and gain scaling of neurons have been theorised, without conclusive experimental demonstration.

This thesis begins with an introduction to the development of cortical neurons in neonatal mouse somatosensory cortex, and an overview of the literature surrounding developmental neuronal biophysics and the computational techniques that can be used to decode these biophysics. It continues by describing the methods of investigation used to attempt to advance our knowledge on the subject. Following the methods are five results chapters, exploring active dynamics, passive dynamics, gap junctions and morphology, the unexpected effects of dyes on the biophysical properties investigated, and the development of optimised conductance-based models that could, in the future, shed light on the experimental results presented. In the final section, the implications of the presented data are discussed, caveats examined and ideas for future work put forward.

1.1 The developing cortical neuron

The growing brain of very young animals

In mammals, the formation of the brain does not reach completion in utero but continues through infancy - this can be seen on the microscopic level by examining the developmental trajectory of individual neurons. The brain forms in an inside-out manner, with the most vital neuronal networks (those that control breathing, for example) formed first, and the cortex formed last (Turco and Kriegstein 1991, Li, Fertuzinhos et al. 2013); consequently, neurons of the cortex have prolonged developmental trajectories.

The mouse model of the brain

In immature brains, the features of cortical formation and organisation are surprisingly well-preserved across evolution. Though the patterns of cortical development are repeated across mammalian species (on different spatial and temporal scales), a favourite and commonly used animal for models of brain development is the mouse. Bred to be close to genetically identical, C57BL/6 mouse pups are born after 19-21 days of gestation into litters of typically

4 to 8 pups (Murray, Morgan et al. 2010). Weaned within three weeks post birth (Williams 2000), the short gestation period, high number of pups per litter, and rapid development of the mouse make it a useful model in studies of brain development. Huge changes in cortical structure and neuronal function can be observed in mouse pups in as short a period as a single week. The use of electrophysiology to observe these developmental changes of cortical neurons is well established. Electrical activity can be triggered within mouse cortical neurons even in the embryonic stages, and repetitive firing of action potentials can be observed from postnatal day 0 (Luhmann, Schubert et al. 1999). This early activity allows biophysical properties of the neuron to be studied across the duration of development.

The barrel cortex

The mouse processes its environment through the tactile sensory experience of whisking: of moving its whiskers back and forth and interpreting the subtle changes in deflection that result when the whiskers encounter environmental stimuli (Feldman and Brecht 2005) - both objects and textures (Jadhav, Wolfe et al. 2009). Thalamocortical projections relay sensory information from the whiskers to the cortex for interpretation (Shi, Xianyu et al. 2017), first to the somatosensory cortex of layer IV, then onto other cortical layers (Osterheld-Haas and Hornung 1996, Valiullina, Akhmetshina et al. 2016). In a quite beautiful example of the specificity of the somatosensory cortex, the projections from each whisker pad reach to one discrete area of cortical layer IV per whisker (Feldman and Brecht 2005, Li, Fertuzinhos et al. 2013, Mizuno, Luo et al. 2014), known as a barrel (owing to its ovoid shape). As the mouse pup senses and integrates its environment, the connections between cells of the barrel cortex form, and the cellular morphologies self-organise to best integrate the information. The somata of barrel cortex neurons self-organise around each barrel edge, their dendrites facing inwards to form connections with afferent thalamocortical axonal projections (Li, Fertuzinhos et al. 2013, Mizuno, Luo et al. 2014). The inter-barrel septa that form in the absence of grey matter define the barrel boundaries as the mouse matures. Barrels in the mature mouse are arranged in a perfect map of the whiskers, provided ample sensory information is gleaned (Woolsey and Van der Loos 1970, Feldman and Brecht 2005, Mizuno, Luo et al. 2014).

The cells of the barrel cortex keep developing into the second postnatal week, as do the barrels themselves. Influenced by sensory experience and consequent synaptic plasticity, the barrels provide a representative region of the brain in which to study postnatal maturation, the development of which is correlated to the advancing behaviour of the young mouse (Feldman and Brecht 2005). Additionally, with the cortex so rapidly developing, the cells of the different cortical layers can easily become confused in the flux of radial migration; the barrels

provide a tangible cortical map that ensures experimental consistency in brain region and thalamocortical input.

Cellular morphologies

The somatosensory cortex contains a great many types of cells. Broadly defined into two classes – excitatory and inhibitory (Feldmeyer, Egger et al. 1999, Staiger, Flagmeyer et al. 2004) – cortical neurons form networks of positive and negative feedback loops for the processing of sensory information. Within the networks of the barrel cortex, the excitatory cells are generally classified as one of three cell types: spiny stellate cells, pyramidal cells, and star pyramidal cells (Feldmeyer, Lübke et al. 2002, Valiullina, Akhmetshina et al. 2016).

The spiny stellate cell is the classic cell of the Layer IV barrel cortex. With a spherical soma and star-like dendritic arbour, the spiny stellate cell grows increasingly asymmetrical with development, as their dendrites reach towards the terminals of the thalamic cell axons in the centre of the barrel (Feldmeyer, Egger et al. 1999, Staiger, Flagmeyer et al. 2004, Li, Fertuzinhos et al. 2013).

Pyramidal cells are more readily associated with layer III and layer V of the cortex but have been reported to be present within and around the barrels, their apical dendrites stretching up towards cortical layer I. Characterised by their triangular soma, pyramidal cells transmit information on to other layers of the cortex and other cortical columns (Staiger, Flagmeyer et al. 2004).

Finally, star pyramidal cells exhibit a morphology that is intermediary between spiny stellates and pyramidal neurons (Staiger, Flagmeyer et al. 2004). It has been reported that star pyramid cells within the barrel cortex retract their apical dendrites with maturation, becoming more stellate in the process (Callaway and Borrell 2011, Li, Fertuzinhos et al. 2013).

The ratio of different excitatory cell types within rat layer IV barrel cortex has been reported as approximately 80% spiny stellate 20% star pyramidal (Feldmeyer, Egger et al. 1999) but given ongoing cell migration during the first week of postnatal development, these proportions may not be accurate for immature cells.

The use of molecular tracers and dyes to illuminate the morphologies of cortical neurons (for example, Lucifer Yellow, Biocytin and Neurobiotin (Huang, Zhou et al. 1992, Peinado, Yuste et al. 1993, Penn, Wong et al. 1994, Staiger, Flagmeyer et al. 2004, Káradóttir and Attwell

2006, Dehorter, Michel et al. 2011)) have been well established for many years and have been used to demonstrate the increases in neuronal size and complexity of dendritic arbour that come with postnatal maturation. Whilst mature and complex dendritic arbours make it easy to distinguish cell types, the relatively simple morphologies of very immature cells, with only a few primary dendrites, and little in the way of dendritic spines (Luhmann, Schubert et al. 1999), make this categorisation more difficult. This is compounded by the spiking behaviours: excitatory cells of the immature mouse have been reported to produce indistinguishable electrophysiological behaviours, and have therefore been grouped in previous analysis (Valiullina, Akhmetshina et al. 2016).

Migration and differentiation

Over the first few postnatal days, the most external layers of the cortex are still forming. From the cortical subplate, neurons extend primary dendrites towards the pial surface and migrate up through their respective cortical columns to their ultimate position in the laminar planes of the cortex (Rakic 1988, Turco and Kriegstein 1991, Osterheld-Haas and Hornung 1996, Elias and Kriegstein 2008). Migrating neurons begin their journey exhibiting a common, immature and relatively simple morphology, resembling pyramidal neurons (Callaway and Borrell 2011, Li, Fertuzinhos et al. 2013). Once neurons arrive in their laminar layer, they undergo the process of differentiation; layer IV neurons between postnatal day 2 to postnatal day 4 are virtually indistinguishable in terms of their morphology, whereas cells only a few days older show dramatically different shapes, owing to the process of differentiation. During differentiation the cell undergoes extensive dendritic and axonal growth (Callaway and Borrell 2011), allowing the formation of synapses with neurons in different cortical layers. The changes in morphology allow the neuron to make synaptic connections and begin to communicate in functional networks (Mizuno, Luo et al. 2014).

1.2 The biophysical neuron

An electrical understanding of the neuron

Thermodynamic perspectives on the neuron underlie the importance of controlling the temperature in studies of neuronal behaviour (Heiurg and Jackson 2007, Andersen, Jackson et al. 2009, Hady and Machta 2015), but biophysical perspectives of the neuron generally consider it as a purely electrical entity (Rall 1969, Durand 1984). Indeed, the individual neuron can be thought of as an electrical circuit of multiple branches, with each branch representative of a different region of the cell, governed by dynamics that reflect the

morphology through capacitor-resistor components (Durand, Carlen et al. 1983), and the voltage-gated ion channels through sources of potential (Hodgkin and Huxley 1952). The contributions of these electrical components can be investigated through electrophysiology.

The maturation of cortical neurons in the neonatal mouse is correlated with a number of changes that can been seen through the lens of electrophysiology, including a more hyperpolarized resting membrane potential (Luhmann, Schubert et al. 1999) increased repetitive firing of action potentials (Bigiani, Cristiani et al. 2002, Valiullina, Akhmetshina et al. 2016), and an increased sensitivity to quickly fluctuating electrical signals (Gjorgjieva, Mease et al. 2014).

Measurements of the input resistance are inherent to most patch-clamping studies in rodents. Across the period of postnatal development, the input resistance has been reported to decrease with age, changes that have been previously related to the surface area of the cells, with highest input resistances correlated to the smallest cells (Luhmann, Reiprich et al. 2000, Valiullina, Akhmetshina et al. 2016). It is this connection between cell size and input resistance, as well as ion channel expression and input resistance, that would appear to drive the age-dependency.

The relationship between biophysics and cell morphology

Corresponding to the change in input resistance, morphological changes with age may influence the sub-action-potential-threshold electrical properties of the lipid bilayer cell membrane (D'Aguanno, Bardakjian et al. 1986). These passive dynamics can be analysed by modelling the cell membrane as a capacitor (Gentet, Stuart et al. 2000). The cell membrane capacitance has been shown to increase both with cell surface area and postnatal age (Zolnik and Connors 2016), leading to a decrease in the cell membrane time constant. The dendritic arbour of a neuron is known to grow with development, particularly during critical periods of spinogenesis (Luhmann, Schubert et al. 1999, Ashby and Isaac 2011), greatly changing the total neuronal surface area and consequently the membrane capacitance. The interdependence of the passive dynamics with the spiking behaviour must therefore be considered when investigating biophysical maturation (Connors, Gutnick et al. 1982, Wright, Bardakjian et al. 1996, Lepora, Blomeley et al. 2011).

1.3 Active Electrical Dynamics of the Cortical Neuron

The action potential

Action potentials, detected as large and distinctive time-dependent changes in the cellular membrane potential, are the primary means of neuronal communication (Hodgkin and Huxley 1952, Hille 2001). The action potential originates within the axonal initial segment (AIS) and propagates back into the soma and dendrites (Yamada 1998). This jolt of electricity quickly traverses the length of the cell, changing the polarity of the membrane through its trajectory, and triggering the release of neurotransmitters at the axonal boutons (Hille 2001). Colloquially known as 'spikes', action potentials drive the patterns of neurotransmitter release that underpin plasticity, controlling calcium influx, influencing gene transcription, and facilitating the formation of functional cell networks (Li, Fertuzinhos et al. 2013). The distinctive action potential waveform is the result of nonlinear and time-dependent currents in and out of the neuron (Hodgkin and Huxley 1952) due to both active (voltage-gated ion channel dependent) and passive (non-voltage-gated) dynamics. The action potential's distinctive shape makes it easily identifiable during electrophysiology experiments; in current clamp electrophysiology, the action potential is observed as a distinctive pulse of voltage over a timescale of milliseconds. The specific dynamics of the AP waveform, along with the spiking frequency, are well known to vary with cell type (Connors and Gutnick 1990, Luhmann, Reiprich et al. 2000, Bean 2007, Guan, Armstrong et al. 2015, Liu, Blair et al. 2017) across animal species (Daou, Ross et al. 2013, Ciarleglio, Khakhalin et al. 2015). Evidence for the changing waveform with age during the period of postnatal maturation has been previously presented, whether in neurons of the thalamic reticular nucleus or layer IV excitatory cortical neurons (Parker, Cruikshank et al. 2009, Valiullina, Akhmetshina et al. 2016), but the specific causes of these developmental changes remain elusive.

The action potential drives synaptic plasticity

In the immature brain, the early firing of action potentials is necessary for synaptogenesis, synaptic plasticity, and the formation of networks (Khazipov and Luhmann 2006, Valiullina, Akhmetshina et al. 2016). Since the 1940s, Hebbian plasticity ("*cells that fire together wire together*") (Hebb 1949) has provided the foundation of our understanding of the interplay between the discharging of action potentials and neuronal connectivity, but a significant interplay also exists between action potential waveform and timing, and synaptic transmission. The duration of the presynaptic waveform has been shown to strongly influence synaptic latency (Katz and Miledi 1967, Boudkkazi, Fronzaroli-Molinieres et al. 2011), and

action potential duration may ultimately determine neuronal coactivity, that in turn drives spike-time dependent plasticity '*out of sync, lose your link*' mechanisms (Bi and Poo 1998).

As the cell grows in size and morphological complexity with postnatal age, the geometry and ionic fluxes across different parts of the morphology give rise to local electric fields which may themselves have an influence on plasticity. Specifically, this may lead to scaling of the voltage response at the synaptic level, providing a method of neuronal encoding. This scaling of synaptic inputs allows the neuron to encode information and maintain optimum levels of excitability, whilst compensating for the variability inherent in neural input (Turrigiano and Nelson 2004).

It is necessary to conclude that the biophysical properties of a neuron isolated from its synaptic inputs may not be an accurate representation of true neuronal behaviour. Observations of synaptogenesis across developmental stages inform our picture of the biophysical underpinning of the changing action potential.

Action potential shape is determined by ion channels

Since the introduction of Hodgkin-Huxley models, developed on squid giant axons in the 1950s (Hodgkin and Huxley 1952), the biophysics of neurons, including cortical neurons, have been implicitly correlated with the densities of voltage-gated ion channels within the cell membrane (Hille 2001, Bahrey and Moody 2003, Moody and Bosma 2005). Changes to the shape of the action potential can therefore be used as a proxy for the varying populations and densities of ion channels (Picken Bahrey and Moody 2003, Richter and Gjorgjieva 2017), and their corresponding current densities, for example, in somatosensory pyramidal neurons (Luhmann, Reiprich et al. 2000).

Voltage-gated sodium (Na) channels hold the role of the instigator of action potentials (Hodgkin and Huxley 1952, Connors, Gutnick et al. 1982, Hille 2001, Baranauskas 2007). When the membrane potential is sufficiently depolarised, these channels open and allow the flow of Na^+ ions, contributing a large and fast membrane current that pushes the neuron quickly to dramatic depolarisation, many tens of millivolts above the resting membrane potential. Returned to the extra-cellular space via the action of a Na+/K+-ATPase enzyme pump (Krouchev, Rattay et al. 2015), the movement of Na ions that and the resulting action potential is a high metabolic cost, and a determinedly active phenomenon.

The re-polarisation phase of the membrane potential is governed by voltage-gated potassium (K) channels (Hodgkin and Huxley 1952, Baranauskas 2007). Voltage-gated K^+ channels come in a wide diversity of subtypes (Storm 1987). Some ($K_v1.1$, $K_v1.2$, $K_v1.3$, $K_v1.6$, for example) are thought to be primarily responsible for maintaining membrane potential and modulating excitability in neurons across the cortex, whilst others are thought to be necessary for neuronal afterhyperpolarisation ($K_v1.4$), or regulation of AP duration (Kv3.2) (Gutman, Chandy et al. 2005). The balance of the populations of ion channels and their respective subtypes varies with cell type to produce different patterns of activity, but can be manipulated via various stimuli; when one potassium current is suppressed, for example in ion channel blocking experiments, others compensate, pointing towards homeostatic mechanisms that ensure robust spike shape (O'Leary, Williams et al. 2014). Amongst the subtypes, BK channels dominate many studies, since they are responsible for a substantial proportion of the hyperpolarising potassium current (Kimm, Khaliq et al. 2015). Other K^+ channel currents may be slower, and follow the fast BK current, moderating the overall kinetics (Pospischil, Toledo-Rodriguez et al. 2008). An inward calcium current follows these sodium and potassium currents (Kimm, Khaliq et al. 2015), but it has been argued that the ratio of sodium conductance to potassium conductance alone is the main determinant behind spiking output and therefore the sensory information encoded within the action potential (prior to the after-hyperpolarisation) (Gjorgjieva, Mease et al. 2014).

Ion channels have been shown to be functionally expressed early in postnatal development in taste neurons of the mouse vallate papilla, with different ion channel types formed at different rates (Bigiani, Cristiani et al. 2002). This biophysical heterogeneity stabilises by adulthood, facilitating optimum electrical activity. However, the path to maturity is not necessarily linear: the proportion of sodium to potassium channels across development is not consistent, with the expression in sodium ion channels reaching high densities much earlier than potassium ion channels in cells of the mouse ventricular zone (Bahrey and Moody 2003). The picture is further complicated by the fact that ion channels may not be homogeneously distributed across the neuronal membrane, with, for example, potassium channel abundance lessened in the more distal axonal membranes of cortical neurons (Boudkkazi, Fronzaroli-Molinieres et al. 2011).

Through the blocking of voltage-gated ion channels, the ionic currents responsible for different action potential aspects can be identified (Krouchev, Rattay et al. 2015). However, computational models of the varying contribution of the currents can also be used to explore

which conductances are the dominant influences on the action potential shape, and determine how this changes across different stages of development (Wester and Contreras 2013).

The different rates of ion channel expression can therefore be implicated in determination of cell growth, morphological changes and electrophysiological signatures via changes in ionic conductance and synaptic plasticity (O'Leary, Williams et al. 2013), ultimately having an effect on the computational function and efficiency of the cell.

Activity-driven genetics underpin ion channel expression

The abundance and density of the ion channels, and the consequential shape of the action potential, is limited by gene transcription and subsequent ion channel protein expression, phenomena triggered by electrical activity (Stemmler and Koch 1999, Khazipov and Luhmann 2006, Li, Fertuzinhos et al. 2013). Strong correlations between mRNA expression and functional ion channel expression in specific neurons have been shown (Schulz, Goaillard et al. 2006, Schulz, Goaillard et al. 2007) and ion-channel specific genes identified (Toledo-Rodriguez, Blumenfeld et al. 2004). Cells that show similar protein expression patterns also show corresponding similarity in electrical properties, further confirming this link (Schulz, Goaillard et al. 2006). This evidence, and the large variations in mRNA expression of ion channel genes found in cortical neurons, point to neuronal activity and subsequent gene transcription being controlled by homeostatic mechanisms (O'Leary, Williams et al. 2013).

The action potential changes with development

The flux of ionic conductances through development is reflected in the changing shape of the action potential across cortical neurons (Bigiani, Cristiani et al. 2002), with action potentials observed to become taller and narrower as the animal matures (Luhmann, Reiprich et al. 2000, Nakamura, Harada et al. 2015). In mouse auditory neurons, for example, a 66% reduction in presynaptic action potential width between postnatal day 5 (P5) and P12 has been observed (Taschenberger and von Gersdorff 2000), and similar developmental profiles of the action potential have been noted in spiking of neurons in other brain regions (Ben-Ari, Cherubini et al. 1989). Previous doctoral thesis work by Laura Murray has provided evidence for the changing shape of the action potential with neuronal development in excitatory cells of the barrel cortex of mice from new-born to two weeks old (Murray 2015), providing the basis of the experimental work presented in this thesis.

Often regarded as discrete units of time-dependent information, the action potential may be specifically shaped to maximise efficiency of the information communicated. A broader action potential may be useful for coincidence detection: by prolonging the spike duration, the likelihood of two cells being coincident in their firing properties would increase. However, with a long spike duration, precision of the signal, and hence the fidelity of the information that can be conveyed, would be compromised. Therefore, it could be hypothesised that a broader spike of lower amplitude would be beneficial to the neuron during the early developmental phase, when the information inputs are minimal due to low synaptic connectivity. As the neuron develops, becoming more morphologically complex and synaptically connected, the increased information input that would be expected would lead to patterns of gene expression, resulting in a more precisely timed spike, with a narrower waveform. Just such changes to the AP waveform have been observed in excitatory neurons of the barrel cortex in earlier work (Murray 2015); this thesis seeks to confirm these observations, but explore the patterns of waveform development, relating them to other observations of development-based change.

Current-clamp electrophysiology in acute ex-vivo slices has been used extensively to investigate the waveform of the AP in a variety of neuron subtypes (Sabatini and Regehr 1997, Kimm, Khaliq et al. 2015, Palacio, Chevaleyre et al. 2017), but questions still remain regarding the particulars of the developmental trajectory of the waveform. Postnatal maturation is known to be a highly dynamic period in terms of cell differentiation and migration (Osterheld-Haas and Hornung 1996, Cina, Bechberger et al. 2007), and developmental changes may correspondingly be expected in cell communication and electrical activity (Winnubst, Cheyne et al. 2015).

Homeostasis of electrical activity in developing neurons

As the neurons of the cortex change and mature, they maintain functionality. In order for a neuron to continue exchanging electrical information throughout the transitions of maturation, the delicate balance of biophysical properties must be maintained despite the massive changes of gating channel proteins and subsequent ionic fluxes (O'Leary, Williams et al. 2013, Ciarleglio, Khakhalin et al. 2015). The maintenance of homeostatic equilibrium through biophysical compensation has been observed across species, with strikingly different combinations of conductances observed to output strikingly similar patterns of behaviour (Turrigiano and Nelson 2004, Ciarleglio, Khakhalin et al. 2015). Such homeostatic regulation of neural activity stops neuronal circuits from becoming either inactive or over-active

(Turrigiano and Nelson 2004), and allows ion channels to become more or less activated or populous to compensate for one another (Kimm, Khaliq et al. 2015, Szücs and Huerta 2015). A large range of conductances through the many different ion channels may result in near identical patterns of neuronal activity; homeostatic tuning approaches have been employed to comprehend this balancing act of variables (Marder and Goaillard 2006).

Computational studies have suggested that each neuron may have a genetically encoded target activity pattern, on which the conductances from different ion channels can converge (LeMasson, Marder et al. 1993, Liu, Golowasch et al. 1998). Alternatively, it has been suggested that the balance of ion channels is underpinned by homeostatic control mechanisms that couple the expression rates of individual conductances to cell intrinsic readout of activity (O'Leary, Williams et al. 2013), a hypothesis that implies that there is considerable flexibility in the patterns of conductances that allow a target activity to be maintained.

As well as ensuring survival throughout maturation, it has been postulated that homeostatic plasticity allows the dynamical range of the neuron to be maximised, therefore ensuring that maximum sensory information can be integrated and learned (Ciarleglio, Khakhalin et al. 2015). Individual cortical neurons have been shown to learn to scale the gain of their active outputs within the first postnatal week (Mease, Famulare et al. 2013). Gain-scaling, the adaptation of the neuron to its electrical inputs and outputs, has been reported to continue through adolescence and adulthood, (Richter and Gjorgjieva 2017). Waves of sensory information that slowly propagate across the cortex in immature rodents are replaced by fast and location specific fluctuations in mature animals, with the gain scaled to optimise sensory integration (Gjorgjieva, Mease et al. 2014). Indeed, this may be the driving force throughout maturation that is visible in the action potential's changing shape. For example, the dynamically changing ratio of sodium to potassium conductance during the first postnatal week may represent a gain-scaling process (Mease, Famulare et al. 2013). Gain scaling may be manifest in broad AP waveforms that maximise coincidence detection fired by immature cells: a broad spike would, hypothetically, be capable of sampling a wide range of time points, and therefore a wide range of inter-spike-intervals, providing the necessary range of inputs to tune neuronal activity through gene expression and physiological changes on the cellular level. The resultant change in action potential waveform may then scale the gain of the information exchanged, improving the efficiency of the individual neurons and their neuronal circuits. Presumably, such improvements in efficiency would result in decreases in AP waveform breadth (duration) as neurons become more tuned to one another, and less

breadth is needed for coincidence detection, along with corresponding increases in AP waveform height (amplitude), and more complicated patterns of spiking activity, as stronger and more intricate patterns of information can be conveyed.

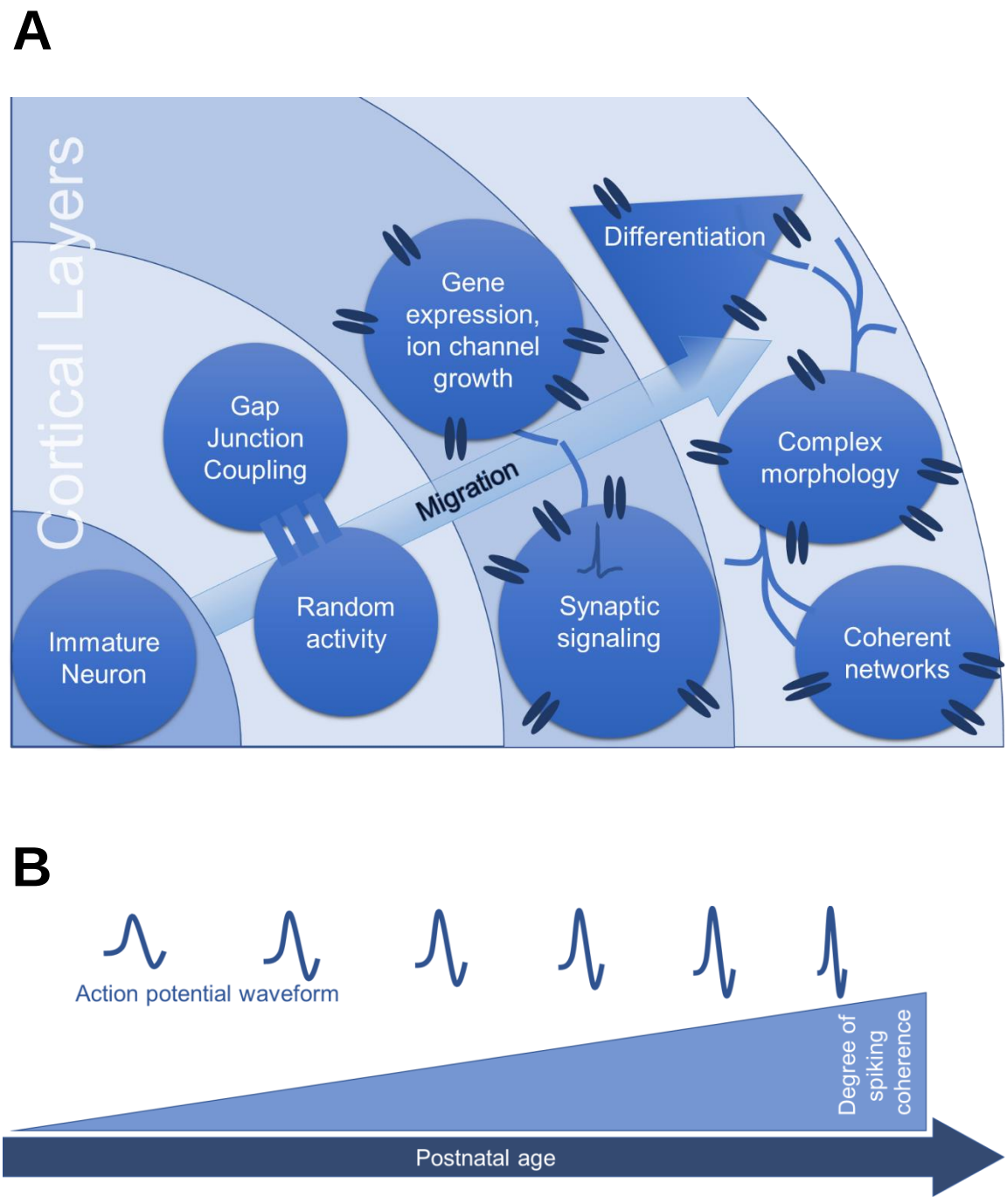

Figure 1.1: The process of maturation for cortical neurons. As neurons develop they undergo changes in connectivity (**A**), facilitated by gap junctions and synapses, changes in the degree of ion channel growth, differentiation, migration, increasing spike-type coincidence, and the formation of coherent networks. **B**: All the while, the action potential waveform is changing

It has been suggested that as neurons grow, the changing membrane capacitance and resistance must be balanced with the synapses and the ion channels to maintain optimal activity for the neuronal network as a whole (Marder and Goaillard 2006). Therefore, these changing intrinsic and passive biophysical properties may provide the limits to ion channel gene transcription. As implicated in studies of the currents underlying the action potential, the proportion of sodium to potassium ion channels is highlighted as a dominant factor in this mechanism, since it has been shown that the ratio of expression of sodium and potassium currents allows the gain to be scaled most effectively (Mease, Famulare et al. 2013).

Development and synaptic plasticity are intrinsically coupled: development is filtered through experience, via the mechanism of synaptic plasticity. In other words, experience dependent plasticity applies strong homeostatic constraints on the mechanisms of biophysical development (Turrigiano and Nelson 2004, Winnubst, Cheyne et al. 2015).

Spontaneous activity in immature neurons

A widely reported phenomenon, common to immature neurons across species, is that of spontaneous activity (Zhang and Poo 2001, Winnubst, Cheyne et al. 2015, Leighton and Lohmann 2016, Valiullina, Akhmetshina et al. 2016, Richter and Gjorgjieva 2017). The spontaneous firing of action potentials, detected in its earliest form from late embryonic periods, drives the earliest patterns of gene expression that set the neuron on its developmental trajectory and ultimately decide cell growth, differentiation and synaptic plasticity (Khazipov and Luhmann 2006). This early activity determines synaptic connectivity within both sensory and motor neuronal ensembles (Zhang and Poo 2001, Winnubst, Cheyne et al. 2015), but does not necessarily continue through to maturity: in mouse sensorimotor cortex, the critical period for gain-scaling of neuronal outputs has been reported to coincide with the end of spontaneous activity (Mease, Famulare et al. 2013). However, synaptogenesis as a consequence of such activity *without* pre-formed synapses and established neuronal networks presents us with a ‘chicken and an egg’ scenario – which comes first, the synapse or the activity? The answer may lie in the early appearance of electrical synapses, or gap junctions, which facilitate the communication of relatively simplistic electrical signals between neighbouring cells from the earliest stages of development (Connors, Benardo et al. 1983, Turco and Kriegstein 1991, Peinado, Yuste et al. 1993, Penn, Wong et al. 1994, Kandler and Katz 1995, Montoro and Yuste 2004).

1.4 Gap junctions

Structure and function of gap junctions

Gap junctions are protein channels between cells that connect the cellular cytoplasm, allowing an intercellular cytoplasmic equilibrium to be reached (Goodenough and Paul 2009, Leighton and Lohmann 2016). Each gap junction is a hexamer structure of connexin proteins that forms a channel between neighbouring cells (Goodenough and Paul 2009). Highly expressed during embryonic stages (Elias and Kriegstein 2008), gap junctions facilitate the bidirectional exchange of information in the form of both electrical signals and some small molecules, allowing neuronal communication in the absence of chemical synapses (Montoro and Yuste 2004, Cina, Bechberger et al. 2007). Gap junctions have been reported to have a phenomenally fast turnover, on the order of minutes, (Belousov and Fontes 2013) implying that, relative to synapses, they have low metabolic costs. Organised radially around the cell, they transmit information on slower timescales than chemical synapses (Yuste, Nelson et al. 1995).

The role of gap junctions in development

In the thalamus, gap junctions have been shown to precede the formation of inhibitory networks and be necessary for the development of complex dendritic morphologies (Zolnik and Connors 2016). Many groups have postulated that gap junction are developmentally transient, hypothesising that their role is that of a functional network blueprint (Kandler and Katz 1995, Montoro and Yuste 2004). Gap junctions may provide a method through which neurons can synchronise their output prior to synaptogenesis, or, alternatively they may provide a homeostatic buffer to allow robust neuronal activity throughout development (Leighton and Lohmann 2016). Presumably, the activity that results from gap junction coupling has an effect on gene transcription and protein expression similar to that of synaptic inputs to the cell, ultimately resulting in the formation of chemical synapses.

Effects of gap junctions on measurable biophysics of developing neurons

When considering the presence of gap junctions in our understanding of the developing neuron, the question arises of how they might affect the balance of biophysical inputs and outputs. They may contribute to the input resistances and passive currents in and out of the neuron (Feldmeyer, Egger et al. 1999), and therefore have an overall effect on the action potential shape.

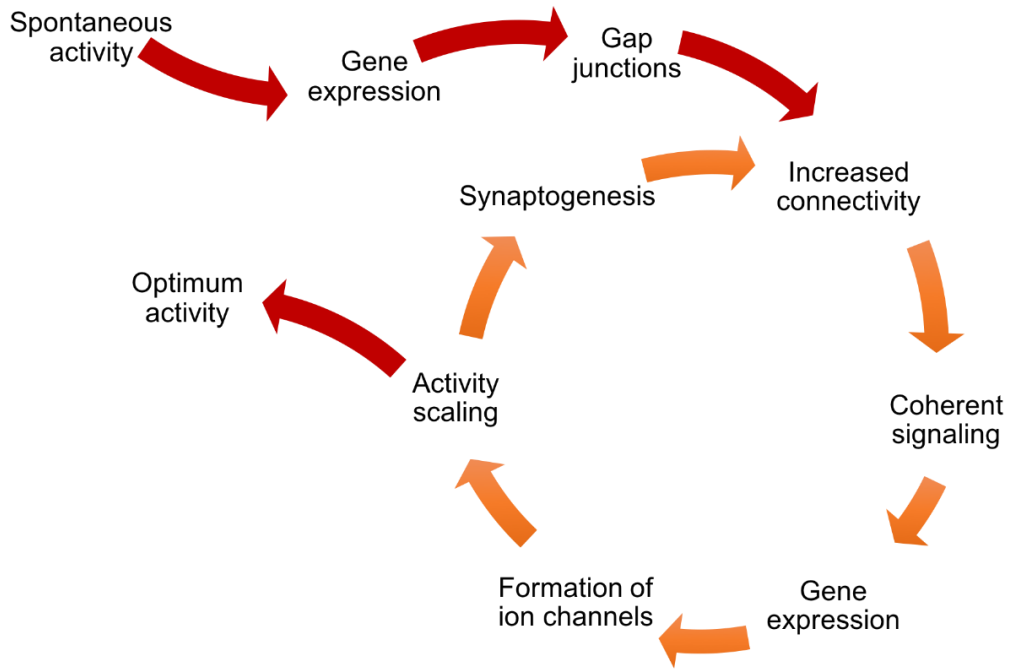

Figure 1.2: A hypothetical pattern of development. A feedback loop between connectivity, gene transcription, activity, and connection that allows the neuron to go from spontaneous activity to optimum activity.

1.5 Hodgkin Huxley models of action potentials

A biophysical understanding of the developing neuron warrants efficient and robust computational models that can provide testable predictions of the balance of currents in and out of the cell at any particular developmental timepoint. From these currents, the proportion of ion channels, and the contribution of morphological changes to passive dynamics can be estimated. Conductance-based Hodgkin-Huxley style computational models (Hodgkin and Huxley 1952) of varying complexity have been used to provide biophysical predictions of ion conductance channels in various different mature cortical neurons (Shaul, Yoav et al. 2007, Geit, Schutter et al. 2008).

Limitations of Hodgkin Huxley models

Like all computational models, the Hodgkin-Huxley model has implicit assumptions that limit its scope. It assumes isopotential compartments of known geometry, consequently the classical version of the model breaks down when small morphological features such as dendritic spines are considered, where the fluxes of ions may be constrained by the limited

space (Sabatini and Svoboda 2000, Biess, Korkotian et al. 2007, Holcman and Yuste 2015). Additionally, the model has been shown to poorly describe the initiation period of the action potential, with cooperative action of voltage-gated ion channels not considered (Naundorf, Wolf et al. 2006). A wholly unphysiological assumption implicit in the model is that the reserves of ionic species are assumed to be infinite: there is no dependence on ionic concentrations beyond the reversal potentials (Yamada 1998). Despite these drawbacks, the Hodgkin-Huxley model is one of the most sophisticated and successful computational tools available for interpreting the action potential.

Multiparameter optimisation

Parameter optimisation of Hodgkin-Huxley style models remains necessary to achieve good fits to data, but this process can be fraught with difficulty (Shaul, Yoav et al. 2007, Geit, Schutter et al. 2008, Wulfram Gerstner 2009). Traditionally, error minimisation between model and data has been performed by comparing the simulated voltage output of the model directly with the spiking data. When the data and the model's output match, the model is judged to be a good fit, and the parameters that underlie the output are taken as accurate estimations. The optimisation of the model using such voltage-based techniques has been studied by many groups who have put forth variations on the method, including straight comparison of trace with data, smoothed by the inclusion of intracellular calcium dynamics (Ye, Rozdeba et al. 2014), root mean square (RMS) comparison between model and data (Brookings, Goeritz et al. 2014, Lankarany, Zhu et al. 2014), and comparison of phase-plane plots (Geit, Schutter et al. 2008).

Frequently, these voltage-based techniques are highly sensitive to spike-timing (Pospischil, Toledo-Rodriguez et al. 2008) and return complex error functions, making them reliant on stochastic exploration methods or evolutionary algorithms to find the correct values of the optimised parameters (Buhry, Pace et al. 2012, Lankarany, Zhu et al. 2014). Such algorithms can be computationally expensive and time consuming, and therefore unsuitable for comparison with highly variable developmental data sets. Alternative statistical mechanics density function methods have shown to produce very good estimates of conductances, but also require computationally expensive algorithms (Toth, Kostuk et al. 2011), whilst state-space methods with adaptive evolutionary algorithms have been shown to fit complex compartment models well to data (Vavoulis, Straub et al. 2012), but are again, computationally expensive.

By instead considering computation of the difference between passive and active neuronal currents, the optimisation can be reduced to a simple linear sum, in which a residual current error is minimised (Morse, Davison et al. 2001, Lepora, Overton et al. 2012). Such current-optimisation techniques are preferable since they not only are less computationally expensive than voltage-based methods, but they also produce a smooth error function where finding the solution is trivial, and does not require evolutionary algorithms.

In addition to providing testable predictions of neuronal biophysics, optimised models can provide us with multiparameter state-space landscapes, that allow us to explore theoretical limitations of biophysical homeostasis. The error function may not converge on a singularity, but instead on a shallow region of equilibrium, in which any solution set of conductances would produce effective firing activity, within certain limits (O'Leary, Williams et al. 2013).

1.6 Summary

The different aspects of cortical neuron maturation are not independent mechanisms, but are instead interdependent processes that influence one another and determine the ability of the developing neuron to communicate. Throughout all the developmental changes, each neuron must remain robust and able to function, even with gross biophysical changes over very short timescales. This implies a method of compensation between neuronal features, adjusting different properties of the neuron to keep it within limits of effective activity. Such compensation and improvement may be visible in changes to the action potential that act to balance coincidence detection with information transfer, specifically, the change from a broad spike of long duration to a narrow spike of short duration. The biophysical parameters move about this phase space to collectively compensate for one another's behaviour; a coupling of parameters that adapts across the course of maturation.

The combination of electrophysiology and multiparameter optimised conductance-based models makes a potentially powerful tool with which to study neuronal development. This thesis investigates the biophysical changes to excitatory neurons in the barrel cortex of mice across postnatal days P3 to P11. Covering changes in input resistance, action potential waveform, changes in surface area and morphology, changes in membrane capacitance and resultant membrane time constants, and the occurrence of networks of gap junction coupled cells, it attempts to describe the neuron as a biophysical entity, traversing a landscape of great

transformation. The use of computational models to interpret these data and make falsifiable predictions is considered, with the necessity of effective and efficient parameter optimisation explored. Additionally, the surprising result that Neurobiotin has an effect on the properties of the action potential waveform is quantified, and a dose dependency established.

As well as developing a fundamental understanding of the developmental pathway of cortical neurons, work on the biophysical changes evident over the first two postnatal weeks could have implications for our understanding of developmental diseases and hereditary conditions such as schizophrenia and autism. The biophysics of individual neuronal development will have implications for our understanding of how neurons begin to create cortical networks, and ultimately our understanding on how variations in such neural networks might manifest, as well as understanding how the brain recovers after ischemia. Finally, an understanding of the trajectory of development can help us to understand the trajectory of neurodegeneration, whether due to disease or aging.

By focusing on one area of the brain, in one species, over one brief window of time, this thesis hopes to elucidate the gross biophysical changes and patterns that occur with maturation, that they might provide predictions for experiments beyond the conditions explored here.

2 Materials and Methods

This thesis discusses both experimental and computational methods. The experimental methods are described in this chapter, whilst the computational methods – fitting of two compartment models to passive dynamics data, and evaluation of parameter optimisation techniques of Hodgkin-Huxley models – are discussed fully in Chapter 4: *Passive Dynamics*, and Chapter 7: *Multi-parameter Optimisation of Conductance-Based Hodgkin-Huxley Models*. An overview of the experimental and computational techniques is shown in **Figure 2.1**.

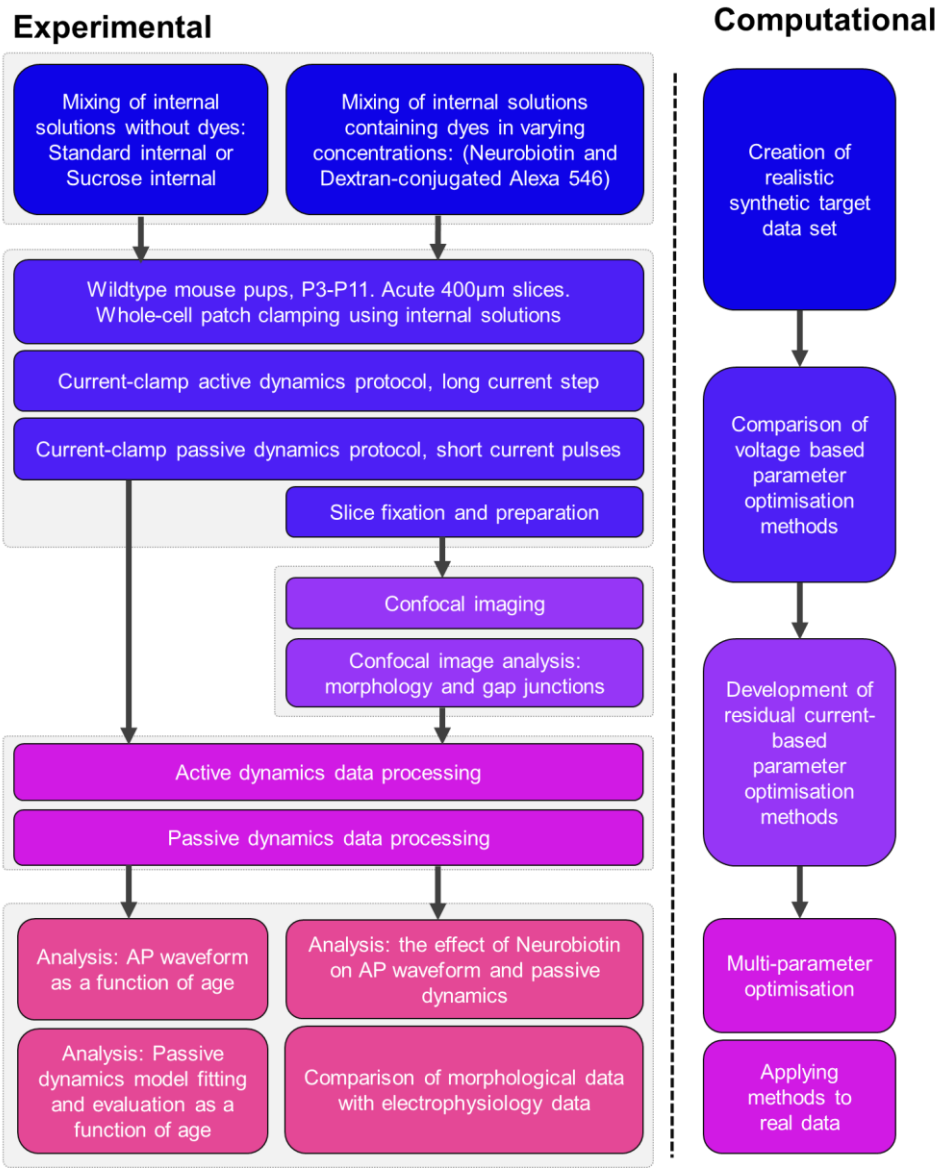

Figure 2.1: Experimental and computational methods used, in sequence. Experimental methods involved the collection of active and passive dynamics data from whole-cell current clamp electrophysiology experiments. In a subset of experiments, the intracellular internal solutions included dyes, which were used for post-hoc confocal imaging and analysis of cell morphology. Computational methods were used both during experimental analysis, and during multiparameter model optimisation based on synthetic target data (Chapter 7).

Age and genetics of mouse pups used

All aspects of these studies were performed with Home Office approval under section 5(4) of the Animals (Scientific Procedures) Act 1986. Wild-type C-57- Black.6 (C57BL/6) mice were used (Harlan Laboratories, Carshalton, UK). Pregnant dams were delivered on embryonic day 16, and typically gave birth after 20±1 days of gestation. Dams and their litters were housed in Techniplast 1144 conventional cages on a 12:12 light/dark cycle with nesting material, environmental enrichment and *ad libitum* access to food and water. Dams and litters were checked daily at the same time each day, but otherwise disturbed as little as possible. Mouse pups of both sexes were taken individually from the litter between days P3 and P11, as measured from discovery of their birth (i.e. postnatal age = Px ±24 hours).

Preparation of artificial cerebral spinal fluid

Chemicals were supplied by Thermo Fisher Scientific (Loughborough, UK), VWR (Leicestershire, UK), or Sigma Aldrich (Dorset, UK) unless otherwise stated.

Artificial cerebral spinal fluid (ACSF) for the maintenance and perfusion of slices was made consisting of 119.0mMol NaCl, 2.5mMol KCL, 11.0mMol D-Glucose, 1.0mMol $NaH_2OPO_4.H_2O$, 26.5 mMol $NaHCO_3$, 1.3 mMol $MgSO_47H_2O$, and 2.5mMol $CaCl_2$, dissolved in double-distilled H_2O. Cutting fluid for use during dissection was made of the same chemical composition as ACSF, except that $MgSO_47H_2O$ was increased to 9mMol to mitigate the excitotoxic effects of dissection.

Preparation of internal solutions prior to experiments

Carefully composed solutions made to replicate the chemical composition of the neuronal cytoplasm were used within the patch-pipette to retain equilibrium and cell vitality throughout the patching process. In total, five different internal solutions were made for use in experiments (**Table 2.1**)

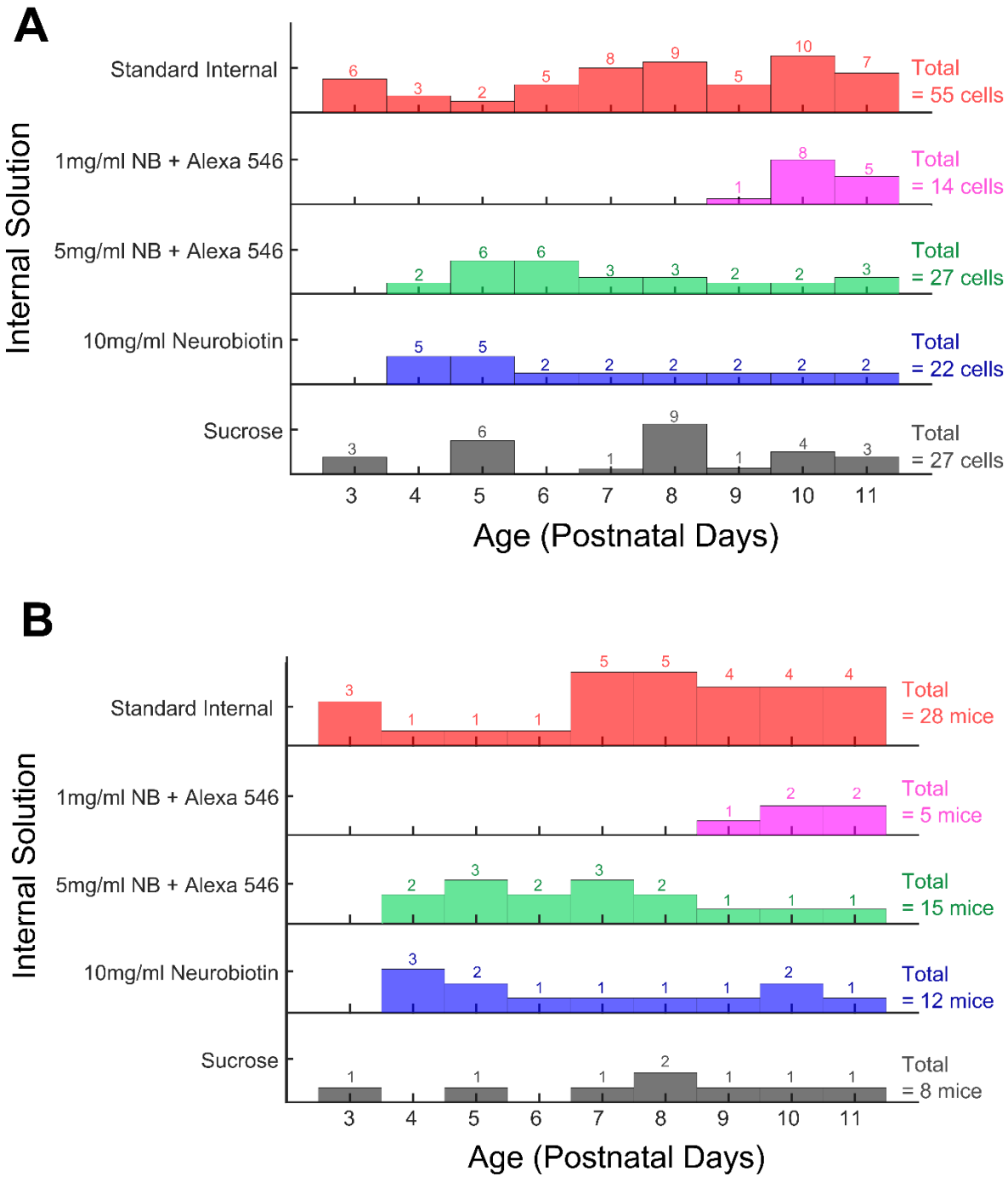

Figure 2.2: Age distributions of cells patched using different internal solutions.
A: The number of cells patched at each age using each internal solution are shown above each bar. Cells were patched from mice aged between 3 and 11 postnatal days. For the internal solution containing 1mg/ml Neurobiotin, only cells from mice aged P9-P11 were patched.
B: The number of mouse pups used.

Standard Internal solution was prepared first, with composition as described in **Table 2.1**. The solution was checked for osmolarity using an Advanced Instruments Model 3320 Osmometer, and acidity using an Accumet Basic AB15 pH Meter (Fisher Scientific, Loughborough, UK). H_2O or KOH was added in minute amounts to bring the osmolarity to 285±3mOsm and the pH to 7.25±0.05, within 5% of the predicted volume of 50ml (50±2.5ml). The 50ml of stock Standard Internal solution was then aliquoted into 50 1ml Eppendorf tubes (Eppendorf, Hamburg, Germany) and frozen for long-term storage. No internal solution was stored for longer than six months.

Morphological analysis of cells and gap junction detection was performed via the inclusion of dyes in three of the five internal solutions. Tracer molecule Neurobiotin (NB) (Vector Laboratories World Wide, CA, USA) was used (**Figure 2.3**); NB has been recommended for morphological analysis at concentrations of 1 to 2mg/ml (Campbell, Ducret et al. 2011), but for gap junction detection it is has been recommended in concentrations of 3-10mg/ml (Káradóttir and Attwell 2006), with concentrations up to 150mg/ml (15% weight/volume) also reported in literature (for example, (Peinado, Yuste et al. 1993, Penn, Wong et al. 1994, Zahs and Newman 1997)). Three different concentrations of Neurobiotin were used here: 10mg/ml (1% weight/volume), 5mg/ml (0.5% w/v) and 1mg/ml (0.1% w/v).

Dextran-conjugated Alexa Fluor 546 (Molecular Probes, Invitrogen, Paisley UK) was included in two of the internal solutions. The conjugation of Dextran, a large glucose molecule ($H(C_6H_{10}O_5)xOH$), pushed the total molecular weight to 10000g/mol, too large to fit through gap junctions (Elias and Kriegstein 2008). The inclusion of this large molecule aided differentiation of primary patched cells from gap-junction coupled cells.

NB stock internal solution was prepared via the dilution of 50mg NB powder in Standard Internal solution. 45ml of Standard Internal solution was prepared as described above, except that the potassium methylsulphanate ($KMeSO_4$) was reduced from 130mMol to 115mMol to compensate for the addition of NB on the overall osmolality (**Table 2.1**). Double distilled H_2O was added to bring the volume to just under 50ml. Under constant stirring using a magnetic stirrer, 4ml of this solution was removed and used to dissolve 50mg NB. Osmolarity and pH were again monitored as 1ml of the remaining Standard Internal solution was added to top up the NB solution to 5ml, at 285±3mOsm and pH to 7.25±0.05. The resulting mixture of 10mg/ml (1% weight/vol) NB internal solution was aliquoted into 20 Eppendorf tubes in volumes of 250µl before being frozen for long term storage.

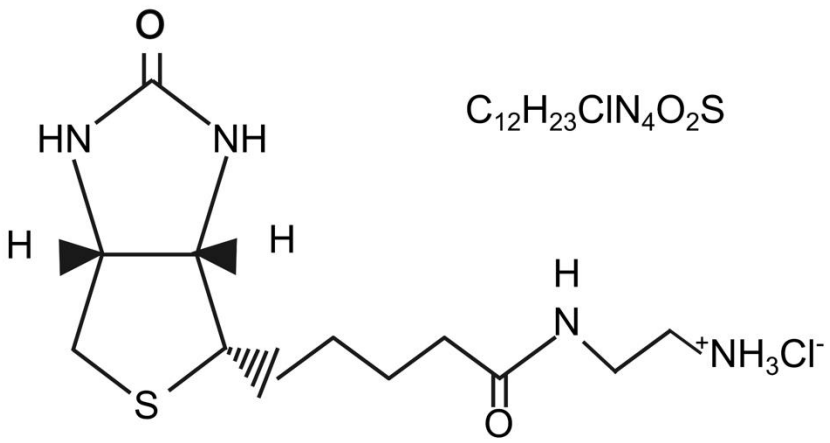

Figure 2.3: Chemical formula for Neurobiotin.

The three concentrations of NB-containing solution were created via different dilutions of NB stock internal solution in Standard Internal solution. For a NB concentration of 10mg/ml (1% w/v), NB stock internal solution alone was used. For a NB concentration of 5mg/ml NB (0.5% w/v), 10mg/ml NB stock internal solution and Standard Internal solution were mixed in the ratio 1:1 (0.2ml in 0.2ml). For a NB concentration of 1mg/ml NB (0.1% w/v), 10mg/ml NB stock internal solution and Standard Internal solution were mixed in the ratio 1:9 (0.04ml in 0.36ml). In each case, the mixture was vortexed (Lab Dancer Digital, VWR, Leicestershire, UK), centrifuged (VWR Ministar Silverline Galaxy centrifuge) and filtered. Prior to use, the 5mg/ml and 1mg/ml NB solutions were also spiked with 10µM Dextran-conjugated Alexa Fluor 546.

A fifth and final internal solution was prepared that had the same reduction in $KMeSO_4$ as that in the NB-containing internal solution, but to which inert sucrose was added to maintain the same osmolality of 285±3 mOsm; this internal solution was labelled as ‘Sucrose’ and was otherwise prepared exactly as described above.

Internal solutions were kept on ice at approximately 0°C to prevent the breakdown of magnesium adenosine 5'-triphosphate (Mg-ATP) and sodium guanosine 5′-triphosphate (Na-GTP). They were transferred into the micropipette using an Eppendorf Microloader (Eppendorf, Hamburg, Germany) in volumes of between 14 and 20µl.

Standard Internal

Material	Concentration (mMol)	Molecular Weight (g/Mol)
$KMeSO_4$	130.0	134.2
NaCl	8.5	58.44
HEPES	5.0	238.31
EGTA	0.5	380.35
Mg-ATP	4.0	507.2
Na-GTP	0.3	523.2

Sucrose Internal

Material	Concentration (mMol)	Molecular Weight (g/Mol)
$KMeSO_4$	**115.0**	134.2
NaCl	8.5	58.44
HEPES	5.0	238.31
EGTA	0.5	380.35
Mg-ATP	4.0	507.2
Na-GTP	0.3	523.2
Sucrose	**31.0**	342.3

10mg/ml NB

Material	Concentration (mMol)	Molecular Weight (g/Mol)
$KMeSO_4$	**115.0**	134.2
NaCl	8.5	58.44
HEPES	5.0	238.31
EGTA	0.5	380.35
Mg-ATP	4.0	507.2
Na-GTP	0.3	523.2
Neurobiotin	**31.0**	322.8

5mg/ml NB + Alexa-546

Material	Concentration (mMol)	Molecular Weight (g/Mol)
$KMeSO_4$	**122.5**	134.2
NaCl	8.5	58.44
HEPES	5.0	238.31
EGTA	0.5	380.35
Mg-ATP	4.0	507.2
Na-GTP	0.3	523.2
Neurobiotin	**15.5**	322.8
Alexa-546	**0.01**	10000

1mg/ml NB + Alexa-546

Material	Concentration (mMol)	Molecular Weight (g/Mol)
$KMeSO_4$	**128.5**	134.2
NaCl	8.5	58.44
HEPES	5.0	238.31
EGTA	0.5	380.35
Mg-ATP	4.0	507.2
Na-GTP	0.3	523.2
Neurobiotin	**3.1**	322.8
Alexa-546	**0.01**	10000

***Table 2.1**: The makeup of the internal solutions used, with different concentrations of Neurobiotin or sucrose. Varying concentrations highlighted in bold.*

Preparation of acute slices

The dissection room was prepared prior to animals being removed from their home cage; all surgical implements were chilled to 0°C, and the vibratome was calibrated to minimise orthogonal oscillation. Mouse pups were removed from their home cage and quickly transported to the dissection room. The time of transfer was minimised to reduce distress and to minimise the chance of hypothermia or hyperthermia, since the pups were too young to regulate their body temperature without the dam.

Pups were sacrificed by Schedule-1 cervical dislocation. The head was sprayed with ethanol (70%) to minimise contamination of the brain tissue. A sagittal incision was made through the skin from the nose to the back of the head, the skull was exposed and cut through the midline using dissection scissors (Vannas Spring Scissors, Fine Science Tools, Heidelberg, Germany). The brain was removed using a spatula and placed into oxygenated cutting solution at 0°C for one minute. The brain was retrieved, the cerebellum was removed, and the frontal cortex was cut at a 45-degree angle to produce a flat plane against which thalamocortical slices could be cut that preserved the connections between thalamus and barrel cortex, as previously described (Agmon and Connors 1991). The brain was then glued down to a stage on the cut plane, and placed in the cutting bath, which was filled with chilled cutting solution. The cutting bath was itself surrounded by ice to keep the temperature of the cutting solution and brain at ~0°C.

400µm slices were cut using a Leica VT1200 vibratome (Leica Microsystems, Milton Keynes, UK), fitted with a razor blade (Agar Scientific, Stansted, UK) oscillating at a frequency of 85±5Hz and amplitude of 2.75mm, with a knife travel speed of 0.09mm/s. Typically, 2-4 usable slices were cut per brain. Once cut, slices were transferred using a Liquipipette into cutting solution at room temperature for one minute, before being transferred to ACSF at room temperature, where they were each held in an individual submerged chamber. All ACSF and cutting solutions were constantly bubbled with pressurised carbogen (5% carbon dioxide, 95% oxygen). Once all the viable slices were cut and transferred to ACSF, the rest of the brain tissue was disposed of, and the slices were left to rest for ~1 hour at room temperature. The slices were typically viable for 8-9 hours.

The electrophysiology rig

The electrophysiology rig held a recording chamber, a shallow bath of approximately 150mm x 200mm x 50mm, with both input and output tubing for perfusion of ACSF. This was mounted upon a table with a Scientifica Patchstar micropipette manipulator headstage (Scientifica, East Sussex, UK) in close proximity, and a microscope mounted above.

Electrodes were made from silver wire of diameter 0.25mm and length ~300-400mm (Advent Research Materials, Oxford, UK). Electrodes were reacted in bleach (Sodium hypochlorite, NaClO) for a minimum of 24 hours to allow a coating of silver chloride to form. Once coated, the bath electrode was soldered to the output wire and carefully positioned in the electrophysiology bath. The patch electrode was positioned within an electrode holder, which was screwed onto the headstage, and connected to the input wire. Signals from the electrodes were digitised using a Micro1401 Analogue to Digital Converter (Cambridge Electronic Design Ltd, Cambridge, UK), and amplified using an Axon Instruments Multiclamp 700A computer-controlled microelectrode amplifier (Molecular Devices, CA, USA). A Picoscope sampling oscilloscope (Pico Technology, Cambridgeshire, UK) allowed the waveforms to be visualised on a nearby computer. Noise was reduced by enclosing the entire electrophysiology rig in a faraday cage, and ensuring all electrical components were adequately grounded.

ACSF, constantly bubbled with carbogen, was continuously perfused through the bath through perfusion tube of diameter 0.8mm using a Gilson Minipuls3 pump (Gilson Scientific UK, Bedfordshire, UK). A total volume of ~600 ml was typically sufficient for a 6-8 hour experiment (~1-2ml /min). Waste ACSF was removed via a vacuum pump (Dymax 5, Charles Austen Pumps, Surrey, UK).

Fire-polished borosilicate glass capillary tubes of diameter 1.5mm (Harvard Apparatus, Edenbridge UK) were pulled into micropipettes using a P-87 Flaming / Brown Micropipette Puller (Sutter Instruments, CA USA) to produce pipettes of resistance of 4-8 MΩ. Patch pipettes, filled with internal solution, were mounted onto the manipulator, being careful not to scratch the patch electrode, nor touch the micropipette tip.

Temperature control

Healthy internal body temperature of the adult mouse is generally accepted to be between 38 and 36ºC (Talan 1984), whereas the temperature of the laboratory was generally between 21 and 25°C. To mirror physiological conditions, the temperature within the bath was both monitored and controlled using a Warner instrument cooperation TC-324B automatic temperature controller, with the ACSF heated to a temperature of 36.9±0.4°C via a thermistor (Warner Instruments, CT, USA) just outside the bath.

Observing barrels and cells using the optical microscope

The slice was submerged in the ACSF-perfused bath and held in place a small metal slice anchor or 'harp'. The slice and cells therein were imaged using a digital camera (UC480, Thorlabs, NJ, USA) at 4x and 40x magnification, using dry and water submersion objectives respectively (Plan N 4x Olympus, Hamburg, Germany; Achroplan 44 00 91 40x, Zeiss, Jena, Germany). This facilitated imaging of both the barrels in the cortex at 4x magnification, providing a visual record of the development of barrels over the period of interest, and the cells within the barrel at 40x magnification. The position and focus of the microscope were adjusted using electronic controls.

The primary quarry of this investigation was the spiny stellate neuron: the regular-spiking cell most associated with layer IV barrel cortex and the processing of thalamocortical inputs from the pads of the whiskers. Spiny stellate cells were identified by their spherical shape and relatively small size, distinguishing them from large fast spiking interneurons and classic pyramidal cells. Glial cells, such as astrocytes, were occasionally visible, whilst red blood cells, suspended in their blood vessels, were easily identified by their classic 'donut' shape. All digital photographs were processed in FIJI ImageJ software and adjusted for brightness and contrast by eye to ensure the features of the image were clear and distinct.

The structure of the barrel cortex was observed to first become visible in ex-vivo cortical slices at P3 (**Figure 2.4**), in accordance with some previous reports (Mizuno, Luo et al. 2014), but earlier than other reports (Barrera, Chu et al. 2013). The barrels were easily located by P5. Therefore, P3 was set as the lower age limit for robust electrophysiology experiments within layer IV barrel cortex.

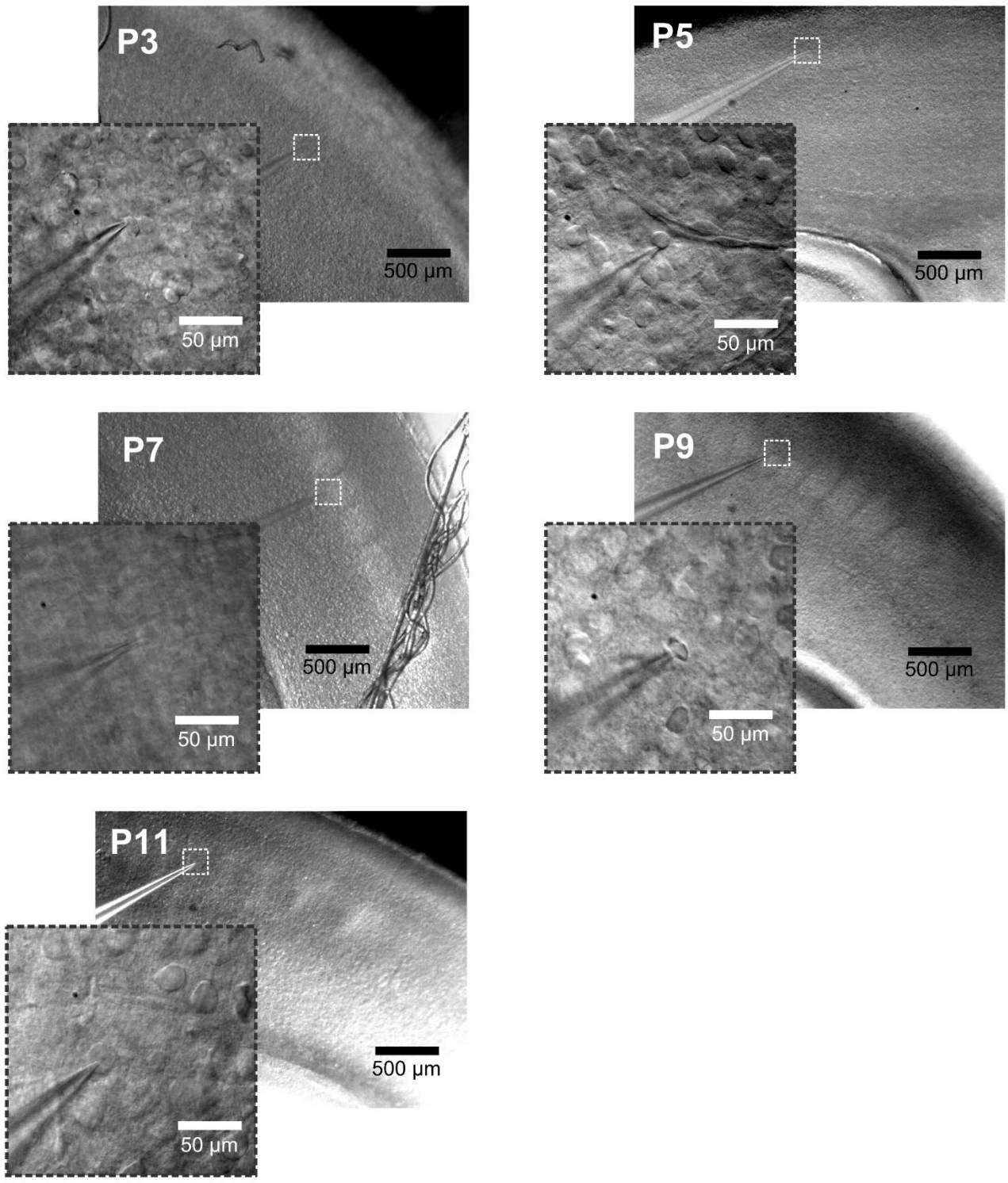

Figure 2.4: The barrels of the somatosensory cortex become more apparent with development. Digital photographs at 4x magnification and 40x magnification (insets) show the barrel cortex, the position of the pipette and the patched cell for mice aged P3, P5, P7, P9 and P11.

Whole-cell patching

Once filled with internal solution and sealed onto the micromanipulator headstage with the patch electrode inside, the micropipette was brought to the surface of the brain slice, beneath the 4x objective and submerged in the ACSF. The pipette was aligned with the centre of a barrel within the barrel cortex. In voltage clamp configuration, the current across the electrodes was minimised by the application of a pipette offset of 47±3mV (mean ± SEM). A square wave of 5mV amplitude was applied to the bath and slice via the patch electrode and visualised via Picoscope 6 oscilloscope software (Pico Technology). The magnification was increased to 40x, and the tip of the pipette was brought to a healthy neuron in the barrel, using positive pressure on the pipette to push away detritus as the neuron was approached. A visible dimple in the target neuron membrane and a simultaneous decrease in voltage amplitude were used to indicate good contact between the neuron and the pipette. By reversing the pressure on the pipette from positive to negative, a gigaseal (resistance >1GΩ) was formed between the neuron and the pipette, as could be visualised in the oscilloscope as the reduction in the square wave amplitude to a negligibly small value (typically <0.2mV). Fast capacitive transients were cancelled using an automatic function in the Multiclamp 700A voltage clamp software. Via manual suction, the membrane of the cell was broken, and an equilibrium established between the inside of the cell and the inside of the pipette. A successful whole cell patch produced large capacitive transients of standard shape, as visualised in the oscilloscope software. Once this distinctive waveform was established, the square wave of voltage was removed, and the software configurations were switched from voltage clamp to current clamp. Signals were Bessel filtered at 10kHz.

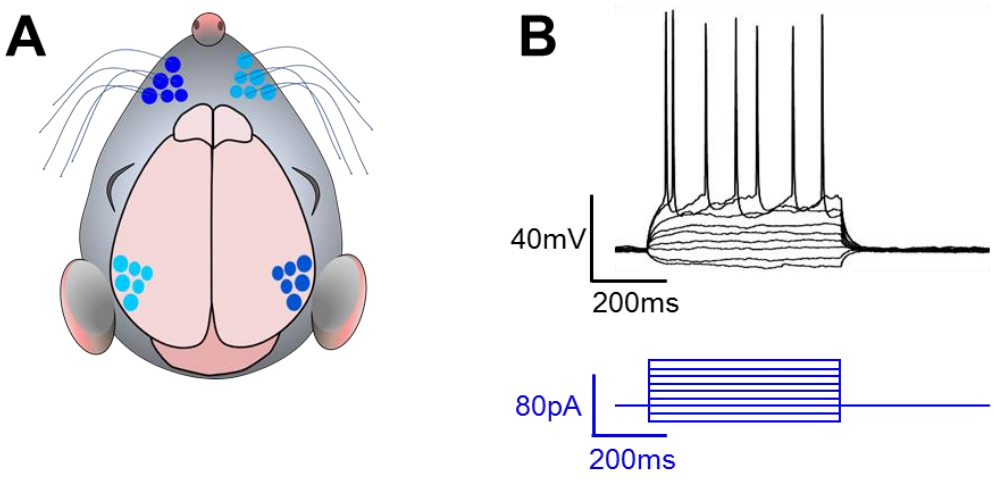

Figure 2.5: The barrels of the barrel cortex and the current-step protocol. **A**: The barrels correspond to the whiskers in a perfect contralateral somatosensory map. **B**: A square-wave 'current-step' injection of current (*bottom*) produces a gradually depolarised voltage response (*top*) that, once the rheobase is reached, triggers the firing of action potentials, or spiking.

Resting membrane potential and holding current

Upon patching the cell, the membrane potential (Vm) was manipulated to be held steadily at a mean value of -72.21±1mV, within a range of -51.81mV to -86.31mV via the application of a holding current (HC) (**Figure 2.6**). The HC was a controlled variable that was set and recorded at the start of each experiment but could vary between experiments. HCs used were typically in the range of -10 to -100pA. When higher magnitude HCs were used it was generally symptomatic of an unhealthy cell that died quickly. If the membrane potential was seen to rise rapidly without the injection of a current the experiment was halted, as this was usually indicative of the degradation or death of the cell (which could be confirmed via quick visual inspection).

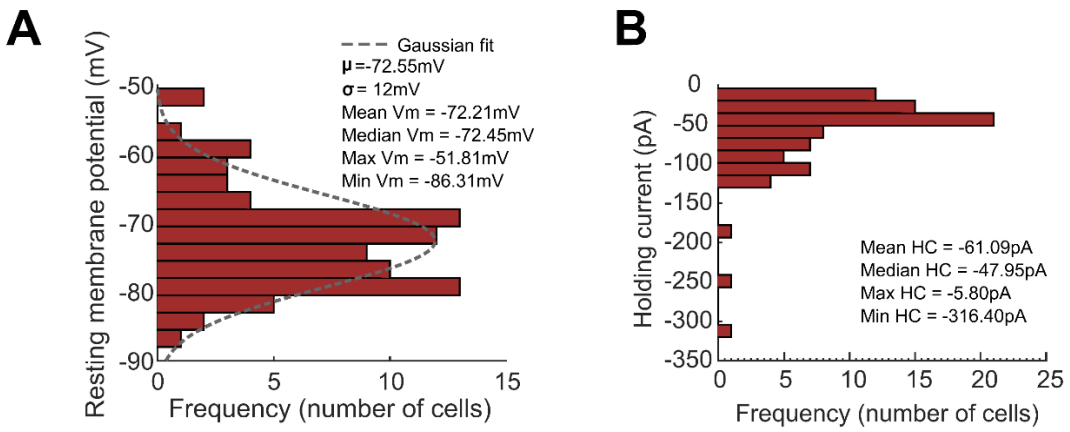

Figure 2.6: The range of membrane potentials and holding currents used during experiments, prior to current injections. A: Histogram of resting membrane potentials used in experiments. Bin width = 2.5mV. Dotted line shows Gaussian fit to data, with μ= -72.55mV and σ = 12mV. **B:** Histogram of HCs used in experiments. Bin width = 15.8pA. The majority of the HCs used were between -10 and -100pA.

Although the Vm of individual cells was dictated by the application of the HC, no overall correlation was found between the two variables across the dataset; the magnitude of HC did not determine the final value of Vm, it was purely incidental to the properties of the cell. No statistically significant correlation between age and HC was detected.

Electrophysiology Protocols

Once a cell was patched and held at a steady membrane potential, software to induce and record the dynamics under investigation was opened. Signal 5.08 x86 (Cambridge Electronic Design Ltd) facilitated the use of different current-clamp protocols to induce both active dynamics (spiking behaviour) and passive dynamics (cell membrane charging and discharging). All recordings were made at a sampling frequency of 50kHz. Bridge balance error was minimised via a 7.3MΩ correction.

The first protocol enacted was a current-step protocol that consisted of 11 square wave injections, or steps, of varying magnitude in both the hyperpolarising (negative) and depolarising (positive) directions. Steps were 500ms duration over a 1s trace, and started at a current injection of -16pA, increasing by 8pA up to a maximum hyperpolarising value of 64pA. The hyperpolarising steps allowed measurement of the intrinsic properties of the cell, whilst the depolarising steps allowed measurement of the active dynamics of the cell. The increase in step size was chosen to show a range of activity in a short timeframe whilst also providing a good approximation for the rheobase (minimum current at which an action potential could be fired); as such the rheobase reported in subsequent chapters should be taken as the reported measure with a negative error bar of 8pA. Action potentials were typically fired by the 9^{th} or 10^{th} step. The cycle of 11 current injections was typically repeated 10-12 times over a time period of 110-132s. Throughout, the cell was carefully monitored for sudden changes in the resting membrane potential or morphology, as visible through the digital camera, that might be indicative of membrane degradation or cell death.

The current-step protocol was applied first to ensure that the neuron was capable of firing action potentials. Once the current-step protocol was completed, the passive dynamics protocol was applied. This consisted of the application of two 1ms pulses of current of magnitude 0.4nA, 500ms apart. These pulses were equal but opposite; one was depolarising, the other hyperpolarising. This protocol avoided the activation of voltage-gate ion channels that could lead to action potentials being fired, allowing purely passive dynamics to be studied.

The number of cells patched in a single slice depended on the internal solution used: where the internal solution included dye(s), a single cell per slice was patched to allow unambiguous identification in post-hoc imaging. Where no dye was present, this was not important, and so multiple cells were patched in a single slice. However, due to being heated to physiological

temperature, degradation of cells over timescales longer than ~1 hour was apparent, so no more than 3 cells were recorded from each slice.

Dye filling

Dye filling protocols were developed from those supplied by Dr Francesco Tamagnini of the University of Reading, as previously described (Káradóttir and Attwell 2006). The patched cell was filled with dye during electrophysiology experiments via passive diffusion of the internal solution, with the pipette in the cell for at least 30 minutes, in accordance with previous work (Mills and Sey 1998) (median time = 33 minutes). A sketch was made of the location of the patched cell, relative to the hippocampus, surrounding barrels and any other appropriate cortical landmarks to provide a map for later relocation (**Figure 2.7**). If a dye-filled cell was observed to degrade at all over the course of the experiment, and the resting membrane potential change to such a degree as to garner any electrophysiological protocols unusable, it was still held for a minimum of 30 minutes to ensure the morphological data from dye-filling and imaging be consistent. Following this diffusion period, the pipette was very carefully retracted from the cell membrane, being cautious not to tear the cell or dislodge it from its position in the barrel. If deemed necessary, a little positive pressure and/or a 1-5ms "zap" of current was used to break the gigaseal between pipette and cell membrane. The accidental removal of the primary cell during this manoeuvre was the main cause of post-hoc non-recovery. Once extracted from the cell, the pipette was hastily removed, as to avoid excess leakage of Neurobiotin or Dextran-conjugated Alexa546 into the surrounding tissue. One dye-filled cell was patched per acute slice, allowing for unambiguous matching of the confocal images to the electrophysiological data, except for the first few slices, where as many as three cells per slice were patched and filled. In such slices, the ambiguity meant that the cells could not be matched to their electrophysiological dynamics, but multiple-cell dye-filling did allow direct comparison of cellular morphology.

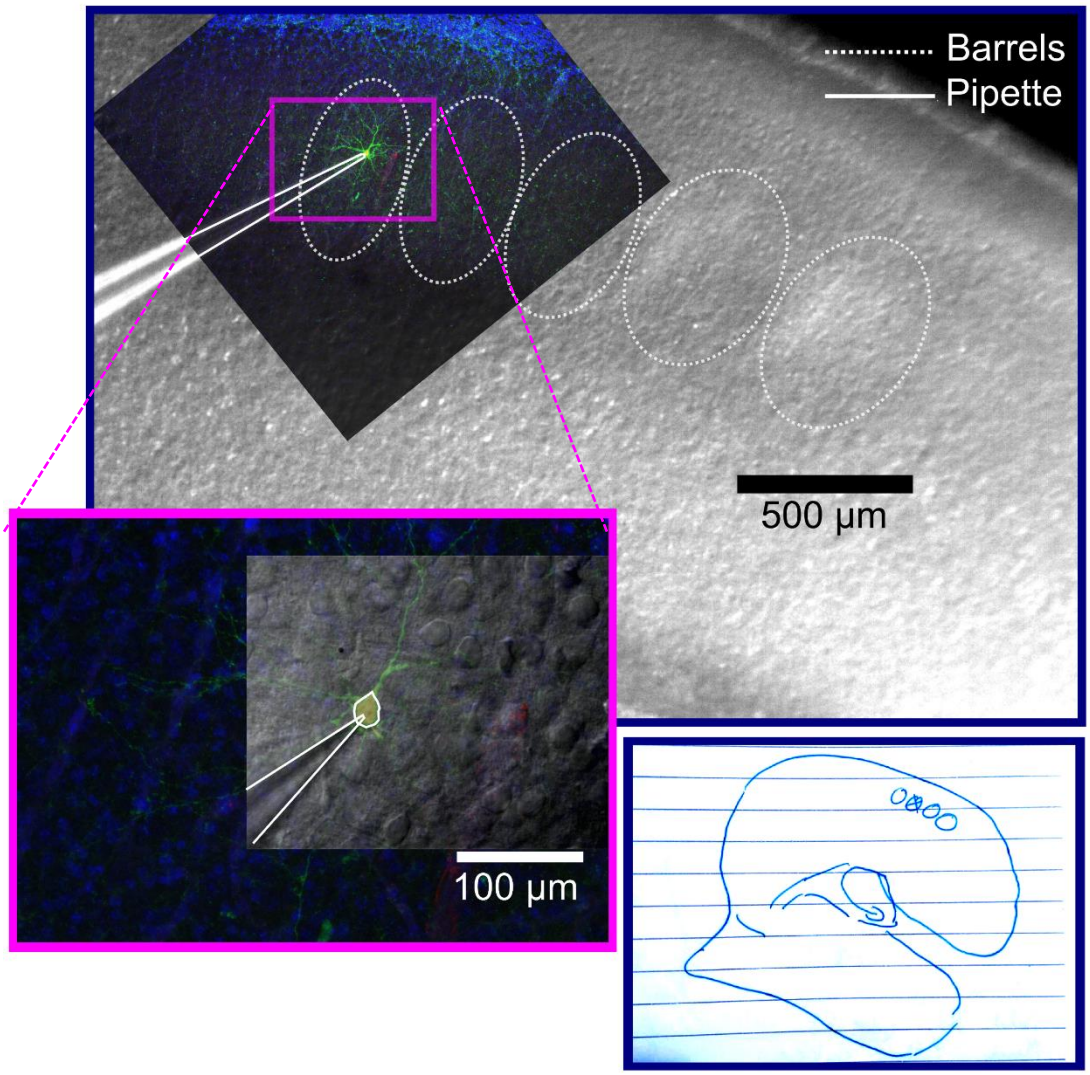

Figure 2.7: Representative P11 spiny stellate neuron within the barrel cortex patched with internal solution containing Neurobiotin and Dextran-conjugated-Alexa546.
Top: Digital photograph of the barrel cortex at 4x magnification overlaid with composite confocal maximum projection image. Dotted white lines show the approximate outlines of the layer IV barrels; solid white line shows the location of the micropipette. Confocal colours as follows: blue = DAPI, green = Neurobiotin with Streptavidin-Alexa488, red = Dextran-conjugated Alexa546. Soma appears yellow due to the colocalization of red and green dyes. Inset shows the confocal composite maximum projection image of the neuron at 20x magnification, with digital photograph (40x magnification) overlaid. *Bottom*: sketch of the location of the barrels within the cortical slice relative to the hippocampus and pial surface. Barrels are shown by circles, location of the patched cell is marked with an 'x'.

Preparing the tissue for imaging

Once sketches and photographs were taken, the acute brain slice was quickly removed from the electrophysiology rig and placed into a 24-well plate containing a solution of 4% paraformaldehyde (PFA), dissolved in 0.1M phosphate buffered saline (PBS) (VWR Laboratories). The PFA solution was removed and replaced three times to ensure that excess ACSF was minimised (all PFA containing solutions were disposed of safely, as it is hazardous to health and the environment). The 24-well plate was covered, sealed, wrapped in foil to protect from light and stored at 4°C for a minimum of 12 hours, but no longer than 24 hours. After this period, cortical slices were moved to another well using a clean paintbrush and washed three times for five minutes each time using PBS solution to remove excess PFA. The slice was then transferred, using a different paintbrush, to another well in the 24 well plate for storage in PBS solution at 4°C for up to a week.

Stock staining solution was prepared that consisted of

9ml 0.1M PBS
1ml 5% Triton x100 (Sigma Aldrich)
0.03g Bovine Serum Albumins protein (Sigma Aldrich)

The fluorescent dye Streptavidin Alexa Fluor 488 (Molecular Probes), which has a high affinity for Neurobiotin, was applied in solution to the slices after post-fixation. Streptavidin stock solution was made up by diluting 1mg of Streptavidin in 1ml 0.1M PBS, and was stored in darkness at 4°C. Streptavidin solution was then diluted in the staining solution, and brain slices were incubated in the resulting mixture. Dilutions of Streptavidin-Alexa488 solution in staining solution were recommended to be in the range of 1/25 to 1/1000; Streptavidin solution was added to the staining solution in either:

- High concentration: 1:200, 5µl Streptavidin per 1ml of staining solution.
  or
- Low concentration: 1:1000, 1µl Streptavidin per 1ml staining solution.

Slices were removed from storage and transferred to a new 24 well plate using a clean paintbrush where they were incubated in ~1ml of Streptavidin/staining solution mixture. They were then sealed, wrapped in foil to protect from light, and placed on a rocker (Labnet Low Speed Laboratory Shaker, Labnet International, NJ, USA), undulating at a rate of 20rpm for a minimum of 6 hours, though more typically 12-24 hours. (On one occasion slices were

left in Streptavidin solution for ~60 hours. This seemed to have no effect on the slices or the cells identified within).

Slices were then washed three times in PBS to remove excess Streptavidin solution, allowing five minutes for each wash. After washing, slices were moved from the 24-well plate to glass microscope slides (Marienfeld Mircoscope Slides, 76x26x1mm, Lauda-Königshofen, Germany) using a clean paintbrush. Excess PBS on the microscope slide was carefully removed using absorbent paper towel. Approximately 25µl of Vectashield Mounting Medium (Vector Laboratories, Peterborough , UK) containing 4′,6-diamidino-2-phenylindole (DAPI), at 1.5µg/ml concentration, was applied to the top of the slice. A coverslip was gently lowered on top of the slide, being very careful to not trap air bubbles within. Finally, a small amount of clear nail polish was used to seal to coverslip to the microscope slide. Slides were kept horizontal until the nail polish had set, and stored at 4°C.

Confocal imaging

The microscope slides were stored for up to a week before imaging and were returned to storage at 4°C and re-imaged on several occasions without notable deterioration of the tissue or the fluorescence signal over time. Prior to confocal imaging, all tissue slices were observed using a Leica DM IRB fluorescence microscope (Leica Microsystems) at 10x and 20x magnification (filter cubes BP340-380, BP360/40, BP 480/40, and BP 546/12). This allowed for quick assessment of the success of the experiment: was the primary (patched) cell visible? Where the primary cell could not be identified, it was presumed that the primary cell was either destroyed or inadvertently removed during removal of the patch pipette, and the samples were not imaged with the confocal microscope.

With the successfully patched, filled and recovered cells identified, confocal microscopy was done on the samples exhibiting the presence of filled cells. A Leica SPE single channel confocal laser scanning microscope attached to a Leica DMi8 inverted epifluorescence microscope (Leica Microsystems) was used to take z-stacks of images using the 10x (dry), 20x (dry and/or oil immersion) and 40x (oil immersion) objectives. The image resolution was initially set to 1024x1024 pixels for images taken at 20x magnification, and 512x512 pixels for images taken at 10x or 40x magnification but was later adjusted to 1024x1024 pixels for images taken at 40x magnification. The z-stack of images facilitated 3D reconstruction, with the limits of the z axis found prior to imaging by setting the highest and lowest focus at which the primary cell could be identified. Blue, green and red channels, corresponding to the

excitation lasers of wavelength 405nm, 488nm, and 532nm, were incident on the tissue to illuminate DAPI, Streptavidin-Alexa488, and Dextran-conjugated-Alexa546, respectively. Z-stacks were produced by taking optical slices through the tissue in increments of 2µm across the range of focus of the objective.

Control experiments

Control experiments were performed to establish that dye filling of neurons was not due to random uptake of Neurobiotin or Streptavidin-Alexa488, but due to the specific filling of the patched cell. A micropipette, loaded with 5mg/ml Neurobiotin + Dextran-conjugated-Alexa546 was lowered into a brain slice kept in identical conditions to those used in current-clamp electrophysiology experiments. The micropipette was brought up to the surface of a suitable cell within the barrel cortex, but the cell *was not patched*. The pipette was then kept in that location for a minimum of 30 minutes, whilst all of the electrophysiology protocols were applied, even though they were not injecting current into any specific cell. The pipette was then removed from the slice, and the slice was fixed in PFA, washed with PBS, treated with Streptavidin-Alexa488 staining solution, washed again with PBS, transferred to a microscope slide, set with DAPI-containing mounting solution, and imaged in the confocal microscope, as described above. In none of these control experiments was any evidence for random uptake of Neurobiotin dye found (**Figure 2.8.A**).

Troubleshooting

In the initial dye-filling experiments, the Streptavidin-Alexa488 dilution of 1:200 resulted in random uptake of Streptavidin-Alexa488, not by other neurons, but by surrounding blood vessels. This made it not only difficult to identify the primary patched cell, but also nearly impossible to unambiguously identify any gap-junction-coupled cells (**Figure 2.8.B**). Even an object that might appear, at first glance, to be a discrete and spherical cell could later be revealed to be a meander in a nearby blood vessel. All subsequent experiments were performed with the lower dilution of Steptavidin-Alexa488 of 1:1000, which showed a marked improvement in reducing random uptake by blood vessels, without detracting from the visibility of the patched cell. There was some uptake of Dextran-conjugated Alexa546 into dead neurons at the surface of the cortical slice. However, this was not a problem as they were only in the most superficial layers of the z-stack of confocal images and could easily be differentiated from the patched and coupled cells during post-imaging analysis.

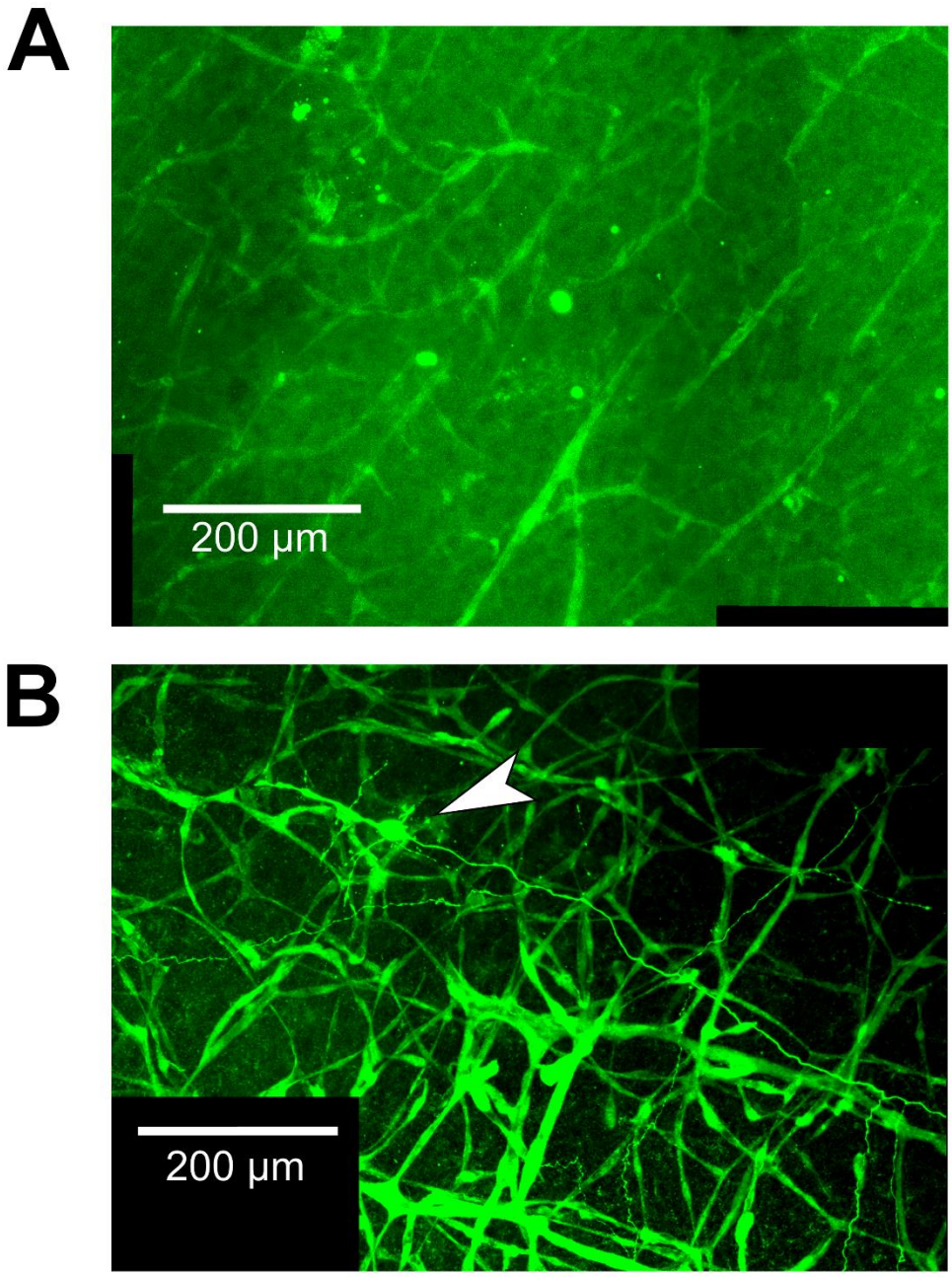

Figure 2.8: Addressing issues in dye-filling and confocal imaging. **A**: Representative confocal max-projection image from control dye-filling experiment. Magnification =20x. Control experiments follow the exact same protocol as normal experiments, except that no cell is patched. Some Neurobiotin / Streptavidin-Alexa488 detritus is visible, as well as some uptake into blood vessels, but there is no dye uptake into neurons. **B**: Representative confocal max-projection image from dye filling with the high-concentration Streptavidin-Alexa488. Magnification =20x. The white arrow shows the position of a patched neuron amongst the blood vessels that have been illuminated by high-concentration Streptavidin.

Calculating the junction potential error

Prior to doing any assessment of patch-clamp data, the value of the junction potential error was calculated to allow adequate compensation. The junction potential error was calculated via the ionic properties of the compounds both within the pipette (the internal solution) and outside of the pipette, in the ACSF. A junction potential error calculator was used, as provided by the ClampeX software, which itself is based on the program JPCalc (Barry 1994), that utilised the generalised Henderson Equation to calculate the potential across solutions with *N* polyvalent ions. A library of compounds was referred to for the valence and mobility of the ions contained within, and a graphical user interface allowed the input of the relevant concentrations of the different compounds. This facilitated the calculation of a junction potential error of +8.9mV. Consequently, this value was subtracted from all electrophysiological data prior to any other analysis.

Preparing electrophysiology data for analysis

Data analysis was performed using MATLAB 2016a (MathWorks, MA, USA). Cells were excluded from analysis if they were unable to demonstrate the ability to fire action potentials. Electrophysiology data recorded in Signal was converted to .mat files and organised according to date of recording, recording number, and internal solution. MATLAB scripts originally written by Jon Brown, developed by Michael Ashby and Sarah Hulme were used as the basis of the experimental analysis scripts used in this thesis, but were further developed to efficiently analyse this data. The analysis methods used will be described as appropriate in the ensuing results chapters.

Distinguishing between regular-spiking and fast-spiking cell phenotypes

To control for cell type and ensure that only the developmental biophysics of regular-spiking neurons was studied, it was imperative to accurately remove erroneously patched fast-spiking interneurons from the dataset. Although regular-spiking spiny stellate cells were targeted, occasionally fast-spiking interneurons were patched by accident. The dramatically different spiking waveforms of regular-spiking and fast-spiking neurons (**Figure 2.9**) made these cells highly conspicuous once patched.

Using the second spiking trace (typically the 9^{th} or 10^{th} trace in the 11-step cycle), fast-spiking cells were identified by eye. To reduce error, the spiking traces were assessed by two separate people, without discussion, but with the same criteria for categorisation, resulting in 20/165

(12%) cells being categorised as fast-spiking, and the remaining 145 (88%) categorised as regular spiking. The fast spiking neurons were excluded from further analysis.

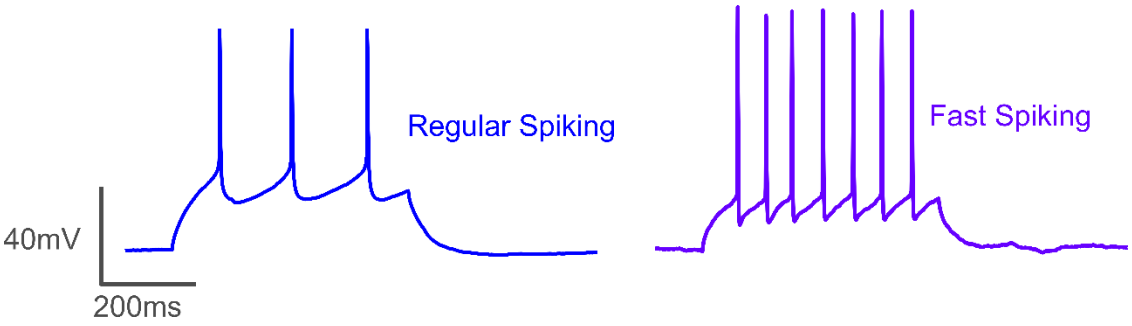

Figure 2.9: Differentiating between regular spiking and fast spiking neurons.
Representative spiking traces from regular spiking (*left*) and fast spiking (*right*) P10 neurons. The spiking frequencies, and the shape of the AHPs identify the cells as either regular or fast spiking.

Statistical methods

For all analysis methods of experimental data, n=number of cells, unless otherwise stated. Mean values were calculated with error bars of the standard error of the mean ($\sigma/\sqrt{n}$), unless otherwise stated. Where tests returned P-values, significance was defined as being $P \leq 0.05$.

A one-way analysis of variance (ANOVA) was used to determine whether the data from different groups had a common mean, i.e. whether there was any statistically significant difference between means from different groups. The null hypothesis assumed that all group means are equal, under the assumption that all groups were normally distributed. It was applied in MATLAB using the command '`anova1`'.

A Tukey Kramer test was used on data that showed statistically significant differences in the mean via a one-way ANOVA to test the hypothesis that the means from different groups are the same. This test assumed that the data tested is normally distributed and that there was homogeneity of variance across the groups tested. It worked under the assumption that the group sizes were the same, but was conservative for one-way ANOVA with different group sizes. The Tukey Kramer test was applied in MATLAB using the function '`multcompare`'.

Pearson's Linear Correlation Coefficient was used to assess the correlation between two variables. It was defined as the covariance between two variables divided by the product of

their standard deviation. In MATLAB this was applied via the function '`corr`'. With two variables, X and Y, their Pearson's linear correlation coefficient is defined as

$$\rho = \frac{\sum_{i=1}^{n}(X_i - \bar{X}\ )\,(Y_i - \bar{Y}\ )}{\left\{\sum_{i=1}^{n}(X_i - \bar{X})^2 \sum_{j=1}^{n}\left(Y_j - \bar{Y}\right)^2\right\}^{\frac{1}{2}}}$$

Values were returned between -1 and +1. -1 indicated perfect negative correlation, and +1 indicated perfect positive correlation.

For purpose-built models, fitting in MATLAB was done using the least-squares function '`lsqcurvefit`'. Via this function, a dimensionless goodness-of-fit of the model to the data was characterised by the nonlinear regression coefficient, R^2:

$$R^2 = 1 - \frac{var(Y^{model} - Y^{data})}{var(Y^{data})}$$

As model → data, the right-hand side of this expression → 0, therefore a good fit is one where $R^2 \rightarrow 1$.

3 Active Dynamics

Key Findings

1. The action potential of regular spiking excitatory neurons is observed to change with postnatal development, becoming significantly taller and narrower in the period between postnatal day 3 (P3) and postnatal day 11 (P11).
2. Analysis of the first derivative of the membrane potential with age indicates a nonlinear change in action potential waveform, possibly indicating an asymmetrical development trajectory of different voltage-gated ion channels.
3. Temperature is observed to affect the action potential waveform, with higher temperatures producing action potentials that are lower in amplitude and narrower (shorter duration) than those from cells kept in cooler conditions.
4. Neuronal input resistance decreased significantly over development, with a possible decrease in input resistance variance also detected.

3.1 Introduction

Originating in the axonal initial segment (AIS), the action potential (AP) propagates down the axonal membrane to axonal boutons, and triggers the release of neurotransmitters that traverse the synaptic cleft and trigger APs in post-synaptic neurons (Bean 2007, Rowan, DelCanto et al. 2016, Telenczuk, Fontaine et al. 2017). Simultaneously back-propagating into the soma and dendrites of the pre-synaptic neuron (Telenczuk, Fontaine et al. 2017), APs facilitate neuronal development (Khazipov and Luhmann 2006) and the formation and organisation of functional networks of neurons through Hebbian plasticity rules "*Neurons that fire together wire together*" (Hebb 1949), and through spike-time-dependent plasticity (Jadhav, Wolfe et al. 2009, Winnubst, Cheyne et al. 2015).

The ion channel hypothesis

The distinctive waveform of the AP elucidates the phases of steep depolarisation and sharp repolarisation that occur within the cell membrane. Since the work of Hodgkin and Huxley (Hodgkin and Huxley 1952), the waveform of the AP has been correlated to the currents of various ionic species in and out of the cell (Bean 2007, Szücs and Huerta 2015), a flux of charged particles through voltage-gated ion channels that are themselves governed by

probability-based kinetics (Hodgkin and Huxley 1952, Hay, Hill et al. 2011, Kimm, Khaliq et al. 2015). These currents are limited by the number, density and action of specific voltage-gated ion channels that perform active transport to produce the electrostatic gradients. The influence of these channels on the AP has been studied extensively in mature cortical neurons via the use of channel blockers, allowing observation of the exact channel subtypes responsible for waveform features and spiking properties (Bean 2007, Deng, Rotman et al. 2013, Kimm, Khaliq et al. 2015, Begum, Bakiri et al. 2016, Rowan, DelCanto et al. 2016).

In a cascade of biophysical events, sub-threshold synaptic inputs combine to produce a voltage gradient that first activates the opening of Na^+ channels, depolarising the cell (Catterall 2000, Krouchev, Rattay et al. 2015, Telenczuk, Fontaine et al. 2017). This depolarisation triggers the action of K^+ channels; fast K^+ channels rapidly re-hyperpolarise the cell, whilst slower-activated K^+ channels mitigate these fast dynamics (Bean 2007, Kimm, Khaliq et al. 2015). The combined dynamics of these gross changes in electrostatics result in an after-hyperpolarisation that overshoots the rectification in membrane potential, before the membrane potential returns to an equilibrium that is either quickly followed by a second AP, or a period of quiescence. These events occur on the timescale of milliseconds, and seemingly subtle changes in the position, action or population of different ion channels can have profound effects on the ultimate waveform of the AP, changing the rate of transfer of charge and changing the height or the duration of the spike (Deng, Rotman et al. 2013). The number and density of ion channels can therefore ultimately determine rate and fidelity of communication within neuronal networks and the function of applicable brain regions and associated cognitive behaviours (Gjorgjieva, Mease et al. 2014).

Temperature

Thermodynamic interpretations of the AP have been presented that argue that the statistical mechanics of the cell membrane ultimately determine its propagation and properties (Andersen, Jackson et al. 2009, Hady and Machta 2015). Though generally the AP is described in terms of electrical phenomena (Hodgkin and Huxley 1952), the effect of temperature on the waveform was considered.

A healthy internal body temperature of a mouse is widely accepted to be between 38 and 34ºC (Talan 1984, Shoji, Takao et al. 2016). Room temperature is generally accepted to be at least 10ºC cooler. Channel gating kinetics are highly temperature dependent (Hodgkin and Huxley 1952, Hille 2001); temperature influences the dynamics of the voltage-gated ion channels by

affecting the flows of ionic species in and out of the cell. A high temperature dependence of AP waveform was therefore also expected. The movement of the ionic species in and out of the neurons can be related to the laws of classical thermodynamics, as developed by Boltzmann, which relate the kinetic energy of particles, and the probability of their different configurations, directly to temperature (Hodgkin and Huxley 1952, Tipler and Mosca 2007):

$$\frac{1}{2}m\overline{v^2} = \frac{3}{2}k_B T \tag{3.1}$$

Where m is the mass of a particle, v is its velocity (with vector quality), k_B is the Boltzmann constant, equal to 1.38×10^{-23} m^2 kg s^{-2} K^{-1}, and T is temperature.

$$P_i \propto e^{\left(\frac{E}{k_B T}\right)} \tag{3.2}$$

Where Pi is the probability of the i^{th} microstate (configuration of a thermodynamic system) and E is the energy of the state.

Input resistance

The biophysics of the developing neurons within the barrels can be studied in terms of their input resistance (Llinás 2014), which has previously been shown to be cell-type dependent (Connors and Gutnick 1990, Luhmann, Reiprich et al. 2000), and age-dependent (Valiullina, Akhmetshina et al. 2016). The input resistance is the measure of the resistance to the flow of charge between the inside and the outside of the neuron. Factors that affect the input resistance can include the cell's morphology (size of dendritic arbour, thickness of cell membrane), the density of organelles within the cellular cytoplasm, and the presence of ion channels (Kandel 2013). It therefore follows that with neuronal growth and the formation of ion channels, developmental variation in input resistance is expected. Hyperpolarising current injections that elucidate the electrical features of the neuron without triggering spiking have long been a feature of current-step protocols in whole-cell current clamp electrophysiology (Ito and Oshima 1965); such steps create a measurable change in potential difference that can be used to find the input resistance of the cell membrane via Ohm's law ($V=I\times R$). The input resistance of cortical neurons has previously been observed to decrease with postnatal age and influence spiking in different animal species (McCormick and Prince 1987, Luhmann, Schubert et al. 1999, Bahrey and Moody 2002, Valiullina, Akhmetshina et

al. 2016). The input resistance was therefore a necessary measure when evaluating neuronal intrinsic properties.

This chapter investigates the changing waveform of the AP in regular spiking cells over the developmental period P3-P11, evaluating the height, width, and first derivative with respect to time of the membrane potential during the first spike fired at rheobase. The input resistance as a function of postnatal age is also investigated, as is the effect of temperature on the dynamics observed.

3.2 Analysis Methods

A total of 82 regular spiking cells from 36 neonatal mice between ages P3 and P11 were patched with pipettes containing either Standard Internal solution or Sucrose solution (see *Methods* for internal solution compositions) and analysed for age-dependent changes to the AP waveform. No difference in measured membrane potential or AP waveform was detected between these two internal solutions, though Neurobiotin-including internal solutions were excluded from this analysis due to their effects on the AP waveform (Chapter 6: *The Effect of Neurobiotin on Spiking Properties*). As described in *Methods*, spiking behaviour was elicited via application of the current-step protocol, which consisted of a cycle of eleven 500ms injections of current of gradually increasing amplitude, each over a 1s period. This protocol of increasing current amplitude produced two hyperpolarised membrane potential responses and nine depolarised membrane potential responses; typically, spiking behaviour was elicited by the 9^{th} or 10^{th} step in the 11-step cycle. The AP threshold was defined as the membrane potential at which the first derivative of membrane potential with time (dV/dt) reached the threshold of 10.5mV/s and the subsequent membrane potential reached a minimum value of -35mV. The size and number of the steps was chosen to provide a quick but reasonably accurate estimate of the rheobase (lowest magnitude depolarising current at which APs can fire, the current that pushes the cell to just suprathreshold). The first spiking waveform at the rheobase was detected (MATLAB command '`findpeaks`'), and the first AP from this trace was isolated for waveform analysis, whilst entire spiking traces allowed qualitative observations of waveform.

Action potential waveform analysis

The first AP fired at the rheobase was analysed for changes to waveform (**Figure 3.1.A**), namely AP height and width (**Figure 3.1.B**). For each cell, the current-step protocol was repeated, typically 10-12 times. For each repeated cycle there was a first spiking trace and a first AP; the waveforms of these first APs, each measured from AP threshold to AP threshold + 16ms, and averaged to give a mean waveform. Using this mean AP waveform, height was measured as the difference in membrane potential between the AP threshold and the AP peak, and width was measured as the full width at half maximum height. For representative examples of spiking behaviour across the trace, the full second spiking trace after rheobase was observed.

The first derivative of voltage with time

From the waveform of the first AP fired at the rheobase, the first derivative of membrane potential with time (dV/dt) was found (MATLAB command '`diff`'). Two values were extracted from this first derivative: the maximum rate of rise, or Max dV/dt (steepest part of the rising phase) and the maximum rate of fall, or Min dV/dt (steepest part of the falling phase). These two measures were used as a representative measure for rate of change of the AP with time.

Effect of temperature on spiking properties

The effect of temperature on the spiking properties was investigated on a separate preliminary dataset of cortical neurons from neonatal mice aged P3-P12 (n=16 cells, 9 animals). For each cell patched in this preliminary experiment, the temperature of the ACSF perfused into the bath was varied via a small thermistor heating element using a feedback controller system (Warner Instruments TC-324B) to temperatures between 22 and 37.5ºC. Using the current-step protocol, spiking behaviour was elicited. The temperature was then varied, and the current-step protocol applied again to the same cell, allowing the features of the AP waveform as a function of temperature to be controlled for cell type and cell age. The mean first AP at each temperature was found, and measured for height and width, as described above. The height and width data were then grouped into two temperature-based sets for analysis: recordings taken at less than 27°C, recordings taken at more than 30°C.

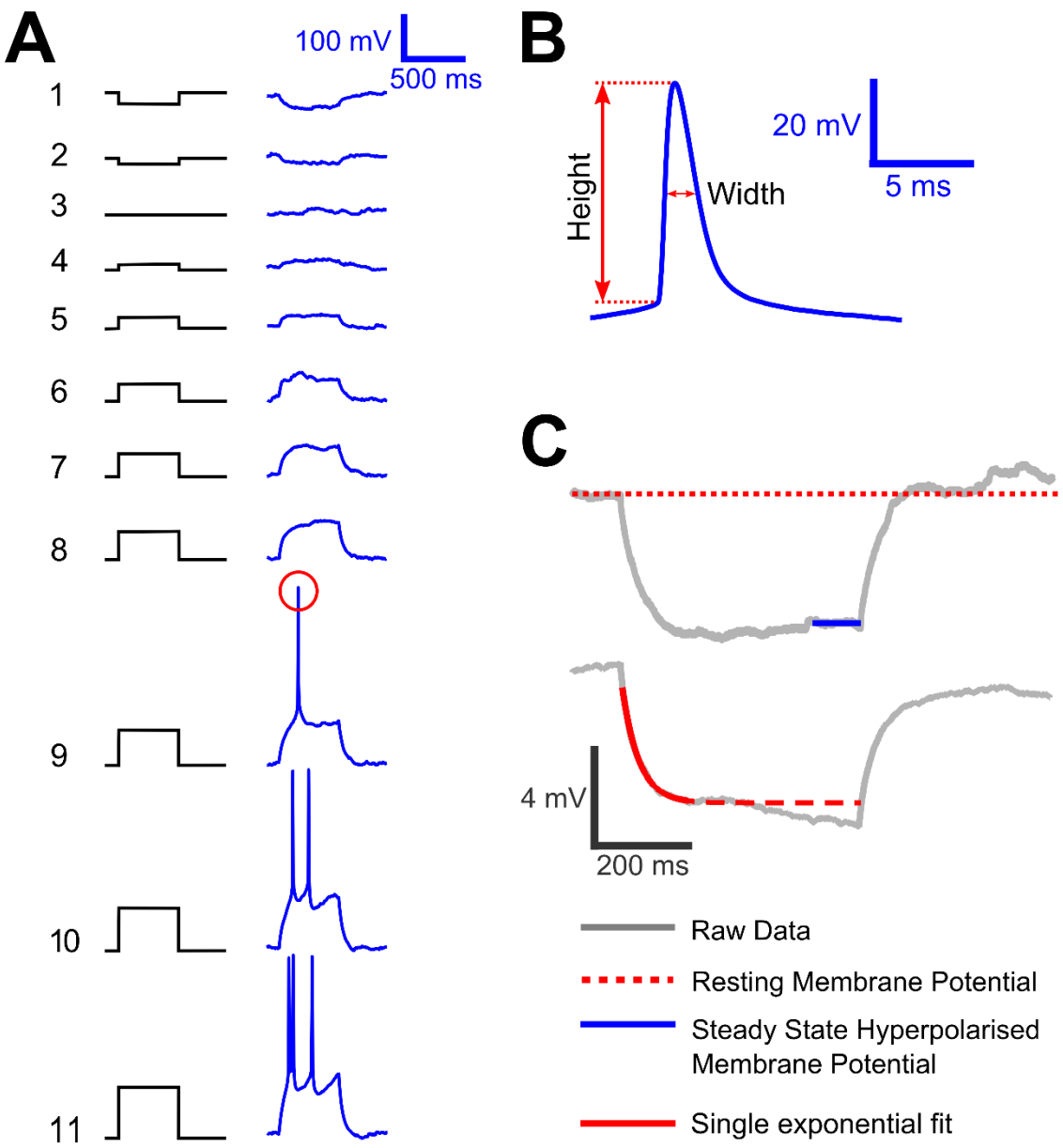

Figure 3.1: Finding the primary features of the current-step protocol voltage trace. **A:** Action potentials were triggered to fire via the injection of 11 gradually-increasing current steps, each lasting for 0.5s of a 1s trace. The first action potential is identified as the maximum point after the first derivative of voltage with time passes 10.5 V/s, trace 9, red circle. **B:** It is this first action potential that was primarily studied, starting by measuring its height and its width. **C:** The first step of the current step protocol is a negative current injection, which hyperpolarises the cell, producing a hyperpolarised voltage response. The membrane potential in the absence of dynamics is found from the mean voltage over the first 0.1s, prior to any current injection (red dotted line). The steady state voltage of the hyperpolarised response is found by taking the mean voltage over the last 0.1s of the current injection (blue solid line). A single exponential can be fitted to the hyperpolarised voltage response (red solid line), from which the input resistance can be determined by the extrapolated value of the hyperpolarised membrane potential (red dashes).

Measuring input resistance

Developmental variations in the input resistance were analysed via the membrane potential response to the first hyperpolarising current injection. The current injected was a controlled variable of -16pA, and the magnitude of the voltage response was found by both measurement of the mean hyperpolarised voltage (steady state response), and by the application of an exponential decay curve (extrapolated response) (**Figure 3.1.C**). Finding both the steady-state input resistance and the extrapolated input resistance required only the simple application of Ohm's law:

$$V = I \times R \tag{3.3}$$

$$R = \frac{V}{I} \tag{3.4}$$

The input resistance, found for each trace, was averaged over repeated cycles to give mean values for each cell (typically 10-12 repeats per experiment). This was done for both for the steady state response and for the extrapolated response. In most cells, the steady-state and extrapolated input resistances were approximately the same value. However, in some cells, the hyperpolarised membrane potential rose by a few millivolts prior to the end of the current injection, in a phenomenon known as 'sag'. The extrapolated membrane potential measure eliminated the contribution of sag, but relied upon adequate fitting of an exponential curve to the hyperpolarised voltage response.

3.3 Results

Temperature affects action potential height and width

Temperature was found to have a significant effect on both the height and the width of APs from cortical neurons: cells were recorded from at both low and high temperatures, and at higher temperatures had narrower and lower amplitude APs (**Figure 3.2**). No further analysis was performed on the preliminary data from this temperature experiment, but it was ensured that all cells in subsequent experiments were perfused with ACSF heated to a temperature of 36.9±0.4ºC. Accounting for heat loss between the thermistor and the bath, this corresponded to a temperature underneath the microscope objective of 34.2 ±0.7°C.

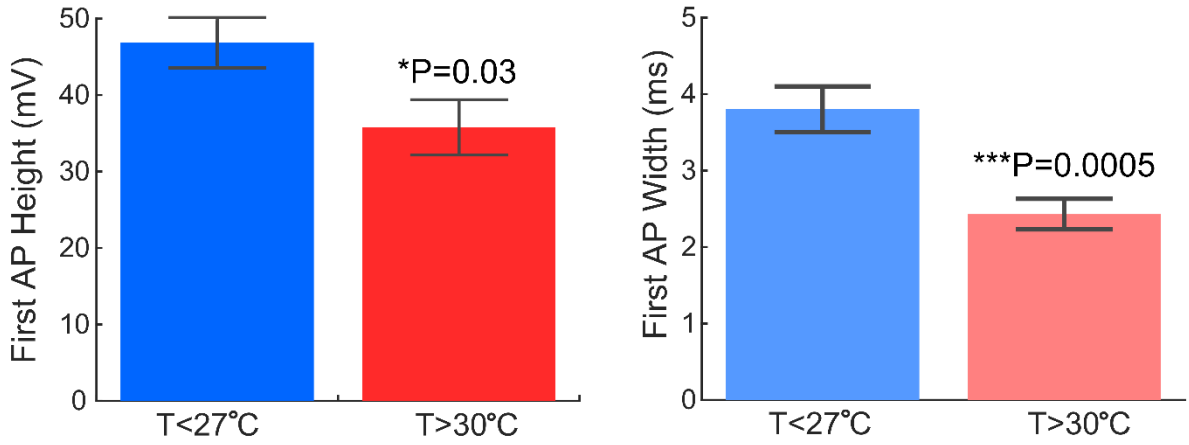

Figure 3.2: Mean height (*left*) **and width** (*right*) **of the first action potentials against temperature of the electrophysiology bath.** Cells patched are aged P3 to P12. Data are grouped by temperature to be either below 27°C or above 30°C (**n=16**). Error bars represent the SEM. One-way ANOVA with Tukey-Kramer test, P values as shown.

Action potential height and width with postnatal age

The AP waveform was observed to change with age; APs grew taller and narrower. The spiking profiles at and above the rheobase demonstrated qualitatively different shapes in terms of AP height and AP width. In observed representative second spiking traces at P3, P5, P7, P9 and P11 (**Figure 3.3.A**), these differences in waveform were apparent at a glance.

The waveforms of the mean first APs from each cell were grouped by age into four sets, P3-P4, P5-P6, P7-P8 and P9-P11, and averaged to give the mean first AP within that age range. These waveforms, in the period from threshold to threshold+16ms, were aligned by starting membrane potential, allowing the kinetics to be more clearly observed. The waveforms were averaged across both Standard Internal and Sucrose solution (**Figure 3.3.B**), Standard Internal only (**Figure 3.3.C**, *top*) or Sucrose only (**Figure 3.3.C,** *bottom*). In each dataset, the waveforms were observed to grow taller, whilst narrowing in terms of duration (AP width).

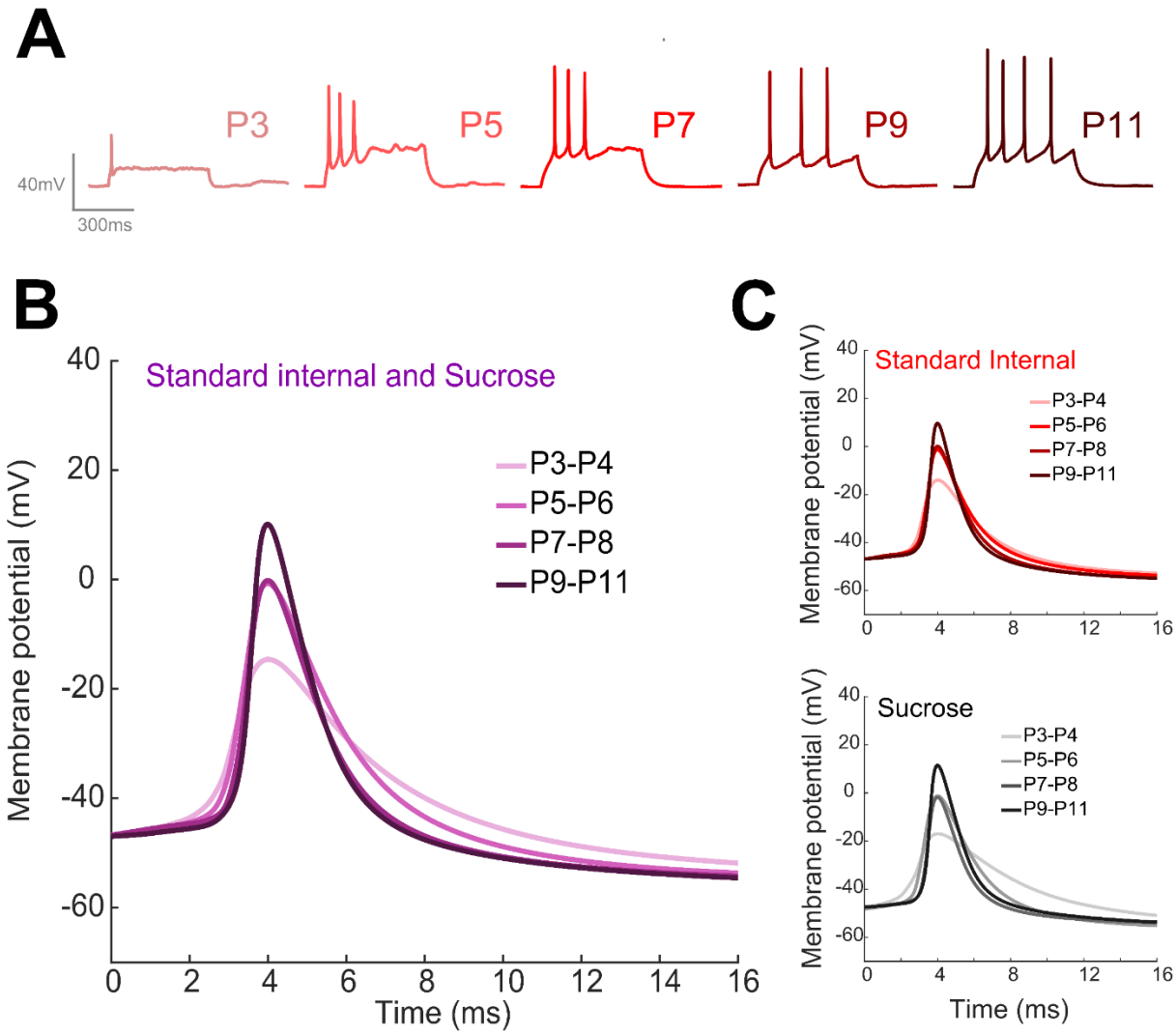

Figure 3.3: The waveform of the action potential changes with postnatal age.
A: Representative second spiking traces in the current-step protocol (typically trace 9 or 10 in the 11-step cycle) for cells of odd-numbered ages between P3 and P11. **B**: The average first AP at rheobase from cells patched with either Standard Internal solution or Sucrose solution for four age groups. The AP is analysed from threshold to 16ms post-threshold. APs are aligned by threshold membrane potential. **C**: The average first AP from cells patched with Standard Internal solution (*top*) or Sucrose solution (*bottom*), again, grouped by age.

First AP height and width data were plotted as a function of age (**Figure 3.4**), both in scatter plots (main figures) and bar graphs of data grouped by age (P3-P4, P5-P6, P7-P8, P9-P11, insets). APs were observed to grow in height from 24±6mV at P3 to 60±3mV at P11, and reduce in width from 2.4±0.5ms at P3 to 1.3±0.1ms at P11. The trends in AP height and width with age were expected to follow a sigmoidal function, levelling off when the maximum possible AP height and minimum width were reached (presumably at maturity). However, the relationship was approximated to be linear for the relatively narrow range of postnatal ages in the data. A linear fit was applied to the scattered data and correlation with age was analysed using Pearson's correlation coefficient. Bar graphs were analysed via one-way ANOVA and Tukey-Kramer tests of significance. Statistically significant decreases in width with postnatal age were observed whether the data was assimilated from cells patched with Standard Internal or Sucrose (**Figure 3.4.A**), or whether the internal solution populations were kept separate (**Figure 3.4.B**). Likewise, statistically significant increases in height with postnatal age were observed, with data grouped to include both Standard Internal and Sucrose (**Figure 3.4.C**) or differentiated by internal solution (**Figure 3.4.D**). Interestingly, the largest increases in height and decreases in width did not appear to occur simultaneously: between P3-P4 and P5-P6 a statistically significant increase in AP height was observed, but no such statistically significant decrease in AP width was seen during the same period (**Figure 3.4.A** and **C**, *insets*). A statistically significant decrease in AP width was observed by P7-P8, but no significant increase in AP height was observed between P5-P6 and P7-P8. Between P7-P8 and P9-P11, changes in AP width were unperceivable whilst the height of the AP again increased.

Dataset	Slope (ms/day)	Intercept (ms)	Correlation	P value
Standard Internal + Sucrose	-0.15	3.07	-0.51	<0.0001
Standard Internal	-0.12	2.79	-0.40	<0.01
Sucrose	-0.20	3.55	-0.72	<0.0001

***Table 3.1**: Linear fits to first action potential width as a function of age.*

Dataset	Slope (mV/day)	Intercept (mV)	Correlation	P value
Standard Internal + Sucrose	3.48	18.60	0.55	<0.0001
Standard Internal	3.65	17.55	0.57	<0.001
Sucrose	3.08	20.89	0.52	<0.01

***Table 3.2**: Linear fits to first action potential height as a function of age.*

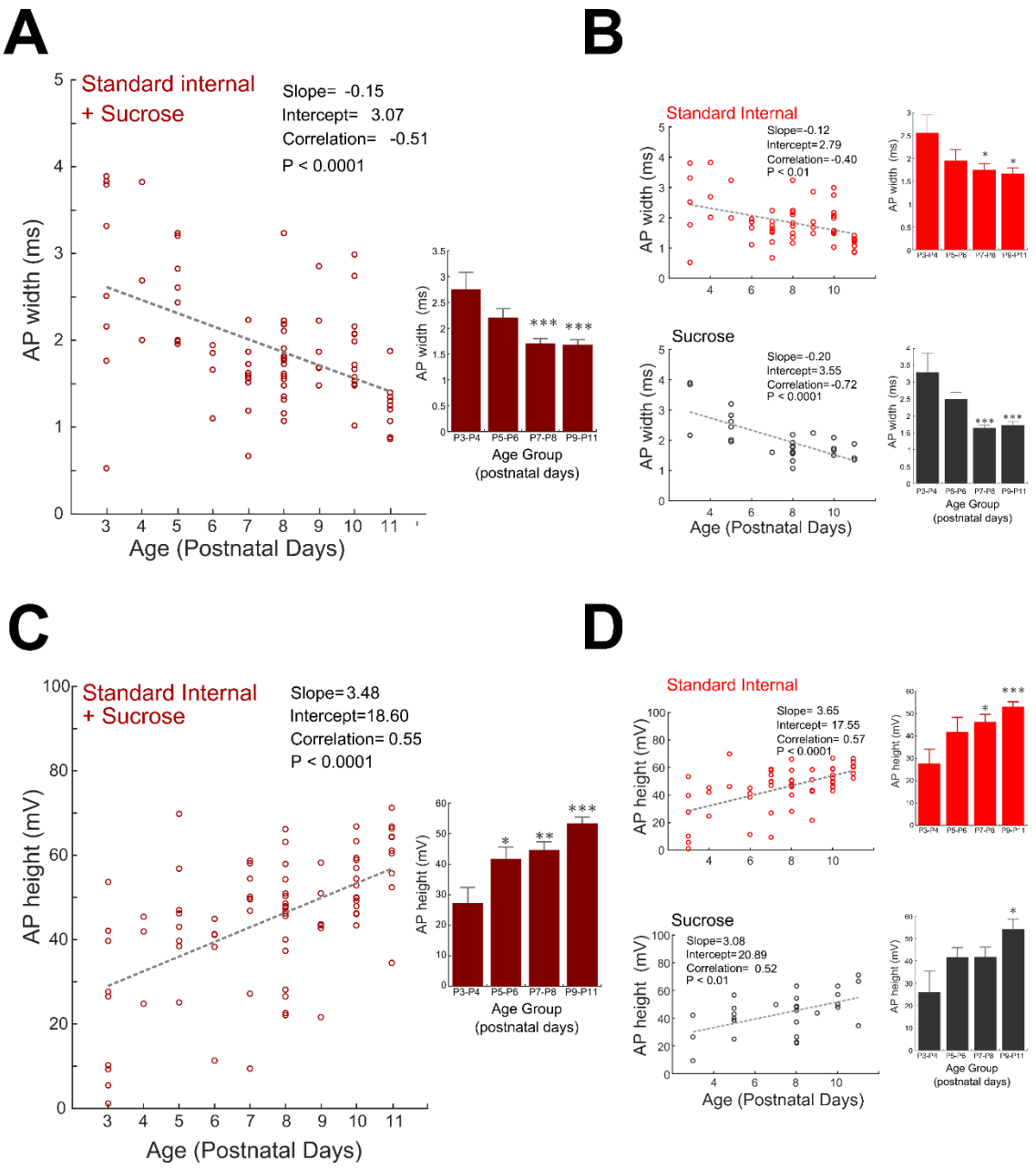

Figure 3.4: The action potential significantly changes in width and height with age. **A:** The first AP width against age for cells patched with Standard Internal solution or Sucrose solution. Empty circles show the individual cells, dotted line shows linear fit to data, Pearson's correlation coefficient =-0.51, P<0.0001. Inset shows bar graph of data grouped into four age groups, P3-P4, P5-P6, P7-P8 and P9-P11. Error bars show the standard error in the mean. A one-way ANOVA and a Tukey-Kramer test show a significant (***P<0.001) difference between the youngest group and subsequent groups. **B**: As before, but data are split by their internal solution to give data from Standard Internal solution experiments (*top*) and Sucrose solution experiments (*bottom*). **C:** The first AP height against age for cells patched with Standard Internal solution or Sucrose solution. Linear fit to data gives positive correlation, with Pearson's correlation coefficient of 0.55, P<0.0001. Inset shows bar graph of data, grouped by age as above. One-way ANOVA and Tukey Kramer test show significant differences (*P<0.05, **P<0.01, ***P<0.001) between the youngest group and subsequent groups. **D:** As before, but data are split by internal solution.

The first derivative of membrane potential

Changes to the AP with development were further illuminated by taking the first derivative of the membrane potential during spiking behaviour (**Figure 3.5.A**). The maximum and minimum of the first derivative, corresponding to the steepest positive gradient and steepest negative gradient of the AP (also known as the maximum rate of rise and maximum rate of fall), were evaluated both in terms of postnatal age, and in terms of their relationship to one another. Since measurements of the waveform already demonstrated that the AP increases in amplitude whilst decreasing in duration, it was already known that the rate of rise and rate of fall grow in magnitude with age. What was deemed more interesting was how they relate to one another: was the increase in height and decrease in width a consequence of either the rising phase or the falling phase, or a combination of both? By observing the relationship between these two measures as a function of age, insight into whether the ionic species that govern depolarisation or hyperpolarisation dominate the maturation of the AP waveform could be found.

The maximum rate of rise was plotted in a scatter graph against the maximum rate of fall for data from cells patched with either Standard Internal or Sucrose solutions grouped into four developmental ages; P3-P4, P5-P6, P7-P8 and P9-P11 (**Figure 3.5.B**). A linear fit (Pearson's correlation coefficient: P3-P4=0.83, $P<0.001$; P5-P6=0.86, $P<0.001$; P7-P8=0.86, $P<0.0001$; P9-P11=0.84, $P<0.0001$) permitted measurement of the slope, or relationship, between the two variables, and hence observation of whether it was the depolarising or hyperpolarising active transport that dominated the shape of the AP at these broad age groups. The slope was observed to change, initially pointing increasingly towards Min dV/dt between P3-P4 and P5-P6, before pointing more towards Max dV/dt, indicating the dominance of the depolarising phase (rate of rise) between P5-P6 and P9-P11. Data was combined from cells patched with Standard Internal and Sucrose solutions, as no difference in the time-dependent dynamics was found (**Figure 3.5.C**). The ratio of Max dV/dt to Min dV/dt was plotted as a function of age in both scattered (**Figure 3.5.D**) and age-grouped (P3-P4, P5-P6, P7-P8, P9-P11) data (**Figure 3.5.D** *inset*)

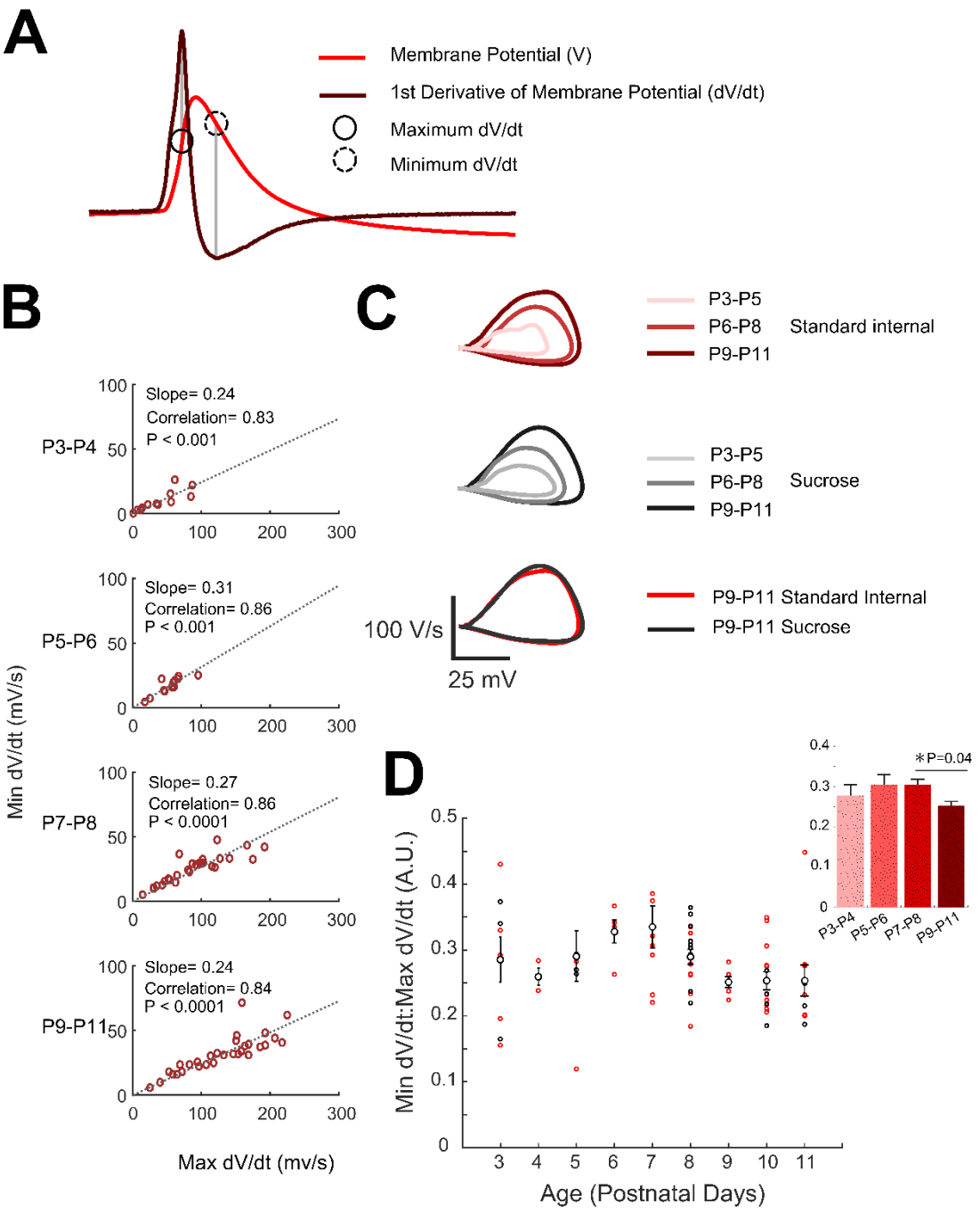

Figure 3.5: The first derivative of the membrane potential. A: A representative first AP with its corresponding first derivative. The maximum and minimum of the first derivative correspond to the steepest part of the AP on the way up (maximum rate of rise) and the steepest part of the way down (maximum rate of fall). **B:** Maximum derivative against minimum derivative for cells patched with Standard Internal solution or Sucrose solution, grouped by age into four groups, P3-P4, P5-P6, P7-P8 and P9-P11. A linear fit ($P<0.01$) to each grouped dataset changes in slope with age. **C:** Phase plane diagrams (dV/dt against Vm) for both Standard Internal and Sucrose solutions illuminate the differences in age groups and show that there is no discernible difference between APs from cells patched with the two solutions. **D:** The ratio of Min dV/dt to Max dV/dt, plotted as a function of age. Empty circles represent individual cells patched with either standard internal (red) or sucrose (black) solutions. White circles with error bars show the mean rate of rise ratio at each age with the standard error in the mean. Inset shows a bar graph of grouped data. One-way ANOVA and Tukey-Kramer test shows a significant difference ($P<0.05$) between P7-P8 and P9-P11 cells.

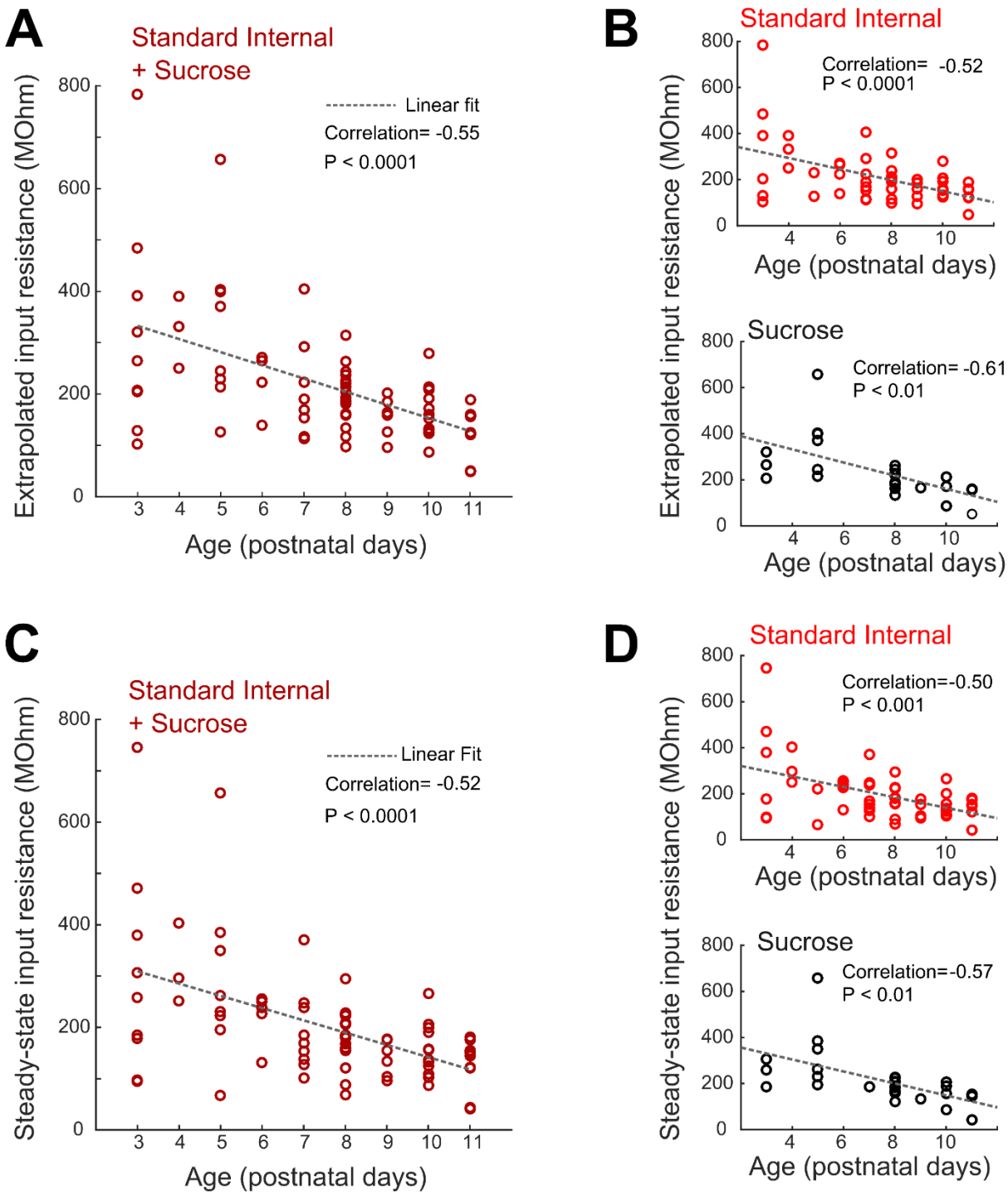

Figure 3.6: The input resistance decreases with postnatal age. For each scatter plot, empty circles represent individual cells, dotted line shows a linear fit, assessed for correlation using Pearson's correlation coefficient. **A:** Extrapolated input resistance data from cells patched with Standard Internal or Sucrose solutions. (Pearson's correlation coefficient = -0.55, P<0.0001). **B**: Extrapolated input resistance data for separate Standard Internal and Sucrose solution datasets. **C**: Steady-state input resistance as a function of age for cells patched with Standard Internal or Sucrose solutions (Pearson's correlation coefficient = -0.52, P<0.0001). **D**: Steady-state input resistance data for separate Standard Internal and Sucrose solution datasets.

Input resistance

The mean steady state input resistance and mean extrapolated input resistance of each cell were plotted against developmental age (**Figure 3.6**). A linear fit returned statistically significant negative correlations between age and mean input resistance for both input resistance measurements (Pearson's correlation coefficient, extrapolated input resistance = -0.55, P<0.0001, steady state input resistance = -0.52, P<0.0001). This was the case whether the data from Standard Internal and Sucrose solution datasets were assimilated (**Figures 3.6.A and 3.6.C**) or kept separate (**Figures 3.6.B and 3.6.D**). The mean extrapolated input resistance was observed to decrease from 321±71MΩ at P3 to 133±15MΩ at P11, whilst the mean steady-state input resistance was observed to decrease from 302±69MΩ at P3 to 129±16MΩ at P11. Additionally, the variation in the input resistance appeared to decrease with development (**Figure 3.7**). To quantify this, the coefficient of variation (standard deviation/mean) of input resistance as a function of age was plotted for each of the two measures at each age point. Negative correlations were found in each case (Pearson's correlation coefficient, extrapolated input resistance = -0.43, steady-state input resistance = -0.46), though these correlations did not reach statistical significance in either case.

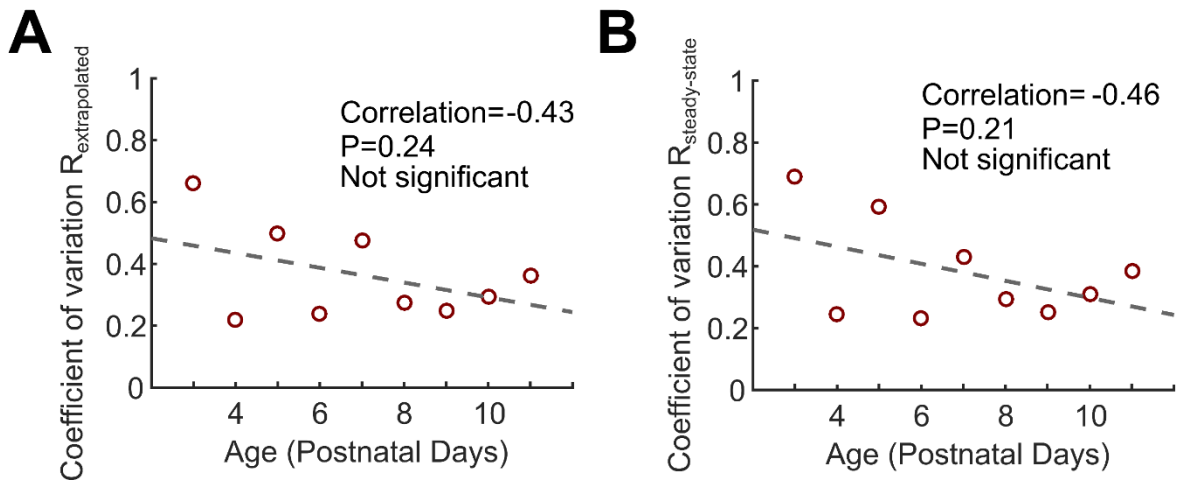

Figure 3.7: A decrease in variation of input resistance with age is suggested, though not statistically confirmed. A: Coefficient of variation (dimensionless units) for extrapolated input resistance. Empty circles are the coefficients at each age point for cells patched with Standard Internal or Sucrose solutions. Dotted line shows linear fit (Pearson's correlation coefficient). **B:** As above, for steady-state input resistance.

3.4 Discussion

Temperature control in electrophysiology experiments

The results presented here demonstrate the necessity of careful temperature control during electrophysiology experiments that examine AP waveform, in accordance with previous work (Liu, Blair et al. 2017). Whilst there is a consensus on the importance of controlling the temperature, there is not the same agreement as to whether the temperature used should be closer to 'room' temperature, typically cited to be in the range of 20-25ºC (Luhmann, Schubert et al. 1999, Luhmann, Reiprich et al. 2000, Valiullina, Akhmetshina et al. 2016), or 'physiological' temperature, which has been listed as between 34-38°C in the wildtype mouse (Talan 1984, Liu, Blair et al. 2017).

When performing experiments on tissues subject to biophysical forces, what is of interest is how they work in their natural conditions. To understand how the biophysical actions and properties of the neuron develop with maturation, the conditions must replicate reality as closely as possible. Of course, ex-vivo slice electrophysiology can only come so close to true physiological conditions but ensuring that the cells are at a temperature within physiological range at least minimises the thermodynamic discrepancies. For this reason, this preliminary temperature experiment informed all subsequent experiments, which were performed with ACSF heated to 36.9±0.4ºC.

An interesting consideration is that across the temperatures studied, cells continued to fire APs. Indeed, temperature robustness in terms of spiking activity may be governed by the homeostatic mechanisms that manipulate ion channel conductances (Rinberg, Taylor et al. 2013, O'Leary and Marder 2016).

Observations of changing waveform

Both the height and width of APs were observed to change with age, becoming taller and thinner, in accordance with similar previous reports on APs from regular spiking cells within the mouse and rat barrel cortex (Parker, Cruikshank et al. 2009, Valiullina, Akhmetshina et al. 2016). The correlations between cell age and AP height and width were observed to be highly statistically significant ($P<0.001$), indicating that changes to AP waveform are a part of neuronal development for regular spiking cells. APs have been observed in cortical cells of rodents from as early as embryonic day 18, with repetitive action potentials detected at P0 (Luhmann, Schubert et al. 1999, Luhmann, Reiprich et al. 2000, Khazipov and Luhmann

2006). Linear fits to the data presented here, though simplistic, provided an interesting estimate of the AP waveform properties at birth, before the AP is subject to sensory experience, with AP width estimated to be 3.1±0.5ms, and AP height estimated to be 18.6±2mV at P0. With the data presented here limited to a brief developmental period, it would be interesting to observe at what age a 'mature' AP appears. It could be hypothesised, for example, that this maturation of waveform occurs when active whisking begins, at 2 weeks of age (Arakawa and Erzurumlu 2015), or around the time of weaning (typically 21-22 days (Bigiani, Cristiani et al. 2002)), where the young animal becomes responsible for finding its own food and therefore reliant on whisking behaviour to explore its environment.

Not only was the AP observed to change with age, but it was observed that the width and height of the AP did not change concurrently, but instead appeared to 'take turns' in dominating the developmental trajectory of the overall waveform. Specifically, the APs first grew in height, then underwent an intermediary period of narrowing, before having a final increase in height towards the end of the developmental period studied. This observation indicates a compensatory mechanism that points to homeostasis underlying this period of maturation. Such mechanisms have been suggested in previous work (O'Leary, Williams et al. 2013, Ciarleglio, Khakhalin et al. 2015), and could be aid our understanding of neuronal development.

Though clear and statistically significant trends were observed in the AP properties, a large degree of variance in these properties at each age point was also present. Some noise in the AP waveform measurements as a function of age was almost certainly due to the imprecise measurements of time of birth. The dates of birth of all mouse pups were recorded, but of course, animals are born when they are ready, and not when would be most convenient to the experimentalist. Though the dams were checked at approximately the same time each day, each postnatal age reported comes with an error of ±24 hours. Mouse pups were sacrificed at approximately the same time of day for each experiment (±3 hours), so relatively speaking, the variance in this factor would have a negligible effect (it was assumed that neurons do not go on developing once the brain has been sliced). An additional consideration was that the gestation period of the mouse pups was not known, except that it fell within the normal range of 20±1 days (Barkley and FitzGerald 1990, Murray, Morgan et al. 2010). Arguably, the development of the barrel cortex and the cells contained within may be more precisely measured from the date of conception, rather than the date of birth, so differences in gestation by only a few hours might make a significant difference to the AP waveform at time of measurement. Another consideration is that dams do not necessarily have consistent maternal

behaviours; differences in feeding and grooming behaviour may lead to developmental deficits. The use of weight as the metric of development, rather than or as well as postnatal age, may be a suitable method of assuaging these variations, though this may be highly dependent on litter size.

As has been shown here, the use of Standard Internal or Sucrose solutions in patch-clamping experiments produced no observable difference in dynamics across any of the ages studied, permitting these data to be assimilated. However, data from cells patched with internal solutions containing any concentration of Neurobiotin were excluded from this analysis, due to the surprising observation that Neurobiotin changed the AP waveform. This is explored thoroughly in Chapter 6: *The Effect of Neurobiotin on Spiking Properties*.

The information contained within the first derivative

The maxima and minima of the first derivative of the AP membrane potential were investigated for age-dependence and further illuminated the nonlinearity of AP waveform maturation, with the later period of maturation (P9 to P11) dominated by the rising phase of the AP at statistically significant levels ($P<0.05$). First derivative dynamics have been analysed in previous work by careful measurement of the features of phase plane diagrams (examples of which are shown in **Figure 3.5.C)**. Such diagrams, produced by plotting the membrane potential against its own first derivative (Bean 2007), can be used to note subtler changes to the AP, in experimental, computational and theoretical studies (Naundorf, Wolf et al. 2006, Telenczuk, Fontaine et al. 2017).

Input resistance

A developmental decrease in input resistance was observed, in accordance with previous work, with the values of input resistance of comparable magnitude to reported values (McCormick and Prince 1987, Luhmann, Schubert et al. 1999, Luhmann, Reiprich et al. 2000, Bahrey and Moody 2002, Parker, Cruikshank et al. 2009, Valiullina, Akhmetshina et al. 2016). The decrease in input resistance variation observed (but not statistically confirmed) here has been previously reported (Valiullina, Akhmetshina et al. 2016), and attributed to the huge developmental diversity between individual neurons at these ages.

High input resistance in immature cells has previously been shown to be correlated to low spiking frequency and low spike height, features that have been hypothesised to correlate to high cell adaptability (Luhmann, Reiprich et al. 2000); presumably the high input resistance

observed in neurons that are still migrating and differentiating is a consequence of the lack of ion channels through which currents could flow. Correspondingly, the steady low values of input resistance seen in more mature neurons could be hypothesised to be a consequence of cells finding a place in their functional network and developing connections, providing electrical inputs that accelerate the formation of ion channels, as well as a consequence of cell growth (Bahrey and Moody 2002).

The input resistance in developing cells may be influenced not only by the morphology, but also the presence of gap junctions. The role of gap junctions in developing cortical neurons is explored in Chapter 5: *Gap Junctions and Morphology*.

Voltage gated ion channels underpin the changing AP waveform

The features of the AP waveform are determined by the currents through voltage-gated ion channels in the neuronal membrane (Bean 2007). The initiation period of the spike, and consequently its height, are determined by the voltage-gated opening of Na^+ channels, with height and Na^+ channel population being observed to both increase with development (Luhmann, Reiprich et al. 2000). The width, or duration, of the spike, meanwhile, has been extensively linked to potassium channels (Bean 2007, Deng, Rotman et al. 2013, Kimm, Khaliq et al. 2015, Liu, Blair et al. 2017), with spike width being manipulated via the application of specific K^+ channel blockers (Kimm, Khaliq et al. 2015), or via the saturation and inactivation of K^+ channels following current injections that pushed the cell to fire long trains of high-frequency spikes (Liu, Blair et al. 2017). Likewise, fast activating currents through K^+ channels have been implicated in narrower APs (Liu, Blair et al. 2017).

Interpreting the results presented here in terms of the established understanding of AP waveform, it can be hypothesised that the changes in waveform observed correspond to an increased population of both Na^+ and K^+ voltage-gated ion channels, with an oscillating dominance between the two. The periods of increased AP height between P3 and P5 and between P9 and P11, point to the effect of Na+ channels being proportionately larger than that of K+ channels during these times. Correspondingly, the period of narrowing, with little change in height, between P5 and P9, implicates the K^+ channels as dominating during this period. This oscillation suggests a homeostatic mechanism, in lines with what has previously been reported (O'Leary, Williams et al. 2013). This oscillation in dominance may repeat one or two more times, until the AP is fully mature and able to communicate information efficiently. What is less clear is whether this change is due to the population or effectiveness

of different ion channels. In fact, all that can be inferred is the proportional influence of the different types.

The use of ion channel blockers has been a feature of many studies for the isolation of the different currents that determine the features of the AP (Bean 2007, Deng, Rotman et al. 2013, Kimm, Khaliq et al. 2015, Begum, Bakiri et al. 2016, Rowan, DelCanto et al. 2016, Liu, Blair et al. 2017). Without the use of these drugs, adverse and unspecific effects on the experimental protocols in this delicate period of maturation are avoided, but different currents go unattributed to their ion-channels. Using the AP waveform as a command waveform and making recordings in voltage-clamp has previously been used as a technique to understand the contributions of different ion channels (Deng, Rotman et al. 2013, Liu, Blair et al. 2017). Such a method could be used in future experiments to better understand development.

Alternatively, computational models can be used to provide insight to the developmental interplay between ion channels and their subtypes. Hodgkin-Huxley style models are a useful tool for determining the contribution of different ion channels in terms of their conductance. For young and developing cells, the nonlinear dynamics of active transport requires models that are adequately optimised for the changes inherent in maturation. Parameter optimisation of Hodgkin-Huxley models, for effective use on data from immature neurons is discussed thoroughly in Chapter 7: *Multi-parameter Optimisation of Conductance-Based Hodgkin-Huxley Models*.

The evolutionary benefit of a changing action potential waveform

Whilst it is apparent that the AP waveform changes with development, what is not so clear is why the AP changes at all, why neurons are not born firing APs with mature waveforms. The developmentally-limited AP fired by immature neurons may be a consequence of the metabolic limitations of the developing brain or may in fact hold benefits determined as favourable over long millennia of evolution.

Previous work has shown extensively the dependence of neuronal activity in the somatosensory cortex on sensory experience, with spontaneous spiking of variable and desynchronised frequencies observed in immature cells (Khazipov and Luhmann 2006, Winnubst, Cheyne et al. 2015, Valiullina, Akhmetshina et al. 2016) and more precise spiking, corresponding to cues within the sensory environment developing with postnatal age (Khazipov and Luhmann 2006, Valiullina, Akhmetshina et al. 2016). This could easily be investigated by the removal of sensory input by simply trimming the whiskers of the neonatal

mouse and conducting experiments that are otherwise identical to those outlined in this thesis. Sensory experience has been shown to be a primer for gene expression that leads to the formation of voltage-gated ion channels (Khazipov and Luhmann 2006). Should ion channel populations and AP waveform be dependent on sensory experience, we would expect the sensory-deprived animal to produce APs that remain it their immature state, and not become taller and narrower with development.

However, an alternative hypothesis may be that the observed changes in AP waveform are independent of sensory experience, and that the AP waveform follows a developmental trajectory predetermined in utero. If this is the case, then questions arise as to why neurons are not born with adequate and balanced populations of ion channels that produce AP waveforms in their mature state. One possible explanation is that, given the migration and differentiation still undergoing during the developmental period studied, it may be inefficient for neurons to have mature ion channel populations, when these may prove ineffectual in their final role. The biophysical properties of the neuron must be able to withstand the flux of maturation (O'Leary, Williams et al. 2013), and this may be simpler for cells with fewer ion channels. Such a hypothesis could be investigated by observing whether mature APs correlate with the appearance of mature functional networks, more than they correlate with age. This could be done simply by considering different cells patched from the same area of cortical slice: it would be interesting to observe whether 'mature' spiking activity correlated to networks, whether gap-junction or synaptically coupled.

It may be that the immature AP is metabolically beneficial to the immature neuron. A low-amplitude AP may communicate the necessary information to trigger gene expression, without the metabolic cost of forming all the ion channels necessary for a mature AP; until networks are formed it may be favourable to keep APs low-amplitude. This could also provide an explanation for developmental changes in spiking frequency previously reported (Luhmann, Schubert et al. 1999, Valiullina, Akhmetshina et al. 2016); for the immature neuron, there may be little or no benefit to firing long trains of APs when there are few synapses with which to build functional networks under Hebbian plasticity rules (Hebb 1949).

The broadness, or duration, of the AP may also provide initial conditions that permit efficient maturation; it may be developmentally beneficial to start with broad spikes. Previously, the breadth of spikes has been implicated as an important factor in the probability of neurotransmitter release (Deng, Rotman et al. 2013). Neuronal communication relies on the summation of many signals from presynaptic neurons in the body of a postsynaptic neuron, a

summation that is time dependent. Coincidence of activity drives synaptic plasticity and the formation of functional networks: "*out of sync, lose your link*" (Winnubst, Cheyne et al. 2015). In developing networks where activity is largely unsynchronised or spontaneous, narrow APs like those seen in mature neurons would have a small probability of triggering ongoing signals within the same time window. The wider APs seen in immature neurons fall over a longer time window, and therefore have an increased probability of being concurrent with one another. Spike-time dependent plasticity may require a larger time signature for the formation of immature networks, therefore, the narrowing of APs with development would correspond to the refinement of functional networks as they are formed. Thus, the cortical networks of the barrels would maintain homeostasis of communication whilst increasing their probability of self-formation and their maximum efficiency.

This hypothesis would also be supported by the observation that APs appear to go through a period of growing taller before they become narrower, emphasising the idea that APs are as wide as is necessary before the formation of effective functional networks leads to the increased spiking activity, that in turn leads to the gene expression that drives increased ion channel formation, and ultimately permits refinement.

The relationship between active dynamics and input resistance

The changes to AP waveform are presumably related to the reduction in input resistance observed. The observed decrease in input resistance could be attributed to the increasing population of voltage-gated ion channels that permit a greater flux of ionic species in and out of the cell, ultimately contributing to larger potential differences across the cell membrane.

The active dynamics are coupled to the passive dynamics

The AP is a perturbation of the cell membrane, triggered by and manifested as a change in charge distributions. Although the active dynamics produce the distinctive shape of these events, they are underwritten by the subtler passive dynamics of the cell membrane (Bean 2007, Guan, Armstrong et al. 2015). These dynamics are determined by the membrane resistance and the cell morphology (Rowan, DelCanto et al. 2016), both of which change with development as the cell grows. When observing how the AP changes with age, the coupling between these two types of dynamics must also be considered. The maturation of the passive dynamics is therefore explored in the next chapter.

3.5 Summary

The AP of excitatory regular spiking cells within the barrel cortex of P3-P11 neonatal mice changes nonlinearly over maturation, demonstrating both increases in height and decreases in width. Meanwhile, the input resistance is shown to decrease dramatically, in accordance with previous reports. This age dependence in input resistance suggests a change in ion channel density, but also gross changes to the cell morphology over the process of maturation. Using qualitative arguments based on Hodgkin Huxley dynamics, the changes in AP waveform and input resistance can be hypothesised to be caused by variations in voltage-gated ion channel populations during maturation. Specifically, the result presented here suggest an initial increase in Na^+ channels, followed by a rectifying increase in K^+ channels, in turn followed by Na^+ again that balances and adjusts the biophysics in accordance with homeostatic rules. This homeostatic compensation may allow the neurons to communicate and begin to form their function networks whilst undergoing the gross changes in position and morphology that occur with brain maturation.

4 Passive Dynamics

Key Findings

1. Passive dynamics, in the form of an exponential membrane potential decay across the cell membrane, correspond to the electrical discharge across the insulating lipid bilayer. A two-compartment model of exponential decay, based on that of a solid-state resistor and capacitor, fits well to the passive dynamics data.
2. The coefficients of the two-compartment model demonstrate age-dependence of the cell membrane resistance and capacitance, indicative of a growing surface area.
3. A fast component of passive dynamics decay is detected in some cells, with a dendritic time constant up to an order of magnitude smaller than that seen in other cells. Possible explanations for this current 'sink' are explored.

4.1 Introduction

The changing biophysics of the action potential (AP) waveform is determined by the active dynamics of the voltage-gated ion channels in the developing neuron, but is underpinned by the dynamics that do not require active transport (Hille 2001, Lepora, Blomeley et al. 2011). For example, the magnitude of post-synaptic potentials at synapses are dependent on the neuronal membrane capacitance (Gentet, Stuart et al. 2000), ultimately contributing to the AP waveform. These so-called 'passive dynamics' (PD) are governed by the diffusive electrostatics of the neuronal membrane but are coupled to the dynamics of fast acting voltage-dependent ion channels. Passive neuronal biophysics of this nature have previously been shown to be highly dependent on geometry (Rall 1969): both the gross cell morphology and the cell membrane thickness (Mason and Larkman 1990). Studying these dynamics over the course of postnatal development therefore provides insight into how the gross geometry of the cell membrane affects its electrical properties as the cell grows and differentiates. Inclusion of these passive dynamics is therefore necessary when formulating models of the dynamically maturing neuron.

The biophysics of the cell membrane

The membrane of the neuron is a lipid bilayer (Montal and Mueller 1972, Gentet, Stuart et al. 2000). Polar lipid molecules, consisting of a hydrophilic phosphate head and hydrophobic 'greasy' tail of two fatty-acid chains, assemble into bilayer structures that form the basis of

the membrane (Bretscher 1972). This lipid bilayer is thin, being only a few nanometres across (Gentet, Stuart et al. 2000), but also impermeable to ions due to its chemical structure, allowing the neuron to self-regulate and generate action potentials via the action of voltage-gated ion channels. Electrically insulating when compared to the conductive cytoplasm of the cell or the extracellular media, the conductor-insulator-conductor formation defines the lipid bilayer as a capacitor: a passive electrical component that stores potential energy in its electric field (Barbour 2014). The cellular cytoplasm, cell membrane, and extracellular media can be approximated as a resistor-capacitor (RC) circuit (Durand, Carlen et al. 1983, Wright, Bardakjian et al. 1996, Barbour 2014), with branches in the circuit representing different morphological parts, or compartments, of the neuron. The level of complexity of the RC circuit can therefore be used to infer neuronal models with an increasing number of compartments, which can in turn be used to model the finer detail of how the cell membrane changes with development.

The cell membrane as a circuit of capacitors

By Coulomb's law, the amount of charge that can be stored within any capacitor is equal to

$$Q = VC \tag{4.1}$$

where Q is the amount of charge stored, V is the potential difference across the capacitor and C is the capacitance, typically measured in Farads (F). The capacitance per unit area of membrane is referred to as the specific capacitance of the membrane, and is generally quoted as ~1μFcm^{-2}, though diversity has been reported (Major, Larkman et al. 1994). This value has been shown to be a good estimate since the pioneering work of Hodgkin and Huxley (Hodgkin and Huxley 1952, Wright, Bardakjian et al. 1996) and has thus historically been assumed to be a constant across all excitable membranes, with the diversity of proteins found in the membrane of little consequence (Gentet, Stuart et al. 2000).

When passive dynamics are triggered via the charging of the capacitive membrane, the voltage discharge measured across the membrane can be described as an extension of the well-known capacitor discharge equation:

$$V = V_{Ci} e^{\frac{-t}{RC}} \tag{4.2}$$

This can be expanded to a potentially infinite sum of exponential components to describe a cell of multiple compartments, where each term represents a compartment in the cell, or a

branch of the RC circuit, , separated by an axial resistance (D'Aguanno, Bardakjian et al. 1986, Amsalem, Geit et al. 2016).

$$V = V_{m_{PD}} + \alpha_1 \cdot e^{\frac{-t}{R_1 C_1}} + \alpha_2 \cdot e^{\frac{-t}{R_2 C_2}} + \alpha_2 \cdot e^{\frac{-t}{R_2 C_2}} + \ldots + \alpha_i \cdot e^{\frac{-t}{R_i C_i}} \quad (4.3)$$

In this model, V is the measured membrane potential during charging and discharging, α_i is the capacitor voltage for each compartment at time t_0 (which is a hypothetical value that assumes the membrane has been fully charged), t is time, R_i is the specific resistance of the membrane in compartment i, C_i is the specific capacitance of the membrane of compartment i, and Vm_{PD} is the resting membrane potential of the cell prior to any passive dynamics.

In each exponential term, the denominator can be expressed as the time constant *tau*, the time taken for the capacitor to discharge through a resistor to ~36.8% of its maximum charge voltage:

$$\tau_i = R_i C_i \quad (4.4)$$

The time constants that can be found from the data are therefore indicative of both the compartment resistance and the compartment capacitance.

When faced with this infinite sum of compartments, it is necessary to estimate the level of complexity necessary to capture the biophysics, and thereby limit the number of compartments in the model.

The first term in the infinite sum has historically been taken as an approximation of the summed dynamics, with the first time constant taken as the most important for understanding the membrane. This dominant time constant has, perhaps misleadingly, been generally referred to as the ‘membrane time constant’ and has previously been determined by ‘peeling’ away the dynamics of all subsequent terms (Rall 1969, Amsalem, Geit et al. 2016), or by parameter optimisation (D'Aguanno, Bardakjian et al. 1986). It has been employed as an empirical measure of neuronal membranes (Durand, Carlen et al. 1983), despite long-standing concerns that this may be insufficient to capture all of the dynamics (Mason and Larkman 1990). Arguments for the inclusion of rectifying secondary time constants in even the simplest models have been postulated since the 1960s (Rall 1969).

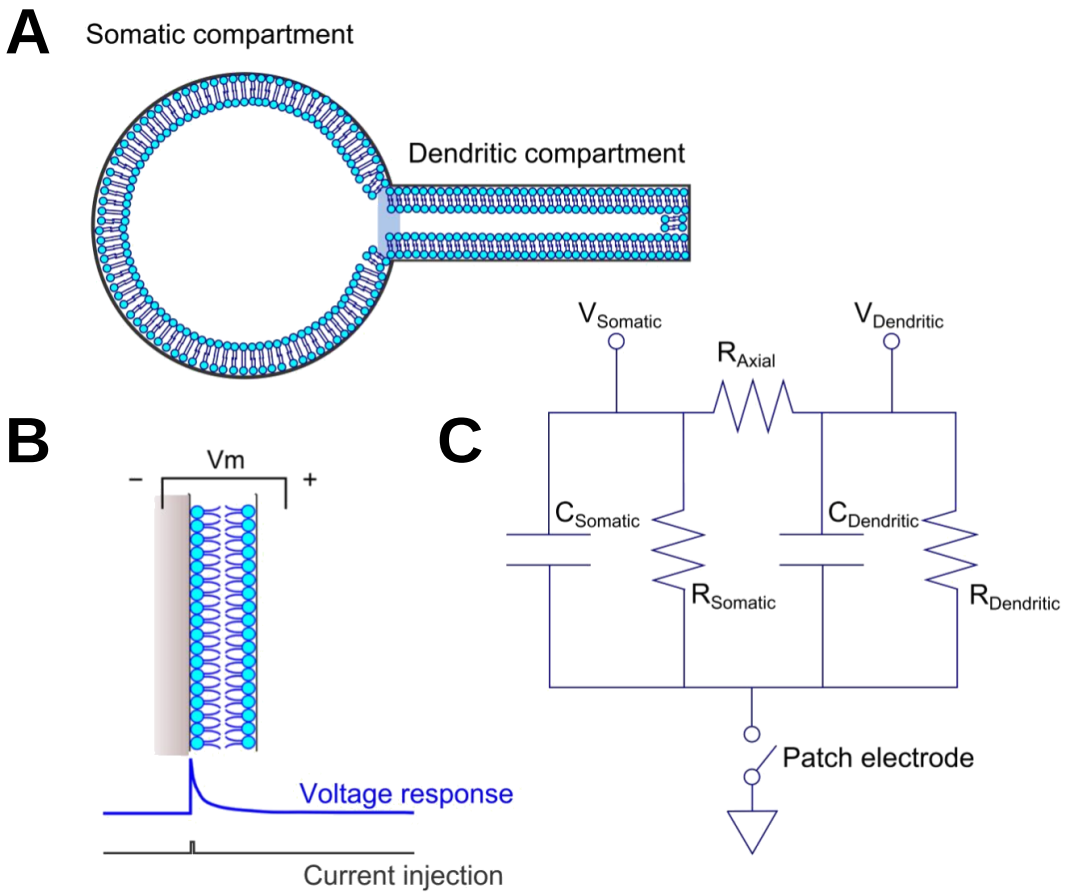

Figure 4.1: The neuronal membrane is modelled as a capacitor. A: The cell is approximated as two compartments, each with a lipid bilayer membrane. **B:** The capacitance of the cell membrane is investigated via small current injections that trigger a capacitive voltage response. **C:** The neuron can be thought of as a two-branch RC circuit, with a single amplified input (the patch electrode) but with two membrane potentials to be measured in the one voltage output: the somatic and the dendritic. An axial resistance separates compartments.

Two-compartment models have been used by several groups (Kita, Kita et al. 1984, Wright, Bardakjian et al. 1996, Kim, Major et al. 2009) to good effect. A two-compartment passive model of striatal medium spiny and fast spiking neurons (Lepora, Blomeley et al. 2011), derived from differential expressions of the membrane equation, has been used to describe the membrane electrodynamics of excitatory neurons via an equation of the form:

$$V = \alpha_1 \cdot e^{\frac{-t}{\tau_1}} + \alpha_2 \cdot e^{\frac{-t}{\tau_2}} + V_{m_{PD}} \tag{4.5}$$

This two-compartment model forms the basis of the work described here.

The implications of passive dynamics on neuronal morphology

Since the work of Rall, the time constants of passive membrane dynamics have been related to the electrotonic geometry of neuronal compartments (Rall 1969, Durand, Carlen et al. 1983, D'Aguanno, Bardakjian et al. 1986). Taking into account the specific membrane capacitance and the magnitude of the current injection that facilitates the charging of the cell membrane, the four coefficients returned from the two-compartment model, $Alpha_1$, $Alpha_2$, tau_1 and tau_2, can be related to an estimation of the neuronal surface area (Lepora, Blomeley et al. 2011). Being determined by both geometry and resistance, the cell membrane time constants have previously been shown to change with age, as neurons grow (Luhmann, Schubert et al. 2011). Passive dynamics predictions of the surface area would be expected to show neuronal growth, with a particularly large increase in dendritic surface area corresponding to the critical period for dendritic spine growth (Ashby and Isaac 2011).

This chapter describes an investigation on the age dependence of PD via the application of the two-compartment model to PD data recorded from the same excitatory neurons that underwent active dynamics investigations, as described in Chapter 3*: Active Dynamics*, in acute slices from mice aged P3 to P11. It describes the extensive data processing methods necessary for fitting this model to experimental data and compares the time constants returned from this fitting to that from the literature. It then explores how the coefficients of this fit vary with postnatal age, and relates the passive dynamics coefficients to the cellular surface area and membrane resistance via the application of previously developed models (Lepora, Blomeley et al. 2011), providing a prediction of the overall increase in neuronal surface area with maturation. It also describes some unusually fast dynamics that were observed in some cells, indicating the presence of a current 'sink'. These fast dynamics are shown to be development dependent.

4.2 Analysis Methods

The passive dynamics of the cell were studied via current-clamp electrophysiology by the application of a current injection that triggered a membrane potential response that fell below the threshold for stimulation of voltage-gated ion channels. PD protocols were used on 145 regular-spiking excitatory cells across the full range of internal solutions used, since no difference in passive dynamics was found between internal solutions (Chapter 6: *The Effect of Neurobiotin on Spiking Properties*).

The experimental protocol used in PD experiments is described in detail in *Methods*, but, briefly, regular spiking excitatory cells in the barrel cortex of neonatal mice aged P3 to P11 were whole-cell patched with a micropipette and held in current clamp at -72±10mV. Following the application of a current-step protocol that elicited spiking behaviour, a PD protocol was applied that consisted of two short pulses of magnitude 0.4nA and duration 1ms, one hyperpolarising and one depolarising, with a gap of 500ms between pulses, as developed from previous work (Lepora, Blomeley et al. 2011). This protocol induced a capacitive charging and discharging of the cell membrane, observed in current clamp as a sudden increase in membrane potential followed by a long exponential decay. This protocol was repeated 40-100 times per patched cell, with the resting membrane potential closely monitored throughout.

Data processing and quality control

Variations in PD recordings between cells were small and subtle; to elucidate the developmental-dependent changes, it was necessary to employ stringent quality control methodologies to ensure that the average PD trace from each cell was indeed representative of that cell **(Figure 4.2)**, and not skewed by noise or other artefacts (Major, Larkman et al. 1994).

It was first necessary to correct for bridge-balance error. This error occurs due to the voltage drop across the electrodes in the electrophysiology rig, and can easily be corrected via the amplifier, given that the current being injected is known. Bridge-balance error was minimised via a compensatory adjustment of 7.3MΩ.

Secondly, it was necessary to remove any traces that displayed markers of active dynamics, to ensure that the dynamics being studied were indeed purely passive. This was achieved by first removing any PD datasets that showed the routine firing of APs. Where the resting membrane potential was found to be of such a magnitude that the small current injection triggered the routine firing of APs, the holding current on the cell was adjusted to reduce the resting membrane potential (keeping it within the -72±10mV range), and the experiment was restarted. For datasets that exhibited sporadic APs, systematic deletion of traces was performed. The amplitude of each PD trace was measured, and the amplitudes were observed to follow a normal distribution (**Figure 4.2.C**). Amplitudes that exceeded one standard deviation from the mean were judged to be indicative of active dynamics and were removed

from the dataset. To ensure that the centre of the normal distribution of PD trace amplitudes was not shifted by this data cleansing, the traces that were more than one standard deviation below the mean amplitude were also discarded. A consequence of this was that in 'good' datasets with no active dynamics present, up to 32% of the data may have been erroneously discarded, but this was deemed necessary to ensure that the dynamics measured were truly passive. In most cases, the presence of one or two AP traces in a dataset of 40-100 shifted the normal distribution towards higher amplitudes, and the 1-standard deviation cut-off performed well.

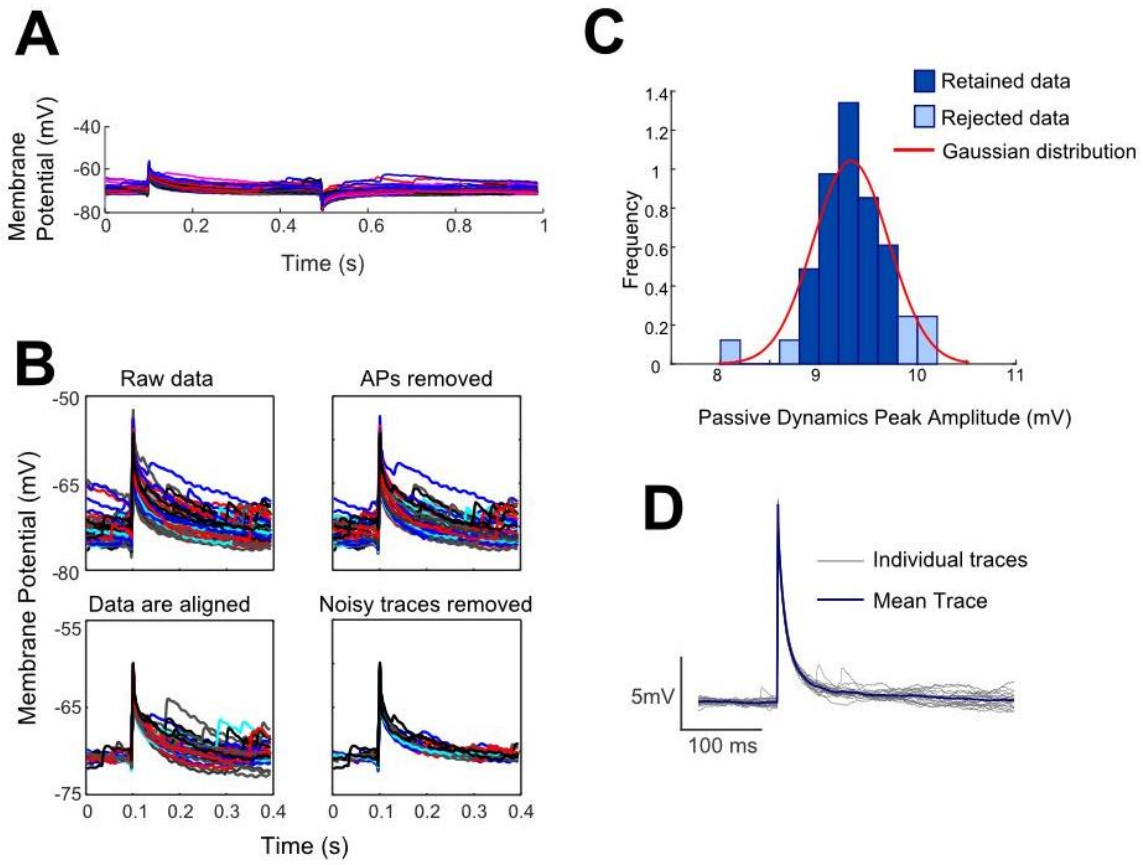

Figure 4.2: Pre-processing of passive dynamics data. **A**: Raw data consisted of the cell's membrane potential response to two short current injections, one hyperpolarising and one depolarising. Each of the current injections resulted in an exponential membrane potential decay. The current injection was repeated 40-100 times. **B:** The entire passive dynamics trace was assessed for quality by the first 0.4s. The amplitudes of the traces followed a normal distribution (**C**). Any traces that fell outside one standard deviation of the mean of this distribution were removed to ensure that no action potentials contaminate the dataset. The data were then aligned around the mean value of the resting membrane potential (first 0.1s of the trace), allowing any data with a particularly noisy 'tail' to be removed.
D: From the processed and aligned data, the mean passive dynamics trace was found.

With active dynamics cleansed from the dataset, the PD traces were aligned, allowing detection of traces that were particularly noisy. Noise was assumed to be primarily due to the breakdown of the cell membrane around the site of pipette patching. In each dataset, the traces were aligned by the mean resting membrane potential, Vm. Once aligned, noisy traces were identified by the later period of decay where the membrane potential had approximately returned to baseline: traces were deleted when the mean amplitude of the PD trace in the period 250-400ms (150ms after the peak) was more than one standard deviation above the mean amplitude of the dataset in this period.

The resultant PD dataset of a cell could be greatly depleted by this process, but what was left produced a robust mean trace, to which a two-compartment exponential decay model could be fitted (**Figure 4.2.D**).

Modelling the exponential decay

A two-compartment model of membrane voltage under capacitive charging (Equation 4.5) was fit to the mean PD trace from each cell. The two compartments within the model were not defined from physiological observations during microscopy but were thought of as approximating 'somatic' compartment and 'dendritic' morphologies. It was therefore expected that the coefficients of the dendritic compartment would indicate a much larger surface area than that of the somatic compartment given what is known about neuronal morphology. The first term in Equation 4.5 was allocated to the somatic compartment, and the second term was allocated to the dendritic compartment. The third term, Vm_{PD}, represents the membrane potential prior to the current injections as returned from the fitting, rather than that measured directly from the experimental data.

This model was first fit to the data decay part of the trace only - the trace data from the period spanning 101ms to 501ms - to extract the PD coefficients (MATLAB command '`fit`' was used in original scripts). This was possible because the dynamics that governed the capacitive discharging of the cell membrane were the same that governed its capacitive charging, except that the rising phase is stopped after only 1ms, whereas the decaying phase stretched over 400ms, allowing more scope for model refinement.

With the two-compartment model fit to the discharging part of the trace, goodness of fit was evaluated using the nonlinear regression coefficient, R^2; the dataset was rejected if a minimum R^2 value of 0.99 was not reached. Such a high threshold for acceptable fit was

necessary because of the exponential nature of the model; small misfits between data and model returned vast differences in the coefficients extracted. The five coefficients returned from good fits, $Alpha_1$, tau_1, $Alpha_2$, tau_2, and Vm_{PD}, were then used to model the brief charging portion of the PD trace. This allowed a 'holistic' model of PD charging and discharging to be made, allowing a secondary evaluation, to ensure that the entire trace reached the minimum R^2 measure of goodness of fit.

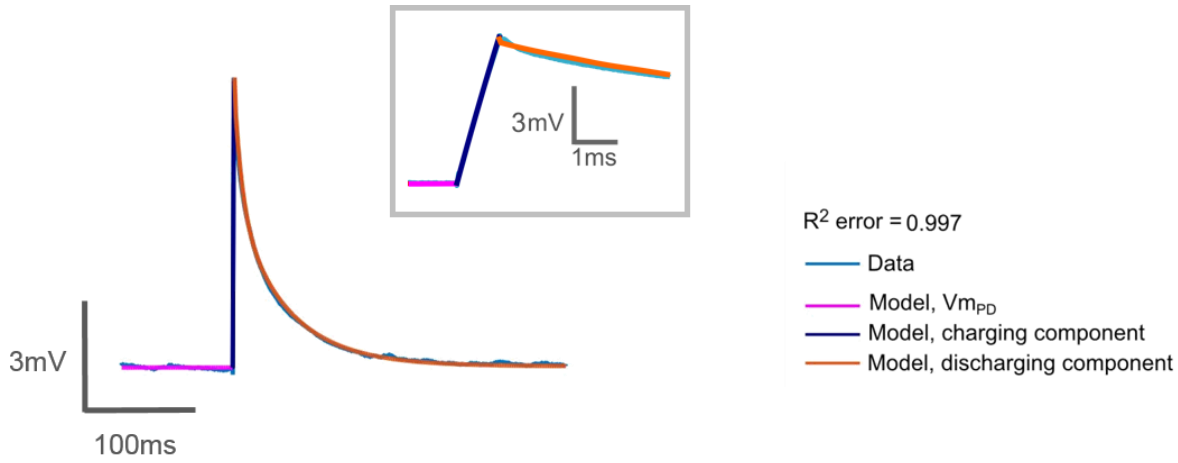

Figure 4.3: Construction of a holistic model of the passive dynamics. The discharging (decay) part of the trace is fit with a two-compartment model (orange). The coefficients of this model are used to inform the resting part of the trace (magenta) and the charging part of the trace (navy). The entire trace is checked for goodness of fit (R^2 measure). Inset shows the region around the peak.

Demonstrating dynamics are purely passive

It was necessary not only to exclude AP dynamics from the PD traces, but also to demonstrate that no active dynamics that could precede the firing of an AP were triggered. To ensure that only true passive dynamics were observed, the experimental protocol was constructed to facilitate observation of any contribution from active dynamics, as has been previously described (Huang, Hong et al. 2015): the depolarising current pulse injection was followed by an equal and opposite hyperpolarising pulse injection. It was hypothesised that if only PD were invoked, then the membrane potential response from both depolarising and hyperpolarising injections would be symmetrical; asymmetry between depolarising and hyperpolarising components of the trace would imply that voltage-gated ion channels were being activated when the membrane potential was increased in one direction but not the other.

Once data were aligned and averaged, and all quality control methodologies performed as described above, the absence of active dynamics was confirmed via three methods (**Figure**

4.4). In the first method, (**Figure 4.4.A**) the PD trace was split into two sections. The first consisted of the data spanning the period of 0 to 400ms, encompassing the depolarising current injection and resultant PD decay, the second section consisted of the data from the period 401 to 800ms, encompassing the hyperpolarising current injection and resultant PD decay. The hyperpolarised section of the data was flipped and overlaid on top of the depolarised section, thereby allowing visual inspection to demonstrate that they were the same shape and there was little to no difference between sections.

The second method compared the coefficients returned from the two-compartment model fit of both hyperpolarising and depolarising sections (**Figure 4.4.B**). If active dynamics were present, the time constants from the hyperpolarised and depolarised sections would be unequal. The ratio of tau_1 to tau_2 for the hyperpolarising component was plotted against the equivalent ratio for the depolarising component, allowing detection of any asymmetry as a deviation from the line of equality. As with the previous method, we found that the hyperpolarising and depolarising sections were largely symmetrical, and no evidence of active dynamics was found.

Finally, the hyperpolarising section of each trace was summed with its corresponding depolarising section to produce a time-dependent measure of the effective difference between the two. When hyperpolarising and depolarising sections were identical, the summation was equal to zero. This effective difference was averaged across cells to give a mean summation, and both the summations from individual cells and the mean summation were plotted (**Figure 4.4.C**). An asymmetry in this average effective difference would indicate dominance of either section, but no such asymmetry was observed; instead, the minor fluctuations of the average effective difference were well within the noise level, and when compared to the mean PD depolarised membrane potential response, these minor fluctuations were clearly negligible.

Therefore, it was concluded that no significant difference between the two membrane potential responses was detected, and since the symmetry was preserved, no active dynamics were triggered.

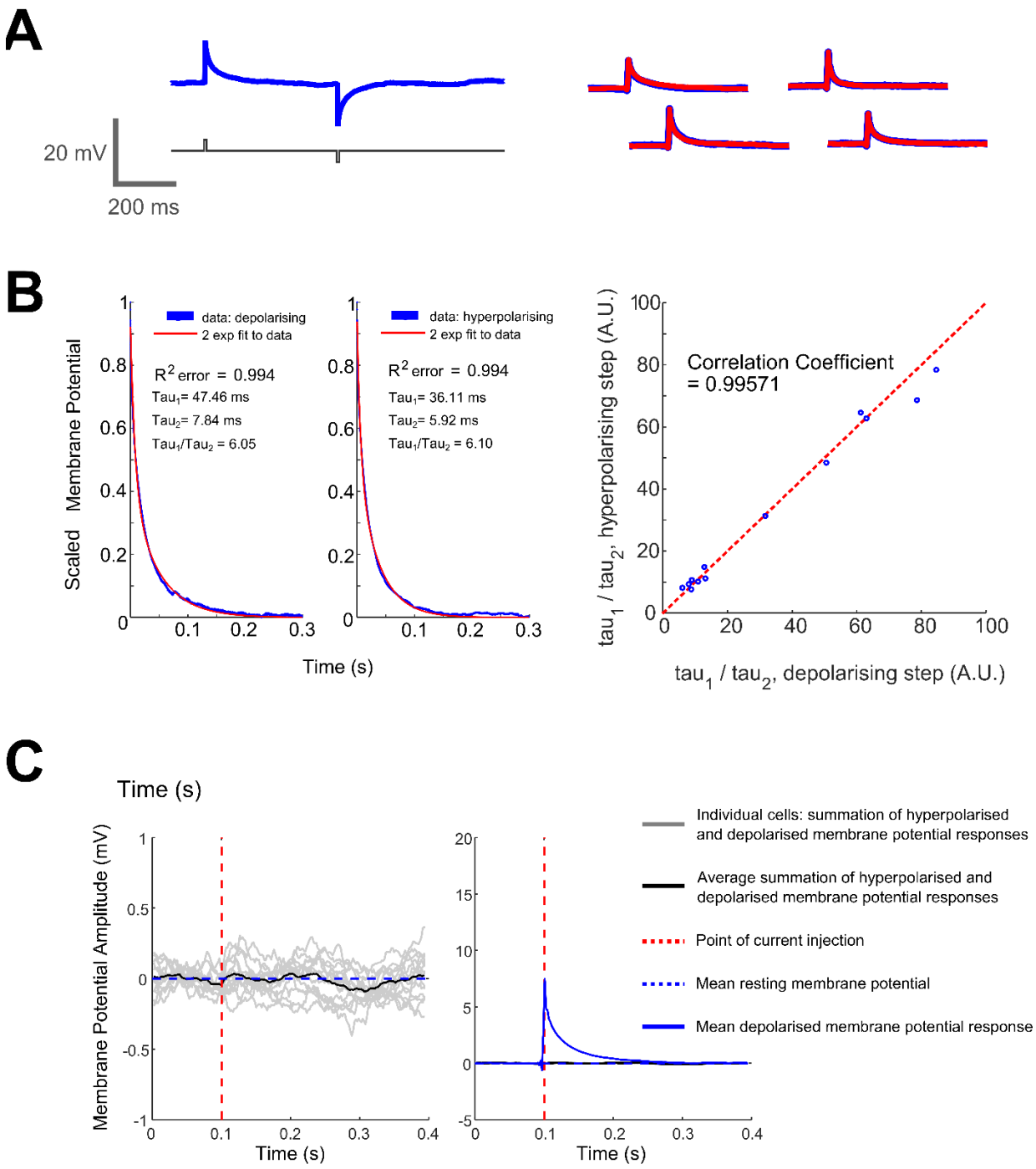

Figure 4.4: Three different methods to ensure there is no difference between the hyperpolarising and depolarising membrane potential decay curves, thereby demonstrating that the dynamics were passive. **A**: *(Left)* Membrane potential decay curves are produced by two brief (1ms) injections of current, one depolarising, the other hyperpolarising, 400ms apart. *(Right)* Method 1: The resulting capacitive decays are sectioned out and are overlaid to check by eye that there is no visible difference (representative traces). **B**: Method 2: a two-compartment model fitted to both hyperpolarising and depolarising curves. The ratios of the time constants (*tau*$_1$, *tau*$_2$) from each curve are plotted and compared (blue circles). A straight line fits to the data with correlation coefficient >0.99. **C**: Method 3: *(Left)* The summation of hyperpolarising curve with the depolarising curve for each trace (grey lines), and the resulting average amplitude (black line). The summation amplitude does not deviate far from 0 and is negligible when plotted against the mean depolarising curve *(right)*.

4.3 Results

Passive dynamics change with age

Mean PD traces were found for each age across all cells patched using all internal solutions. The mean shape of the PD trace was observed to change with age. When aligned by Vm, an age-dependent decrease in PD amplitude was detected, indicating a reduction in the amount of charge that can be stored in the cell membrane (**Figure 4.5.A**). PD traces were then scaled for amplitude to allow comparison of kinetics. This showed a subtler age-dependent variation: PD traces appeared to become narrower over the period P3-P6, before becoming wider over the period P7-P11. This nonlinear variation was expected to be reflected in the measured time constants, and therefore in the membrane capacitance and resistance (**Figure 4.5.B**).

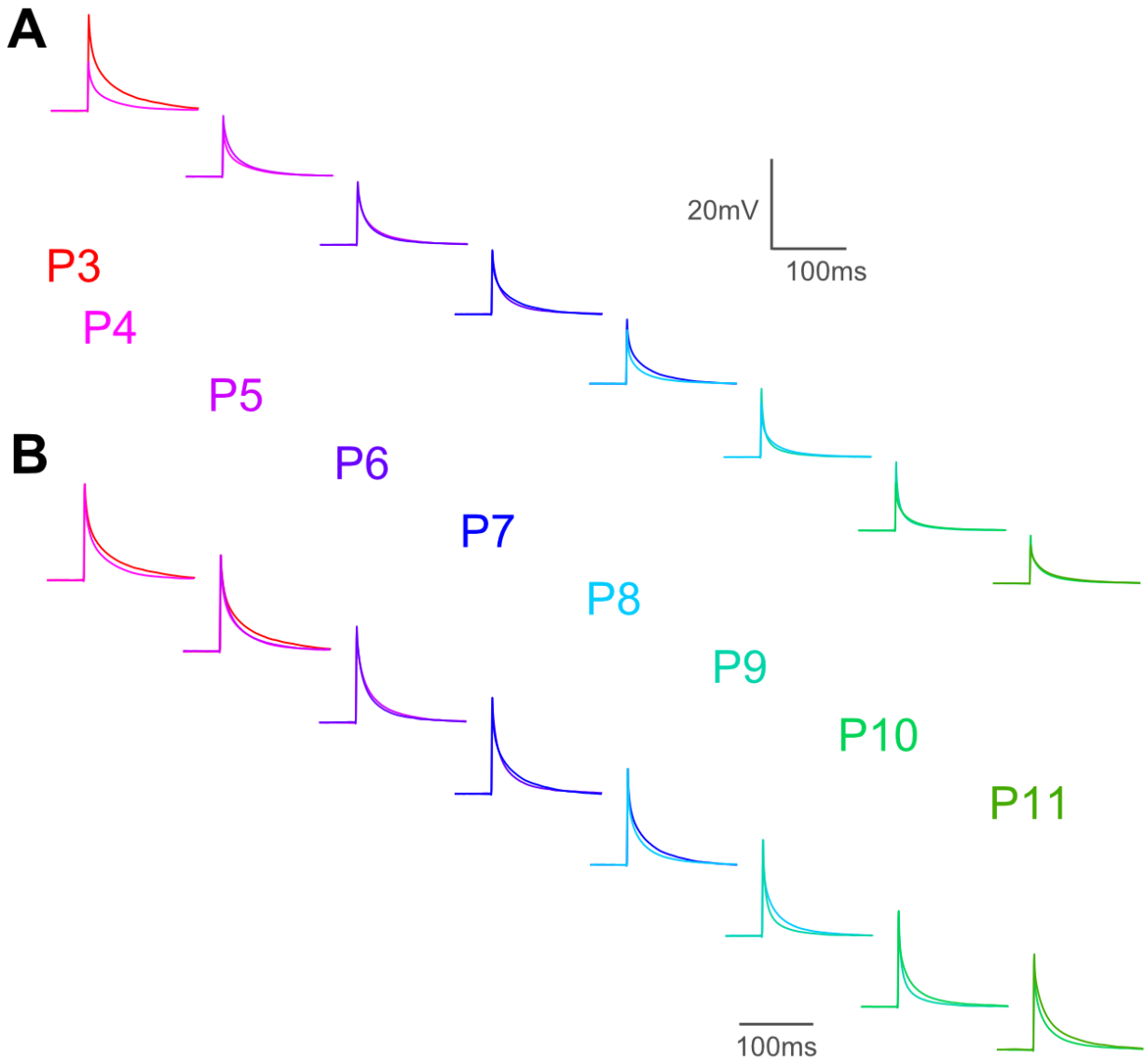

Figure 4.5: The passive dynamics appear to change with developmental age. A: Mean PD trace at each age, overlaid with the previous age to show the change in amplitude.
B: As above, except traces are scaled for amplitude to show the changing kinetics.

Comparison of models with different numbers of compartments

Exponential decay models with different numbers of compartments were trialled on all PD datasets, with all models being assessed by their R^2 measure of goodness of fit (**Figure 4.6.A**). A one-compartment model generally produced poor fits to the data, as assessed by a 'good fit' of $R^2 \geq 0.99$. A two-compartment model fit well to the passive dynamics data in 122 (84%) of cases. Models of three and four compartments made no significant improvement on the R^2 value, and consequentially, the two-compartment model was judged to be sufficiently complex to capture most of the information from the data without overfitting.

Regarding the PD from cells that did not fit well to the two-compartment model, and were therefore rejected from the overall dataset, the majority (12 cells) were from early experiments where the apparatus had not been corrected for bridge-balance error. However, there were some data that did not fit to the two-compartment model despite being bridge-balanced. In three cases the PD trace was too noisy to produce an adequately high R^2 measure. In two cases, a two-compartment model fit well to the data, but the dynamics were very different to those seen in other cells, producing coefficient outliers. Since these outliers were so anomalous, and dynamics so unusual, it was judged that in this case the cells exhibited partially-active dynamics that surpassed all our quality checks. These cases were isolated and not indicative of the effectiveness of the quality controls.

For the remaining six cells, the two-compartment model was observed to be a 'bad fit' despite these cells appearing to have fairly typical dynamics with low noise. Interestingly, for these six rejected datasets, a three-compartment model was observed to fit reasonably well to each of these cells, with R^2 measures of goodness of fit that fell within our thresholds (**Figure 4.6.B**). Using a three-compartment model on these 'bad fit' data lead to an improvement on the R^2 measure for each of these six cells; for five of these cells, the improvement was modest (~2% improvement with three compartments), but for one cell the improvement was noticeably larger, with a ~20% improvement with three compartments. This outlier may be a different type of neuron with different dynamics, but other explanations are also possible. These datasets came from cells with an average age of P9; the three-compartment model may therefore become necessary as the cells mature and develop more complex morphology. For example, the third compartment may be indicative of an explosion of spine growth, as has been previously reported at this postnatal age (Ashby and Isaac 2011).

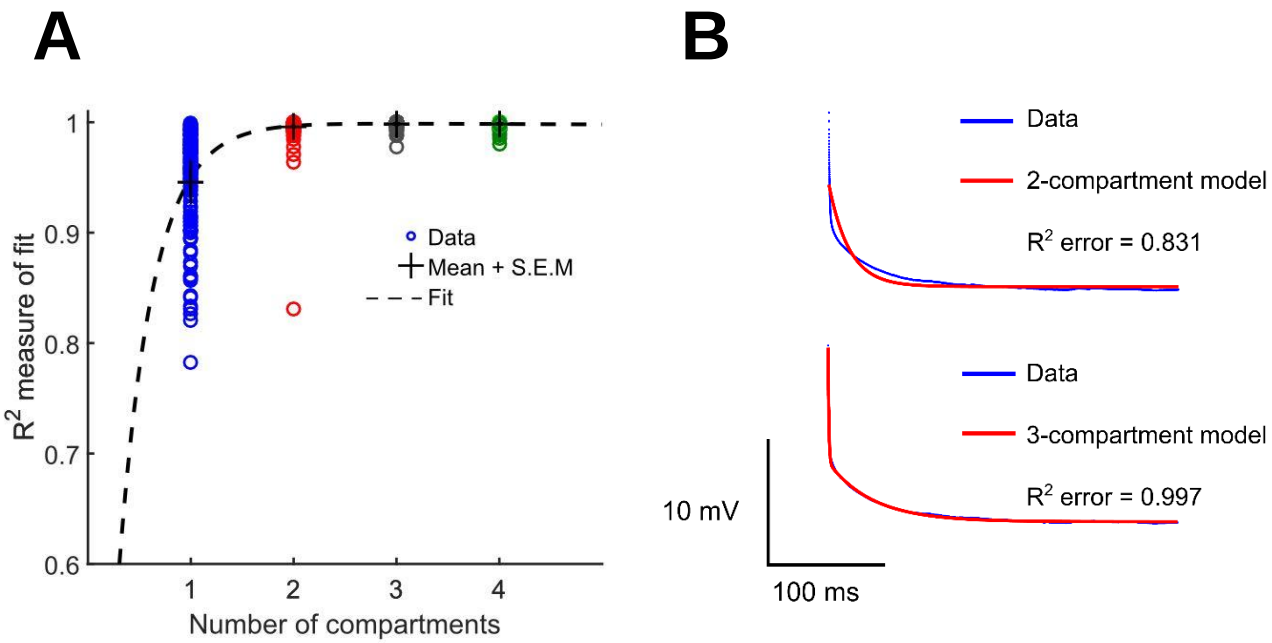

C

File	Age	R^2 for 2 compartments	R^2 for 3 compartments	Improvement with 3 compartments
141215_043	8	0.9844	**0.9978**	0.0134
211116_016	7	0.9703	**0.9882**	0.0179
241116_038	10	0.8311	**0.9970**	0.1659
251116_022	11	0.9642	**0.9880**	0.0238
251116_028	11	0.9841	**0.9995**	0.0154
251017_029	7	0.9830	**0.9899**	0.0069

Figure 4.6: A two-compartment model of exponential decay fits well to most passive dynamics (PD) **traces. A**: The R^2 measure of goodness of fit as a function of the number of compartments. Empty circles show the R^2 value for models of various compartments fitted to PD traces from each cell. Black crosses show the locations of the mean R^2 value for each number of compartments, with the length in the y axis representing the standard error in the mean. Dotted black line shows an exponential fit to the mean R^2 values. Two compartments are shown to be as good as three or four in most cases. **B**: Representative PD trace to which a two-compartment model did not fit well, but a three-compartment model did. Data shown in blue, models of two (*top*) and three (*bottom*) compartments shown in red. R^2 measure of goodness of fit dramatically increases with three compartments. **C**: Table of R^2 error for the six PD traces to which a two-compartment model did not fit. In each case, a three-compartment model gives an improvement.

A fast component of passive dynamics decay

Of the 122 cells tested for PD and fit with a two-compartment model, 57 (47%) exhibited a fast component of membrane potential decay, or a 'kink', visible as a very sharp initial phase of the PD decay. Two cells, judged to be representative of a 'kink' trace, and a 'no kink' trace, were used to categorise the rest of the cells in the same way by visual inspection (**Figure 4.7.A**). For this analysis, the entire PD trace was plotted alongside the 9ms surrounding the PD peak (**Figure 4.7.A**, *insets*). This allowed for careful comparison between the PD of each cell and these two representative traces. This evaluation of the dynamics was binary: all cells were assigned either a 0 for 'no kink' or a 1 for 'kink'.

When fitted with the two-compartment model, the cells that exhibited the kink returned a second time constant, tau_2 that was as much as an order of magnitude smaller than that observed in other cells (**Figure 4.7.B**). No such change was observed in tau_1. The brevity of this time constant raised doubts as to whether it could be attributed to electrostatic diffusion across the lipid bilayer. It was therefore hypothesised that this fast membrane potential decay was due to a current 'sink' – an unexpected leak or channel in the cell membrane that facilitated membrane potential decay on a much faster scale than the physics of lipid bilayer cell membranes would be expected to permit.

The proportion of cells exhibiting kink dynamics on each postnatal day, as defined from visual inspection, was then calculated and plotted in a bar graph against age (**Figure 4.7.C**). This showed that there was a visible qualitative difference between ages, with an apparent minimum at P6 where only 15% of cells exhibited kink dynamics, as opposed to an apparent maximum at P8, where 79% of cells exhibited kink dynamics. A Gaussian distribution fit to these data (R^2 value = 0.59) showed a peak at 8.76 postnatal days, despite returning a relatively poor fit. Both this distribution and the raw data seem to indicate that these dynamics are somewhat transient, dropping back to lower levels in more mature cells.

The age-dependent dynamics of tau_2 approximated the inverse of the dynamics seen in the kink dynamics. To confirm that the kink was related to the value of tau_2, the proportion of cells exhibiting the kink at each age was drawn on the same plot as the inverse of the mean value of tau_2 at each age (**Figure 4.7.D**). Quadrature was used to find the standard error in the mean for the inverse of tau_2. When overlaid in this way, the covariance between the presence of the kink and the value of tau_2, and the age-dependence of both, became apparent.

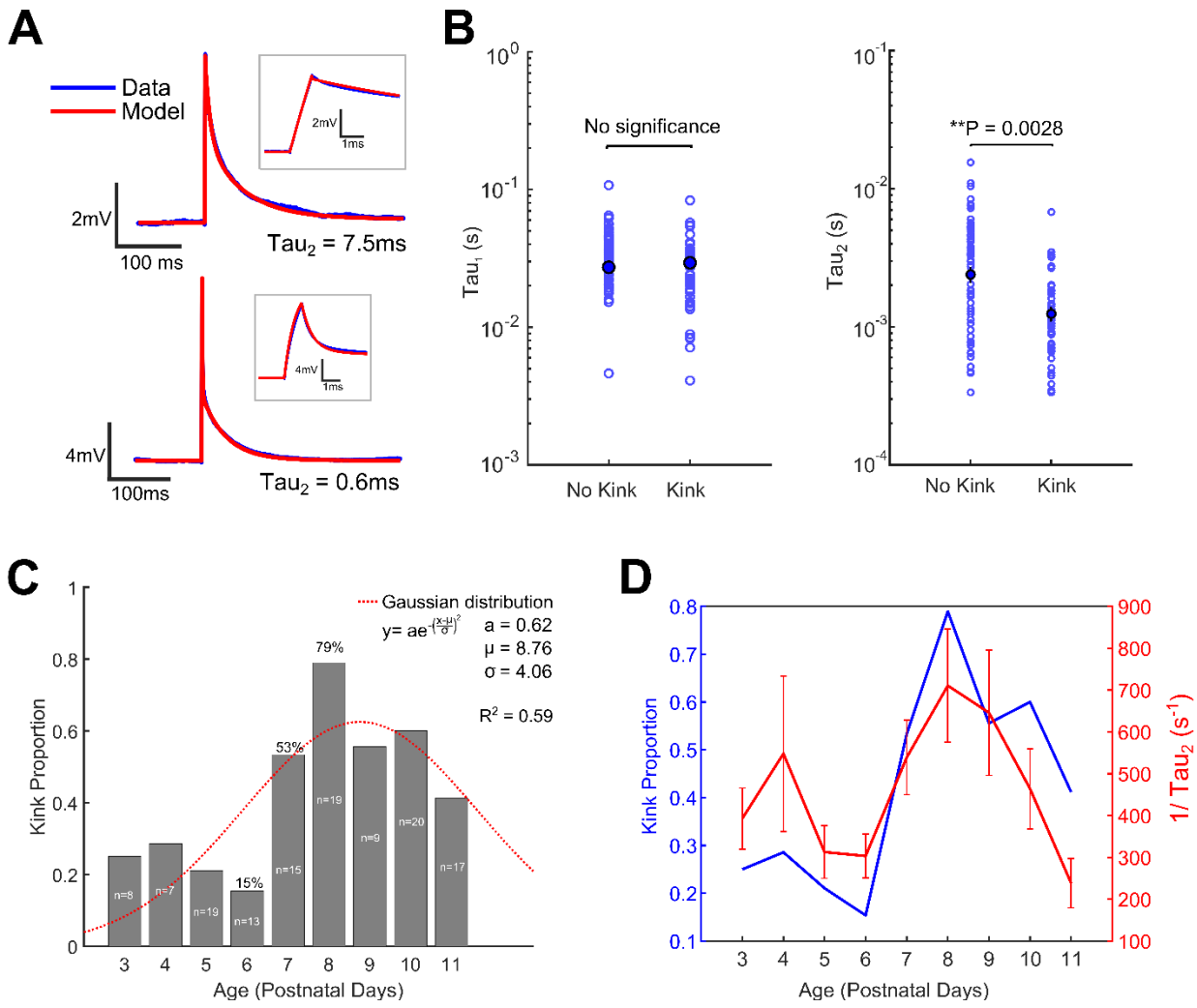

Figure 4.7: A fast component of passive dynamic decay. Of the 122 cells that underwent the passive dynamics protocol and fit to the two-compartment model, 57 of them exhibited dramatically different dynamics, evident by the presence of very fast dynamics, or a 'kink' in the voltage decay. This was confirmed by the statistically significant difference in the tau_2 dendritic time constant. **A:** Two representative PD traces (blue) with their corresponding two-compartment models. These traces were used to categorise all other traces as 'kink' or 'no kink' via visual comparison. Inset in each case shows the dynamics of the 9ms surrounding the peak. There is a difference of more than an order of magnitude between the returned time coefficient tau_2 for these two examples. **B:** Scatter plot of tau_1 and tau_2 for cells exhibiting no kink vs those exhibiting a kink. The Y axis has a logarithmic scale. Empty circles show individual cells, filled circles with error bars show the mean with the standard error in the mean. No relationship was found between tau_1 and the presence of the kink, but tau_2 was shown to be related to the kink (one-way ANOVA, Tukey-Kramer test, P= 0.0028).
C: The proportion of cells at each age that exhibited a kink in their dynamics, as defined via visual inspection, varied with age. **D:** Covariance of the kink proportion with the value of tau_2 as a function of age provided confirmation that these dynamics are related to the second time constant. The proportion of cells that exhibited kink dynamics (kink proportion) plotted as a function of age (blue), overlaid with the inverse tau_2 as a function of age (red). Error bars represent the standard error in the mean, calculated via quadrature.

To ascertain that the fast component of membrane potential decay seen in some cells was not due to an artefact of the experimental apparatus, a model cell, a small electrical circuit of resistors used to calibrate and check the electrophysiology rig, was used to attempt to recreate these dynamics. The model cell was mounted on the electrophysiology rig and subjected to the passive dynamics protocol with the Multiclamp 700A amplifier settings varied across their range. The bridge-balance error seen in some cells was recreated easily, but no dynamics resembling the 'kink' could be artificially created, regardless of the experimental setup used. It was therefore concluded that the origins of the kink are either physiological, or are due to interactions with the pipette, or a combination of the two.

Coefficients of the fitted model against age

Two time constants were returned from the model fit to data across ages P3-P11. The first, tau_1, was found to be between 4.1 and 107.1ms, with a mean value of 34.5±1.5ms. The second, tau_2, was found to be between 0.3 and 15.5ms, with a mean value of 2.6±0.2ms. These values were of the same order of magnitude as time constants that have been reported from two-compartment models across neuron types and species (Kita, Kita et al. 1984, Wright, Bardakjian et al. 1996, Kim, Major et al. 2009, Lepora, Blomeley et al. 2011)

To investigate the age-dependence of the PD, the coefficients of the two-compartment fit, $Alpha_1$, $Alpha_2$, tau_1 and tau_2 were each plotted against age (**Figure 4.8**). A statistically significant age dependence was found for $Alpha_1$, appearing to show a linear negative correlation, reflecting the earlier observation that the amplitude of PD decreases with age. No age-dependence was found for $Alpha_2$, nor for tau_1, the time coefficient from the compartment designated as 'somatic'. However, tau_2, the time coefficient from the compartment designated as 'dendritic' demonstrated some very interesting dynamics, appearing to show an oscillatory relationship: an initial increase in tau_2 with age between P3 and P5, followed by a decrease at between P5 and P9, followed by a dramatic increase between P9 and P11. A statistically significant difference was found between the data at P8 and at P11, due to the steepness of this increase. These time points may be significant in terms of morphology, corresponding to phases of dendritic elaboration within the barrel, pruning of dendrites as the barrels become more discrete, and later spinogenesis (Ashby and Isaac 2011).

Taken together, these data appear to show two interesting age-dependent effects: the capacity of the neuron to store charge decreases with age, and the speed of membrane discharge changes with age, with the fastest dynamics at around P8.

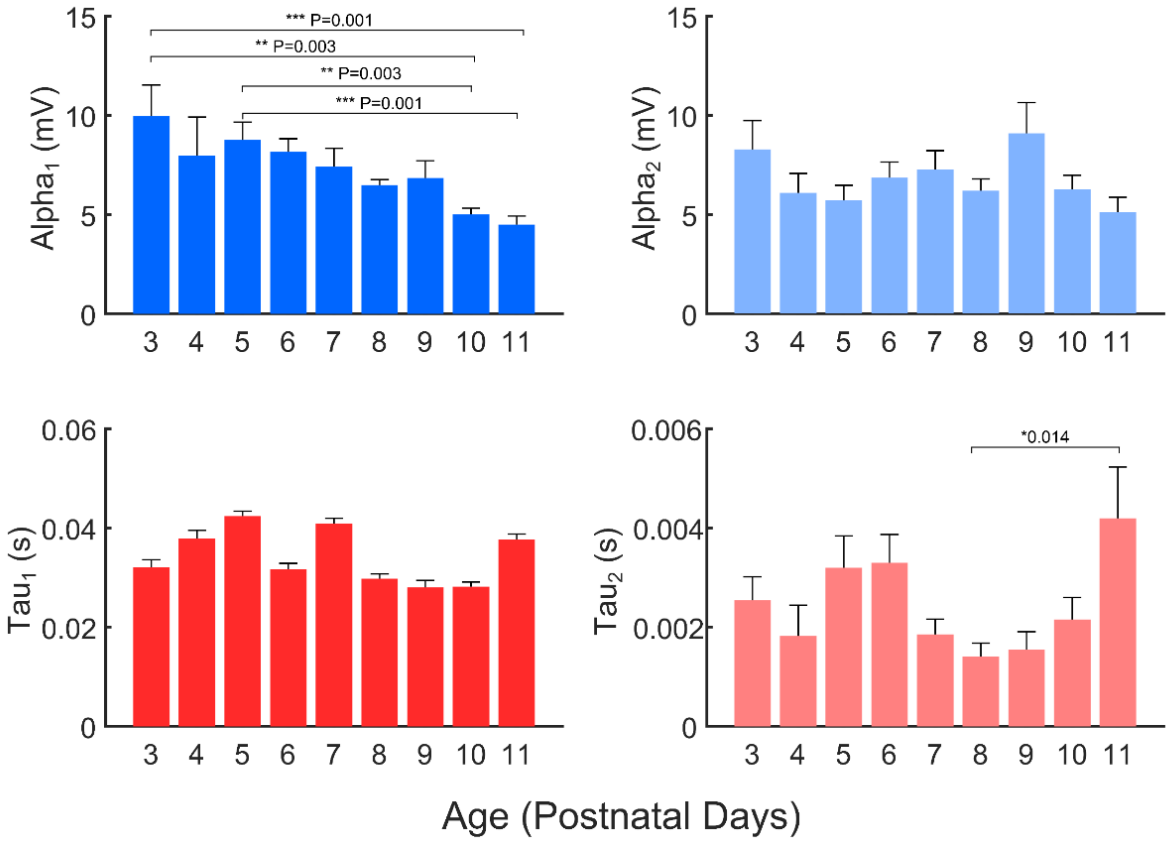

Figure 4.8: The passive dynamics coefficients from the two-compartment fit to the data show age dependent variance in both *Alpha$_1$* and *tau$_2$*. The four age-dependent coefficients returned from the two-compartment fit. Bars represent mean values; error bars show standard error in the mean. A one-way ANOVA and Tukey-Kramer test of significance was performed on each coefficient, and found age-dependent variation in *Alpha$_1$*, which significantly decreased with age, and *tau$_2$*, which appeared to exhibit nonlinear age-dependent variability.

Passive dynamics predictions of the neuronal surface area

Within the two-compartment model, the 'somatic' and 'dendritic' names are not meant to strictly define the scope of the biophysical compartments, rather, they are given to provide some contextual physiological basis to the analysis. The two compartments instead represent the regions of the cell that can be regarded as separate isopotentials. By referencing a previously described model of neuronal surface area that utilises the coefficients of the two-compartment model to provide predictions of both somatic and dendritic compartments (Lepora, Blomeley et al. 2011), an age-dependent prediction of neuronal surface area for the two compartments was made.

$$Surface\ Area_{\ Somatic} = \frac{\frac{I_0}{C}}{\frac{\alpha_1}{\tau_1} + \frac{\alpha_2}{\tau_2}} \tag{4.6}$$

$$Surface\ Area_{\ Dendritic} = \frac{\alpha_2 \cdot \tau_1}{(\alpha_1 \cdot \tau_2) \cdot Surface\ Area_{\ Somatic}} \tag{4.7}$$

This assumes a specific membrane capacitance of 1μFcm^{-2}, as is typically quoted, and uses the known current injection of 0.4nA. Via the application of this model, both compartments returned surface areas of an order of magnitude appropriate for neurons. Reassuringly, the 'dendritic' compartment returned a surface area prediction that was approximately an order of magnitude larger than the 'somatic' surface area across each age in the developmental period studied. For both dendritic and somatic compartments, the surface area prediction increased with postnatal age (**Figure 4.9**), indicating the expected neuronal growth. Approximating the relationship between postnatal age and surface area as linear, a positive correlation was found for both somatic and dendritic compartments (Pearson's correlation coefficient, somatic compartment correlation = 0.2, P = 0.02, dendritic compartment correlation = 0.261, P = 0.005). By finding the intercept of these linear fits ($y=mx+c$), a somatic surface area of 0.03mm^2 and a dendritic surface area of 0.6mm^2 at birth (P0) was suggested. However, despite providing statistically significant results, the linear model did not fit very well to the data, with an R^2 measure of goodness of fit through the mean values from somatic and dendritic compartments returning values of only 0.187 and 0.299 respectively. A linear model was therefore judged to be an oversimplification, and other models of the relationship between neuronal surface area and development were explored.

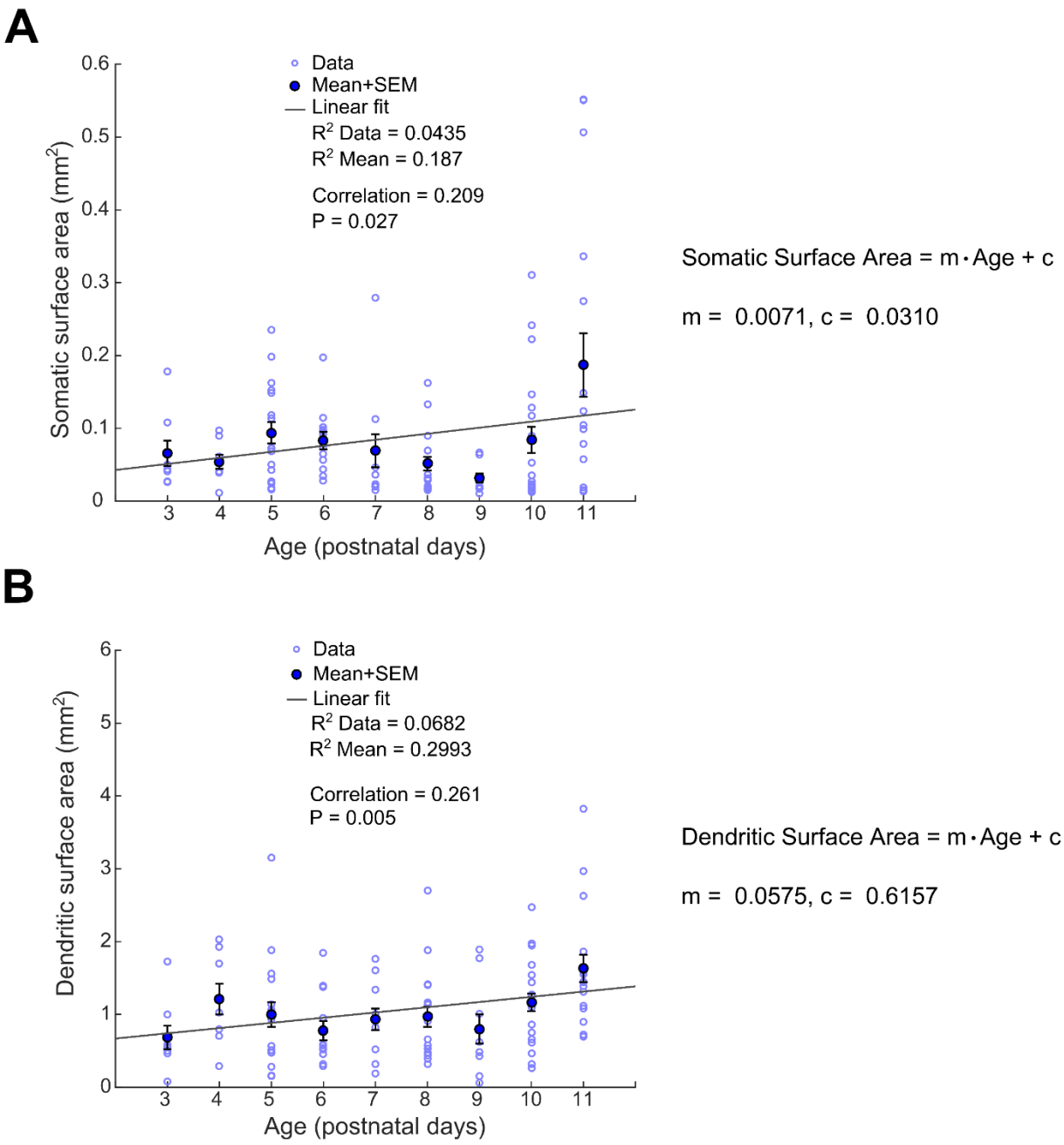

Figure 4.9: Surface area of both the dendritic and the somatic compartments increases with age. A: The somatic surface area as a function of age. Empty circles show individual cells, filled circles with error bars show the mean with the standard error in the mean at each age. Grey line shows a linear best fit to the data. Pearson correlation coefficient shows a positive correlation of 0.209 (P=0.027). Linear fit indicates minimum somatic surface area of 0.031mm^2 at P0. R^2 measures of goodness of fit on both the data and the means shows a linear model to be a poor approximation. **B**: The dendritic surface area as a function of age. Data and statistical tests as above. Pearson correlation coefficient shows a positive correlation of 0.261 (P=0.005). Linear fit indicates minimum dendritic surface area of 0.616mm^2 at P0. As above, R^2 measure of goodness of fit shows a linear model to be a poor approximation.

Higher order models of surface area developmental dynamics

Given the limitations of the linear fit to the increase in surface area of both somatic and dendritic compartments, subtler patterns of neuronal growth were investigated. One interesting observation was that the PD-predicted increase in surface area appeared to fit well to a cubic function of the form:

$$Surface\ Area = a \cdot Age^{3} + b \cdot Age^{2} + c \cdot Age + d \tag{4.8}$$

This polynomial was constrained to have a lower limit on the fourth coefficient, *d*, of zero, since the surface area cannot be negative (if the surface area of a cell is zero or below, the cell does not exist). When age =0, i.e. at postnatal day P0, the expression simplifies to:

$$Surface\ area = d \tag{4.9}$$

and since surface area ≥ 0, then by definition *d* must also be ≥ 0. No constraints were set to any of the other coefficients of this polynomial as the fitting was purely exploratory. The cubic function fit well to both the somatic and dendritic surface area predictions (**Figure 4.10**), indicating an initial increase in total cell surface area, followed by a brief period of reticence between P5 and P9, followed by an apparent explosion in neuronal growth between P9-P11 for both compartments. Both growth trajectories would be expected to plateau as the cell approaches maturity, and therefore this cubic model of development does not provide a complete picture of these developmental dynamics. However, it is interesting that the sudden increase in surface area predicted here corresponds to the previously reported explosion in dendritic spines observed at P10-P11 (Ashby and Isaac 2011).

An R^2 assessment of goodness of fit of this model to the mean surface area at each age-point returned a much-improved value of 0.702 for the somatic compartment and 0.731 for the dendritic compartment, indicating that this cubic function is a much closer approximation to the dynamics of neuronal growth than a linear model.

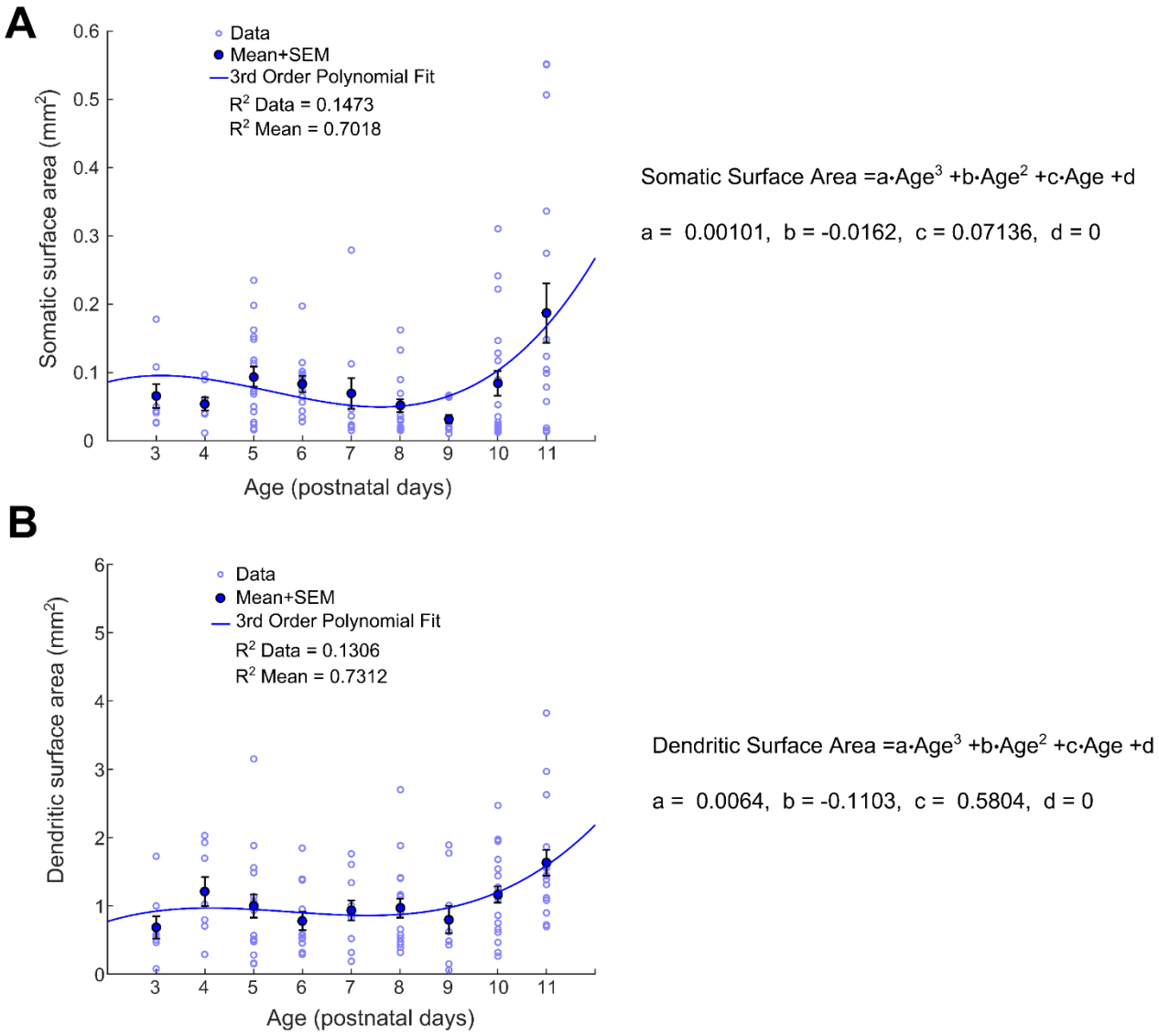

Figure 4.10: A third-order polynomial (cubic) fit to surface area against age hints at some interesting dynamics. A: The somatic surface area as a function of age. **B**: The dendritic surface area as a function of age. Empty circles show individual cells, filled circles with error bars show the mean with the standard error in the mean at each age.

4.4 Discussion

Are the dynamics truly passive?

It has previously been argued that what are regarded as passive dynamics are in fact determined by voltage-gated ion channels open at the resting membrane potential (Wright, Bardakjian et al. 1996). Specifically, it has been suggested that they are due to the contribution of sub-AP-threshold voltage-sensitive very-slow-inactivating K+ and Na+ channels (Connors, Gutnick et al. 1982). Others have argued that the PD are dependent on ionic concentration as well as neuronal morphology and that a Goldman-Hodgkin-Katz-based model that describes the flux of ionic compounds is necessary to explain the dynamics fully (Huang, Hong et al. 2015). The data presented here do not provide any information to falsify this hypothesis; it was found that the hyperpolarised and depolarised passive dynamics traces observed were symmetrical, which would imply that whatever ion channels are open stay open throughout this experimental protocol. It is possible that the change with maturation that we see is more due to the changing population of these resting-state ion channels than the changes in morphology; in reality, it is probably a combination of factors.

Considerations of experimental protocol ordering in passive dynamics measurements

When designing and developing the experimental protocols used, it was necessary to make compromises that may have had an influence on the data collected. It was decided to elicit the spiking behaviour of the cell by first running the current step protocol, therefore ensuring that the cell was healthy and capable of firing APs. This meant that the PD protocol ran second, after a period of voltage-gated ion channel activation. It is therefore feasible that the after-effects of this active period contributed to the measured PD. However, since it has been thoroughly demonstrated that the PD observed were as free from active transport as can be observed, we conclude that this ordering of protocols is no cause for concern.

Are passive dynamics indicative of age dependence?

The data presented here clearly demonstrate that the PD of the developing cortical neuron change with postnatal age, both in terms of the membrane potential and time constants of capacitive charging and discharging. However, these dynamics do not change in a simplistic fashion. Although the amplitude of the dynamics shows a linear age dependence, the kinetics of the dynamics are nonlinear, appearing to correlate to the established critical periods in neuron surface area expansion (Ashby and Isaac 2011).

Are two-compartment models the most appropriate for these data?

Excluding the datasets that exhibited bridge-balance error, the two-compartment model fit to 92% of PD datasets with an R^2 value of 0.99 or more. The two-compartment model is attractive for its simplicity, but the presence of datasets (one in particular) that only fit well to the higher order compartment models raises the question of whether some dynamics are being missed by oversimplification. Arguments have long been made for a minimum of three compartments within models, with the dendritic structure and the endoplasmic reticulum suggested as physiological factors responsible for the subtler dynamics (Ito and Oshima 1965). It may be the case that a three-compartment model gives more robust fits and more accurate predictions of neuronal physiology at different developmental stages. However, this raises philosophical questions about the nature of building mathematical models of biological structures; we do not expect our models to provide us with an entire description of the developing neuron, but we do expect them to provide testable hypotheses on the changing dynamics of the cell ("*All models are wrong, but some are useful*" (Box 1987)). Whilst the two-compartment model provides good fits to the majority of data and testable hypotheses, the justification for adding complexity is low.

Even with little justification for adding complexity, it is still interesting to ponder the physiological basis of more compartments. The improvement in fitting seen for one cell may be simply due to it being a different cell type, or otherwise unusual morphology, but it could also be hypothesised that the third compartment may be indicative of more complex morphology that occurs later in development. The relationship between morphology and passive dynamics was examined via dye filling and post-hoc confocal imaging experiments described in the next chapter (Chapter 5: *Gap Junctions and Morphology*). Unfortunately, none of the six cells that preferably fit to a three-compartment model were successfully imaged in these experiments so for this dataset, this question will remain unanswered.

The fast component of exponential decay

A 'kink' in the PD, indicative of a particularly fast component of capacitive discharge, was observed to be present in 47% of cells measured. Such dynamics have been observed before, and have been attributed to the experimental apparatus: to pipette artefacts (Major, Larkman et al. 1994), to an 'unbalanced electrode' (D'Aguanno, Bardakjian et al. 1986), or to a shunt caused either by pipette damage or an otherwise unspecified decrease in somatic resistance (Durand 1984). However, the frequency of the occurrence of these dynamics was observed to follow an age-dependent probability distribution and could not be correlated to any changes in

the pipette or other experimental apparatus or internal solution, raising the intriguing possibility that these dynamics are instead related to morphological or otherwise physiological developments. The kink was particularly notable for the fact that it corresponded to a tau_2 coefficient that was as much as an order of magnitude smaller than what was seen in non-kink cells. Such a fast component of membrane potential decay defies our understanding of charge diffusion across the cell membrane, implicating an unattributed leak current or current 'sink'. However, these dynamics have previously been attributed to the redistribution of charge across the neuron (Mason and Larkman 1990), which could simultaneously provide a simple explanation whilst also being dependent on cell morphology, and hence development.

Potentially, the kink could be attributable to morphology: differences in the dendritic arbour between cells, for example. One intriguing possibility was the potential presence of development-dependent gap junctions between cells. Gap junctions, also known as electrical synapses, are hexamer protein structures between neurons that permit the transfer of electrical information and some biological molecules (Belousov and Fontes 2013, Amsalem, Geit et al. 2016, Belousov, Fontes et al. 2017). Observed via electron microscopy as connections between adjacent cells (Goodenough and Paul 2009), they could hypothetically provide the current sink by virtue of essentially being holes in the membrane through which a current could flow. They have previously been implicated in passive dynamics recordings, with a distortion to the dynamics thought to be correlated to the size of the gap-junction network (Amsalem, Geit et al. 2016), predicting a decrease in the time constant from a single-compartment model of up to 65%. Gap junctions could potentially provide the mechanisms necessary for a charged neuron to passively discharge over these brief timescales. The presence of gap junctions would absolutely affect models of the developing neuron, particularly if they were developmentally transient (Ko, Cossell et al. 2013). The following chapter (Chapter 5: *Gap Junctions and Morphology*) investigates this hypothesis by use of dye-filling and post-hoc confocal imaging.

A Gaussian curve was fit to the distribution of kink against age, returning a peak in kink probability at 8.76 postnatal days; it could be that this corresponds to a peak in the occurrence of whatever physiological phenomenon is responsible. However, the nonlinear regression coefficient returned from this fit indicated that this data is not normally distributed, and therefore a Gaussian fit is an oversimplification. Looking again at this data, it is possible that the kink-probability is bimodal, having an early peak at around P4, followed by the later peak at around P8. This would imply two critical periods for whatever physiological properties of

the cell result in the fast dynamics across the cell membrane that give rise to the kink. These two time points may potentially correspond to the formation of barrels (Wu, Rosado et al. 2011) and the onset of spinogenesis (Ashby and Isaac 2011).

Surface area model

Using the PD as a measure of neuronal morphology has previously been explored (Lepora, Blomeley et al. 2011). Specifically, the coefficients of the two-compartment model have been shown to provide a prediction of neuronal compartment surface area. The work presented here demonstrates a development-dependent increase in both somatic and dendritic compartment surface areas, with the dendritic compartment being around an order of magnitude larger than the somatic compartment. The positive correlation between postnatal age and the surface area prediction corresponds with the simple expectation that neurons grow during development.

The titles attributed to the two compartments are, however, simplistic misnomers, and brute application of the model to the expected geometry would lead to an overestimation of 'somatic' size (Lepora, Blomeley et al. 2011). It can be demonstrated that the 'somatic' compartment cannot only encompass the soma, as it is far too large; if the soma of the spiny stellate cell is approximated to be spherical, with a diameter no more 30 microns (and typically between 12-17 microns (Staiger, Flagmeyer et al. 2004)), then via application of the geometrical definition of spherical surface area, $A=4\pi r^2$, a somatic surface area could not be any greater than 3000μm^2. The mean somatic surface across all ages predicted from the two-compartment model is equal to 87800μm^2, which would give a mean somatic diameter of 167 μm. Since this is clearly not the case (the mean diameter of the somas observed in Chapter 4: *Gap Junctions and Morphology* is roughly a tenth of this), the 'somatic' compartment must in fact encompass other parts of the cell. A more accurate model may include the axonal initial segment (AIS, 10-60 microns in length (Kole and Stuart 2012)) and the primary dendrites (**Figure 4.11**). This would also correspond with previous work that assigned the primary dendrites as a necessary part of the somatic compartment (Lepora, Blomeley et al. 2011).

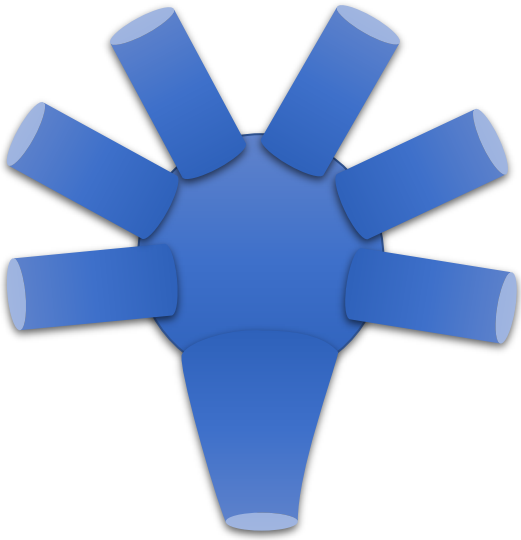

Somatic diameter = ~15 microns
Approximating the soma as a sphere,
somatic surface area= ~700 microns squared

AIS minimum diameter = ~ 2 microns,
AIS maximum diameter = ~ 10 microns,
AIS length = ~ 50 microns
Approximating the AIS as a frustum,
AIS surface area = ~2000 microns squared

Primary dendrite length = ~ 1500 microns
Primary dendrite diameter = ~ 3 microns
Approximating dendrites as cylinders, surface area = ~14000 microns squared per primary dendrite
Total surface area of soma, six primary dendrites and AIS = ~ 87000 microns squared

Figure 4.11 A model of the 'somatic' compartment that includes primary dendrites and the axonal initial segment *(not to scale)*

With a model of the 'somatic' compartment that included the primary dendrites and the AIS, the 'dendritic' compartment would comprise the rest of the axon, the axonal boutons, the secondary and tertiary dendrites, and the dendritic spines. Given that in layer IV excitatory neurons, the number of dendritic spines *per mm* of dendrite length has been observed to be on the order of ~500 (Miquelajauregui, Kribakaran et al. 2015), and the surface area of a spine has been estimated to be of the order of 6µm^2 (Segev, Friedman et al. 1995), the spine surface area contribution could be approx. ~0.003mm^2 per mm of dendrite. If secondary and tertiary dendrites are estimated to be cylinders of ~1mm length and 2µm diameter, the total surface area per dendrite, including spines, would be of the order of 0.01mm^2. Therefore, with ~100 secondary and tertiary dendrites and an axon, the surface area prediction for the 'dendritic' compartment of ~1mm^2 would seem to be of the correct order of magnitude.

As well as increasing with age, as would be expected from a population of growing neurons, the surface area also appeared to follow a cubic function that pointed to a more interesting pattern of dendrite growth, retraction and spinogenesis. To correctly address this interesting observation in future investigations, it would be necessary to establish a model of neuronal growth that takes these dynamics into account over a larger developmental period, *a priori* of any data being collected. Such a model would require a physiological basis for the values of

the coefficients *a*, *b*, *c* and *d*. Given the preliminary fits to the two compartments performed here, the coefficient *d* is returned as zero. This coefficient presumably represents the surface area of the compartment at P0, before the period of postnatal development; this value could be found experimentally from simple morphological analysis at this age. If coefficients *a* and *b* are set to zero, then the solution becomes a linear function; the coefficient *c* therefore presumably represents the gradient of a component of the surface area that increases linearly. As with the coefficients of the two-compartment model of PD decay, coupling between coefficients would make simplistic attributions of coefficients to morphological features highly unlikely; it is much more feasible that these coefficients interact in thus far unforeseen ways.

4.5 Summary

This chapter developed a methodology for the experimental investigation of passive membrane dynamics in developing cortical neurons. The dynamics were demonstrated to be passive by virtue of an experimental protocol that allowed for comparison of both hyperpolarising and depolarising traces, which were shown to be symmetrical, exhibiting no voltage-dependent active dynamics. Stringent quality controls allowed for robust fitting of a two-compartment capacitive decay model to 92% of bridge-balanced datasets with an R^2 value of 0.99 or more. The fitting of this two-compartment model returned five coefficients, including membrane potential amplitudes and capacitive time constants, that were intrinsically related to the morphology and resistance of the cell membrane. The values of these time constants fit within the range reported in previous literature. The faster of the two time constants, tau_2, was shown to vary with postnatal age, a variation which was also evident in a surface area prediction model, developed from previous work (Lepora, Blomeley et al. 2011). The application of the surface area prediction to both compartments showed a significant increase in surface area with age, corresponding to expected neuronal growth. A cubic function was shown to fit surprisingly well to the surface area prediction, hinting at interesting dynamics that align to previous work investigating dendritic spinogenesis. A fast component of PD membrane potential decay was observed in some cells in the form of a kink in the PD traces, hinting at the presence of a current sink, possibly caused by developmentally transient gap junctions between cells.

5 Gap Junctions and Morphology

Key Findings

1. Dye filling, done concurrently with patch clamp electrophysiology, is an effective tool for determining the morphology of patched cortical cells.
2. A diverse range of morphologies of excitatory neurons were observed in layer IV of the cortex of the neonatal mouse, with spiny stellate, star pyramidal and pyramidal cells being identified within the barrel. The ratio of spiny stellate to star pyramidal cells was similar to that reported in previous work (Feldmeyer, Egger et al. 1999).
3. Cellular morphology was observed to become more complex over development, in accordance with passive dynamics surface area predictions.
4. The use of Neurobiotin, a small tracer protein, allowed for the detection of gap junctions between the patched (primary) cell and gap-junction-coupled cells (GJCC) in the near vicinity of the patched cell.
5. Evidence of a relationship between gap junction coupling and age was observed, with a positive correlation between the occurrence of gap junction coupling and postnatal age, and an apparent peak in GJCC per primary cell at P5-P6.
6. No apparent correlation between the presence of gap junctions and the time constants of passive membrane dynamics was found.

5.1 Introduction

Electrophysiology is not the only tool for unpeeling the biophysics of the developing cortical neuron; much can be discovered about the size, shape and potentially even the networks of neurons by dye-filling. The biophysical properties observed via electrical stimulation are intrinsically linked to the geometry of the cell and the current sources and sinks that provide the necessary conditions for spiking behaviour and neuronal communication (Torben-Nielsen and Schutter 2014). Observing the changing morphology over the course of cell development is therefore a necessary part of the electrophysiologist's repertoire, should they wish to have a

complete picture of dynamic neuronal biophysics. Dye injection can be performed concurrently with electrophysiology by simply including dyes in the internal solution within the patch pipette and allowing sufficient time for ample dye diffusion once the cell is patched and the electrophysiological protocols are completed. Post-hoc recovery and confocal imaging of the cell then allows for comprehensive analysis of the cell morphology. Should the injected dye remain solely in the patched cell, recovery and imaging can reveal its type, size, and clues to such subtle measures as dendritic spine density, as well as confirmation of the location of the cell within the cortical layers and its position within the barrel. If the dye traverses gap junctions into secondary, gap-junction-coupled cells (GJCC), imaging can reveal the foundations of functional networks that may precede synaptogenesis (Kandler and Katz 1995, Montoro and Yuste 2004).

Cellular Morphology

The spiny stellate cell, a relatively compact but dendritically complex neuron (Venance, Rozov et al. 2000), has been observed to be the most common resident of the barrels of layer IV cortex (Feldmeyer, Egger et al. 1999). These cells are morphologically distinct from the pyramidal cells of layer II/III and layer V and from fast spiking interneurons, even at low optical magnification, due to their spherical cell bodies and stellate dendritic arbour (Feldmeyer, Egger et al. 1999, Staiger, Flagmeyer et al. 2004) . However, since neuronal migration and differentiation continues over development, the cells of the cortex found within or surrounding the barrel may not be in their final location, or indeed of their final form (Luhmann, Schubert et al. 2011). As well as the established spiny stellate cells, observations of star pyramidal neurons within the barrel have been reported by several groups (Staiger, Flagmeyer et al. 2004, Mizuno, Luo et al. 2014). These cells have morphologically similar basal dendritic arbours to spiny stellate cells, but have apical dendrites resembling those of pyramidal cells. It may be the case that spiny stellate cells within the barrel cortex initially possess a morphology similar to that of pyramidal neurons, before their developmental metamorphosis retracts their apical dendrite and produces a much more rotund dendritic arbour; such a retraction of dendrites during postnatal development has been reported (Li, Fertuzinhos et al. 2013, Mizuno, Luo et al. 2014). Dye filling can identify whether the cells patched in the barrel cortex are in their final positions, with their final functions, or if they are simply passing through.

Dendritic arbour

The dendritic arbour of the developing excitatory neuron in the somatosensory cortex has been previously shown to grow dramatically in size, surface area and complexity over the first two postnatal weeks, with a particular increase in surface area due to a rapid growth in dendritic spines at postnatal days P9-P11 (Ashby and Isaac 2011). Changes to dendritic reach and surface area are thought to be connected to the integration and refinement of sensory information. Previous work (Ashby and Isaac 2011) has implicated the changing morphology of excitatory neurons within the barrel cortex with evolving plasticity, showing that sensory deprivation has a marked effect on the growth and complexity of the dendritic arbour of a developing neuron.

It was expected that these same changes would be observed in the dye-filling and imaging experiment, to correspond not only with previous work, but also to the surface area predictions made via the passive dynamics coefficients in Chapter 4: *Passive Dynamics*. These results predicted an overall rise in the surface area of the dendritic compartment in particular, but with a marked increase in the surface area in the period between P9 and P11.

Gap Junctions

Electrical synapses, or gap junctions, have been reported between neighbouring neocortical neurons, primarily with cells of the same subtype (Zhang, Li et al. 2017). Providing a fast pathway for the communication of electrical signals (Pereda 2016), gap junctions were of particular interest to the scope of this thesis given previously reported work that suggested their presence might be crucial for development (Elias and Kriegstein 2008), specifically that they may be implicated in the formation of functional networks (Yuste, Nelson et al. 1995, Venance, Rozov et al. 2000, Yu, He et al. 2012, Hatch, Mendis et al. 2017). Some groups have presented evidence for the theory that gap junctions between neurons are developmentally transient (Belousov and Fontes 2013, Belousov, Fontes et al. 2017), perhaps setting a ‘blueprint’ for the locations of more permanent chemical synapses (Katz 1995, Yuste, Nelson et al. 1995, Rörig, Klausa et al. 1996); gap junctions may arrive in the cell for a couple of days and set up a functional network before being dismantled. Such a gross change to cellular biophysics could have a visible effect in the current clamp recordings, either passive or active (Yuste, Nelson et al. 1995), particularly if such an assembly and disassembly occurred within the developmental window studied in this thesis.

What biophysical benefits could gap junctions provide? They may facilitate the early propagation of calcium waves (Elias and Kriegstein 2008), but it may also be the case that a gap junction is a less energetically expensive structure than a synapse. A rough-and-ready method of neuronal communication for the young brain, prior to experience-dependent plasticity, is certainly an attractively simple hypothesis.

Gap junctions are formed from connexin proteins (Katz 1995). Neuronal gap junctions are most commonly associated with a structure of six hexamer proteins called connecxin36 (Cx36) (Belousov, Fontes et al. 2017), with molecular analysis by reverse transcription polymerase chain reaction demonstrating that spiny stellate cells within the barrel have gap junctions comprised of only this protein (Venance, Rozov et al. 2000). Additionally, connecxin proteins Cx26 and Cx40 have been suggested to contribute to the degree of gap junction coupling between developing neurons (Belousov and Fontes 2013). Gap junctions communicate information between cells via the electrostatic redistribution of charge and by the passive diffusion of small molecules such as glutamate and adenosine triphosphate in a nonspecific manner (Belousov, Fontes et al. 2017, Su, Chen et al. 2017). Common in cardiac neurons and in astrocytes (Belousov, Fontes et al. 2017), their role in developing cortical neurons is not fully understood. Dye filling using molecules small enough to traverse intracellular gap junctions is a proven method of identifying GJCC and a basis for hypotheses on the corresponding cellular networks (Yuste, Nelson et al. 1995).

Neurobiotin as a tool for gap junction detection

The Biocytin derivative Neurobiotin can be used to identify gap junctions in cortical neurons (Katz 1995). Neurobiotin is a small molecule that can be included in the internal solution of the patch micropipette for effective transfer into the cell, provided ample time is allowed for diffusion (Rörig, Klausa et al. 1996). Once inside the cell, it can diffuse through the cytoplasm of the soma to the dendrites and axon. There, should it encounter any gap junctions, it is small enough to be able to pass through them, and into the secondary cells (Penn, Wong et al. 1994). Neurobiotin itself is not fluorescent, but it has a high affinity for Streptavidin-Alexa488, a highly fluorescent molecule that can be applied to the acute slice post electrophysiology experiments (Zahs and Newman 1997, Mills and Sey 1998).

This chapter describes work on dye filling of barrel cortex excitatory neurons, done concurrently with current-clamp electrophysiology. This work was motivated by the fast dynamics observed during passive dynamics experiments, which were thought to be

independent of the lipid bilayer membrane biophysics; these dynamics were seemingly too fast to be described by any capacitive relaxation across the cell membrane. It was hypothesised that gap junctions between cells might be the origin of these dynamics; the presence of a current 'sink' in the form of gap junctions could explain the sharpness of the voltage decay curves observed. The occurrence of GJCC was related to postnatal age and the relationship between GJCC and passive dynamics coefficients was examined.

5.2 Analysis Methods

Image analysis

Confocal images were analysed with Fiji ImageJ software. Images were optimised by eye for brightness and contrast based on the visibility of the soma of the primary (patched) cell for each of the three channels (green, blue and red) separately. A composite maximum projection image was built for two-dimensional examination. A maximum projection image at 20x magnification in the green channel only, edited to produce a clearer black-and-white representation, was built for straightforward analysis of the morphology. Where necessary, images were 'stitched' together using the ImageJ tool MosaicJ (P. Thévenaz 2007). This tool allowed for the formation of a composite image of two or more separate images, providing there was some overlap.

For the detection of GJCCs, the z-stack of confocal images was processed into three different formats:

1. A looping movie traversing down through the z-stack of tissue, slice by slice.
2. A three-dimensional projection and reconstruction of the tissue that rotated on a central vertical axis.
3. A graphics interchange format (gif) image that showed the back-and-forth rotation of the three-dimensional projection about 60 degrees on the central vertical axis.

Observing the morphology of the primary cell

The injection of dyes afforded the opportunity to observe the fine morphology of layer IV cortical neurons. Via the observed size and shape of soma and dendrites, each filled and recovered cell was grouped into one of four categories: *spiny stellate*, *star pyramidal*, *pyramidal*, and *unknown*. Cell types are categorised in accordance with criteria previously described (Feldmeyer, Egger et al. 1999, Staiger, Flagmeyer et al. 2004):

- *Spiny stellate cells* were observed to have an approximately spherical soma 10-15µm in diameter. They were noted for their lack of apical dendrite, and in older cells, for their typically asymmetrical dendritic arbour, owing to the fact that most dendrites were projecting from the soma into the centre of the barrel.
- *Star pyramidal cells* were observed to have either a spherical or triangular soma approximately 15-20µm in diameter. They had a clear apical dendrite that reached no further up through the cortex than layer II/III. Their dendritic arbour was otherwise similar to that of the spiny stellate cell, being star-like, though typically a little more symmetrical.
- *Pyramidal cells* were observed to have a triangular soma 15-19µm across. They had an apical dendrite that stretched up through the cortex to layer I, where it typically terminated in an apical tuft. The remaining dendritic arbour was concentrated around the base of the soma in a basal skirt distribution.
- *Unknown cells* occurred where the soma of cell was ripped from the tissue slice during the removal of the patch-pipette. Although all efforts were made to prevent this happening, the presence of dye-filled dendritic and/or axonal projections without the corresponding soma was present in 4 slices. Despite the lack of somata the projections and/or the presence of GJCC can be observed.

Detecting gap junction coupled cells

To complement the injection of Neurobiotin into cortical neurons, a second molecule, Dextran-conjugated-Alexa546 was also used. Injection of Dextran-conjugated-Alexa546 fulfilled two roles: it provided additional validation of the presence and location of the primary (patched) cell, and it provided a control against which to test the hypothesis that gap junction coupled cells will be visible by the presence of Neurobiotin; if only Neurobiotin and not Dextran-conjugated-Alexa546 was observed in secondary cells, then gap junctions would be implicated. GJCC were detected via both the *presence* of Neurobiotin (green) and the *absence* of Dextran-conjugated Alexa546 (red), indicating that the small Neurobiotin molecule had traversed gap junctions that were too narrow for the large Dextran-conjugated Alexa546. It was assumed that both molecules would diffuse at a similar rate and have sufficient time to diffuse throughout the accessible morphology. The minimum loading time was 30 minutes.

Objects resembling GJCC were identified within the three-dimensional representations of stacks of images taken at 20x magnification. This allowed for assured differentiation between

neurons and blood vessels. When a potential a GJCC was identified, the following criteria for confirmation were implemented:

1. The primary cell must clearly be identified by having the brightest fluorescence in the examined tissue.
2. GJCC must be approximately spherical in shape and have a demonstrably discrete volume.
3. GJCC cells must contain Neurobiotin (appear green).
4. The presence of Dextran-conjugate-Alexa546 within GJCC (red) must not be brighter than background.
5. Gap-junction-coupled cells must have an identifiable nucleus, as shown by the presence of DAPI (blue) in the soma.

It was important to carefully consider the method of quantification of the degree of gap junction coupling. For some tissue slices, one or two cells appeared to be very strongly coupled, with the brightness of the secondary cells being almost equivalent to the brightness of the primary cell. In other slices, there could be many gap-junction-coupled secondary cells (Belousov and Fontes 2013), but with visibly less fluorescence than primary cells. From a biophysical perspective, what is of interest is the conductance between the primary and secondary cell(s), and how this affects the overall balance of currents in and out of the primary neuron (Venance, Rozov et al. 2000, Gibson, Beierlein et al. 2005). Therefore, a single cell that provides a large current sink, either by location, or by the number of gap junctions that connects it to the primary cell, may be more influential on the biophysics than ten secondary cells that are more distal (Penn, Wong et al. 1994, Pereda 2016). Within this dataset of confocal images, the large diversity of secondary cell locations and relative fluorescence led to a simple binary measure of gap junction coupling: if secondary cells were observed, then the patched cell was given a coupling parameter =1, whether it was coupled to 1 or 100 secondary cells. If no secondary cells were observed, then the coupling parameter was set to zero. This crude measure of gap junction coupling allowed analysis of the relationship between gap junctions and developmental biophysics. To provide some finer detail, the number of visible GJCC were also counted, but with the caveat that this number may have had no relation to the biophysics of the primary neuron, and was highly susceptible to human error in both imaging and counting.

To summarise, once GJCC were detected, two measurements were taken:

1. A binary measure of the presence or absence of GJCC, where presence=1, absence=0.
2. A count of the number of GJCC visible in the cell gif.

Quantitative Data Analysis

Data was analysed using a purpose-built MATLAB script. This script performed quantitative analysis on the morphology and GJCC against developmental age. All confocal image analysis and electrophysiological analysis was done separately and blinded, as to not bias the search for GJCC.

5.3 Results

The morphology of the primary patched cells

Morphological analysis was used to determine the proportion of cell types within the barrels of layer IV of the cortex. Previous groups have reported excitatory cells within the barrel cortex in rats or mice are limited to spiny stellate and star pyramidal morphologies, at a ratio of approximately 8:2 (Feldmeyer, Egger et al. 1999). Accounting for only the spiny stellate and star pyramidal cells, populations within the barrel at a similar ratio of 21:8 were found here (approximately 7:3) but a smaller number of pyramidal cells were also identified. This warranted further investigation and utilised some of the otherwise erroneous imaging data: when attempting simultaneous current clamp and electrophysiology experiments, occasionally the first patched cell would not spike, particularly in the earliest experiments when the technique was still being perfected. As to not waste the slice, the position of the patched cell was carefully recorded and a second (or indeed a third) attempt was made at patching a healthy cell in another barrel. On a few occasions, multiple cells were identified in post-hoc confocal imaging, in separate barrels of the barrel cortex, with the number of cells visible equal to the number of patching attempts. A remarkable diversity of cell morphologies was observed in this small data set, with pyramidal cells and spiny stellate cells found in neighbouring barrels in the same cortical layer. This therefore implies that pyramidal-type cells can in fact be found in the barrels of layer IV (**Figure 5.1**) in these young mice.

Of the 67 cells patched with dye in the internal solution, dye-filled cells were recovered via fluorescent and later confocal microscopy in 43 cases (a 64% success rate). These cells comprised postnatal days P4 to P11, as no cells at P3 were successfully recovered. The majority (49%) were spiny stellate, but a significant number were also star pyramidal (19%) or pyramidal (23%) (**Figure 5.2**). A small number of cells (9%) were categorised as 'unknown', due to the soma being absent. The cell-type populations were observed to change over the developmental period studied (**Figure 5.3**): both the number (**Figure 5.3.A**) and the

proportion (**Figure 5.3.B**) of spiny stellate cells increased over development, starting at 25% of the total cell population at day P4, and reaching 57.1% of the total cell population by day P11. Meanwhile, the pyramidal and star pyramidal cells showed an overall decrease in population with age, dropping from 37.5 to 14.3% and 37.5 to 28.6% respectively. This data hints that spiny stellate cells become more populous within the barrel cortex, perhaps at the expense of other cell types, although this is not statistically confirmed.

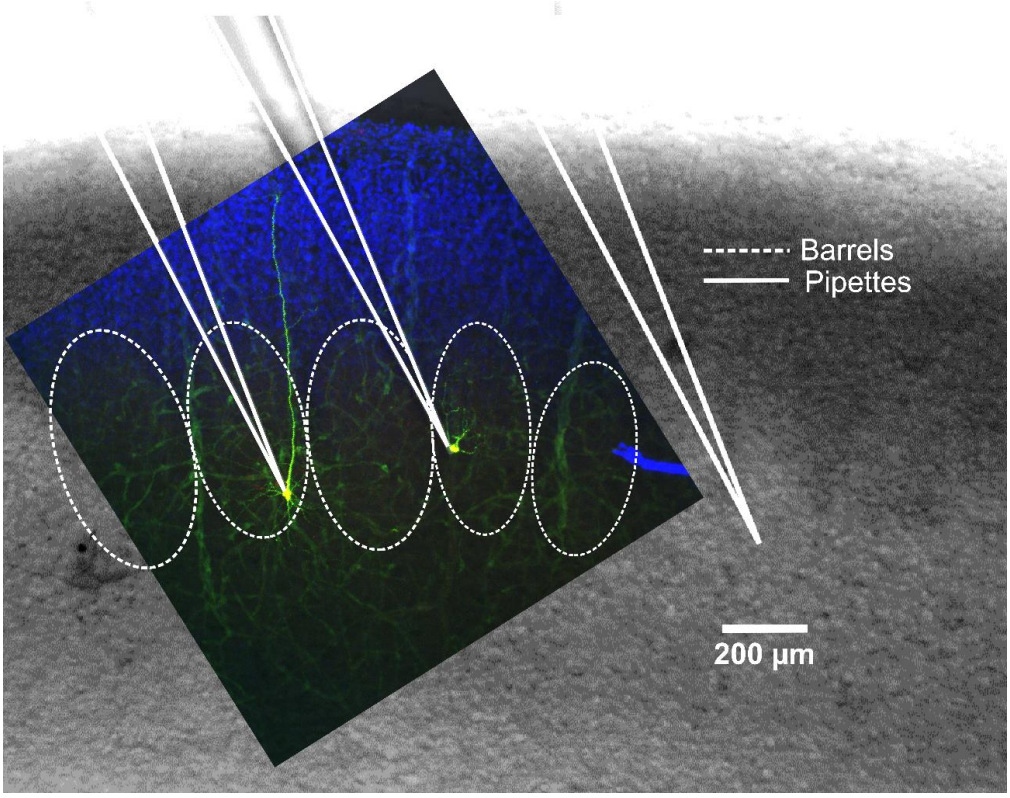

Figure 5.1: Cells patched within or the barrels of layer IV of the cortex exhibit surprising diversity in their morphology, with pyramidal and spiny stellate cells found within a few hundred micrometres of one another. Digital photograph composite images of the barrel cortex (greyscale images) at 4x magnification, overlaid with composite confocal maximum projection images at 10x magnification. White dotted lines show the approximate positions of the barrels, based on digital photograph. Solid white lines show the location of the patch pipettes.

Dendritic arbour grows with postnatal age

There was a marked change in neuronal morphology with postnatal age. In particular, the dendritic arbour became much larger and more complex (**Figure 5.4**), with presumably a much-increased surface area. This corresponds both to what has previously been reported in various brain regions and species (Luhmann, Schubert et al. 2011), and to the earlier prediction of dendritic surface area from the passive dynamics coefficients, as reported in Chapter 4: *Passive dynamics*.

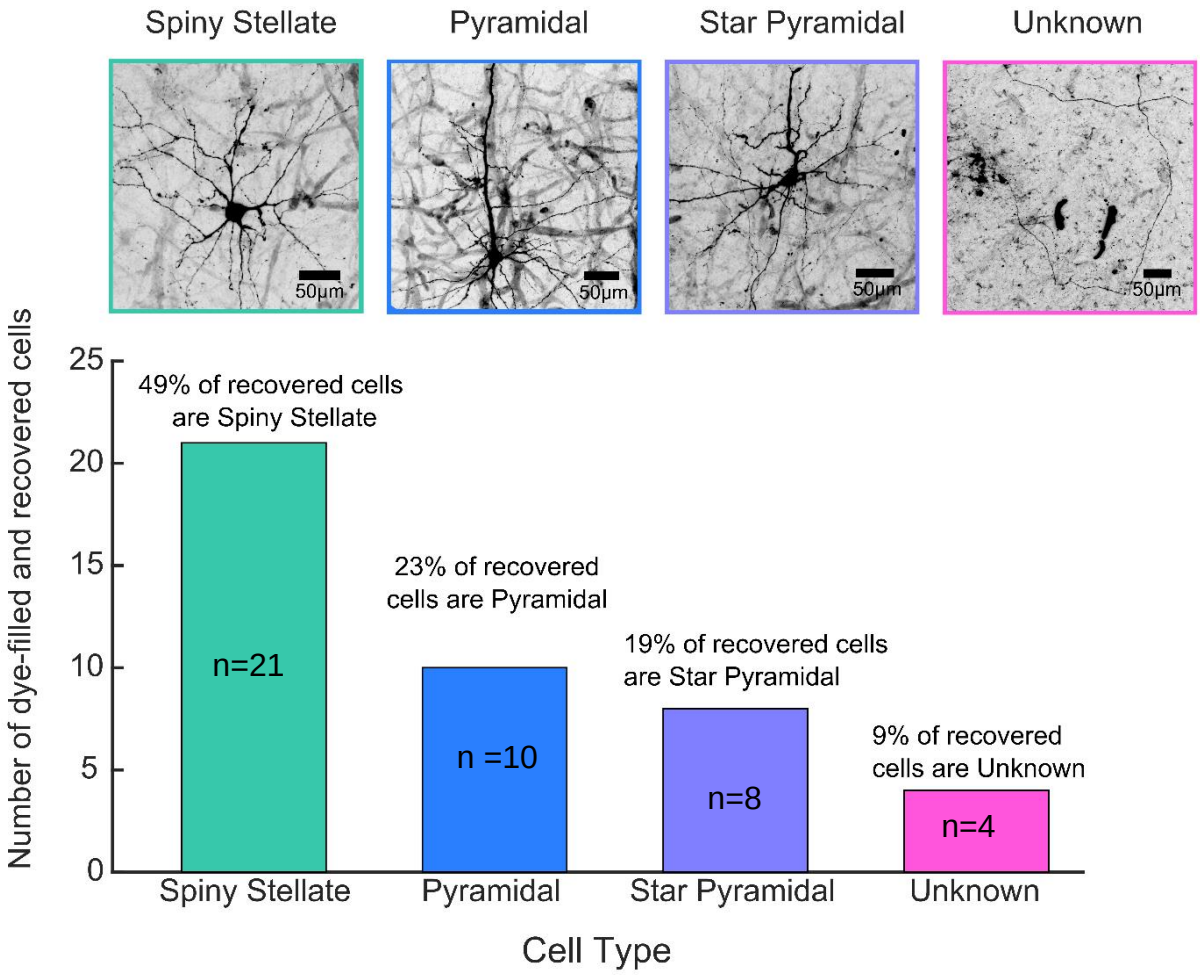

Figure 5.2: Cell types identified by morphology. Spiny stellate cells are identified by their star-like appearance, small, round cell body, absence of apical dendrite, and generally asymmetric dendritic arbour. Pyramidal cells are identified by the presence of an apical dendrite that projects to layer I of the cortex, ending in an apical tuft, with all other dendrites are polarised to a basal 'skirt'. Star pyramidal cells fall in between spiny stellate and pyramidal cells in terms of morphology, having a prominent apical dendrite that does not stretch beyond layer II/III, and an otherwise non-polar dendritic arbour. The remaining cells recovered during confocal imaging are categorised as 'unknown', due to their soma being removed or destroyed during removal of the patch-pipette.

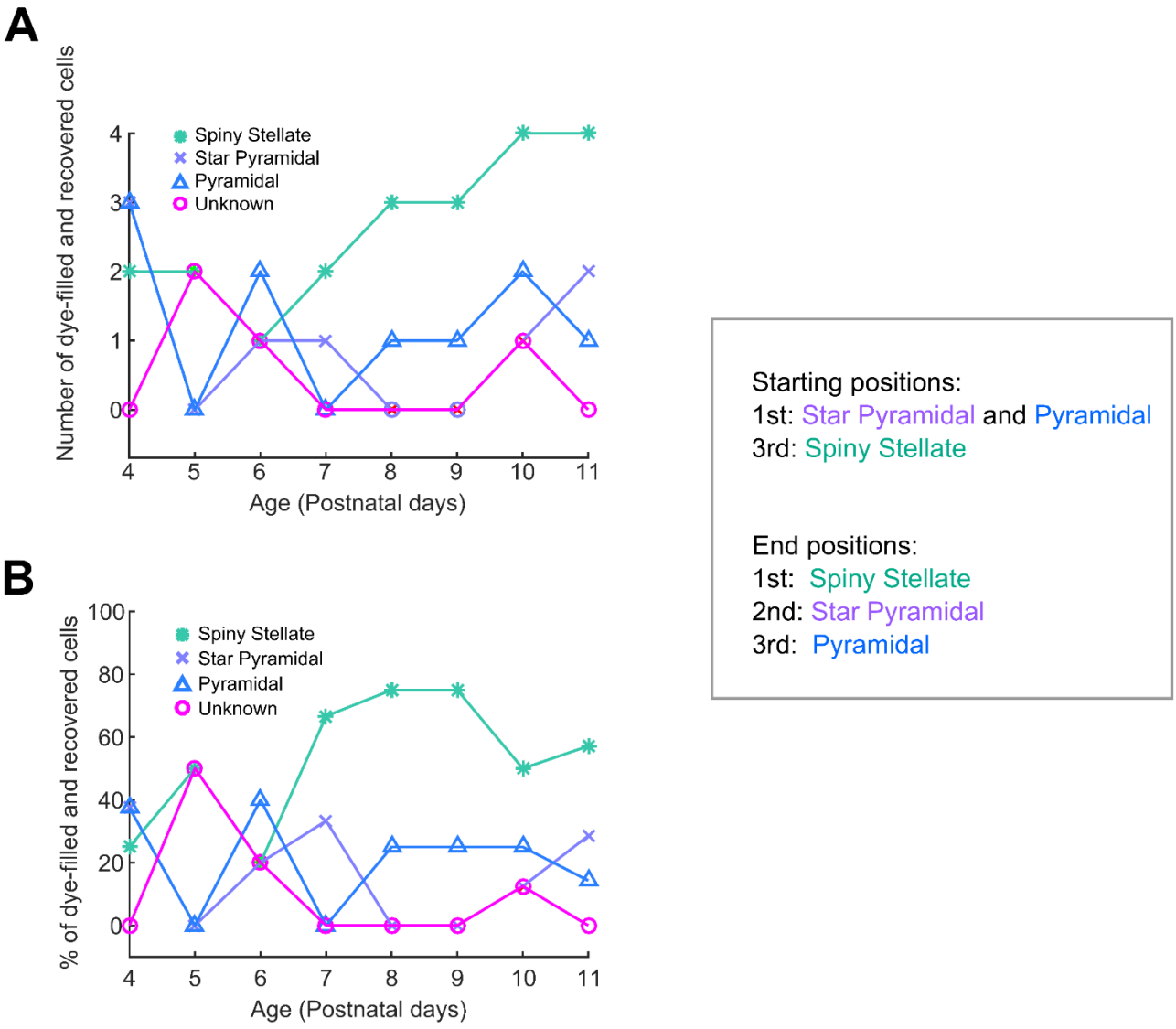

Figure 5.3: Cell type plotted against postnatal age. The number (**A**) and the percentage (**B**) of cell types observed via dye-filling and post-hoc confocal imaging over the developmental period P4-P11.

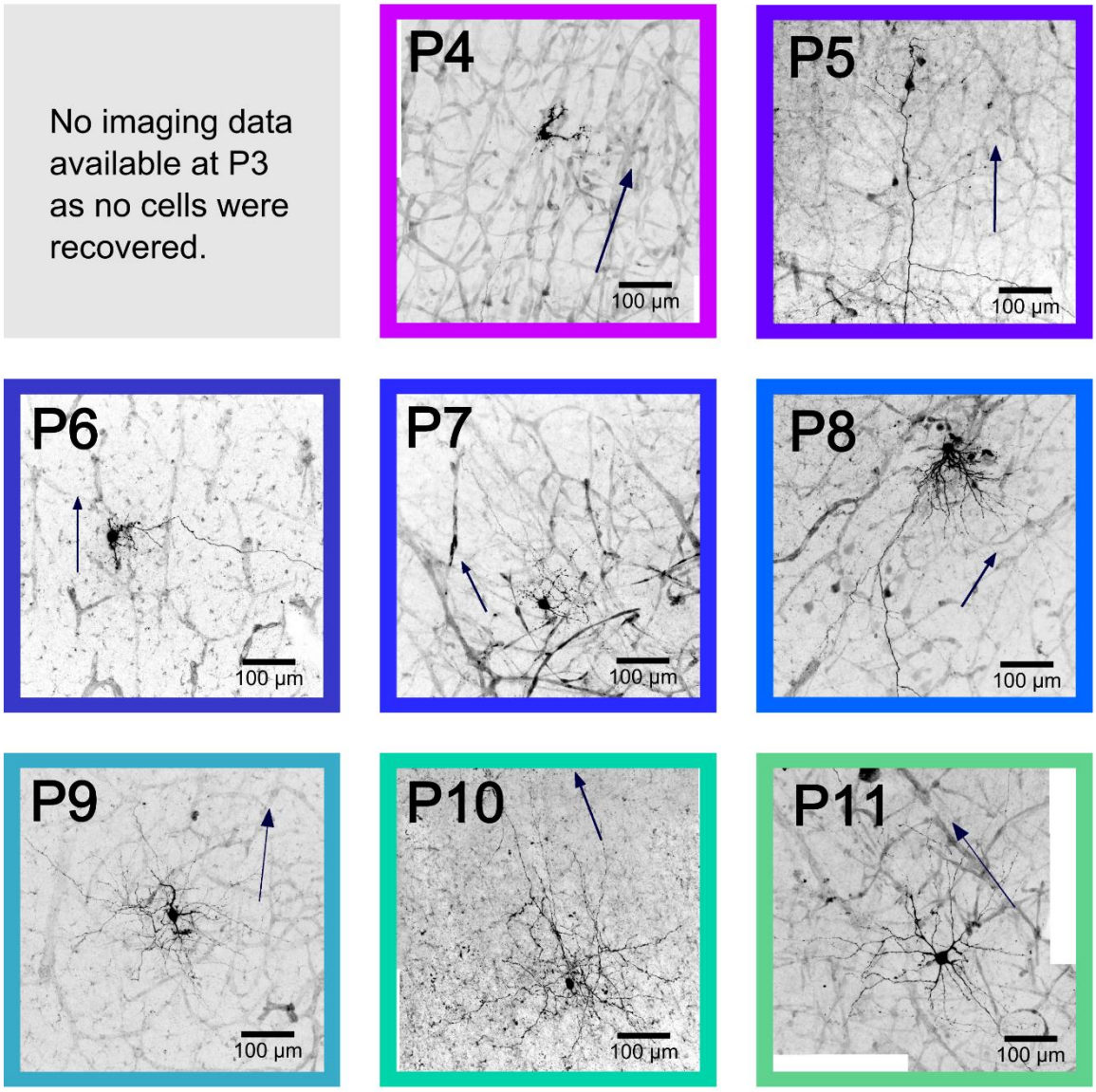

Figure 5.4: Confocal imaging reveals an increase in dendritic arborisation with postnatal age. Maximum projections of z-stack confocal images in the green channel at 20x magnification of representative cells between P4 and P11. Images adjusted by eye for brightness and contrast. Arrows show the direction of the pial surface

Gap junction coupled cells are clearly visible in some slices

Of the 39 patched cells of identifiable morphology recovered during post-hoc imaging, GJCC were visibly coupled to 22 (56%) (**Figure 5.6**). GJCC are not observed to be particularly prevalent to any one cell type: they were coupled to 11/21 spiny stellate cells (52.4%), 4/8 star pyramidal cells (50%) and 7/10 pyramidal cells (70%). In two instances, the number, size and distribution of GJCC apparent during confocal imaging indicated that the primary neuron was not, in fact, coupled to other neurons, but instead glia (**Figure 5.5.A**). Certainly, previous groups have reported the presence of gap junctions in networks of astrocytes, (Zahs and Newman 1997, Belousov and Fontes 2013, Belousov, Fontes et al. 2017), but this does contradict previous work that asserted the coupling is never observed between neurons and glia (Katz 1995). In one instance the morphology was seen to resemble two conjoined cells (**Figure 5.5.B**). Conjoined cells within cortical columns, coupled by gap junctions are a phenomenon in the developing brain that has been previously described (Yu, He et al. 2012), and this may be further evidence of this effect. However, given the low frequency of these types of coupling in this dataset, explanation of these phenomena was not pursued, nor was its effect on neuronal biophysics.

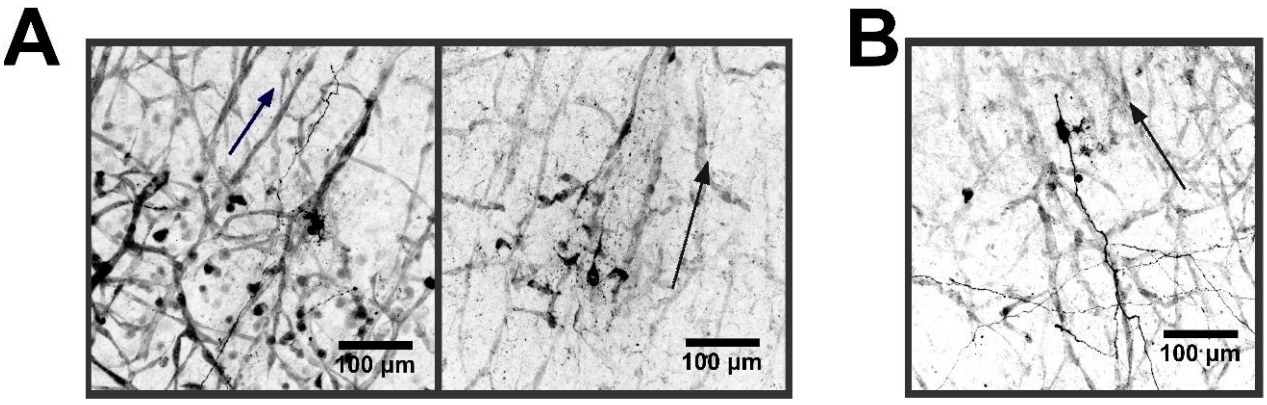

Figure 5.5: Unusual morphologies are visible in some confocal images. A: Neurons gap-junction-coupled to glia. **B**: What appears to be conjoined neurons. Arrows show direction of pial surface.

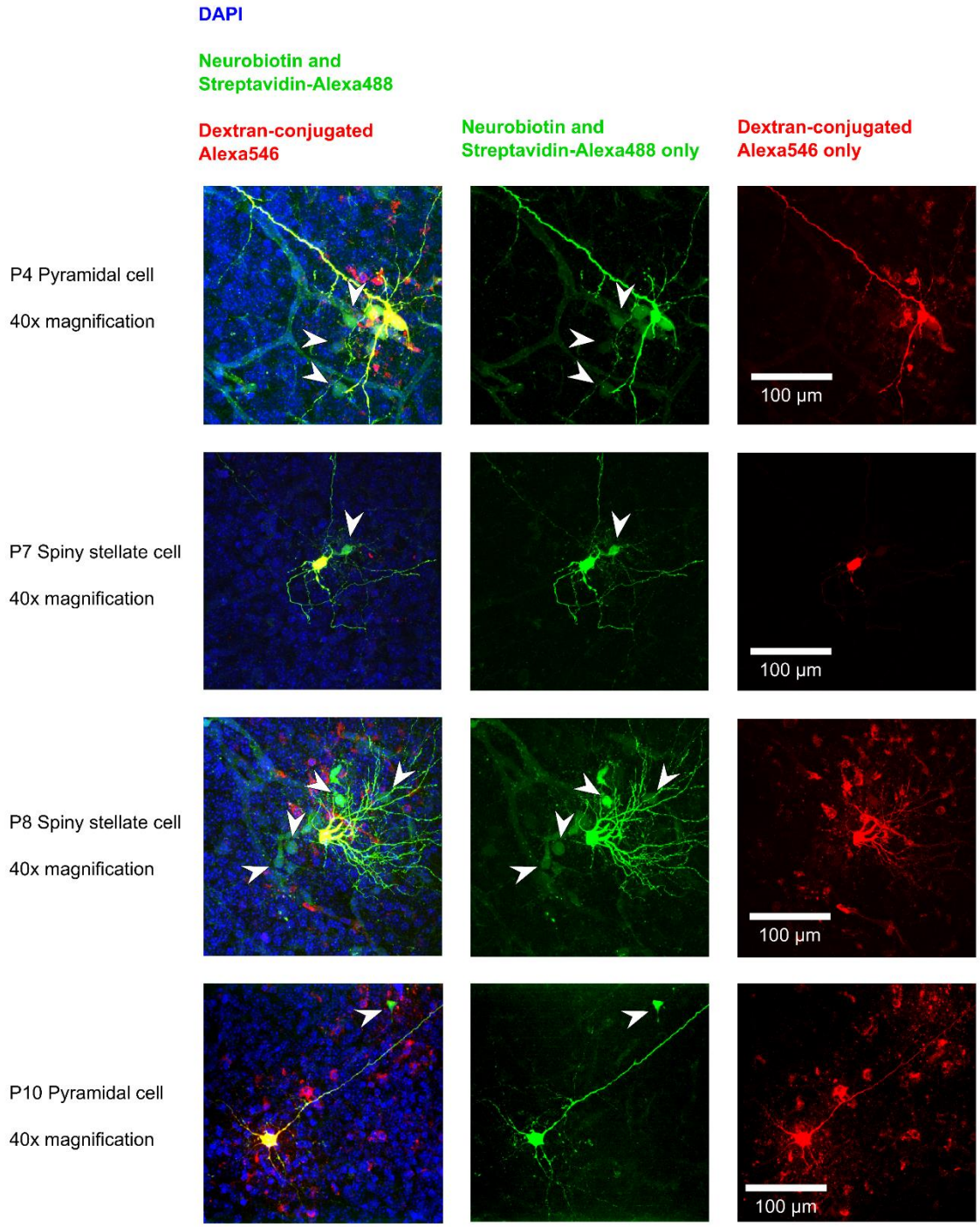

Figure 5.6: Gap junction coupled cells (GJCC) **are clearly identifiable via the presence of Neurobiotin.** Confocal images of four cells of varying ages and morphologies at 40x magnification, with (*left)* all three channels shown in a composite maximum projection, (*centre)* the green channel only, showing the presence of Neurobiotin, and (*right)*, the red channel only, showing the presence of Dextran-conjugated Alexa546. White arrows show the location of GJCC. Red staining away from the patch cell is due to uptake of Dextran-conjugated Alexa546 by dead cells at the acute slice surface.

Postnatal age and gap junction prevalence

Where GJCC were observed in a slice, the number of secondary cells were counted. Between 1 and 70 secondary cells were observed per primary cell (mean = 8.39, median = 3, mode = 1). The number of GJCC per primary cell as a function of postnatal age was counted (**Figure 5.7.A**) and compared and contrasted with the mean number of GJCC at each age. No statistical significance was found using the tests employed here, but there remains the hint of developmentally transient GJCC as has been previously reported across species (for example, (Rörig, Klausa et al. 1996)). The frequency of GJCC occurring in slices was investigated via the binary measure of gap junction coupling (**Figure 5.7.B**); this appeared to show an age dependent increase in the occurrence of GJCC, though a linear fit with Pearson's correlation coefficient provided a result that did not reach statistical significance (P=0.051).

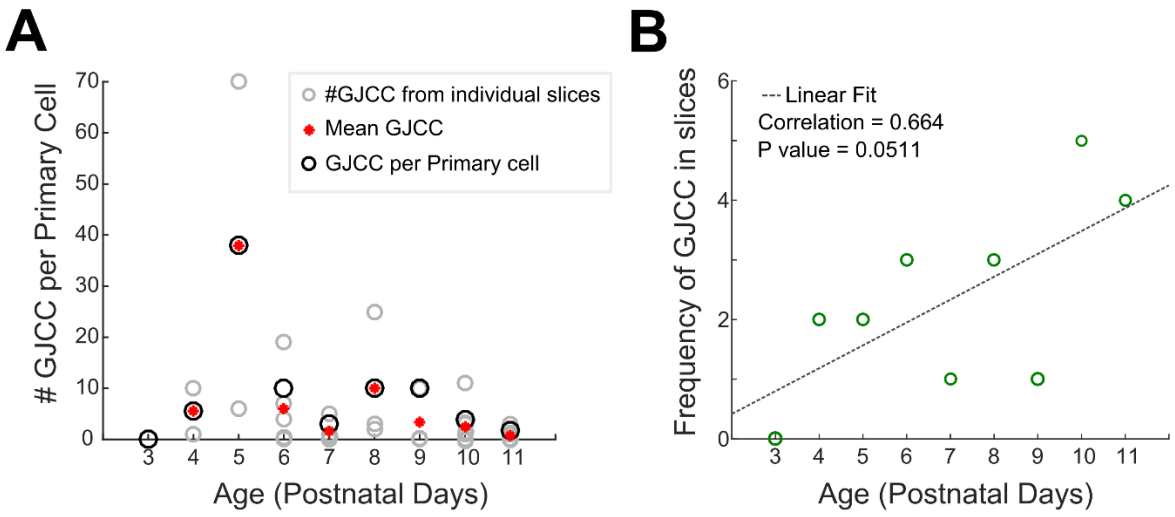

Figure 5.7: The presence of gap junction coupled cells (GJCC) **appears to potentially change with age A:** Number of GJCC per primary (patched) cell against age. Grey circles are the number of GJCC visible, black circles are the mean number of GJCC per primary cell, red stars are the mean number of GJCC at each age point. A peak is apparent at P5, though this is due to the unusually high number of GJCC within one slice. **B**: Frequency of GJCC appearing within slices as a function of age, binary measure per slice. Linear fit assessed with Pearson's correlation coefficient and found a positive correlation of 0.664 with P=0.0511

Gap junctions and passive dynamics

Following the observation of a fast component of passive voltage decay in some cells (Chapter 4: *Passive Dynamics*), it was hypothesised that GJCC were correlated with the time constant coefficients gleaned from the fitting of a two-compartment model. The value of the faster time constant, tau_2, was expected to be directly correlated to the presence and/or extent of GJCC, since it is the dramatic variation of tau_2 – in some cases as much as an order of magnitude smaller than that observed in other cells – that was identified as the cause of the

'kink' seen in some passive dynamics traces. To test the hypothesis that the presence of GJCC leads to a lower value of the second passive dynamics time constant tau_2, tau_2 was plotted against the number of GJCC (**Figure 5.8.A**), but no significant correlation was found. It was expected that any effect of GJCC on the time constants would likely be amplified by considering the ratio of tau_1 to tau_2 (**Figure 5.8.B**), but again, no significant correlation was found. Looking at the binary measure of GJCC, a significant difference between the mean values of tau_2 from primary cells exhibiting GJCC when compared to those with no GJCC was predicted (**Figure 5.8.C**), but no such difference was found. This lack of significance was replicated for the ratio of tau_1 to tau_2, and the product of tau_1 and tau_2.

Finally, the frequency of coincidence between the presence of GJCC and the presence of the kink seen in some passive dynamics traces was assessed. Passive dynamics traces were defined as having a kink via visual inspection: each trace was plotted in two figures, one of the entire trace, the second spanning the 9ms around the membrane potential peak. Each pair of figures was then compared to two representative passive dynamics traces: one of a trace defined as having no kink, the other defined as having a kink. By comparison, passive dynamics data were assigned '1' if their dynamics were more similar to the kink trace, and 0 if their dynamics were more similar to the no kink trace. Where the binary measure of kink matched the binary measure of GJCC, a coincidence measure was given the value 1. Where they did not match, it was given the value 0. The cumulative sum of coincidence was calculated and plotted against the number of recovered and imaged primary cells (**Figure 5.8.D**) and was compared to the coincidence of two random distributions of zeros and ones (repeated 100 times). As shown in the figure, the coincidence of kink and GJCC is no more likely than the coincidence of random numbers; in fact, it lies right in the middle of the random distribution. Given the assessment of all these measures, it was necessary to conclude that the fast component of passive dynamics decay seen in some traces was not correlated to the presence of GJCC.

An unexpected effect: Neurobiotin affects the spike waveform

During these experiments, a strange effect on the spike waveform was noticed: Neurobiotin appeared to have a concentration-dependent effect on the spike width and height, making them lower in amplitude and longer in duration. This is obviously a problem if Neurobiotin is used to correlate electrophysiological dynamics with morphology or gap junction coupling. The following chapter, Chapter 6: *Neurobiotin has an Effect on Spiking Properties*, investigates the effect of Neurobiotin on spike waveform in detail.

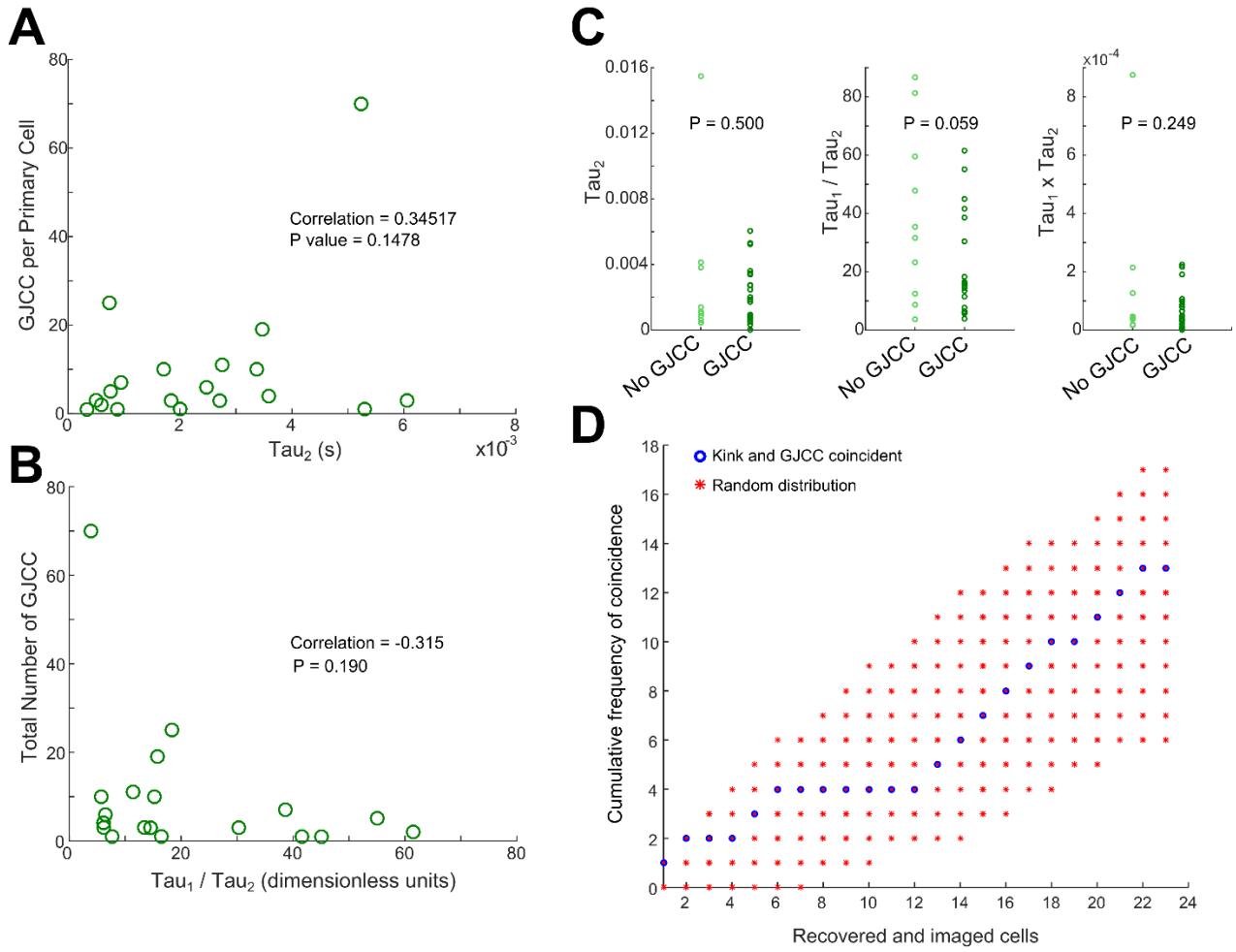

Figure 5.8: Gap junction coupled cells (GJCC) **have no influence on the passive dynamics time constants.** **A**: GJCC per primary cell plotted against each cell's *tau*$_2$. **B:** total number of GJCC plotted against tau ratio. Both relationships assessed via Pearson's correlation coefficient, with no significant correlation detected. **C**: Binary measure of GJCC against *tau*$_2$, tau ratio and tau product. Light green circles are primary cells without GJCC, dark green circles are primary cells with GJCC. One-way ANOVA finds no significance. **D**: Cumulative frequency of coincidence between passive dynamics kink and GJCC (blue circles), compared with a distribution garnered from a random number generator (red stars).

5.4 Discussion

Via the use of Neurobiotin, Streptavidin-Alexa488, Dextran-conjugated-Alexa546 and DAPI, dye-filling was performed concurrently with electrophysiology experiments, producing three-dimensional confocal images of filled cells, allowing examination of their morphology and networks of GJCC. The proportion of different morphological phenotypes found in the barrels of the developing neocortex, and how this proportion changes with age, was examined. The occurrence of GJCC with age and their correlation (or lack thereof) with passive dynamics time coefficients was also investigated.

Cell morphology

Previous work has put the proportions of regular-spiking neurons in the barrel cortex of rats and mice at approximately 80% spiny stellate, 20% star pyramidal (Feldmeyer, Egger et al. 1999). Examination of the cells imaged in this work showed a very similar morphological ratio, except that pyramidal cells within the barrels were also observed across the entire developmental period studied. There are four possible explanations for this discrepancy:

1. These pyramidal cells are simply outside of the barrel cortex and were patched due to inaccuracy of pipette positioning. This is the simplest explanation; pyramidal cells are well known to be present in both layer V and layer II/III of the cortex in rodents (Larsen and Callaway 2006). Therefore the question arises of whether it is necessary to exclude these pyramidal cells from the electrophysiological analysis. Over this developmental period, the large variation in observed dynamics, particularly at the youngest ages, makes the task of cell-type differentiation more complicated. Consequently, the electrophysiological data presented in this thesis is categorised only as 'fast spiking' or 'regular spiking' (with fast spiking cells being excluded from the data set). With 36% of cells patched with Neurobiotin in the internal solution not recovered during post-hoc imaging, presumably the total number of pyramidal cells patched is much larger than the 10 observed. By extrapolating the percentage of pyramidal cells seen via imaging to the total population, the total number of pyramidal cells can be estimated to be ~40 out of the total of 166 cells studied. Removing these data from the electrophysiological data set without accidentally removing spiny stellate or star pyramidal cells would be a near-impossible task, and, as can be seen in **Figure 5.1**, pyramidal cells can be found within the barrels and at the same cortical depth as spiny stellate cells.

2. Neuronal differentiation is still ongoing over the developmental period investigated in this thesis; groups have previously shown the differentiation of cortical neurons in rodents to continue up to postnatal day P12 (Osterheld-Haas and Hornung 1996). Cells resembling pyramidal or star pyramidal cells have been shown to retract their apical dendrite, becoming increasingly stellate as they mature (Li, Fertuzinhos et al. 2013), with the development of spiny stellate cells reported as a two-step process, starting with a pyramidal morphology before sculpting a stellate morphology (Callaway and Borrell 2011). Given this dynamic state of differentiation, more pyramidal cells may be expected to be observed at the earliest stages of development. An overall decrease in the populations of both pyramidal and star pyramidal cells with age is seen, alongside a simultaneous increase in the population of spiny stellate cells, but at

present the numbers of cells observed are too low to state with any confidence that this is a consequence of differentiation.

3. Cells are still migrating to their final location when these cells are patched. The process of migration of cells through the cortex is known to continue throughout the first two weeks of postnatal development in a number of mammals including mice (Li, Fertuzinhos et al. 2013), with gap junction coupling reported to mediate neuronal migration (Elias and Kriegstein 2008). The pyramidal cells patched within the barrel cortex may not yet be in their final position and may ultimately localise in layer II/III. As with the diversification hypothesis, this would imply that pyramidal and star pyramidal cells would be seen in the barrel cortex in higher numbers at younger ages. With a larger data set, it may be possible to observe this distribution at statistically significant levels.

4. Pyramidal cells remain in the barrel throughout life and have just not been observed before. This seems very unlikely, given the plethora of confocal, two-photon, fluorescence and light-microscopy studies performed on cell morphologies within the barrel cortex.

These hypotheses work under the assumption that there was no experimental bias in the proportion of cells that were patched and recovered. It is possible, however, that cellular morphology may be an influencing factor in cell survival; that the morphologies of particular cells may be more robust and less likely to be destroyed through the process of dye filling. In this case, this dataset could be weighted towards one particular cell type.

Of the 43 cells recovered in confocal imaging, 13 were determined to have both identifiable morphology and a fast component of passive dynamics decay, or kink. As a percentage of the total number of cells recovered with each morphology, the pyramidal cells appeared to be the most likely to exhibit kink dynamics, with the fast component of decay apparent in n=5/10 cells, whilst spiny stellate cells appeared to be the least likely to exhibit these dynamics, with the kink only present in n=5/21 cells (**Figure 5.9**). A Fisher's Exact Test was performed to detect any intergroup differences, but no statistically significant difference was found (P=0.22). The test being conservative, it may be that these numbers are too low to produce any statistically significant conclusions. A larger data set may be used in the future to test the hypothesis that the presence and indeed dynamics of the kink may be intrinsically related to the presence and/or length of the apical dendrite. A large apical dendrite may provide a

sufficiently separate compartment to perform the role of the current sink that facilitates these dynamics.

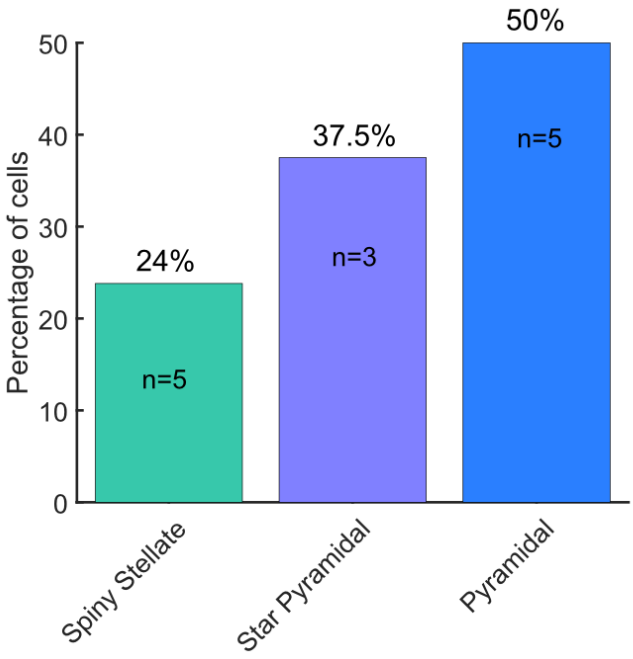

Figure 5.9: The proportional frequency of recovered and identified cells exhibiting 'kink' dynamics. The percentage of cells exhibiting kink dynamics is different for the three different morphologies recovered and identified, but a Fisher's exact test on these data finds no statistically significant difference between groups (P=0.22).

The presence of gap junction coupled cells

Here, gap junctions are implied by the combined dye-filling of single patched cells with Neurobiotin and Dextran-conjugated-Alexa546, the molecular weights of these two dyes being used to differentiate between patched and gap junction coupled cells within layer IV barrels and the surrounding area.

GJCC were observed to be coupled to 56% of dye-filled and recovered cells. However, there are caveats to consider that may have introduced a bias into these observations. The presence of GJCC could influence the robustness of the primary cell to this experimental technique. It must also be considered that GJCC might be outside of the 400 µm range of the tissue slice thickness used in these experiments. Although GJCC have been reported to be organised within cortical column domains (Katz 1995, Yuste, Nelson et al. 1995, Yu, He et al. 2012), these domains may not be constrained to the 400µm-deep plane of the acute cortical slice. Since GJCC were observed far from the soma, it is not inconceivable that GJCC may have been cut off by the slicing procedure. If this is the case, then the quantification methodologies of GJCC may be incorrect. Indeed, gap junction coupling between distal axons or dendrites of

cells could, hypothetically, extend across the cortex; to be filled with Neurobiotin, such cells may require much longer diffusion times. With the diffusion time limited to 30-40 minutes the number of GJCC observed could have been affected, particularly cells that were distal or low conductance. Longer diffusion periods may be needed to allow dye diffusion that fully illuminates gap junction coupled networks (Rörig, Klausa et al. 1996).

The role of gap junction coupling in cortical development

The precise role of gap junctions within the cortex is still a subject of contention and debate, but what is clear is that they facilitate the exchange of information between coupled neurons. Previous work (Venance, Rozov et al. 2000, Gibson, Beierlein et al. 2005, Yu, He et al. 2012, Hatch, Mendis et al. 2017, Zhang, Li et al. 2017) has illuminated the transfer of action potentials between GJCC via multi-cell electrophysiology, and gap junctions have been shown to have a dramatic effect on the firing probability of secondary neurons (Hatch, Mendis et al. 2017). What is not so clear is why this is necessary. Synapses are known to be the primary pathway of neuronal communication, so the question arises of what benefit gap junctions provide cortical neurons.

One possible answer is that the formation of gap junctions may be development-dependent, necessary for healthy dendritogenesis and spinogenesis, (Su, Chen et al. 2017), and a necessary precursor to synaptogenesis (Belousov, Fontes et al. 2017). Between interneurons, gap junction coupling has been reported to accelerate between P7 and P10 (Zhang, Li et al. 2017). The work presented here provides hints, if not conclusive evidence, towards the developmental dependence of gap junctions: the number of primary cells exhibiting some degree of gap junction coupling appears to increase with age, but the number of GJCC appears to peak at some point between P5 and P8. This corresponds to previously presented evidence of developmentally transient gap junctions (Belousov and Fontes 2013). It is possible that there is a mass formation of gap junctions at one age point until entire networks of neurons are established; this could then be followed by a period of refinement where all but a few gap junctions are replaced by synapses (Belousov, Fontes et al. 2017). Thus, an early peak in the total number of GJCC followed by a slower accumulation of cells exhibiting gap junction coupling would be seen, as those networks were formed and refined. However, the numbers of cell observed here are too low to draw these conclusions with any statistical significance.

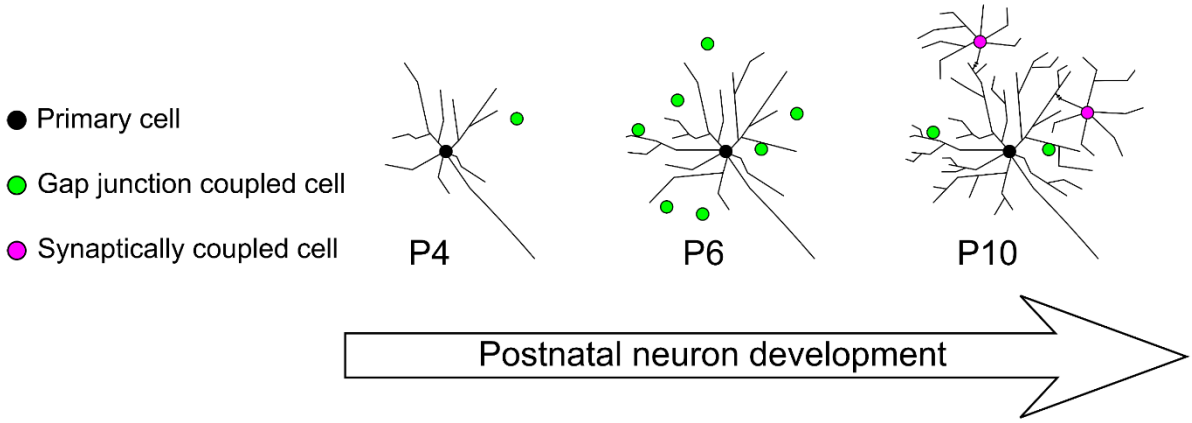

Figure 5.10: The appearance of gap junction coupled cells may be developmentally transient and followed by synaptogenesis of some of these cells.

Should the development-dependent gap junction hypothesis prove correct, what would be the biophysical benefits and/or consequences of this over the early formation of extensive synaptic networks? Previous studies have suggested that gap junctions are necessary for the generation of synchronised oscillations (Katz 1995, Belousov and Fontes 2013, Su, Chen et al. 2017), specifically that they may act as a low-pass filter for the synchronisation of slow cortical waves (Katz 1995). Spike-time dependent plasticity in immature neuronal networks may rely on early gap junction coupling.

Given the relatively simple hexamer structure of gap junctions (Montoro and Yuste 2004), it may be possible that they are a less energetically expensive investment than synapses within the developing neuron. Given the migration and diversification of neurons, and the rapid growth and formation of barrels, the early appearance of synaptic boutons and spines that are later proved redundant may be a high price to pay for this area of the growing brain. However, some have argued that the gap junction is far more complex than its superficial reputation (Pereda 2016), giving a counterpoint to this hypothesis. This energy-cost hypothesis could be investigated by observing the mitochondrial density in dendritic spine and axonal boutons across this developmental age range and investigating any age-dependence. Since gap junctions work via electrostatic charge distributions and passive diffusion, presumably they do not require mitochondria to work.

Gap junctions facilitate the exchange of action potentials in networks of cells (Belousov and Fontes 2013) which may lead to the formation of synapses in a secondary neuron (Pereda 2016, Su, Chen et al. 2017). Therefore, their presence may become unnecessary as synapses provide a more refined method of information communication. Regarding the relationship

between chemical synapses and gap junctions, some groups have found no correlation between the occurrence of gap junctions and chemical synapses (Zhang, Li et al. 2017), whilst others have reported developmental uncoupling of gap junctions coinciding with a major period of synaptogenesis and increased synaptic activity (Belousov and Fontes 2013). An inverse correlation between the presence of gap junctions and synaptogenesis would presumably result in the observation that GJCC become less populous at exactly the period in development where dendritic spine density and synapse formation explodes, namely P9-P12 in cortical neurons in mice (Ashby and Isaac 2011). The data presented here appear to indicate a drop-off in GJCC between P9 and P11; meanwhile the morphological data and passive dynamics analysis of neuronal surface area suggest a simultaneous surge in dendritic arborisation. To confirm this hypothesis, cells at later stages in maturation would need to be studied. Should the formation of gap junctions follow a developmental trajectory that is independent of synapses, yet follows similar Hebbian plasticity rules, a decrease in gap junction coupling with sensory deprivation would be expected to be seen. Given previous work (Feldman and Brecht 2005, Ashby and Isaac 2011) on the consequences of sensory deprivation via whisker trimming on the dendritic arbour of cells within the barrel cortex, it could be argued that a depleted dendritic arbour with a smaller neuronal surface area would leave less space available for the formation of gap junctions. This could be tested experimentally by incorporating whisker trimming experiments into our dye-filling and electrophysiology experimental protocol. Of course, the opposite hypothesis may instead be true: with sensory deprivation and synaptic depletion, the role of gap junctions may be amplified to compensate, and to maintain electrical homeostasis.

The effect of gap junctions on passive dynamics and active dynamics

Having observed an unexpectedly fast component of passive dynamic voltage decay in the earlier experiments (Chapter 4: *Passive Dynamics*) that was identified as a current sink of timescales faster than usually seen across the capacitive cell membrane, it was hypothesised that this was due to the presence of gap junctions. This analysis has shown that there is, in fact, no correlation between the presence of GJCC and passive dynamics time constants, nor any correlation between the presence of gap junctions and a kink in the passive dynamics. The lack of effect of the gap junctions on the electrophysiological profile, as determined by the passive dynamics, may be due to the low conductance of gap junctions in comparison to other current channels. The fast component of the passive dynamic decay present in some neurons may instead be caused by changes in dendritic arbour.

5.5 Summary

Neuronal morphology and gap junction coupled cells can be illuminated via the injection of Biocytin derivative Neurobiotin and post-hoc confocal imaging. A surprisingly diverse range of neuronal morphologies were observed with in the barrels, providing evidence for ongoing neuronal differentiation and migration. Gap junction coupling was detected via the presence of gap junction coupled cells in 56% of neurons patched, dye-filled and recovered in post-hoc analysis, but the degree of gap junction coupling proved difficult to define, leading to a binary measurement for gap junction coupling being determined. Gap junction coupling was found to not be correlated to the time constants of a two-compartment fit on the passive dynamics across the cell membrane.

6 The Effect of Neurobiotin on Spiking Properties

Key findings

1. Neurobiotin, in its typically recommended concentration for gap-junction detection, influences the active dynamics of the spiking excitatory cell in the barrel cortex of neonatal mice.
2. Neurobiotin has no detectable effect on passive dynamics, the dynamics of the cell membrane without activation of the voltage-gated ion channels, nor on any observed intrinsic properties.
3. A reduced concentration of Neurobiotin, to a tenth of what has been recommended for gap junction detection, can still successfully fill gap-junction coupled cells and be recovered in post-hoc confocal imaging without effect to the active dynamics of the cell.

6.1 Introduction

Electrophysiology can be used to measure the action potential (AP) waveform of the developing cortical neuron, and dye filling can be used to ascertain its morphology. Previous studies have extolled the virtues of Neurobiotin (NB), a derivative of Biocytin (Kita and Armstrong 1991), as an effective tool for dye-filling that can also be used to illuminate presence of any secondary cells coupled to the patched cell via gap junctions (Mills and Sey 1998, Montoro and Yuste 2004, Curti, Hoge et al. 2012). As described in the previous chapter (Chapter 5: *Gap Junctions and Morphology*) dye filling that involves the diffusive injection of impermeant dye or tracer molecule into the cell via the patch pipette internal solution can be used to good effect when coupled with confocal microscopy. The molecule fills the cell by diffusing throughout the cellular cytoplasm, and visualisation of the dye distribution by post-hoc microscopy can be used to reveal the cellular morphology. NB is small enough to traverse gap junctions and fill the somas of secondary cells; the detection of secondary cells via NB-filling has therefore been used as a proxy for the detection of gap junctions in a number of studies (Peinado, Yuste et al. 1993, Penn, Wong et al. 1994). In these studies, the experimental analysis was performed under the assumption that the NB itself does not have any effect on the electrophysiological properties of the cell.

A small number of studies (Xi and Xu 1996, Schlösser, ten Bruggencate et al. 1998) have reported a significant effect of NB on neuronal spiking properties, with an increase to spike width observed, but no significant effects on membrane properties. From these studies, an effect of NB on potassium conductance has been postulated, but this phenomenon has been otherwise largely ignored by the scientific community. Since electrophysiological properties are closely related to the cell morphology, as shown in previous chapters, any effect of NB on those electrophysiological properties presents a serious problem if morphological and electrophysiological results are to be combined. However, in order to account for the effects of gap junctions on neuronal development, concentrations of NB high enough to detect gap junction coupling between cells were needed.

This chapter seeks to demonstrate the effect of NB on the spiking properties, quantify this effect, allude to its origins, and assess what could be regarded as a "safe" concentration of NB that can be used in experiments without detriment to the electrophysiological recordings. It examines the effect of NB on the neuronal dynamics produced via the different patch-clamp protocols: the passive dynamics, the intrinsic properties and the active dynamics.

6.2 Analysis Methods

The experimental methods used were as described in *Methods*; neurons within the barrel cortex, whole-cell patched with NB-containing internal solutions, were taken through the electrophysiological protocols as previously described, allowing investigations into active and passive dynamics of the developing cells.

The spiking behaviour was analysed as described in Chapter 3: *Active Dynamics*. Only cells identified as regular-spiking excitatory neurons were included in analysis. This was done via analysis of mean measurements of those dynamics, and via monitoring of those properties over the course of the current-step protocol. To establish whether the effect of NB on active dynamics was dose-dependent and provide a corresponding dose response curve, the AP properties were examined as a function of NB concentration.

Three different doses of NB were included in the internal solutions:
1. 10mg/ml, as suggested in (Káradóttir and Attwell 2006), reported as a concentration adequate to detect gap junctions between cells,

2. 5mg/ml, or 50% of the initial dose,
3. 1mg/ml, or 10% of the initial dose.

It was necessary to test whether any changes to the AP waveform were due to the *presence* of the NB molecule, or due to the *absence* of $KMeSO_4$, which was reduced in concentration to compensate for the increase in osmolarity that the addition of NB would bring. This test was performed via comparison of measurable electrophysiological features between cells patched with NB-containing solutions and cells patched with Sucrose internal solution. This internal solution had the same reduction of $KMeSO_4$, but with the osmolarity compensated for by the addition of sucrose instead of NB.

Cells aged between P3 and P11 were patched with Standard Internal solution, 10mg/ml NB internal solution, 5mg/ml NB internal solution, and Sucrose internal solution. Cells aged between P9 and P11 were also patched with 1mg/ml NB internal solution. The compositions of all internal solutions were as described in *Methods*.

Finally, gap junction coupling via confocal imaging was investigated across the range of NB concentrations used, with a view to revise the accepted lower-limit of NB necessary for gap junction imaging investigations.

Calculating the junction potential error

As previously mentioned *Methods*, it is necessary to calculate the junction potential error (JPE) prior to performing any analysis on patch-clamp data (Neher 1992, Haas 2015). The JPE is a function of the concentrations, valences and mobilities of the ions contained within the internal solution and the ACSF. Therefore, the addition of NB may have a marked effect on this correction. Unfortunately, no documents or literature containing the ionic valance and mobility for NB were found that could allow calculation of a precise value of its contribution to the JPE. It was assumed that the charge (valence) must be +1 because it is often electroporated into cells using negative voltage pulses, but we recognised that would likely be balanced by the chloride ion of -1, so this was included in the calculations. With regards to the mobility, with no literature to refer to it was concluded that it would be necessary to make a best guess from which a sensible range of JPE values could be established. For each of the concentrations of NB (10mg/ml, 5mg/ml, 1mg/ml and 0mg/ml), the JPE was calculated at mobilities of 0.01, 0.1 and 1, relative to the mobility of K^+. For this range of concentrations and mobilities, the range of JPE calculated was between 5 and 8.9mV. Since is it beyond the

scope of this thesis to calculate the precise mobility of NB, for the sake of this chapter it was decided to maintain consistency with the JPE calculated for the Standard Internal solution and keep it at 8.9mV for all internal solutions, including those containing NB, as has previously been done (Káradóttir and Attwell 2006, Zolnik and Connors 2016).

NB Concentation	Relative mobility	Junction Potential Error (mV)
10mg/ml	0.01	5
10mg/ml	0.1	5.2
10mg/ml	1	7.7
5mg/ml	0.01	6.9
5mg/ml	0.1	7.1
5mg/ml	1	8.3
1mg/ml	0.01	8.5
1mg/ml	0.1	8.6
1mg/ml	1	8.8
0mg/ml	n/a	8.9

Table 6.1: *Calculating the junction potential error for the internal solutions with different concentrations of NB*

Post-experiment data processing

Data processing was done using purpose-built MATLAB scripts that allowed the separate but concurrent analysis of data by both age and internal solution.

6.3 Results

Neurobiotin influences action potential waveform across all observed developmental time points

A significant effect of NB on the spiking properties of cells, was observed: NB appeared to make APs lower-amplitude and longer in duration (**Figure 6.1.A**). Both the width and height of APs were observed to change with the concentration of NB in the internal solution (**Figure 6.1.B** and **6.1.C**). For the 10mg/ml concentration, on average, APs increased in duration by ~4ms ($P=4x10^{-9}$), and decreased in height by ~15mV ($P=4x10^{-7}$). For the 5mg/ml concentration, on average, APs increased in duration by ~2ms ($P=4x10^{-9}$) and decreased in height by ~10mV ($P\leq0.0005$). No difference in AP height or width was found between cells patched with Standard Internal and Sucrose solutions. This confirmed that it is the addition of NB, not the reduction in $KMeSO_4$, that produced a change to both AP height and width across developmental time points. Across all figures in this chapter, waveforms and scatter plots are

colour coded for internal solution: Standard Internal is shown in red, 1mg/ml NB in pink, 5mg/ml NB in green, 10mg/ml NB in blue, and Sucrose in black.
With the mean AP widths and heights observed to change with NB across the full age range investigated (P3-P11), the data set was restricted to the oldest age group (P9-P11) for more stringent quantitative analysis, since it has already been demonstrated (Chapter 3: *Active Dynamics*) that AP waveform changes with postnatal age. The breadth of the age range of P9-P11 was chosen to balance sufficiently large n number with minimal age-related waveform change. For this data, the 1mg/ml NB with Alexa-546 internal solution was included, since it was used in cells aged P9-P11 only.

The waveform of each cell's average first AP was again measured using the same techniques as outlined previously, and AP width against internal solution (**Figure 6.2.C**) and height against internal solution (**Figure 6.2.D**) were analysed. In these age-matched recordings, 5mg/ml and 10mg/ml NB led to increased AP width. Indeed, APs were, on average, ~3 times longer in the presence of 10mg/ml NB. ($P=0.00025$ for 5mg/ml NB and $P=1 \times 10^{-8}$ for 10mg/ml NB). For cells patched with both Sucrose and 1mg/ml NB, there was again no statistically significant difference in mean AP width. For AP height, a statistically significant difference between 10mg/ml NB and Standard Internal was detected ($P=2 \times 10^{-7}$) but no difference was found between Standard Internal and any of the other internal solutions.

It was therefore concluded that the effect of NB on the AP height and width is dose dependent and becomes negligible when the concentration of NB is kept at or below a threshold of 1mg/ml (0.1% w/v). For future electrophysiology and dye filling experiments NB concentrations are recommended to be kept at or below this level

Does Neurobiotin affect the relationship between postnatal age and action potential waveform?

Having established that NB effects AP properties, the amplitude of this effect was investigated across the course of development. If NB was affecting a voltage-gated ion channel, such an effect would be amplified at developmental age points where that ion channel is proportionately more populous. To investigate this, the changing AP properties with postnatal age were observed for cells patched with the range of internal solutions. NB was not expected to affect the relationships between AP waveform and postnatal age, but instead have an approximately equal effect on voltage gated ion channels across the developmental period studied. **Figure 6.3** shows the waveforms of the average AP at four

different developmental timepoints (left), a scatter plot of AP width against postnatal age from P3-P11 (centre) and a scatter plot of AP height against postnatal age from P3-P11 (right), for each of the five internal solutions.

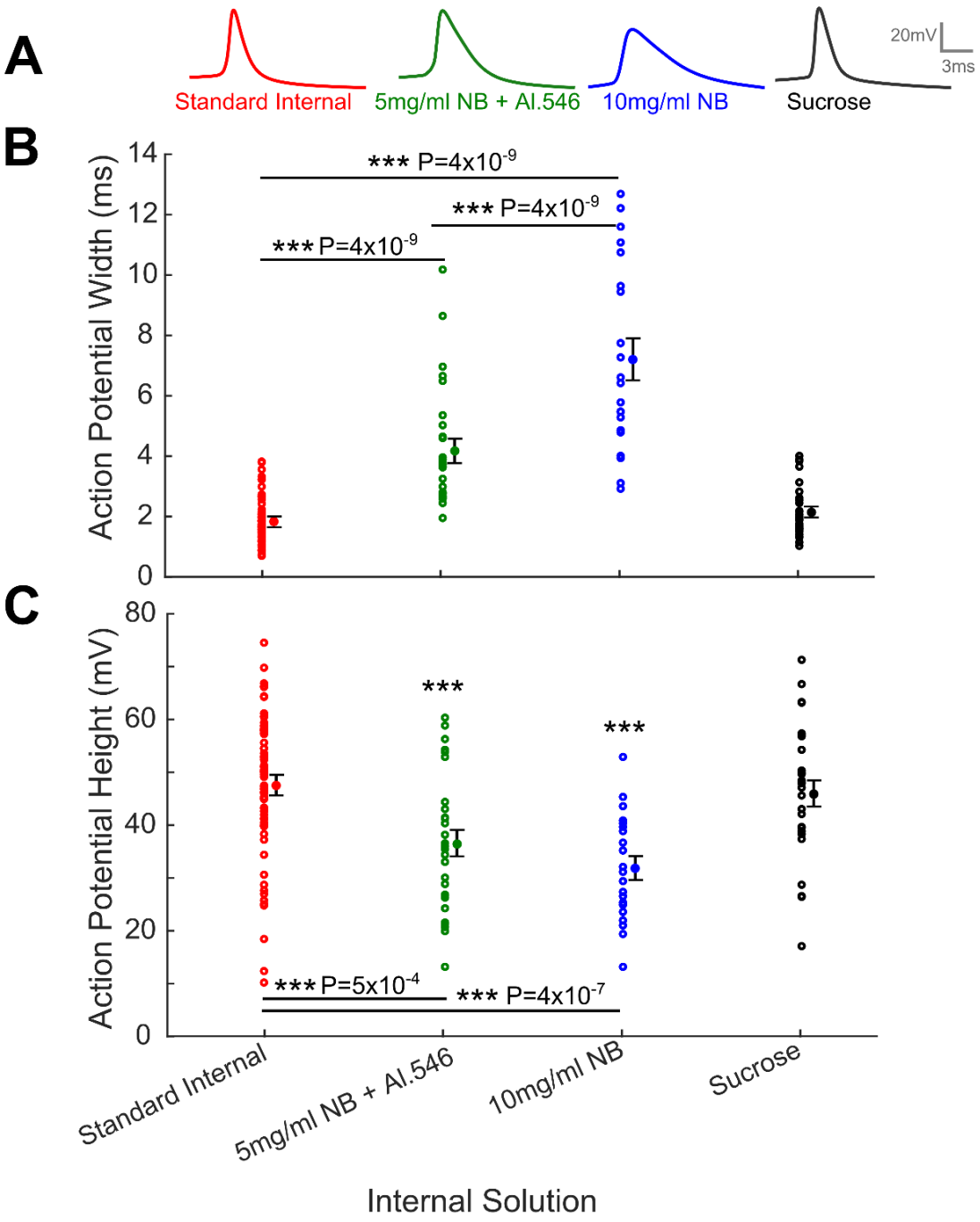

Figure 6.1: Neurobiotin (NB) **appears to affect the action potential** (AP) **waveform, specifically AP height and width, in developing cortical neurons aged between P3 to P11**. **A**: The mean first AP for neurons under the current-step protocol, patched with internal solutions containing different amounts of NB. Time scale from AP threshold to threshold +16ms. Qualitatively, NB appears to decrease the amplitude and increase the duration of the AP. **B**: Mean first AP full width at half maximum for each cell. For each internal solution, the number of cells is as follows: Standard Internal **n=68**, 5mg/ml NB + Al.546 **n=28**, 10mg/ml NB **n=21**, Sucrose **n=29**. Empty circles are individual cell AP widths, solid circles are the mean AP width, and error bars are the standard error in the mean. The AP becomes significantly wider with the application of increasing concentrations of NB. Mean width is significantly different for both NB-containing internal solutions with *** $P=4x10^{-9}$. There is no difference in the means of AP widths between Standard Internal and Sucrose solutions. **C**: Mean first AP height, measured from threshold to AP peak, data populations as above. Cells patched with internal solutions containing NB have lower amplitude APs with ***$P \leq 0.0006$. All data analysed using a one-way ANOVA with Tukey-Kramer test.

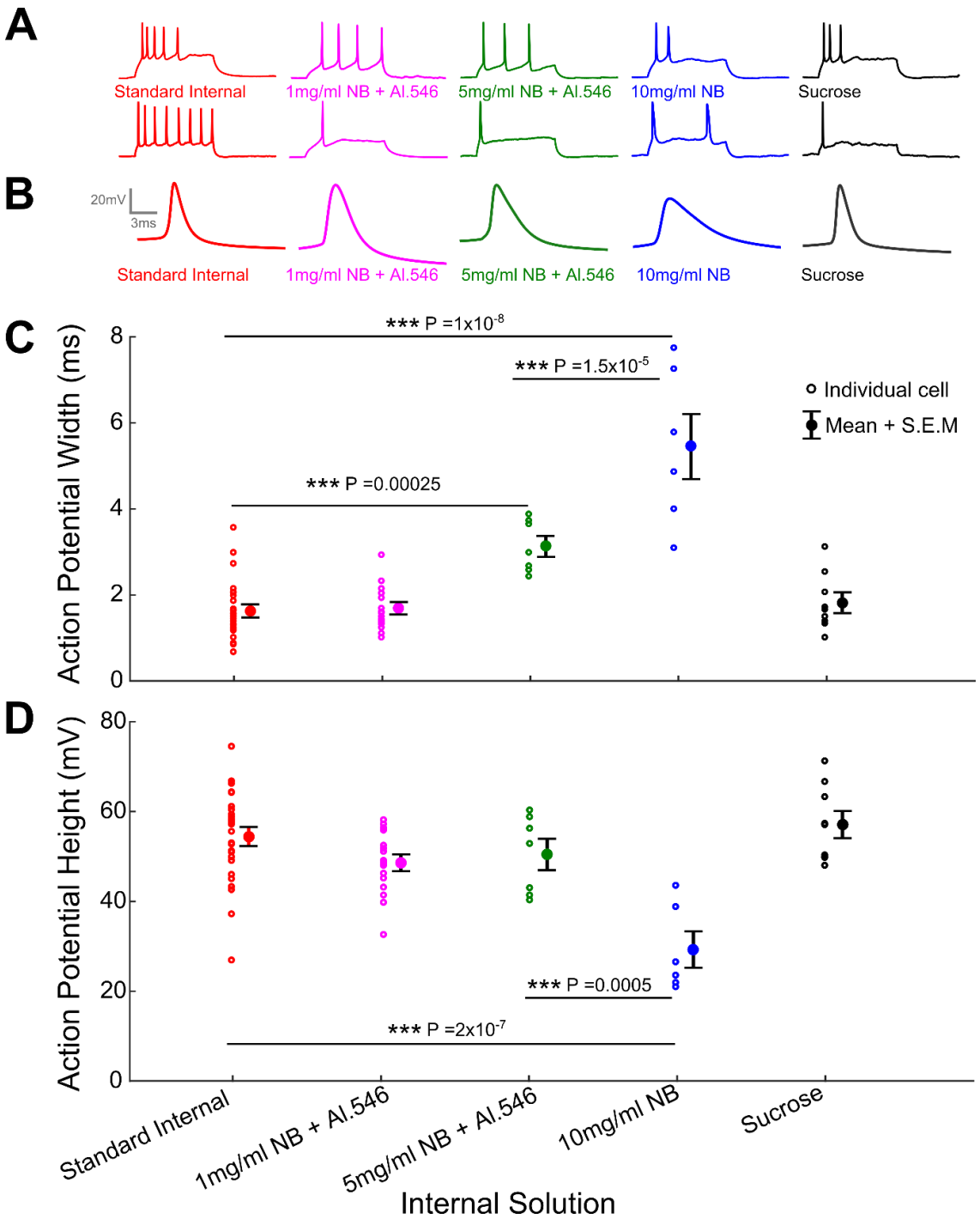

Figure 6.2: Neurobiotin (NB) **has a significant effect on the action potential (AP) width and height in developing cortical neurons aged P9 to P11. This effect is eliminated at concentrations at or below 1mg/ml.** **A**: Representative example traces of AP firing following current injection to the rheobase. **B**: The mean first AP, time scale from threshold to threshold + 16ms. **C:** Mean first AP full width at half maximum. Each empty circle point represents an individual cell; Standard Internal **n=27**, 1mg/ml NB +Al.546 **n=17**, 5mg/ml NB +Al.546 **n= 7**, 10mg/ml NB **n=6**, Sucrose **n=9.** Solid circles with error bars represent the mean and the standard error in the mean. Significant difference in the values of the mean AP for the internal solutions made with the two higher concentrations of NB, with P =0.00025 and $P=1x10^{-8}$, but no significant difference at 1mg/ml NB + Al.546. **D:** Mean first AP height, measured from threshold to AP peak. Data populations as above. Cells patched with internal containing10mg/ml NB have significantly lower amplitude APs with $***P=2x10^{-7}$. All data analysed using a one-way ANOVA with Tukey-Kramer test.

This allowed direct comparison of how NB affected the developmental trajectory of the cortical neuron. A linear fit to each scatterplot was used to test for correlation between width/height and age, and determine any NB-dependent change in slope or intercept. As discussed in Chapter 3: *Active Dynamics*, the linear fit is an approximation; previous postnatal studies have shown that the AP waveform stabilises with maturation (Valiullina, Akhmetshina et al. 2016), meaning that a closer approximation for the relationship would be a sigmoid or exponential function. However, for the age range investigated here, it is a reasonable approximation.

For all internal solutions, a negative slope was returned on the linear fit to postnatal age against AP width, as expected i.e. APs became narrower with age. However, for the internal solutions containing NB, the negative correlations of these variables did not reach significance. This implies that the relationship between age and width weakens with the application of NB, but no significant results can be inferred from the slopes or intercepts of these linear fits.

Internal Solution	Age: AP Width Correlation	Slope	Intercept
Standard Internal	-0.40	-0.12	2.79
1mg/ml NB+Al.546	Does not reach significance	-0.37	5.56
5mg/ml NB+Al.546	Does not reach significance	-0.28	5.77
10mg/ml NB	Does not reach significance	-0.46	9.92
Sucrose	-0.72	-0.20	3.55

***Table 6.2**: Linear relationship between postnatal age and AP width across cells patched with different internal solutions. All data sets except 1mg/ml NB+Al.546 constitute data from cells aged P3-P11. 1mg/ml NB+Al.546 data is from cells aged P9-P11 only.*

For AP height, a statistically significant positive correlation with age was observed for four of the five internal solutions, with only the 10mg/ml NB destroying the correlation.

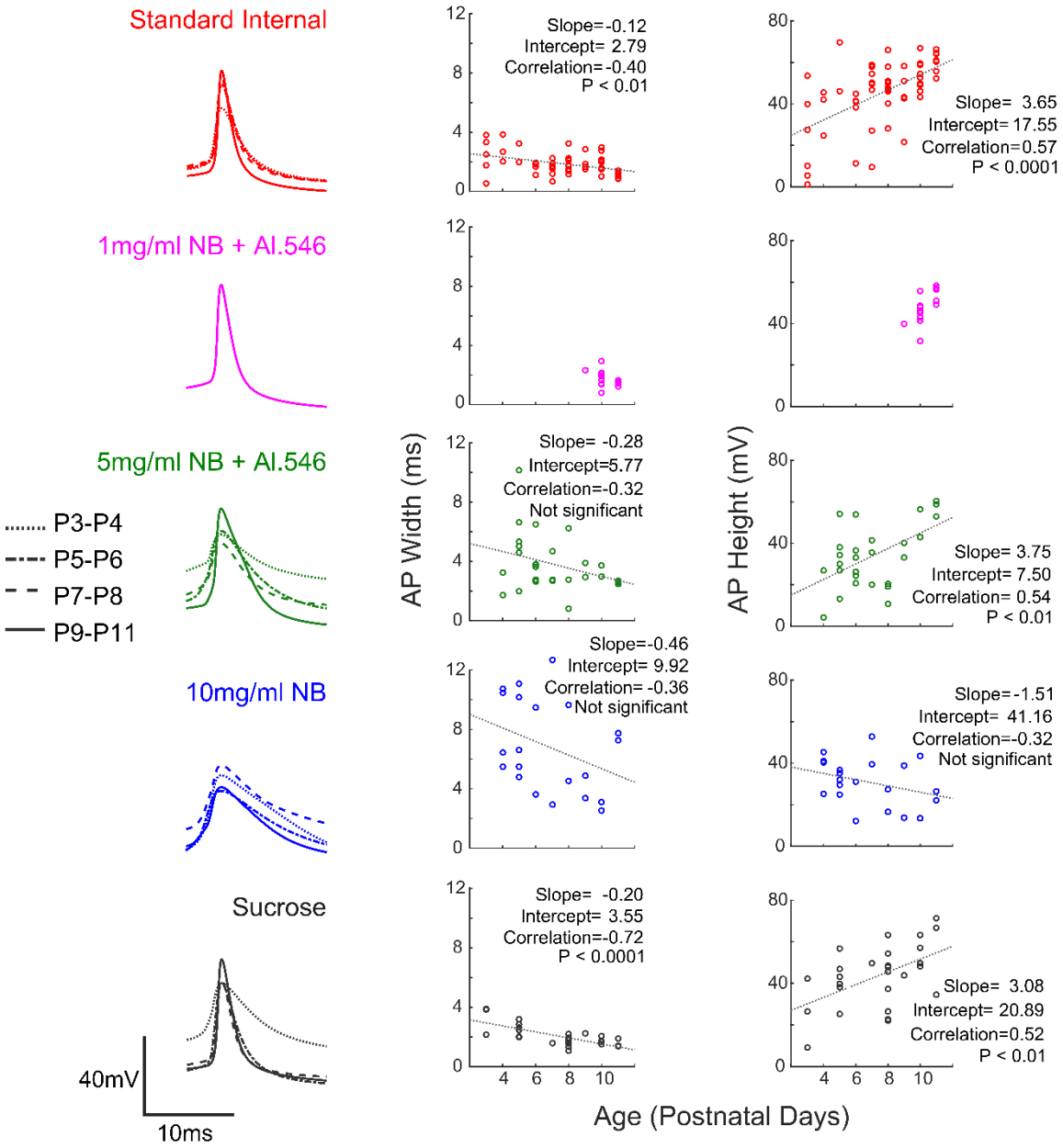

Figure 6.3: Neurobiotin (NB) **affects both height and width of the action potential** (AP) **waveform.** *Left* The mean first AP at four different developmental time-points, P3-P4, P5-P6, P7-P8 and P9-P11 for cells patched with each of the different internal solutions. *Centre* First AP width plotted against age. Empty circles are individual cells. Linear fit plotted as dotted line. Pearson's correlation coefficient finds significant negative correlation for Standard internal and Sucrose datasets, but this correlation breaks down for NB-including internal dataset. *Right* First AP height plotted against age. Data plotting conventions and statistical tests as above. Positive correlation present for all datasets except the highest dose of NB. Intercept of linear fit shifted with the application of 5mg/ml NB, when compared to Standard Internal and Sucrose solution datasets.

Internal Solution	Age: AP Height Correlation	Slope	Intercept
Standard Internal	0.57	3.65	17.55
1mg/ml NB+Al.546	0.67	8.31	-37.44
5mg/ml NB+Al.546	0.54	3.75	7.50
10mg/ml NB	Does not reach significance	-1.51	41.16
Sucrose	0.52	3.08	20.89

Table 6.3*: Linear relationship between postnatal age and AP height across cells patched with different internal solutions. All data sets except 1mg/ml NB+Al.546 constitute data from cells aged P3-P11. 1mg/ml NB+Al.546 data is from cells aged P9-P11 only.*

Together, these data suggest that at high concentrations NB occludes the developmental changes in ion channel expression that lead to the appearance of narrower and taller action potentials.

The first derivative of membrane potential with time illuminates the effect of Neurobiotin further

The subtler measurement of the change in the first derivative of membrane potential (voltage) with time during spiking behaviour (dV/dt) was then investigated (**Figure 6.4.A)**. As described in Chapter 3: *Active Dynamics*, dV/dt reaches its peak at the steepest part of the rising section of the AP; this point is also known as the maximum rate of rise. dV/dt reaches its minimum at the steepest part of the falling section of the AP, the point also known as the maximum rate of fall. Plotting Vm against dV/dt produces a circular plot, as the first derivative rises to its zenith where the AP is steepest before returning to zero at the point of inflection: the apex of the spike, before finally going through a negative phase that follows the downwards slope of the AP.

Phase plots of the mean APs of cells aged P9-P11 (**Figure 6.4.B)** allowed the changes to the first derivative of the membrane potential with time to be compared across internal solutions. Each phase plot, overlaid with the corresponding mean phase plot from cells patched with Standard Internal, was examined for evidence of how NB might affect the dynamics of the voltage-gated ion channels. Via comparison, Sucrose internal solution was found to have no effect on the phase plot and overlap with the Standard Internal phase plot perfectly. The phase plot from 1mg/ml NB showed that the rate of rise reached its peak at a slightly lower membrane potential, but otherwise the dynamics are nearly identical. At higher concentrations

of NB, both the rising and falling phase are significantly affected, but the rate of fall was particularly impacted, being completely flattened at 10mg/ml NB.

Interesting dynamics in the initial section of the phase plot from each NB-including dataset (**Figure 6.4.B**, inset) were observed, with NB appearing to produce a 'shoulder' in the phase plot that increased in length (membrane potential) in a dose-dependent manner, indicating that the rate of rise remains constant for an initial, brief part of the rising portion. This shoulder is apparent even at 1mg/ml NB, becoming particularly pronounced at the higher concentrations.

The effect of NB on the first derivative of membrane potential with time was examined across the range of postnatal ages studied. The maximum and minimum values of dV/dt were each plotted against postnatal age and the resulting relationship was examined via a linear fit (**Figure 6.4.C**). As with the relationship between AP height/AP width and age (*Chapter 3: Active Dynamics*), the linear fit represented an approximation to the changing dynamics, as the relationship would be expected to be sigmoidal over the entire trajectory of development.

For Max AP dV/dt, a positive correlation was found - i.e. the rising part of the AP becomes steeper with age - for all internals except the highest dose of NB, where the correlation broke down and did not reach significance. This result implies that high doses (10mg/ml) of NB destroy the correlation between rising phase and postnatal age.

Internal Solution	Age: Max AP dV/dt Correlation	Slope	Intercept
Standard Internal	0.58	13.41	-5.86
1mg/ml NB+Al.546	0.72	54.41	-447.94
5mg/ml NB+Al.546	0.66	12.24	-38.88
10mg/ml NB	Does not reach significance	-0.78	34.96
Sucrose	0.63	14.54	-21.78

***Table 6.4**: Linear relationship between postnatal age and AP maximum dV/dt (rate of rise) across cells patched with different internal solutions. All data sets except 1mg/ml NB+Al.546 constitute data from cells aged P3-P11. 1mg/ml NB+Al.546 data is from cells aged P9-P11 only.*

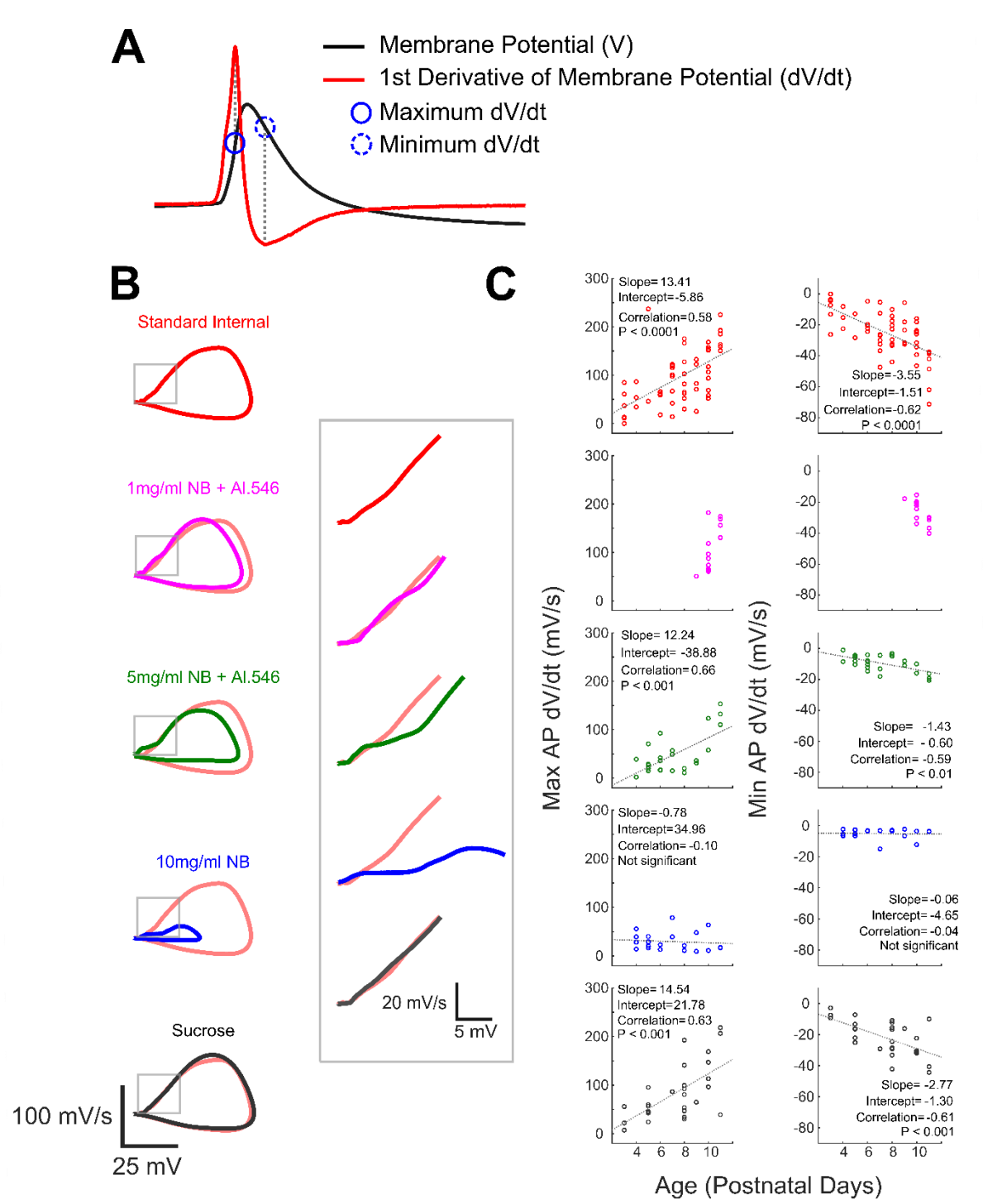

Figure 6.4: The first derivative of membrane potential with time illuminates the effects of Neurobiotin (NB) **on the active dynamics. A:** Representative action potential (AP) (black line) with its corresponding first derivative with time, dV/dt (red line). The maximum rate of rise, Max AP dV/dt, occurs at the steepest point of the rising part of the AP. The maximum rate of fall, Min AP dV/dt, occurs at the steepest point of the falling part of the AP. **B**: Phase plots of the mean AP from cells aged P9-P11 patched with each internal solution. Pale red line represents the phase plot from Standard Internal. Both the rising and falling parts of the AP are affected by the application of NB, but some interesting dynamics occur at the start of the phase plot (inset). **C**: The max rate of rise and rate of fall plotted against age for each internal solution. Each circle represents an individual cell. Correlation assessed using Pearson's correlation coefficient. NB appears to diminish the correlation.

For Min AP dV/dt, the correlation was negative, i.e. the falling part of the AP became steeper with age, again for all internals except 10mg/ml NB, where the correlation did not reach significance: the correlation between falling phase and age was destroyed by high doses of NB.

Internal Solution	Age: Min AP dV/dt Correlation	Slope	Intercept
Standard Internal	-0.62	-3.55	1.51
1mg/ml NB+Al.546	-0.73	-9.10	66.98
5mg/ml NB+Al.546	-0.59	-1.43	0.60
10mg/ml NB	Does not reach significance	-0.06	-4.65
Sucrose	-0.61	-2.77	-1.30

Table 6.5*: Linear relationship between postnatal age and AP minimum dV/dt (rate of fall) across cells patched with different internal solutions. All data sets except 1mg/ml NB+Al.546 constitute data from cells aged P3-P11. 1mg/ml NB+Al.546 data is from cells aged P9-P11 only.*

The relationship between Max AP dV/dt (rate of rise) and the magnitude of Min AP dV/dt (rate of fall) was then investigated for the effect of NB (**Figure 6.5)**. By definition, this relationship was expected to go through the origin, since when the steepest part of the upward slope is equal to zero, the downwards slope must be the same, i.e. there is no slope. Such a relationship was also expected to be linear - that APs that are steeper on the way up will generally be steeper on the way down also; a linear relationship was plotted, simplified to $y=mx$ since, in this case, $c=0$. However, the slope of this relationship and its variation with the inclusion of NB was of interest: the ratio of these two values could indicate whether the rising component or falling component of the average AP dominated its shape. Such a result can be used to infer whether NB primarily affects the Na^+ channels or the K^+ channels (Hodgkin and Huxley 1952). Max AP dV/dt is associated with the population of Na^+ ion channels, as they are generally understood to be responsible for the rising phase of the AP (Bahrey and Moody 2002, Baranauskas 2007). Accordingly, Min AP dV/dt is associated with the population of K^+ channels as they are generally held to be responsible for the falling phase of the AP (Niday, Hawkins et al. 2017, Vivekananda, Novak et al. 2017).

Across the full age range of P3-P11 (**Figure 6.5.A**) NB was found to affect the slope, as assessed via Pearson's correlation coefficient. For cells patched with Standard Internal,

1mg/ml NB or Sucrose, the slope was consistent at ~0.24 (dimensionless units). With the application of higher doses of NB - 5mg/ml and 10mg/ml - the slope became 0.16, which indicated that the rising phase of the AP was steeper than the falling phase, seemingly following normal developmental patterns, whilst the falling phase was affected. Since the rising phase of the AP has been associated with sodium channels This result implies that potassium channels are disproportionally affected by the application of NB.

Examining the same relationships in the age range P9-P11 (**Figure 6.5.B**) a decrease in slope with higher doses of NB is again observed (**Table 6.6**).

Internal Solution	Max AP dV/dt: Min AP dV/dt Correlation (P9-P11)	Slope	Intercept
Standard Internal	0.83	**0.26**	0
1mg/ml NB+Al.546	0.86	**0.23**	0
5mg/ml NB+Al.546	0.97	**0.14**	0
10mg/ml NB	0.96	**0.18**	0
Sucrose	0.97	**0.21**	0

***Table 6.6**: Linear fit to the ratio of Max AP dV/dt to Min AP dV/dt (rate of rise : rate of fall) across cells patched with different internal solutions at P9-P11.The slope decreases at higher doses of NB.*

These examinations of the first derivative of the AP waveform with time allow for better understanding of the way that NB affects cell dynamics. Although the ‘shoulder’ present within the phase plots indicates some specific effects on the activation of some sodium channels responsible for the rise of the AP, the steepness of the AP waveform in the rising phase with higher doses of NB indicates that NB primarily has a detrimental effect on potassium channels, dulling the dynamics responsible for the falling phase of the AP.

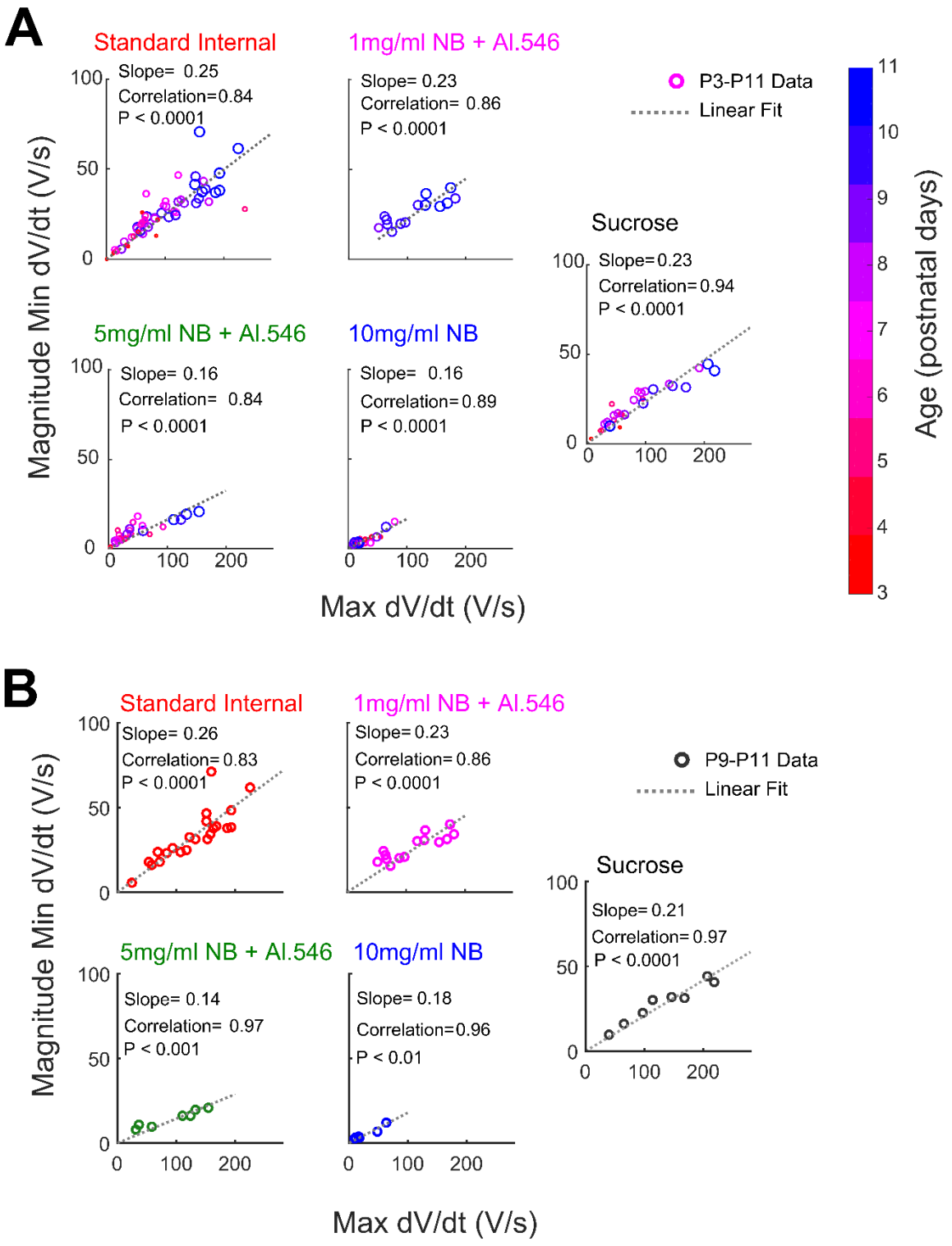

Figure 6.5: Ratio of Max dV/dt (rate of rise) **to magnitude of Min dV/dt** (rate of fall) **across internal solutions.** **A**: Data between ages P3 and P11. Small red circles = P3, large blue circles= P11. By definition, a linear fit goes through the origin. Slope represents the balance of rate of rise and rate of fall: shallow slope indicates that the rate of rise dominates, whereas a steep slope indicates the rate of fall dominates. Correlation analysed using Pearson's correlation coefficient. Data show no real decrease in correlation with the addition of Neurobiotin (NB), but a decrease in slope, indicating that NB primarily affects the rate of fall, or the downslope of the AP. **B:** Data between ages P9 and P11, showing that it is the addition of NB and not a difference in age that causes the change in Max dV/dt: Min dV/dt ratio. Again, with the application of NB, the balance is shifted towards Max dV/dt, symptomatic of an effect primarily on the downslope of the AP.

Membrane potential as a function of time under the influence of Neurobiotin

The effect of NB on the membrane potential of the neuron (Vm), prior to any injection of current aside from the holding current (HC) was examined. Should NB have any effect on Vm, we might expect such an effect to increase over the course of the experimental protocol, as NB diffuses through the cellular cytoplasm and interacts on a molecular level with the voltage-gated ion channels (Mills and Sey 1998). Vm prior to current injection was therefore measured for each cell longitudinally across the course of the current-step experimental protocol, a period of typical duration 110-220s. Logically, if an effect of NB on Vm was present, however subtle, it would be expected to become more pronounced as NB diffuses out of the pipette and into the cell where it can interact with the cellular membrane. Therefore, a recurrent Vm gradient over time may indicate a NB-based effect.

For each cell, the average value of Vm found by taking the mean membrane potential in the first 100ms before the current-step injection. This value was averaged across cells of the same age and plotted against the time course of the experiment (1 cycle of 11 current injections =11 seconds, typically cycles were repeated 10-20 times, so the entire current-step protocol = 110-220 seconds). Average Vm traces were aligned to allow for clear comparison of the gradients (**Figure 6.6**). Any effect of NB on the resting membrane potential would be observed in a gradient of the membrane potential over cycle number, corresponding to a time-dependent effect on the cell membrane properties, and such an effect would be expected to be replicated across all ages measured. No consistent gradient in the membrane potential / experimental time course plot was observed; Vm remained relatively steady throughout current-step protocol experiments for all patched cells, regardless of internal solution or age (**Figure 5.7**). However, a weakness in this analysis is that we did not define significance in the gradient *a priori*. In any future work, these results could be used to define a sensible range of gradients, against which statistically significant variations could be compared. This analysis also suffers from only considering the period of the current-step protocol, which generally did not extend much beyond 3 minutes. It is possible that the effects of NB only become apparent after longer time-scales.

With these caveats, no evidence was found that NB has any effect on Vm prior to the active dynamics triggered by current injection. This supports the hypothesis that NB affects the voltage-gated ion channel dynamics, and not the intrinsic properties of the developing cortical neuron.

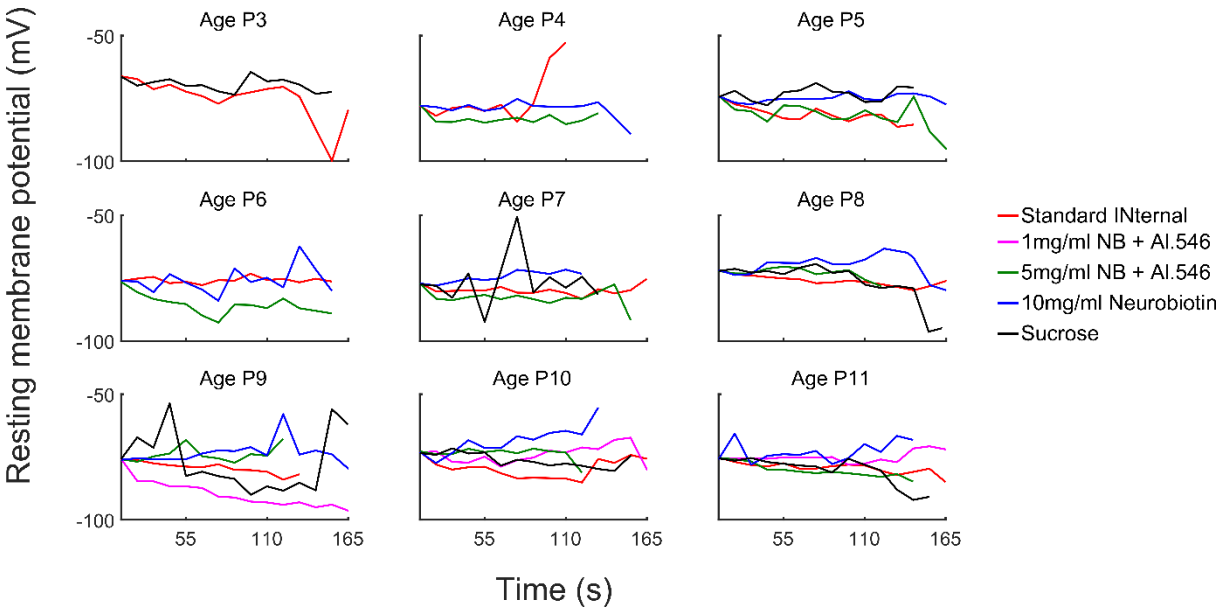

Figure 6.6: The diffusive effect of Neurobiotin on the resting membrane potential over the course of the current-step protocol. A: Mean Vm over the time course of the current step protocol experiment for cells patched at all ages using the internal solutions with different concentrations of NB. Data are aligned at the start for ease of gradient comparison.

The influence of Neurobiotin on pre-active-dynamics variables

Properties of the cell that can be described as 'intrinsic' but are closely related to the active dynamics responsible for the changing AP waveform were then examined, namely the AP threshold, and the two measures of the input resistance: the steady state resistance (Rss) and the extrapolated resistance (Rxtr). These values were obtained via methods described in Chapter 3: *Active Dynamics*; briefly, The AP threshold was defined by a dV/dt of 10.5mV/s where the subsequent membrane potential reached a minimum value of -35mV. The input resistance was found from the first 'step' in the current-step protocol. This step involved the injection of a current of -16pA that hyperpolarised the cell, producing a hyperpolarised voltage trace, the deviation of which was related to the input resistance via simple application of Ohm's law ($V=IR$). The steady state resistance was calculated as the minimum of the trace, divided by the magnitude of the current injection, whereas the extrapolated input resistance was calculated via a voltage calculated from the extrapolated minimum of the fitted exponential decay curve. The data was averaged across the repeat cycles (typically 10-12 cycles in a current-step protocol), separately for each of the two measures.

Changes in AP threshold with age were examined for each internal solution data set (**Figure 6.7.A**). Each data set was analysed for correlation via a linear fit evaluated with Pearson's correlation coefficient, but no significant correlations were found. Therefore, no evidence for age-dependence of AP threshold for cells patched with any internal was found. The AP

threshold in cells aged P9-P11 across the five internal solutions was also analysed (**Figure 6.7.B**). As before, a one-way ANOVA was applied to check for variance between internal-groups, but no evidence was found for any change to the AP threshold with the application of NB.

Average hyperpolarised membrane potentials for cells patched with each internal solution were qualitatively examined across three grouped age ranges: P3-P5, P6-P8 and P9-P11 (**Figure 6.7.C)**. A general trend, across internal solutions, for the magnitude of the hyperpolarisation to decrease with age was observed. Although variation between the internal-solution groups was seen, no internal solution-dependent pattern to this variation was observed; cell to cell variationf appeared to be greater than any variation due to the application of NB. Therefore, no conclusions can be drawn on the effect of NB on voltage-gated ion channel dynamics triggered by a hyperpolarising current injection.

Analysis of input resistance revealed an apparent increase in input resistance with NB for both the steady state and extrapolated measures on cells aged between P9 and P11 (**Figure 6.7.D**, *left column*). Since it was not clear whether the data were normally distributed, and the statistical tests used were done so under the assumption of a normal distribution, an Anderson-Darling test was applied to each data set prior to further statistical analysis. In each case, the null hypothesis of a normal distribution was returned. Via the application of a one-way ANOVA and a Tukey-Kramer test a significant difference in the mean was detected between Standard Internal solution and 10mg/ml NB internal solution (steady state input resistance, P=0.0011; extrapolated input resistance P=0.0009).

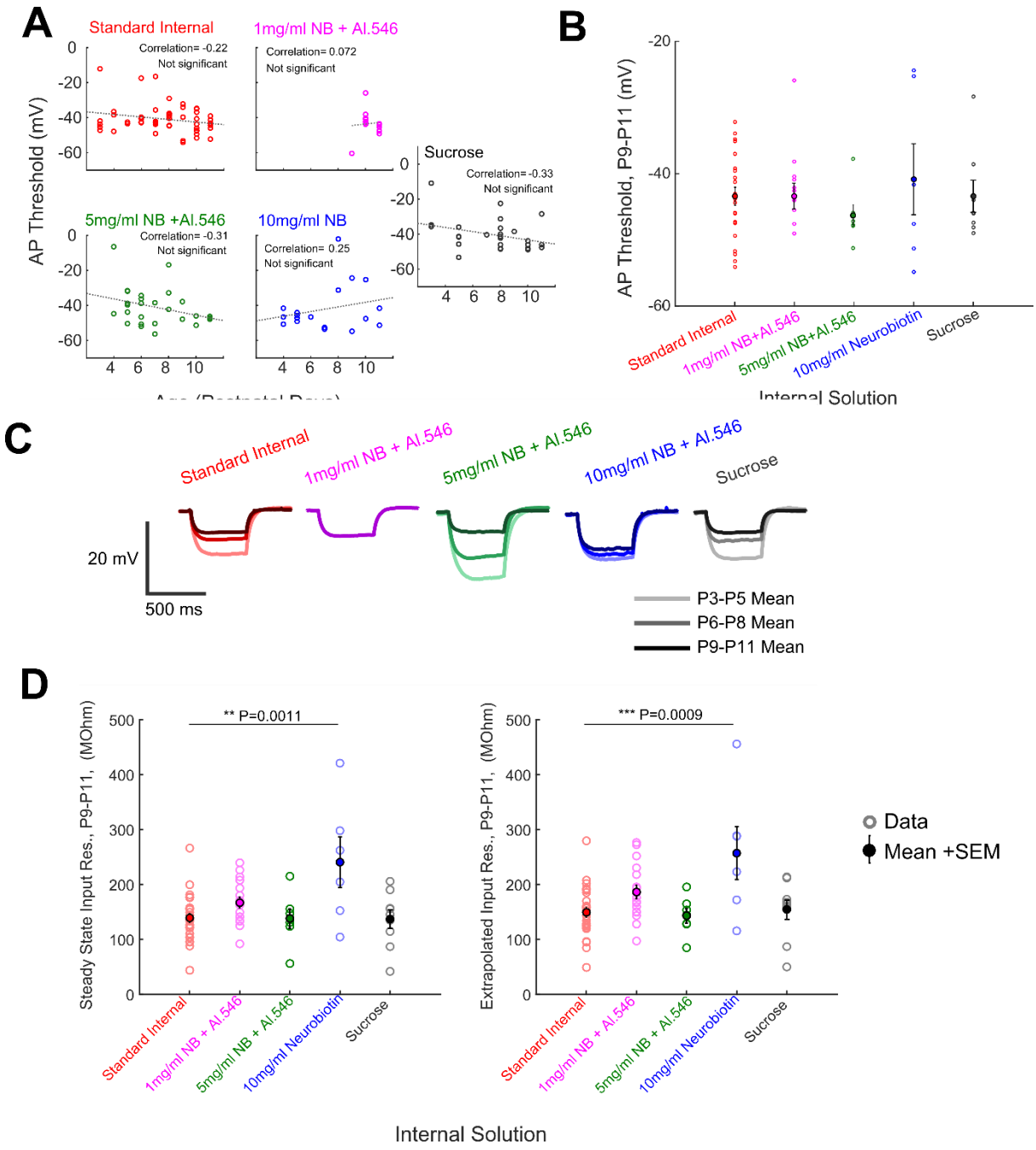

Figure 6.7: Neurobiotin (NB) **has no observable effect on AP threshold or magnitude of hyperpolarised membrane potential response. An effect on input resistance observed at high dose. A**: No significant correlation between AP threshold and age is detected for any of the internal solution groups (Pearson's correlation coefficient). **B:** The AP threshold of P9-P11 cells patched with each internal solution. Empty circles represent cells, filled circles with error bars represent the mean with the standard error in the mean. A one-way ANOVA is performed and finds no significant difference between groups. **C**: The hyperpolarised membrane potential changes robustly with age, but no particular dose-dependent change with NB is detected. **D**: Input resistance of P9-P11 cells against internal solution, analysed with a one-way ANOVA and Tukey-Kramer test on the null hypothesis that the mean input resistance is the same across groups. Data tested for normal distribution by Anderson-Darling test. A significant difference is detected between Standard Internal and 10mg/ml NB.

The effect of Neurobiotin on passive dynamics

Should NB only act on the voltage-gated ion channels, no change to any of the passive dynamics parameters would be expected to be observed with the inclusion of NB in the internal solution. This is particularly important for the validity of the gap junction studies presented in Chapter 5: *Gap Junctions and Morphology*, as any influence of NB on the passive dynamics would invalidate these results. Data from cells patched with Standard Internal, 5mg/ml NB, 10mg/ml NB, and Sucrose were examined for passive dynamics across the age range P3-P11 (**Figure 6.8**). For all four of the parameters garnered from the coefficients of a two-exponential fit, $Alpha_1$, $Alpha_2$, tau_1 and tau_2, no variation was found across the range of internal solutions. A one-way ANOVA was performed but no statistically significant difference was detected.

Passive dynamics data from ages P9 to P11 only was then examined to eliminate any age-dependent effects when comparing internal solutions, including internal solution made with 1mg/ml NB (**Figure 6.9**). Mean passive dynamics traces from all five internal solution data sets, averaged over cells between P9 and P11, were plotted, with the average P9-P11 trace from Standard Internal solution plotted underneath each subsequent trace for comparison (**Figure 6.9.A**). Variations in traces with internal solution were visible but no trend with increasing NB dose was found; it can therefore be presumed that this is due to variations unrelated to NB. The parameters drawn from the two-exponential fit were examined, but again no statistically significant evidence for any change in the passive dynamics with the application of NB was found.

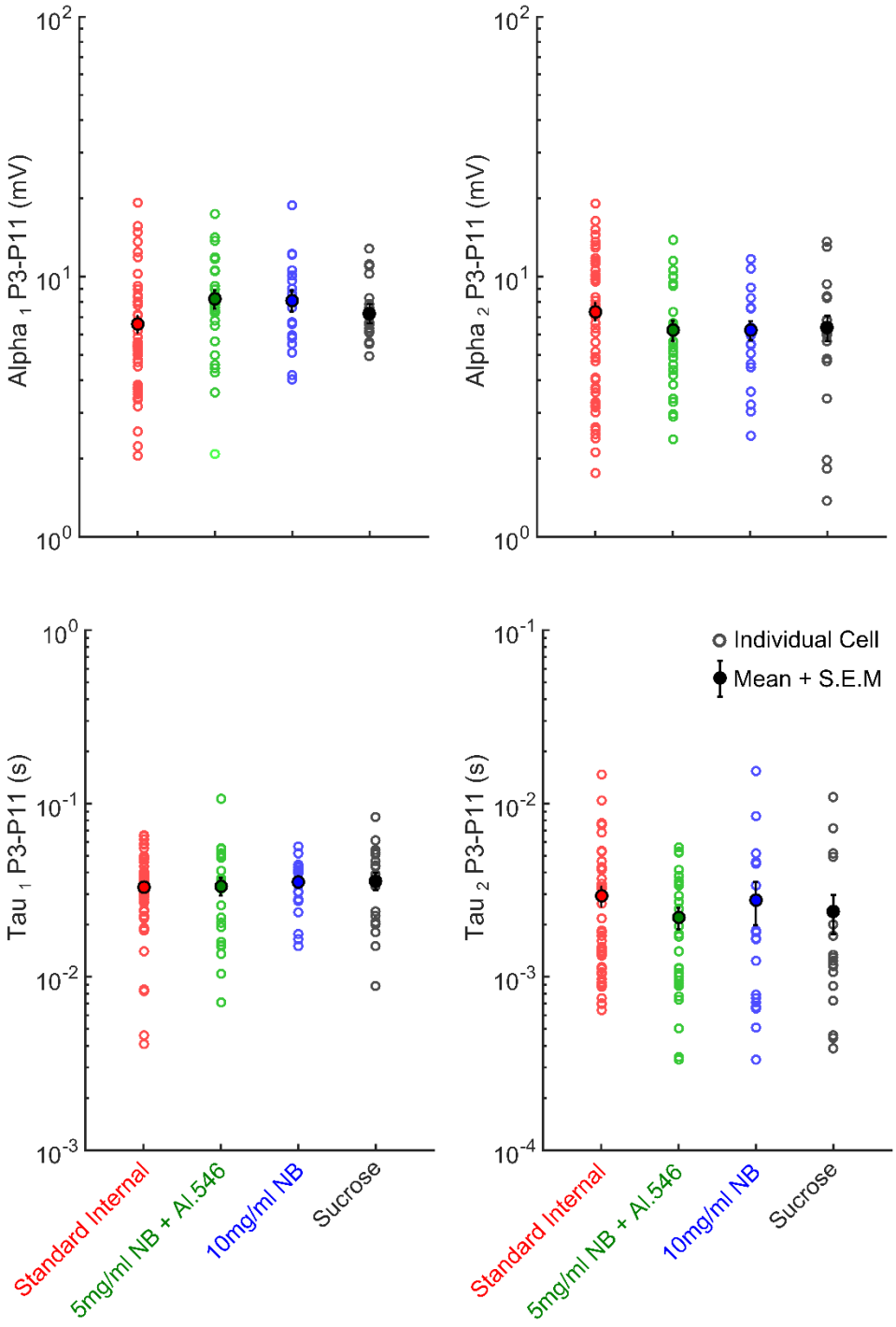

Figure 6.8: Neurobiotin has no significant effect on any of the coefficients of passive dynamics decay between ages P3-P11 for any of the internal solutions tested across this age range. Top left: *Alpha*$_1$, first voltage coefficient of two compartment exponential voltage decay from cells aged P3 to P11, plotted against all five different internal solutions. Empty circles are individual cells and filled circles with error bards are the mean and standard error in the mean. Y axis is plotted in logarithmic scale. Top right: *Alpha*$_2$, the second voltage coefficient of exponential decay. Bottom left: *tau*$_1$, first time coefficient of exponential decay. Bottom right: *tau*$_2$, second time coefficient of exponential decay. All four coefficients were assessed with a one-way ANOVA and Tukey-Kramer test of significance.

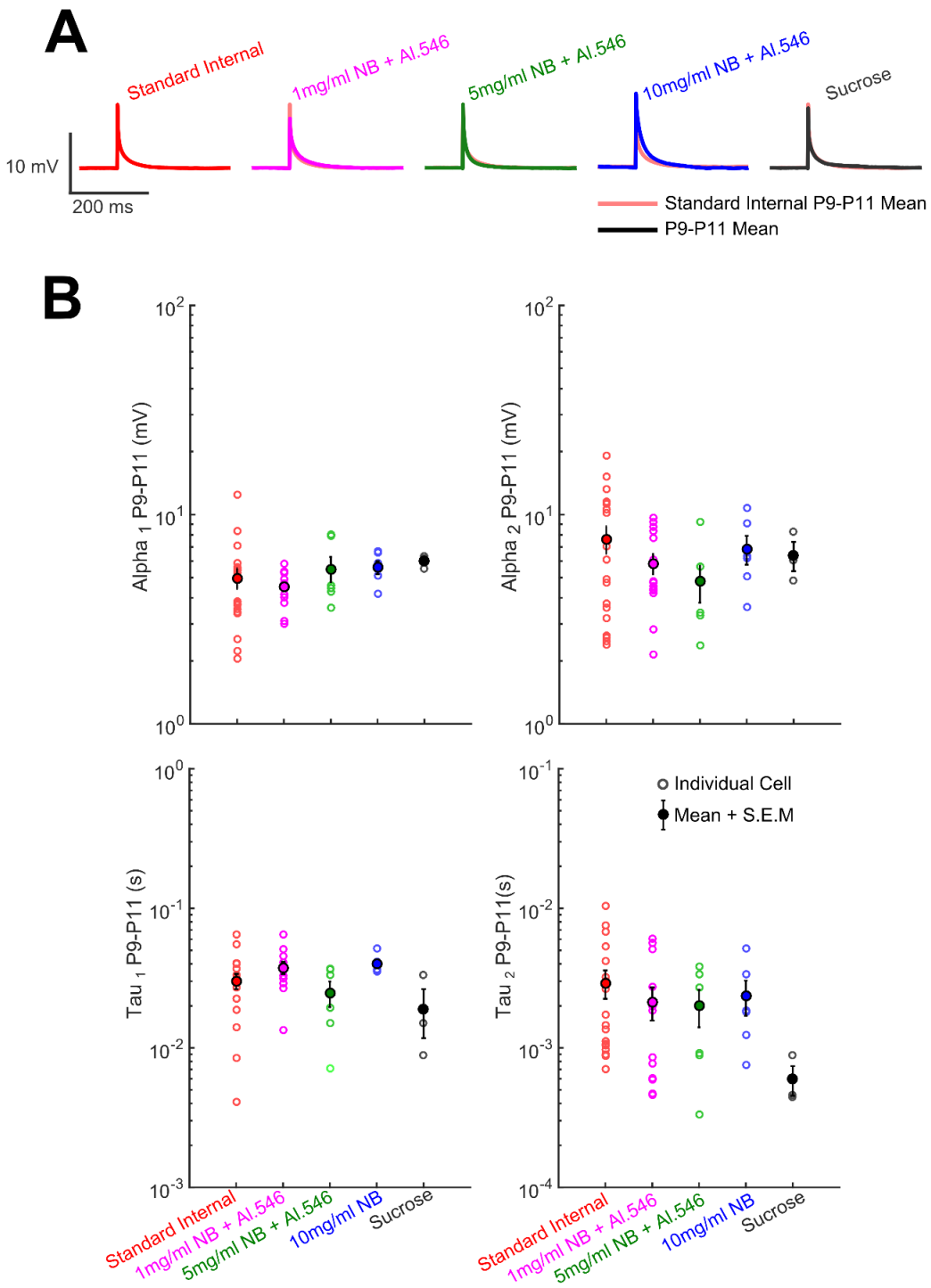

Figure 6.9: Neurobiotin does not appear to have any significant effect on any of the coefficients of passive dynamics decay between ages P9-P11. **A**: Mean passive dynamics traces from cells aged P9-P11, patched with different internals overlaid on top of the mean trace from cells patched with Standard Internal. **B:** Top left: *Alpha*$_1$, first voltage coefficient of two compartment exponential voltage decay from cells aged P9 to P11, plotted against all five different internal solutions. Empty circles are individual cells and filled circles with error bars are the mean with standard error in the mean. Y axis is plotted in logarithmic scale. Top right: *Alpha*$_2$, the second voltage coefficient of exponential decay. Bottom left: *tau*$_1$, first time coefficient of exponential decay. Bottom right: *tau*$_2$, second time coefficient of exponential decay. All four coefficients were assessed with a one-way ANOVA and Tukey-Kramer test of significance.

Imaging cells patched with different concentrations of Neurobiotin

Previous studies (Káradóttir and Attwell 2006) have suggested that to reliably ensure illumination of gap-junction-coupled cells (GJCC), a minimum concentration of 5-10mg/ml NB is needed, the implication being that gap junction coupling cannot be observed at lower doses. After cells had been patched and filled, slices were prepared and imaged using a confocal microscope as described in Chapter 5: *Gap junctions and Morphology*. It was expected that the proportion of cortical slices containing evidence of gap junction coupling would differ between high and low concentrations of NB: that a higher dose of NB would mean more robust gap-junction detection, and that GJCC would not be visible at lower concentrations. However, GJCC were detected in slices patched with the full range of NB concentrations (**Figure 6.10**).

The subtler question of whether a decrease in NB leads to a proportional decrease in the number of observations of gap junction coupling was then addressed. Confocal images of acute slices were categorised as either 'Visible GJCC', 'No Visible GJCC', or 'Ambiguous', i.e. it could not be stated with any certainty whether GJCC were present or not. No evidence was found for a decrease in GJCC detection with a decrease in NB; approximately half of all slices imaged via confocal microscopy were found to have GJCC, regardless of whether those cells were patched with 10mg/ml, 5mg/ml or 1mg/ml NB (**Table 6.7, Figure 6.11**). These data were further examined using Fisher's Exact Test, finding no significant difference between the number of GJCC in each dosage-group (minimum P=0.35). Together, these results imply that a NB concentration of 1mg/ml, 0.1% w/v was sufficient to discern whether a patched neuron has gap junctions, without adverse effect.

Internal Solution	Slices with visible GJCC	Slices with no Visible GJC	Ambiguous slices	Proportion of total slices with GJCC
1mg/ml NB+Al.546	5	6	1	0.4167
5mg/ml NB+Al.546	15	8	3	0.5769
10mg/ml NB	2	3	0	0.4000

***Table 6.7**: Confocal imaging of cells patched with different concentrations of NB showed that GJCC were visible in 40-56% of slices regardless of NB dose.*

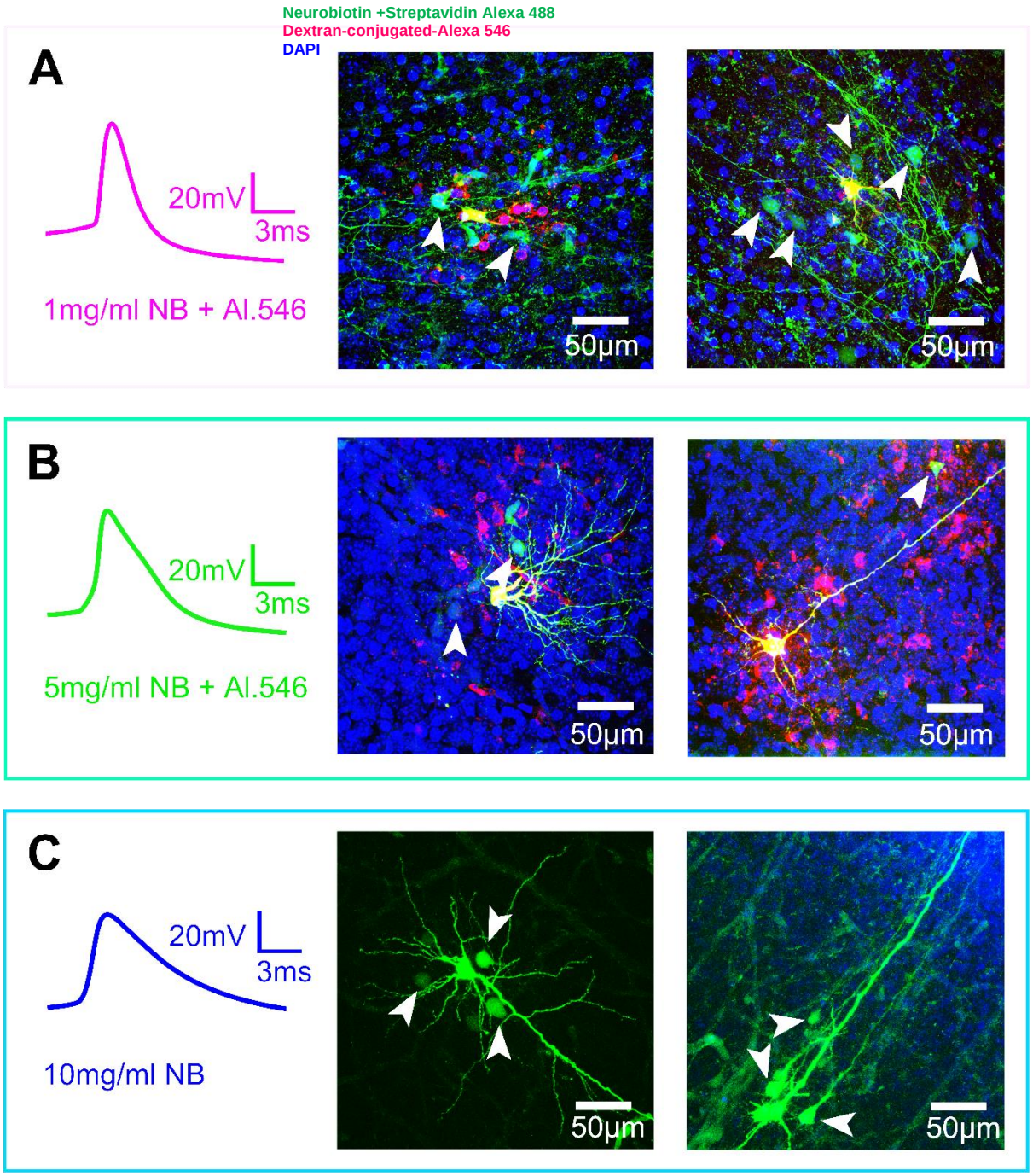

Figure 6.10: Neurobiotin allows the detection of gap-junction coupled cells, even at low concentrations. **A:** Left, the mean AP waveform of cells aged P9-P11 patched with internal solution containing 1mg/ml NB with Alexa546, right, representative confocal images of cells patched with this concentration of NB. White arrows point to gap junction coupled cells. **B:** As above, but with internal solution containing 5mg/ml NB with Alexa546. Gap junction coupled cells are slightly brighter against background signal. **C:** As above, but with internal solution containing 10mg/ml NB. Gap-junction-coupled cells are noticeably brighter, but the AP has become lower amplitude and longer duration.

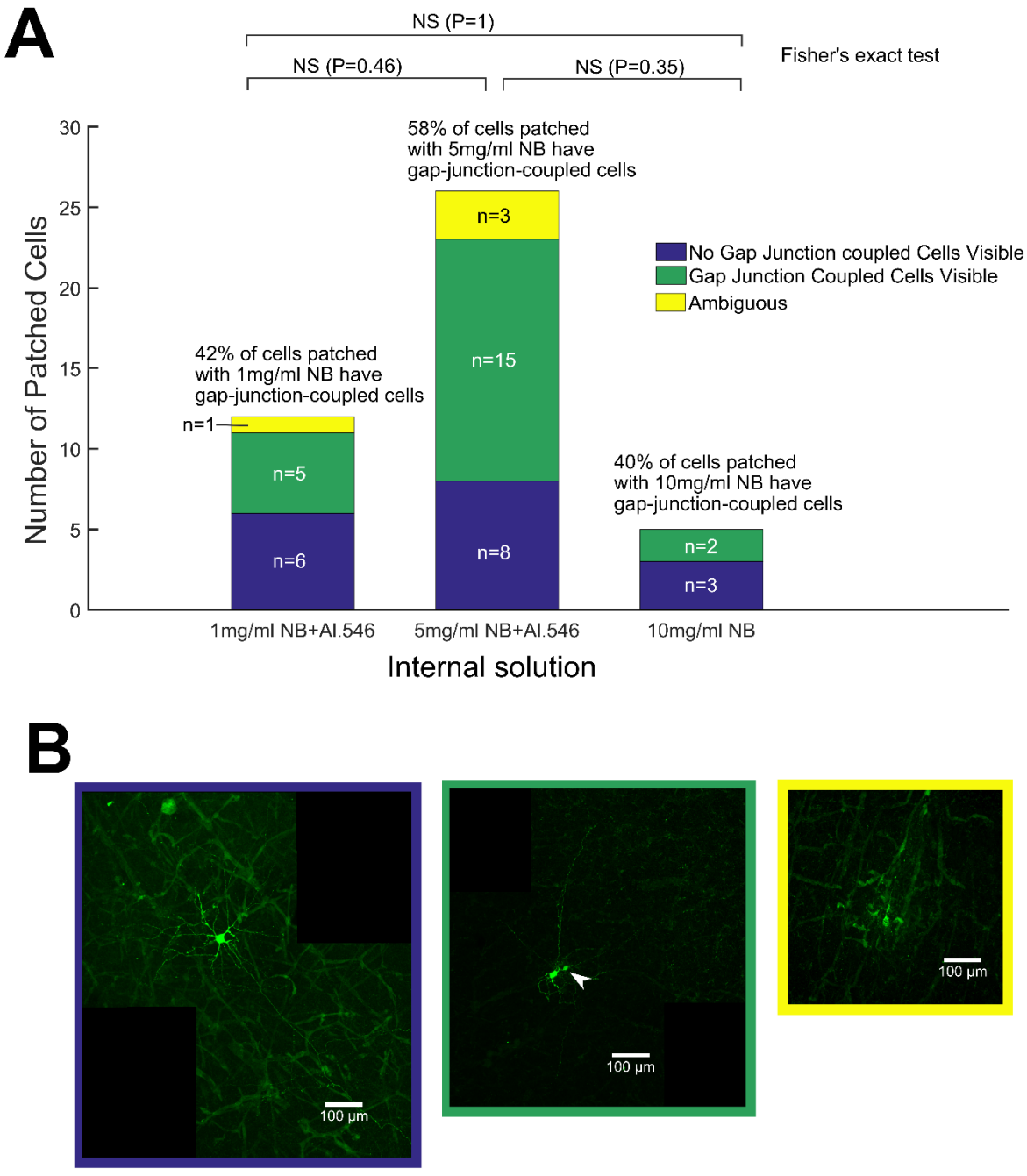

Figure 6.11: The concentration of Neurobiotin used does not appear to affect the rate of gap junction detection. **A:** The number of patched cells exhibiting gap junction coupling for each of the three NB concentrations; 1mg/ml, 5mg/ml and 10mg/ml. For each of the three concentrations, approximately half of the patched cells were accompanied by gap-junction-coupled cells. Cells were labelled as 'ambiguous' if it was unclear if gap-junction coupling of neurons had occurred, for example, when the soma of the patched cell was removed with the patch pipette, meaning the primary cell couldn't be identified, or when removal of the patch pipette resulted in leakage of some NB. No difference in the proportions of GJCC was observed between internal solution concentration groups (Fisher's exact test, P=0.46, P=1, P=0.35). **B:** Representative examples of confocal images exhibiting (L-R) no visible gap junction coupled cells, visible gap junction coupled cells (white arrow), and ambiguous gap junction coupling.

6.4 Discussion

Neurobiotin affects active dynamics

Neurobiotin is a useful tool for investigation of the morphology of cortical neurons. In particular, its relatively small size, having a molecular weight of just 322.8g/Mol, gives it the unusual ability to traverse intercellular gap junctions and illuminate secondary GJCC (Penn, Wong et al. 1994). However, as has been demonstrated in this chapter, NB is not an innocent, inert molecule. The effects of NB on AP waveform, in particular AP width, are striking, as well as consistent over the age ranges investigated. Measurement of the effects of NB within a restricted age group of P9 to P11 cells returned statistically significant effects on both the height and width of the AP.

Analysis of the first derivative of membrane potential with time demonstrated that NB affects the voltage-gated ion channel dynamics responsible for both the rise and fall of the AP, with a larger effect on the falling section. These results are indicative of a major effect on K^+ voltage-gated ion channels, slowing the repolarisation of the action potential. These results were particularly apparent in the latter stages of the period studied; NB appears to suspend the AP waveform in their immature form.

Although NB primarily appeared to affect K^+ channels, some interesting dynamics were apparent in the rising section, in the form of a rise-time delay, or 'shoulder' effect in the AP phase plane diagram. This result implies that NB has a minor effect on (some) sodium voltage-gated ion channels. Specifically, this shoulder in the phase plane appears after an initial phase of increasing gradient that tracks that of Standard Internal, implying that NB has a limiting effect on the activation kinetics of voltage-gated sodium ion channels *after* they are first activated. It may be that this effect occurs due to time-dependent kinetics. Alternatively, it may be that only certain types of sodium channels are affected by NB, but that the sodium channels responsible for the initial active dynamics remain unaffected.

With such a clear effect of NB on the active dynamics of the excitatory neuron, it was necessary to explore its wider effects on the dynamics of the cell that do not involve the voltage-gated ion channels. However, no consistently concentration-dependent effect on intrinsic properties (obtained by applying hyperpolarising currents), nor on passive dynamics (obtained by applying a short current pulse) were observed. Therefore, for the purposes of the data presented in this thesis, there is no reason to discount passive dynamics data based on the presence of NB inside the internal solution. Additionally, longitudinal analysis of Vm over

the period of the current-step protocol showed no apparent diffusion-dependent changes, though a statistically significant range was not defined *a priori*, and the time period analysed was brief. Input resistance showed a possible change with NB at high concentrations, but no evidence of a dose curve was detected in these input resistance data. Presumably, NB affects the input resistance insofar as it affects the ion channels, but it does not affect the membrane properties that also contribute to the input resistance.

To compensate for the additional osmotic pressure of the NB dye, a corresponding reduction in $KMeSO_4$ to is necessary to keep the internal solution osmolarity at 285±3 mOsm, and therefore in equilibrium with the cytoplasm of the cell. This begs the question of whether the addition of NB or the reduction of $KMeSO_4$ was responsible for the change in active dynamics. However, by inclusion of a Sucrose control internal solution, it was demonstrated that the reduction of $KMeSO_4$ results in neuronal active dynamics indistinguishable from that of cells patched with Standard Internal, leaving the addition of NB as the remaining culprit behind AP waveform change.

Application of computational models to Neurobiotin concentration data

Since it has been shown that the addition of NB to the internal solution only affects the active dynamics of the cells studied, it can be hypothesised that multi-parameter-optimised Hodgkin-Huxley-style computational models could be applied to these experimental data. This would allow the relative effects of NB to be attributed to different voltage-gated ion channels responsible for the AP waveform. For example, given the increased width of the APs with the higher doses of NB, it may be hypothesised that NB primarily interferes with the fast potassium channels, with effects on other voltage-gated channels being minimal by comparison. With Hodgkin-Huxley models of varying fast potassium channel conductance, gK, a negative correlation between NB concentration and gK would be expected, indicating a reduction in the flow of potassium ions in and/or out of the cell. Should this hypothesis be proved correct, a specific effect of NB on the fast potassium channels of neonatal excitatory neurons in the barrel cortex would be implicated.

Use of Neurobiotin in imaging experiments

With NB an essential constituent of much neuroscience research, it is useful to establish what is a ‘safe’ concentration to use. The dose dependency curve of NB presented in this chapter showed no significant difference between the active dynamics of cells of similar ages patched with Standard Internal and with a low concentration NB Internal (1mg/ml). These results

therefore recommend that this concentration is not exceeded in experiments that require the electrophysiological characteristics of the patched cell to be preserved. Post-hoc confocal imaging of brain slices with patched and dye-filled cells showed no difference in the fraction of cells that can be identified as exhibiting gap-junction coupling across the concentrations of NB used. Aside from the increase in brightness, there is nothing left to recommend using higher concentrations of NB when 1mg/ml will suffice, though ample time to allow dye diffusion is a necessity. However, the analysis presented in this thesis only attempted to make a binary measure of whether gap junction coupled cells are visible at all (yes or no?), not a measure of the number of gap junction coupled cells. For a continuous measure of gap junction coupling, which might allow more thorough statistical analysis, it cannot be confirmed if this low NB concentration will be sufficient.

6.5 Summary

To summarise this chapter: use high concentrations of NB in your current-clamp electrophysiology experiments at your peril. A dose of 1mg/ml was found to be adequate to detect some gap junction coupled cells, though it may not be sufficient to identify them all. A dose higher than that will likely affect the AP waveform, as the probable result of interactions between the NB molecule and the proteins within potassium channels, but also as a result of some effects on some voltage-gated sodium channels. Given that the interaction is most likely potassium-channel based, Neurobiotin shows no significant effects on dynamics that are merely characteristic of the lipid bilayer cell membrane, such as capacitive time constants.

7. Multi-parameter Optimisation of Conductance-Based Hodgkin-Huxley Models

Key Findings

1. Voltage-comparison based methods of parameter optimisation of Hodgkin-Huxley models are vulnerable to noise, with complex error functions, whereas current-comparison based methods of parameter optimisation produce single-value optimisations that are less vulnerable to noise
2. Algebraically rearranging the ion-channel gating variables, and using simple numerical methods to solve them, reduces the computational cost of current-based methods of parameter optimisation, increasing efficiency of multi-parameter optimisation even further.
3. Pseudo-inverse matrix algebra methods allow for fast, simultaneous calculation of estimates of multiple parameters.
4. A minimum of two compartments is necessary to create realistic Hodgkin-Huxley neuronal models.

7.1 Introduction

As has been shown in previous chapters, the dynamical systems of the cortical neuron undergo massive changes over the course of development. Some of these transformations are married to changes in cell morphology or membrane capacitance, while others are associated with the delicate homeostatic balance of ion channel populations, but what is clear is that the presented experimental techniques and statistical analysis alone are insufficient to peel apart the nonlinear dynamics of neuronal behaviour over such a period of flux. To understand the underlying biophysical molecular mechanisms of neuronal development, and make predictions that can be tested in future experiments, computational models are needed.

The shape of the AP can be modelled as a changing voltage over time, determined by the interaction of time-dependent biophysical parameters (Hodgkin and Huxley 1952, Ermentrout and Terman 2010). However, a wise choice of model, and the corresponding choice of model optimisation methodology, is crucial for accurate and unambiguous neuronal modelling.

The Hodgkin-Huxley model

Since the 1950s, the Hodgkin-Huxley model of neuronal membrane potential has been used by electrophysiologists and computational neuroscientists to provide a description of the non-linear dynamical interplay of ion channels behind the shape of the AP (Hodgkin and Huxley 1952). The classic Hodgkin-Huxley model is a differential equation describing the change in membrane potential, V, over time, t, in terms of the currents in and out of the cell. The terms of the equation include the injected current, I_{inj}, and the leak across the membrane, but also the contributions of the voltage-gated ion channels. Each ionic current is determined by the Nersnt potential for its corresponding ionic species, otherwise known as the reversal potential, and by probabilistic gating variables that determine whether each specific ion channel being open or closed, themselves a function of voltage and time. The coefficients are constrained by the capacitance of the cell membrane, C, which is generally taken as 1μFcm^{-2}.
In general form, the Hodgkin-Huxley model can be expressed as:

$$C\frac{dV(t)}{dt} = I_{inj}(t) - \sum_{i=1}^{N_{\{ion\ channels\}}} I_i \tag{7.1}$$

Where I_i is the current contribution from each of the N channels, which can be written as

$$I_i = g_i {Q_i}^x (V(t) - E_i) \tag{7.2}$$

Where g_i is the maximal conductance of that ion channel, E_i is the reversal potential of that ionic species, and both are scaled by the specific ion channel probability, Q_i, which is raised to the power, x, of the number of gates within the ion channel. In practice, the Hodgkin-Huxley equation is more typically given in a form that specifies the voltage-gated ion channel contributions modelled, for example, in a simple form that includes contributions from Na^+ and K^+ channels and a leak current:

$$C\frac{dV(t)}{dt} = I_{inj}(t) - g_{Na}M^3H(V(t) - E_{Na}) - g_kN^4(V(t) - E_k) - g_L(V(t) - E_l) \tag{7.3}$$

Many of these parameters can be found from experiment, or can be estimated: the injection current, I_{inj}, is controlled by the experimentalist, the membrane potential as a function of time, *V(t)* is measured during the experiment, and the reversal potentials, E_i, can be calculated from the chemical compositions of internal solutions and external artificial cerebral spinal fluid (ACSF). *M* is the sodium channel activation gating variable, *H* is the sodium channel inactivation gating variable, and *N* is the potassium ion channel gating variable. Each of the ion channel gating variables are unitless values between 0 and 1. The ion channel gating variables are themselves determined by time dependent nonlinear differential equations of the form:

$$\frac{dM(t)}{dt} = \alpha_M(t) \cdot \big(1 - M(t)\big) - b_M(t) \cdot M(t)) \tag{7.4}$$

$$\frac{dH(t)}{dt} = \alpha_H(t) \cdot \big(1 - H(t)\big) - b_H(t) \cdot H(t)) \tag{7.5}$$

$$\frac{dN(t)}{dt} = \alpha_N(t) \cdot \big(1 - N(t)\big) - b_N(t) \cdot N(t)) \tag{7.6}$$

Where, for each gating variable, the parameters were determined by kinetic equations of the form (Pospischil, Toledo-Rodriguez et al. 2008, Ermentrout and Terman 2010):

$$\alpha_M\big(V(t)\big) = \frac{-0.1 \cdot (35 + V(t))}{e^{(-0.1 \cdot (35 + V(t))} - 1} \tag{7.7}$$

$$\beta_M\big(V(t)\big) = 4 \cdot e^{-\frac{60 + V(t)}{18}} \tag{7.8}$$

$$\alpha_H\big(V(t)\big) = 0.07 \cdot e^{-\frac{60 + V(t)}{20}} \tag{7.9}$$

$$\beta_H\big(V(t)\big) = \frac{1}{e^{(-(30 + V(t))/10)} + 1} \tag{7.10}$$

$$\alpha_N\big(V(t)\big) = \frac{-0.01 \cdot (50 + V(t))}{e^{(-0.1 \cdot (50 + V(t))} - 1} \tag{7.11}$$

$$\beta_N\big(V(t)\big) = 0.125 \cdot e^{-\frac{60 + V(t)}{80}} \tag{7.12}$$

This leaves the maximal conductances, g_i, and their associated ion-channel gating functions to be found. Together, these factors describe the flow of charge through each type of ion channel.

This version of the equation models the cell as a single isopotential, homogeneous compartment. It neglects any geometric effects on the biophysics, for example, axial resistance between the soma and dendrites, or soma and axon. It also neglects any synaptic or network contributions, but considers the neuron a single, isolated unit.

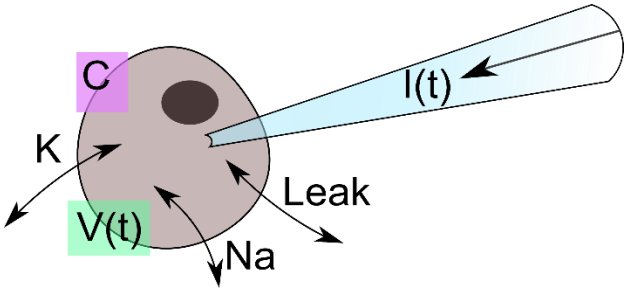

Figure 7.1: A simple model of a neuron that considers only a single compartment. The time-dependent voltage across the membrane (*V(t)*), mitigated by the capacitance (*C*), is modelled as the sum of the injected current, *I(t)*, and the currents from the through *K*, *Na* and *Leak* channels.

The Hodgkin-Huxley equation can be expanded to model more subtle and precise dynamics by the inclusion of additional, specific voltage-gated ion channels, and by the inclusion of additional compartments, separated by defined resistances. Whilst this can aid the understanding of how the cell works, it can have an exponential effect on the complexity; as with all models, what is sought is not perfection, but a reasonable approximation that can generate predictions to be tested in experiments.

Conductance-based Hodgkin-Huxley style models can be used to implicate the contributions from different ion channels in the changing shape of the AP waveform, and observe how the relative dominance of each voltage-gated channel changes across maturation. Indeed, the results from Chapter 3: *Active Dynamics* have already indicated a change in dominance between sodium and potassium channels over the maturation period studied. Conductance-based models can also be used to infer the contribution of 'leak' currents that correspond to the passive dynamics when no voltage-gated activation taken place; such dynamics were themselves shown to be development-dependent in Chapter 4: *Passive Dynamics*.

Assumptions of the Hodgkin Huxley model

Like all mathematical models of real phenomena, the Hodgkin-Huxley model contains implicit assumptions: all compartments are assumed to be isopotential, leak currents are assumed to be isotropic across the membrane, and all ionic currents are assumed to flow only through ion channels, with each ion channel being absolutely specific to each ionic species. The instantaneous current-voltage relationship is assumed to be linear, with no amendments made for temperature dependent resistances or local intracellular or extracellular electrochemical gradients (Yamada 1998).

Parameter optimisation

Whilst Hodgkin-Huxley equations can be used to computationally model the highly dynamic and nonlinear event that is the firing of an action potential, the fact that the parameters under investigation are changing with age, and experimental data can be noisy, adds a layer of complexity to the modelling. With such a complex parameter environment, potentially changing with every passing day, it is a worthwhile endeavour to assess the success of different parameter optimisation techniques, prior to their application on real data (Geit, Schutter et al. 2008, Wulfram Gerstner 2009, Friedrich, Vella et al. 2014). Once the assessment of optimisation techniques is performed thoroughly, Hodgkin-Huxley style models can be fit with confidence to the action potential recordings obtained during experiments. The established method of such evaluation is to create an artificial data set, and then test the ability of different parameter optimisation techniques to find a target parameter, or parameters.

The solution discussed in this thesis, based on work by Lepora et al.(Lepora, Overton et al. 2012), which itself was based on previous work (Morse, Davison et al. 2001), does not attempt to solve voltage-based parameter optimisation, but instead turns the problem around, to be one instead of balancing currents. This turns the problem from a difficult solution via a multi-parameter differential equation to a simple linear sum, producing solutions that are not only more accurate, but are also much more computationally efficient.

The error landscape

When examining parameter optimisation techniques, a useful tool for both computation and intuitive demonstration is the error landscape. This visual representation of optimisation can show clearly the problems with different methods. An error landscape plots the difference between the target data and the modelled data, or the error function, against the value of one

or more parameters. This plot reaches a minimum when the parameter or parameters from the model equal that from the data. The simplest error landscapes are (usually) the best; in these the difference between the data and the model converges to zero at a single point where the parameters match perfectly. Less successful error landscapes are characterised by their roughness, where local minima in error can point to incorrect parameter values, which appear indistinguishable from the true values.

Much previous work has been devoted to the development of algorithms that address the issue of rough-error landscapes – error landscapes that have many local minima. Evolutionary algorithms, such as the genetic algorithm explore the error environment and iteratively improve the estimation of the parameters. Increasingly sophisticated versions of such algorithms work to avoid constraint in local minima by including random jumps, but intrinsic to evolutionary algorithms is high computational cost; exploring the entire, multidimensional landscape takes time and computational power (Geit, Schutter et al. 2008, Brookings, Goeritz et al. 2014).

The problem of parameter optimisation can be reframed by considering it not of finding the lowest error, but on creating the *smoothest* landscape, that being the error landscape in which, no matter the degree of dimensionality, there is only one minimum; in this way, a successful error landscape becomes trivial as it points to a single minimum, without ambiguity.

Beyond considerations of roughness and smoothness (i.e of the number of local minima), error landscapes can raise larger theoretical questions of neuronal homeostasis (Marder and Goaillard 2006). As has been remarked upon in previous chapters, the biophysical properties of the developing neuron change dramatically in the first two postnatal weeks, yet neurons still manage to survive, communicate and build functional networks. This implies a degree of flexibility in the biophysical properties of the neuron; in multidimensional error landscapes, this may manifest as shallow valleys of near-equal error for slightly different parameter values, where the slightly-too-large contribution of one parameter compensates for the slightly-too-small contribution of another, and the same patterns of behaviour can still be seen.

An error landscape can be plotted across the range of whatever parameter, for example sodium ion channel maximal conductance, is being tested; the minimum in the landscape represents the minimum error that can be found over that range of maximal conductances, and the location of this minimum should be at the best fitting parameter for the model, where the

output membrane potential supplied by the model is a close enough fit to the data to return an accurate estimate of the current. This presents a problem: how can we be sure that the minimum we find in an error landscape is the absolute minimum error over all possible values of that parameter, which may stretch to infinity in both negative and positive dimensions? Certainly, most work requires a sanity check of the parameters returned, but even with a 'sensible' range established, however arbitrarily, the absolute minimum of the resultant error landscape may still be difficult to decipher. Much time and effort has been devoted to improving algorithms to avoid local minima in the error landscape that could provide false positives; indeed, some beautiful mathematics for solving this problem, in ever more complicated iterations has been provided (Toth, Kostuk et al. 2011, Vavoulis, Straub et al. 2012).

The position of the peak of the action potential might seem like a simple yet effective method, certainly a method that would be of low computational workload, as it only requires the comparison of one data point, that of the position of the apex of the action potential. However, it could be argued that this method relies too much on the timing of the spike; the spike waveform might be a perfect replica of our target action potential, but if it is not at the same time, the model and target data won't match. Conversely, a spike that had a completely different shape, demonstrating completely different dynamics, *but happened to have its apex at the same point,* would be deemed a perfect match. The error landscape would go to zero at this point, and that value of the conductance would be returned as the 'correct' value.

Parameter optimisation of the maximal conductance-based Hodgkin Huxley style models of active neuronal dynamics in excitatory cortical neurons is the main focus of this chapter, which begins with a brief 'wish-list' for successful optimisation, before examining how well-established voltage-based techniques address this list. It then proceeds to explore current-based techniques, before presenting new work that aids computational efficiency whilst reducing the influence of noise on parameter optimisation and fitting. These current-based techniques are expanded to optimise multiple parameters simultaneously. The models are then considered against real data, and evaluated for how they may be made sufficiently realistic to be able to return accurate estimates of the ion channel proportions. This chapter does not attempt to present new methods of exploring an error function between (synthetic) data and model; instead, it attempts to create the smoothest and most accurate error function possible, so that the methods of optimising parameters during model fitting become trivial.

7.2 Methods

All the work presented in this chapter was done using MATLAB. Original scripts were written for purpose, based on published work (Lepora, Overton et al. 2012).

Criteria for successful parameter optimisation

Prior to testing different methods of calculating error functions for their effects on multiparameter optimisation, it was useful to define what successful optimisation would look like. The ideal optimisation technique is one that fulfils the following criteria:

- The optimisation should return a single value of each maximal conductance optimised
- The returned values should be in good agreement (±5%) with the synthetic data target values
- The maximal conductances should be determined simultaneously
- Sensible initial conditions should not be required
- The maximal conductances should be found within a convenient amount of time
- The protocol should robustly avoid grossly incorrect combinations of variables that result in the same overall membrane potential profile (spiking pattern).

Producing an artificial data set with target conductances of known values

To test the ability of both voltage and current-based parameter optimisation techniques, it was necessary to create an artificial data set, where the parameters under question, the maximal conductances were of known value. The majority of 'data' within this chapter is artificial data, produced from a simulation of spiking behaviour for the purpose of developing and evaluating parameter optimisation methods.

The first artificial dataset was created from a simple version of the Hodgkin-Huxley equation (Equation 7.3). The reversal potentials and ion channel gating variables were taken from literature (Ermentrout and Terman 2010), though the values of these were arbitrary; the value of specific controlled variables was of little importance. The maximal conductance values used in the first target action potential are listed in **Table 7.1**:

	gNa (mS/cm^3)	gK (mS/cm^3)	gL (mS/cm^3)
Target:	**120**	**36**	**0.3**

***Table 7.1**: Target values of maximal conductances from artificial data set 1.*

These values were inserted into equation 7.3, and solved within a MATLAB script via the ordinary differential equation solver '`ode45`' to produce a time dependent membrane potential, V(t), providing the target data. When the injected current, I_{inj} was zero, only equilibration dynamics were observed. Only when I_{inj} was nonzero and above a certain threshold could the output be identified as an action potential. For the first target data set, a current injection of duration 10ms was used, enough to produce a single spike. Noise was added via the MATLAB command '`awgn`' – 'add white Gaussian noise'. The amount of noise was not constant over the target data set; when no current is being injected the signal to noise ratio was 50:1, during the current injection the signal to noise ratio was 65:1. The combination of these noise inputs produced an artificial data set that is far noisier than any seen in real experimental data; this excessiveness was to test the limits of parameter optimisation.

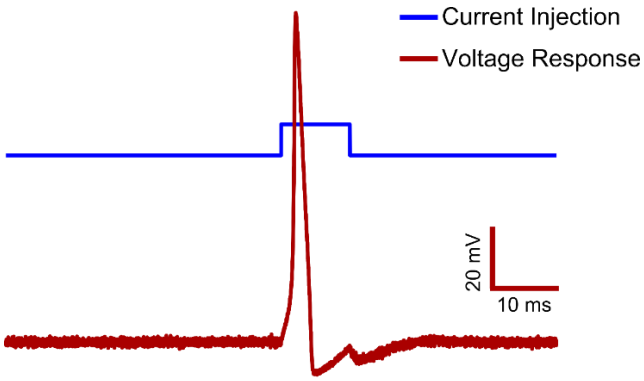

Figure 7.2: A noisy artificial target action potential, created from the simple version of the Hodgkin-Huxley model (Equation 7.3) with Gaussian white noise added.

This artificial target dataset was used to test the error functions returned by the voltage-based methods (and their resultant effect on parameter optimisation) against the current based methods.

An artificial target data set of repetitive spiking behaviour

To test current-based methods of producing an error function for parameter optimisation further, artificial target data sets were needed that resembled the experimental data. Using the same version of the Hodgkin-Huxley equation (Equation 7.3), the artificial target data set was adjusted by the extending the current injection to 500ms, to replicate the experimental conditions. As expected, this resulted in a spike train. Noise was added as described above.

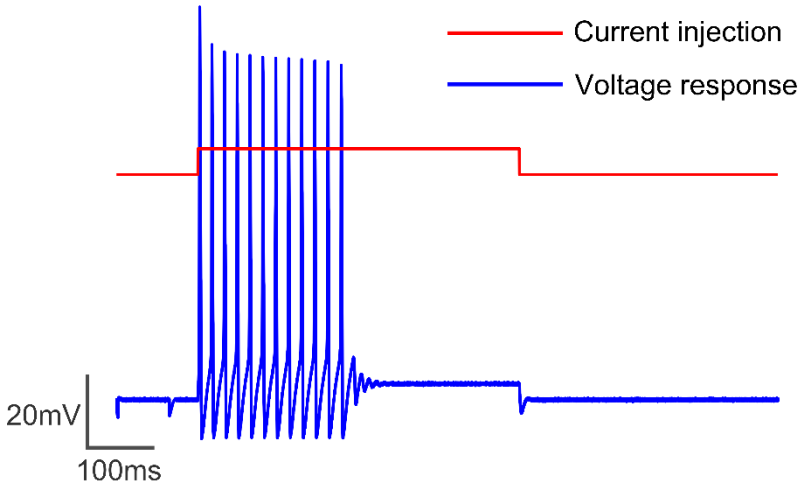

Figure 7.3: A noisy artificial target spike train, created from the simple version of the Hodgkin-Huxley model (Equation 7.3), with Gaussian white noise added. The high spiking frequency shown was not observed experimentally in developing excitatory cortical neurons.

However, this membrane potential output was observed to have a spiking frequency far higher than what was seen in experiments with young, regular-spiking excitatory neurons. Adjustments made to the balance of maximal conductances resulted in 'bunching' of spikes, which was not a phenomenon observed routinely in experiments. No variation of any of the terms in this version of the Hodgkin Huxley model could create the lower frequency consistent spiking observed in experiment. This presented a problem, since a synthetic target data set resembling real data was desired to allow much smoother translation of any developed parameter optimisation techniques to real data. It also confirmed that a two voltage-gated ion-channel Hodgkin-Huxley model was insufficient to replicate the dynamics of a regular spiking excitatory neuron; as has been previously reported (Pospischil, Toledo-Rodriguez et al. 2008).

Realistic artificial datasets

To address this problem, and create a realistic target data set, an additional term was included in the Hodgkin Huxley model: a small, slow, non-inactivating potassium current, mediated by an ion channel gating variable, P. This slow K^+ current was incorporated into the synthetic target data simulation via the Hodgkin Huxley equation, now amended to be written as:

$$C\frac{dV_m}{dt} = I_{inj}(t) - g_{Na}M^3H(V - E_{Na}) - g_kN^4(V - E_k) - g_mP(V - E_k) - g_L(V - E_l) \quad (7.13)$$

The addition of this slow K+ current allowed for greater control over the spiking properties, bringing them closer to what is seen in experimental data. Again, the maximal conductances

used to create this waveform were arbitrary, since parameter optimisation techniques should not rely on sensible initial choices, and, as before, Gaussian white noise was included in the creation of the artificial target data set of this more realistic spiking pattern (**Figure 7.4**).

In addition, to create a more realistic artificial target data, the following criteria were set:

1. The parameter values must be physically possible.
2. Known input variables (I_{inj} and the reversal potentials) must have values that match those that are used in the laboratory.
3. The membrane potential output must resemble the real data attained in the laboratory.

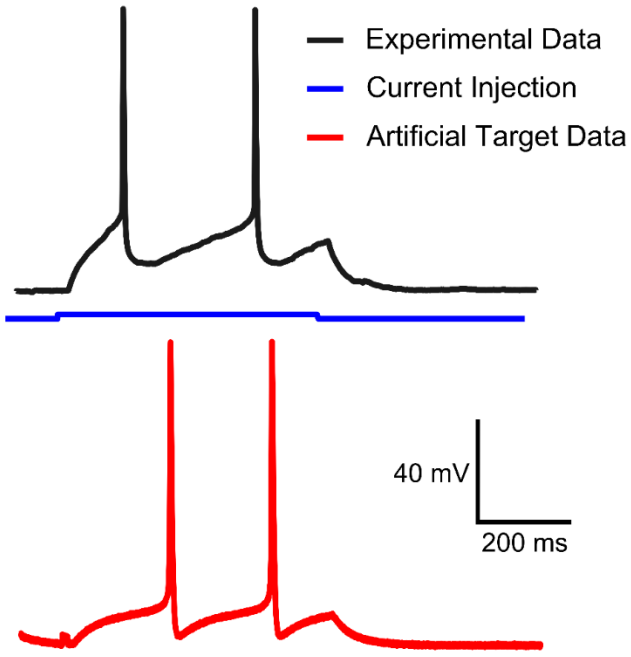

Figure 7.4: A realistic artificial target data set is created by the addition of a slow potassium current. The spiking frequency and threshold of the artificial target data (*red line)* more closely resemble that of the real experimental data (*black line*).

	gNa (mS/cm^3)	gK (mS/cm^3)	gM (mS/cm^3)	gL (mS/cm^3)
Target	**15.00**	**0.44**	**0.026**	**0.015**

Table 7.2*: Target values of maximal conductances from artificial data set 2. All units are arbitrary.*

Testing the ability to find a target parameter

In order to evaluate the effectiveness of different techniques for producing error functions that allow parameter optimisation to find the correct target parameter(s), it was necessary to input a range of values for the parameter(s) in question, where only one value was correct. The function of the parameter range against the amount of error between data and model could therefore be used to construct the resulting error landscape. For example, a matrix of values of maximal sodium conductance, gNa, that varied over a sensible range around the target value could create an equal number of very similar spiking traces. However, only one such output trace would contain the correct value of gNa in its construction. An error landscape could then be constructed by plotting the difference between model simulation and target data as a function of gNa.

7.3 Results

Comparison of different voltage-based metrics of parameter optimisation

Using the first artificial target data set, describing a single action potential, a range of different voltage-based techniques for producing an error function were first assessed:

1. ABS-error: The absolute error between model and data traces, simply taking one value of the voltage from the other across the whole trace.
2. PEAK error: comparison of the position of the maximum voltage in the action potential trace.
3. AHP error: after-hyperpolarisation error, comparison of the position of the minimum voltage in the action potential trace; the trough immediately after the action potential peak.
4. RMS error: Root mean squared error (RMS), comparison of the simulated data to the target data via the calculation of the root mean squared difference between data and model at each time point.
5. PHP error: Phase-plane error, the difference between plots of the first derivative of voltage with time against time (for examples of phase plane traces, see **Figure 7.11.B**, or **Figure 6.4**).

For each of the target conductances, gNa = 120 mS/cm^3, gK = 36 mS/cm^3 and gL = 0.3 mS/cm^3, a matrix of values surrounding the target was created. The difference between model simulation and target data was then plotted as a function of each conductance (**Figure 7.5**), also referred to as an error landscape. The value of the conductance estimate

was then calculated by simply finding the minimum of the error landscape matrix (using the MATLAB command `'min'`). Each of the voltage-based error landscapes plotted failed to produce a single trivial minimum at the correct sodium conductance value. The resultant error landscapes were either rough with many local minima (ABS and RMS), trivial but inaccurate (PEAK) or flat, (PHP and AHP error). Only the two rough error landscapes (ABS and RMS) had minima close to the target values. Without the use of genetic algorithms, more complicated versions of this error landscape from real experimental data would produce a difficult problem in trying to find the correct minima that corresponded to the correct parameters. This difficulty would be amplified if multiple parameters were attempted to be found simultaneously. In addition, these methods were all measured to take more than 2 minutes to return their estimation of the target value of gNa.

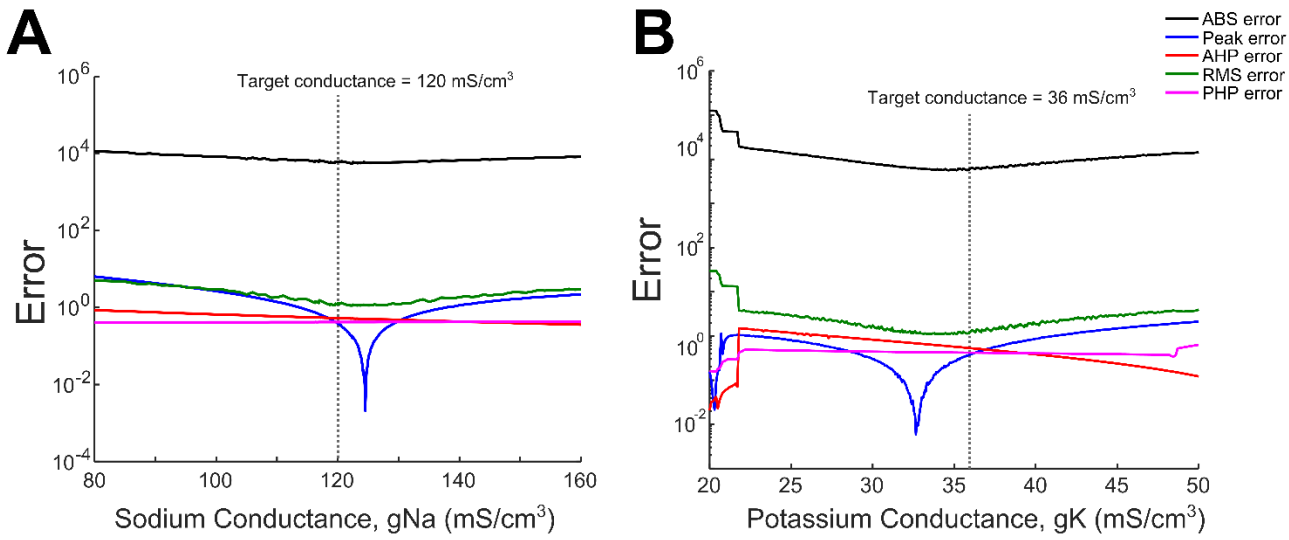

Figure 7.5: Error landscapes for different voltage-based parameter optimisation techniques. **A:** Error as a function of maximal sodium conductance, gNa **B:** Error as a function of potassium conductance, gK.

Optimisation Method	gNa (mS/cm^3)	gK (mS/cm^3)	gL (mS/cm^3)	Time to find gNa
Target	**120**	**36**	**0.3**	**-**
ABS (Trace) Comparison	122.25	35.15	0.301	134.7s
Peak Comparison	124.50	32.65	0.275	137.3s
AHP Comparison	160.00	20.00	0.090	134.8s
RMS Comparison	122.25	34.30	0.301	137.6s
Phase Plane Comparison	80.00	20.40	0.207	135.8s

***Table 7.3**: Assessment of different voltage-based optimisation techniques to find the target conductances.*

Current-based methods of parameter optimisation to a single spike, single parameter

An alternative to voltage-based methods of error function creation and parameter optimisation, that could robustly provide more accurate estimates of the ion channel conductances, in less time, was desired. Therefore, a current balancing method, where the error is equivalent to a current residual between input and output currents, was explored (Lepora, Overton et al. 2012). The Hodgkin Huxley equation can be expressed as a linear sum that compares the passive currents (the injected current and the capacitive current across the membrane) to the active currents (the currents through the ion channels):

$$I_{inj}(t) - C\frac{dV_m}{dt} \approx I_K + I_{Na} + I_M + I_L \tag{7.14}$$

Where the term I_{Na} is an array of values due to the variation of the maximal conductance gNa, as before. The error function is then calculated as the residual current: the root mean squared difference between the passive and active currents.

$$I_{res} = \sqrt{\frac{1}{N}\sum\left(I_{act} - I_{pas}\right)^2} \tag{7.15}$$

From equation 7.2, we know that each current in the sum can be expressed as:

$$I_i = g_i {Q_i}^x (V(t) - E_i) \tag{7.2}$$

Where the current is scaled by the value of the ion channel gating probability, Q.
For the simple version of the Hodgkin-Huxley equation, the ion channel gating variables used were M, N and H.

Integral forms of ion channel gating probabilities provide faster and more accurate estimates of the residual current

Given the limitations of the voltage-based methods of parameter optimisation of models to noisy synthetic data, the residual current method was applied to the same data, initially using inbuilt MATLAB ordinary differential equation solvers to provide time-dependent values of M, N and H. However, the functionality of these inbuilt solvers, and the estimations within, led to inaccurate predictions of the target conductances. Therefore, different approaches to determining the time-dependent values of M, N and H were considered, that would not be

reliant on the solvers, namely, algebraic rearrangement of the differential equations into integral form. It was predicted that robustness to noise would be improved by integral form, since noise is suppressed by integration and amplified by differentiation. Additionally, by taking on the work of computation through algebraic rearrangement, the overall computational time was predicted to be lessened.

Following on from previous work (Lepora, Overton et al. 2012), the ion channel activation / inactivation gating variables, M, N, and H, were rearranged from differential to integral form. Each gating variable was expressed in the Hodgkin-Huxley model as a time varying differential equation, for example, gating variable M is described by equation 7.4:

$$\frac{dM(t)}{dt} = \alpha_M(t) \cdot \big(1 - M(t)\big) - b_M(t) \cdot M(t)) \tag{7.4}$$

With substitution and rearrangement, this can be expressed in the form

$$\frac{dM(t)}{dt} + M(t) \cdot \gamma_M(t) = \alpha_M(t) \tag{7.16}$$

Where

$$\gamma_M = \alpha_M(t) + b_M(t) \tag{7.17}$$

In this form, it can be solved with the help of an integrating factor:

$$e^{\int \gamma_M(t)dt}$$

Giving:

$$e^{\int \gamma_M(t)dt}\frac{dM(t)}{dt} + e^{\int \gamma_M(t)dt}M(t) \cdot \gamma_M(t) = e^{\int \gamma_M(t)dt}\alpha_M(t) \tag{7.18}$$

Which can be rearranged to:

$$e^{\int \gamma_M(t)dt}\frac{dM(t)}{dt} + M(t) \cdot \frac{d}{dt}e^{\int \gamma_M(t)dt} = e^{\int \gamma_M(t)dt}\alpha_M(t) \tag{7.19}$$

This can be solved by using chain rule in reverse

$$\int \frac{d}{dt} M(t) e^{\int \gamma_M(t)dt} dt = \int e^{\int \gamma_M(t)dt} \cdot \alpha_M(t) dt$$

$$M(t) \cdot e^{\int \gamma_M(t)dt} + c = \int e^{\int \gamma_M(t)dt} \cdot \alpha_M(t)\, dt$$

(7.20)

Allowing the gating variable to be expressed as a function of time:

$$\boldsymbol{M(t)} = \boldsymbol{e^{-\int \gamma_M(t)dt}} \left(\int \boldsymbol{e^{\int \gamma_M(t)dt} \cdot \alpha_M(t)\, dt + c} \right)$$

(7.21)

The algebraic rearrangement can be applied to the other gating variables to give:

$$\boldsymbol{N(t)} = \boldsymbol{e^{-\int \gamma_N(t)dt}} \left(\int \boldsymbol{e^{\int \gamma_N(t)dt} \cdot \alpha_N(t)\, dt + c} \right)$$

(7.22)

$$\boldsymbol{H(t)} = \boldsymbol{e^{-\int \gamma_H(t)dt}} \left(\int \boldsymbol{e^{\int \gamma_H(t)dt} \cdot \alpha_H(t)\, dt + c} \right)$$

(7.23)

These integral equations were solved numerically, by use of the trapezium rule method of integration, though other numerical integration techniques would be equally suitable. Their solutions were plotted as a function of time (**Figure 7.6**).

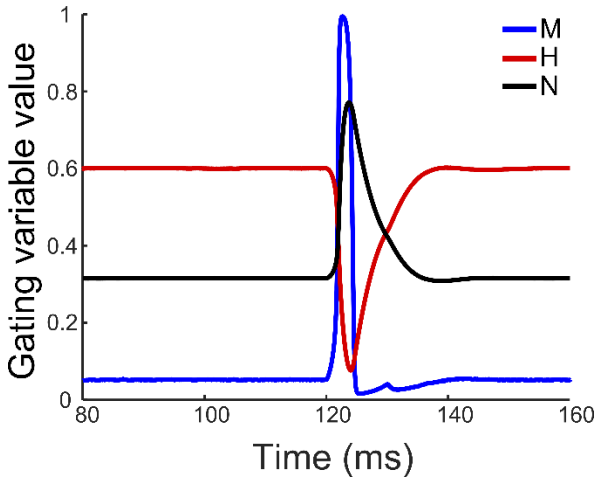

Figure 7.6: The gating variables, M, H and N, as a function of time for an artificial noisy target data set of a single action potential.

The active currents through the ion channels are defined in terms of these gating variables. Rearranging the differential equations behind the gating variables into integral form before solving them numerically has the effect of reducing the contribution of noise to the optimisation. Hence, for the noisy single action potential defined from the first artificial target

data set, smooth error functions with single minima were returned (**Figure 7.7**). As with the voltage-based methods, the value of the conductance estimate in each case was found simply by finding the minimum of the output matrix. These produced good estimates of all the target conductances (within 5% of the target values), with the time taken to return an estimate of gNa reduced to just under 36s.

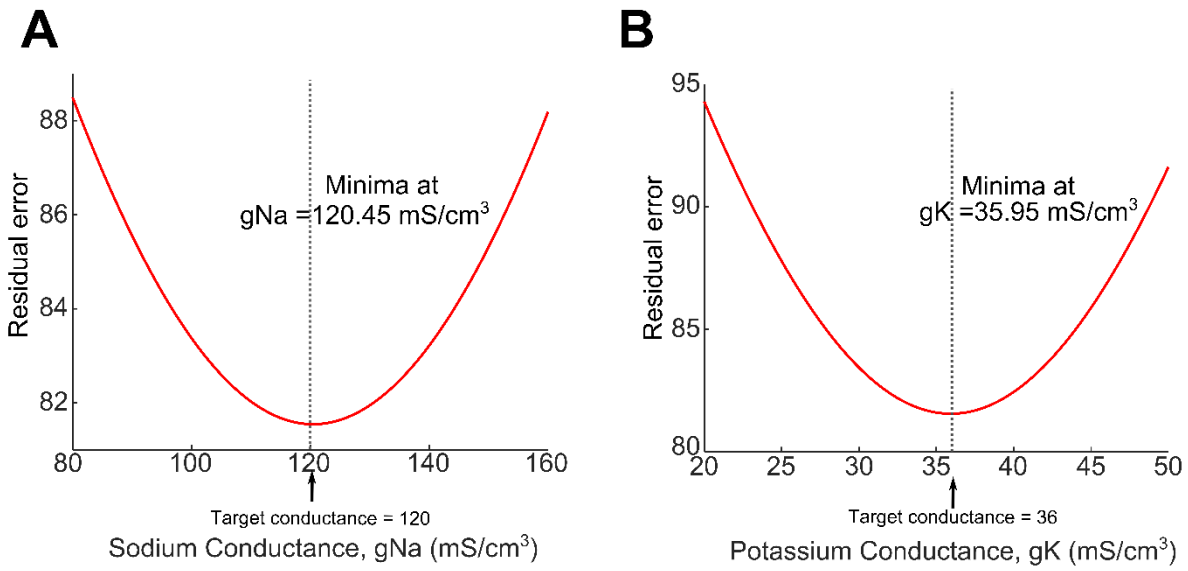

Figure 7.7: Error landscapes for single-parameter optimisation using current-based methods. Landscapes show the residual error from fitting to an artificial noisy single spike. **A:** the error as a function of sodium conductance, gNa. **B:** the error as a function of potassium conductance gK.

	gNa (mS/cm^3)	gK (mS/cm^3)	gL (mS/cm^3)	Time to find gNa
Target	**120**	**36**	**0.3**	**-**
Residual Current	120.45	35.95	0.3	35.9s

***Table 7.4**: Assessment of the current-based optimisation technique to find the target conductances.*

Current-based methods of parameter optimisation to a single spike, multiple parameters

The next criterion to be addressed was that of being able to find multiple conductances simultaneously. For noiseless action potentials created using the simple version of the Hodgkin-Huxley equation, the error as a function of both gNa and gK was visualised quite easily by plotting the error functions for both sodium and potassium conductances on x and y axes, with the residual error on the z axis, allowing a three-dimensional error function to be plotted (**Figure 7.8**). This returned values of the conductances of gNa = 119.85 mS/cm^3 and

gK = 35.94 mS/cm^3, in good agreement with the targets of gNa = 120 mS/cm^3 and gK = 36 mS/cm^3.

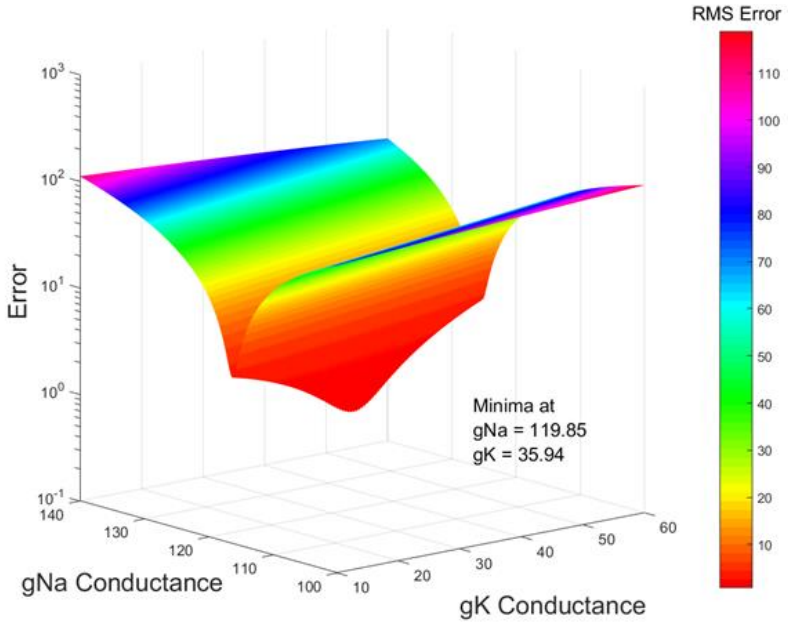

Figure 7.8: **Multi-parameter error function for noiseless artificial target data, optimised for both gNa and gK**. Units of conductances are mS/cm^3.The single minimum occurs at values of the two conductances that are in good agreement (<5%) of the target.

When noise was included, the multidimensional error function continued to return a minimum of error at a reasonably good estimate of both sodium and potassium conductances (gNa = 121.22 mS/cm^3, gK = 36.53 mS/cm^3), though the position of the minimum was more difficult to visualise (**Figure 7.9**).

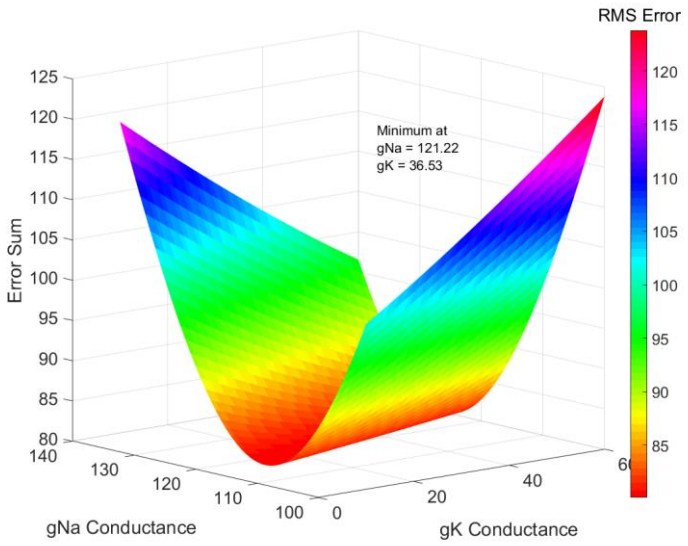

Figure 7.9: **Multi-parameter error function for noisy artificial target data optimised for both gNa and gK**. Units of conductances are mS/cm^3. The single minimum occurs at values of the two conductances that are in good agreement (<5%) of the target.

Current-based methods of parameter optimisation to a realistic artificial data set

The more realistic version of the Hodgkin-Huxley model included a slow potassium current, which prevented high frequency spiking. In order to compute this additional ionic current, $I_m = g_m P(V-E_K)$, the gating variable P was rearranged into integral form in much in the same way as was done for ion channel gating variables M, N and H.

$$\boldsymbol{P(t)} = \boldsymbol{e^{-\int b_p(t)dt}\left(\int e^{\int b_p(t)dt} \cdot \alpha_p(t)\, dt + c\right)} \tag{7.24}$$

However, when computing P, the exponential phrases in the integral form reached values so large that they could not be computed by the simple numerical methods (trapezium rule) that had been previously used. This was identified as an issue of computational power, and was solved by dividing the numerical integration of the function P into time-bound 'chunks'. This necessitated the calculation of the integration constant at the start of each 'chunk' of P, but was otherwise not computationally expensive. The ion channel gating variables could then be computed and plotted as a function of time, as before (**Figure 7.10**).

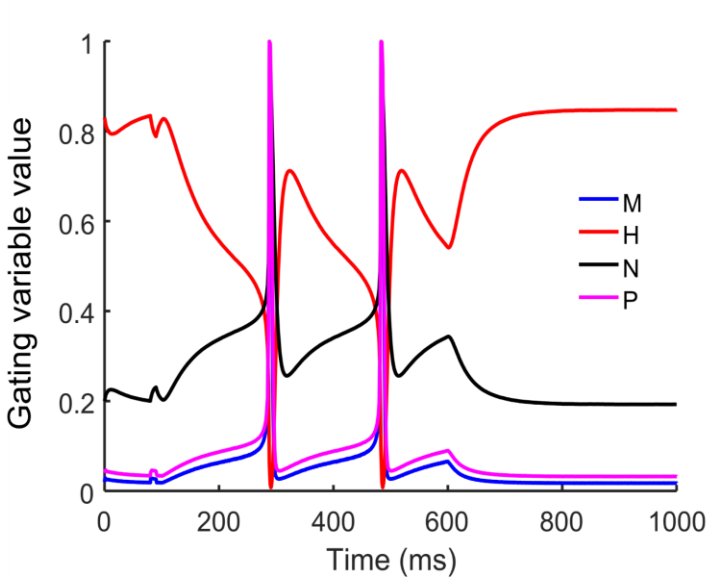

Figure 7.10: Gating variables as a function of time, including a slow potassium gating variable, P.

Limits of the error landscape method of multi-parameter optimisation

With the inclusion of gK, gM and gL, the dimensionality of error landscape expanded to 5D. Projections of this multidimensional error landscape could be plotted, but this presented a non-trivial problem. An additional limitation was identified in that the success of the error landscape method of multi-parameter optimisation rested on the assumption that the difference between each iteration of the conductance variable in any one dimension is large enough to produce a discernible change in the gradient of the landscape. As more accurate

values of the conductances are approached, focusing in on the nadir of the landscape, the presence of smooth 'basin' becomes apparent, the gradient of which is too smooth for the error landscape method to distinguish a single minimum.

To obtain a single set of values for multiple unknown parameters, finding the value of the conductances through the minima of the error landscape method had to be abandoned as the primary method of computation: it no longer returned a single value as the absolute minimum. Other mathematical techniques are needed to compute the location of the minimum.

Matrix methods of parameter optimisation

Algebraic matrix methods, as previously presented, (Lepora, Overton et al. 2012), can be employed to find the values of multiple conductances simultaneously. The basis of these methods is that they rely upon the calculation of the probabilistic voltage across *n* ion channels, denoted A_i. A_i is the time dependent voltage $(V(t)-E_i)$ multiplied by the corresponding ion channel gating probabilities. For example, $A_{Na} = M^3H(V(t)-E_{Na})$.

The active current contributions can be described as

$$I_{act} = I_{Na} + I_k + I_m = \sum_{i=channel}^{n} I_i \tag{7.25}$$

Viewing each current, I_i in terms of its ion-channel gating variable, potential difference and maximal conductance, this can be written as:

$$I_{act} = \sum_{i=channel}^{n} Q^N (V(t) - E_i) g_i \tag{7.26}$$

Via the substitution:

$$A_i = Q^N (V(t) - E_i) \tag{7.27}$$

The contribution from active currents can be written as a sum of matrices, in the form:

$$I_{act}(t) = \sum_{i=channel}^{n} A_i(t)\, \bar{g}_i \tag{7.28}$$

Allowing us to state, via the equivalency between passive and active currents at the confluence of target maximal conductances, that

$$I_{pas}(t) = \sum_{i=channel}^{n} A_i(t)\,\bar{g}_i \tag{7.29}$$

All the constituent parts of A_i can be either measured experimentally or calculated. Therefore, by taking the pseudoinverse of $A_i(t)$, and multiplying it by the passive current, an expression for the maximal conductances can be retrieved:

$$I_{pas}(t) \cdot A_i^{\#}(t) = \sum_{i=channel}^{n} \bar{g}_i \tag{7.30}$$

Where

$$A_i^{\#} = pseudoinverse\ of\ A_i$$

Then the conductance of each current can be found via the summation of the resultant conductance matrix over time. In short, matrix algebra allows for unambiguous and quick computation of all four maximal conductances, gNa, gK, gM and gL, in a few short lines of code.

	gNa (mS/cm^3)	gK (mS/cm^3)	gM (mS/cm^3)	gL (mS/cm^3)
Target	**15.00**	**0.44**	**0.026**	**0.015**
Current Based Matrix Method	14.98	0.44	0.025	0.016

Table 7.5: The estimates of the maximal conductances returned, simultaneously, from current-based methods of parameter optimisation. Multi-parameter optimisation is performed on noisy and realistic artificial target data.

With the values of the maximal conductance parameters derived, they can be checked by substitution into the differential form of the Hodgkin Huxley equation to produce a modelled membrane potential output as a function of time. (**Figure 7.11.A**). This can be assessed for goodness of fit using, for example, phase plane comparison methods (**Figure 7.11.B**).

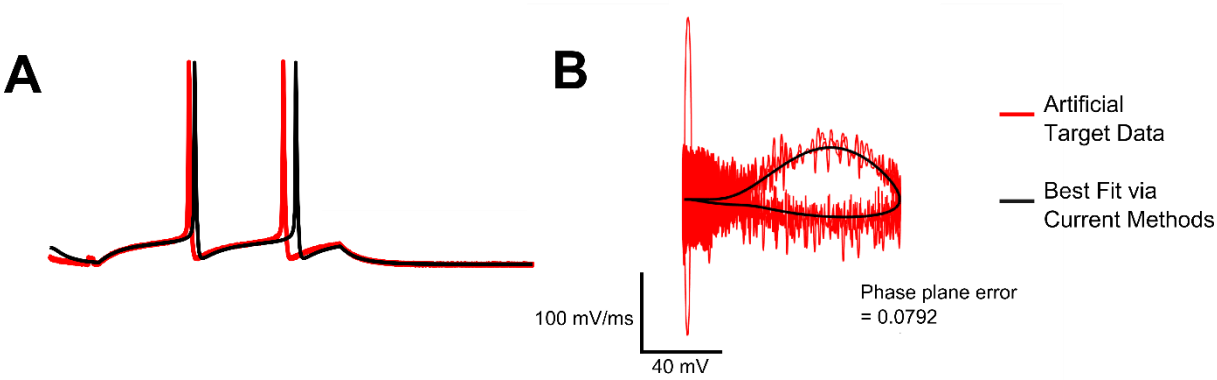

Figure 7.11: The maximal conductances returned by the matrix current-based method of parameter optimisation. A: The returned maximal conductances produce a spiking pattern that is very similar to that of the artificial target data. **B**: Goodness of fit can be quantitively assessed via, for example, phase plane comparison methods.

7.4 Discussion

Hodgkin-Huxley style models of neuronal conductances can be used to model neuronal spiking behaviour but robust multi-parameter optimisation is needed to accurately replicate the subtle changes in action potential waveform with development. Voltage based methods of multi-parameter optimisation produce non-trivial error functions, or landscapes, that are easily disrupted by the inclusion of noise. This chapter has shown by comparison that residual current based methods perform better than voltage based methods (absolute (trace) comparison, peak comparison, AHP comparison, RMS error, phase plane error) when tested against synthetic target data, returning better estimates of multiple parameters in less time, providing support to previous work (Lepora, Overton et al. 2012).

Using MATLAB, this work was further developed by writing the differential equations of the ion channel gating variables into integral form, and numerically evaluating the result. In doing this, the computational expense of solving the differential equations is removed, and smooth error landscapes with single minima are returned. As more maximal conductances are attempted to be found, matrix inversion methods perform well at simultaneously returning good estimates of the parameters in question.

Physical interpretations of the multi-parameter error landscape

As neuronal models approach realism, the shape of the error function close to the target maximal conductance(s) becomes a shallow basin. Physical interpretations of this basin can be considered, for example, it might be representative of the homeostatic mechanisms to

allow neurons to function over a constrained range of variables (O'Leary, Williams et al. 2013). It could therefore be hypothesised that any model neuron whose parameters falls within this basin would be able to exhibit robust spiking behaviour despite deviation from a single minimum. Alternatively, the limits of the basin could be representative of the limits of the residual current technique: the error bars on the returned values of the maximal conductances.

Two-compartment models require an axial current

The current-based multi parameter optimisation technique presented here was successful at finding the target maximal conductances in artificial data sets but was unsuccessful when applied to real experimental data. Though the model was able to return time-dependent functions of the gating variables and the currents through the neuron, the estimations made were unfortunately too unrealistic to be able to produce spiking behaviour from real experimental data (**Figure 7.12**). This indicates that the version of the Hodgkin-Huxley model used was not sufficiently complex to capture all the behaviour present in real data.

The parameter optimisation techniques developed here assumed a neuron that could be modelled with a single compartment. As was demonstrated in Chapter 4: *Passive Dynamics*, single compartment models of the neuron cannot adequately capture the biophysics; a minimum of two compartments are needed. A second compartment that represented the dendritic arbour, for example, would require a different geometry, with a much larger surface area. Although it may be presumed that the dendritic morphology supports active currents, the presence of a second compartment could be modelled most simply by assuming that the dendritic compartment is passive, and that an axial resistance exists between compartments. The addition of a passive axial current to the Hodgkin-Huxley model represents further work to be undertaken.

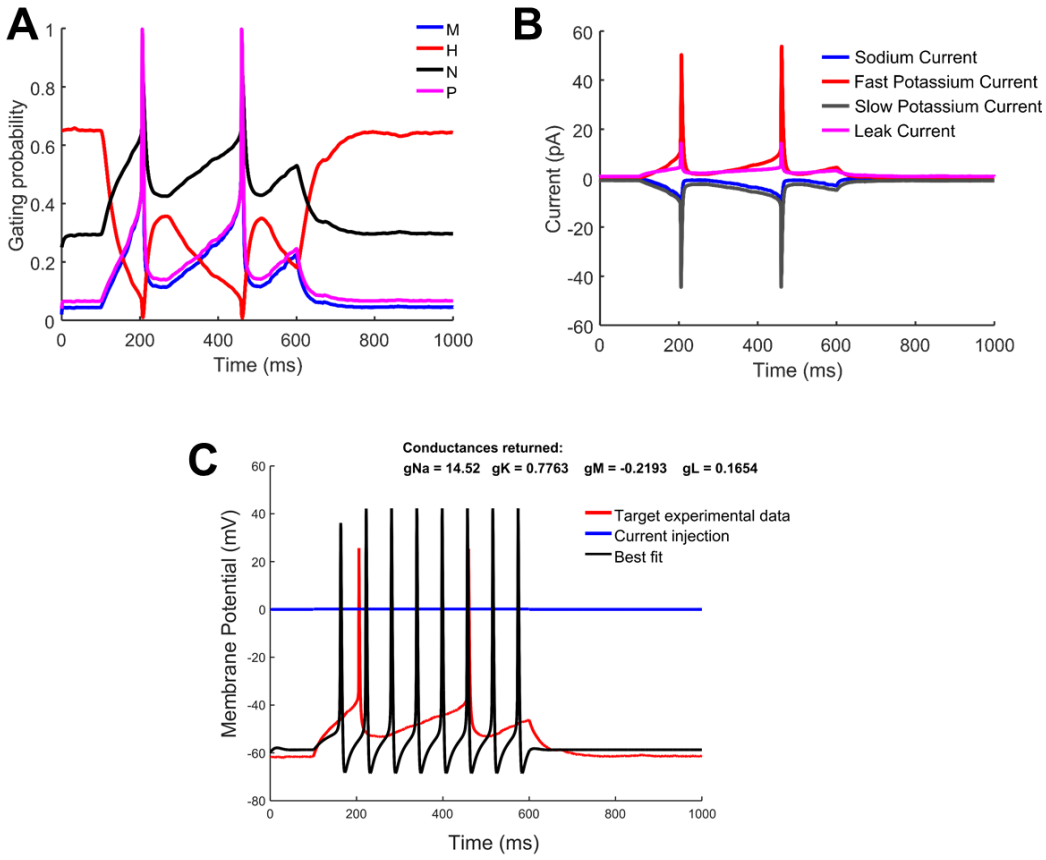

Figure 7.12: **Multi-parameter optimisation performed on real experimental data returns unphysiological maximal conductances, indicating that an additional current is needed**. **A**: Ion channel gating variables, as a function of experimentally measured membrane potential and time. **B**: Estimates of the currents through the neuron. **C**: The spiking pattern produced by the returned maximal conductances is not comparable with the experimental data.

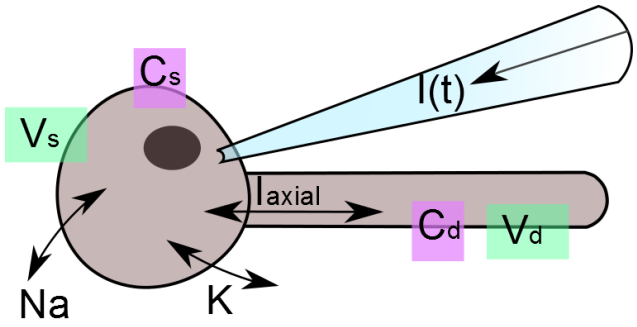

Figure 7.13: A two-compartment model of the neuron that includes a passive dendritic compartment and an axial current.

7.5 Summary

The use of conductance-based Hodgkin-Huxley models relies on robust parameter fitting. This chapter presents an addition to previous work on current-based methods of multi-parameter optimisation, that rearranges the ion channel gating variables into integral form to reduce the influence of noise on estimates of maximal conductance parameters and improve computational efficiency. Error landscapes visually demonstrate the benefit of such methods over widely used voltage-based parameter optimisation, though the shape of error landscape minima raises philosophical questions about homeostasis in neuronal biophysics. With higher dimensionality optimisation, matrix methods of computation come to the fore as the preferred method of maximal conductance optimisation.

8. Discussion

The excitatory cells within the immature mouse barrel cortex have long been used as a model of neuronal development (Osterheld-Haas and Hornung 1996, Larsen and Callaway 2006, Ashby and Isaac 2011, Li, Fertuzinhos et al. 2013). Though applications of electrophysiology and mathematical models of neuronal spiking behaviours have been used to explain behaviour of mature neurons, characterisation of the biophysical changes underpinning neuronal development has thus far evaded the field. When considering the covariant, interrelated and complex biophysical changes during development, the question arises of why they are necessary at all, why the neuron is not born with an 'optimum' balance of biophysical features that produce the behaviours seen in mature brains. Thorough description of neuronal spiking, biophysics of the cell membrane, and neuron morphology, then subsequent observation of how these observables vary with respect to age and to one another, is necessary to begin addressing this question, before mathematical models can be employed to make appropriate predictions.

Focussing on neurons found in this region between postnatal days P3 and P11, this thesis presents a biophysical view of the development of such cortical neurons, accounting for morphological growth, differentiation and cell-type, early networks of gap junctions, changing input resistance and membrane capacitance, increasing surface area, and changing proportions of ion channels that result in an action potential that grows in height whilst decreasing in width (or duration). The overall effect is a neuron that undergoes many perturbations throughout its maturation.

The predictions of increased surface area with maturation returned by the passive dynamics recordings were in pleasing agreement with the increase in neuronal size and complexity observed in confocal images of neuronal morphology. The nonlinear relationship between surface area and postnatal age that begins to emerge corresponds to previous reports of a critical period in neuronal development, specifically the massive increase in the number of dendritic spines (Ashby and Isaac 2011). These observed changes in passive dynamics, and hence surface area, were shown in this thesis to be free from the contribution of gap-junction-coupled cells, though a possible development-dependence of gap-junction-coupled cells was detected.

How are we to interpret these findings? The lack of linearity in both action potential waveform development and, potentially, neuronal surface area growth as a function of membrane capacitance, points towards homeostatic mechanisms, where biophysical phenomena compensate for one another (O'Leary and Wyllie 2011, O'Leary, Williams et al. 2013, O'Leary, Williams et al. 2014). Such compensation allows the neuron to survive and thrive whilst undergoing extreme changes in position, shape and function. Within this homeostasis hypothesis, we can hypothesise that the specific and highly complex patterns of action potentials fired by mature neurons do not happen by happy coincidence. Instead, we can think of the period of neuronal maturation as a time when neurons are exploring a state-space of different biophysical parameters, finding the combinations of factors that allow them to communicate efficiently, whilst not breaching the limits of their survival and basic function. As their communication improves, first aided by gap junctions, later by synaptic plasticity (Todd, Kristan et al. 2010), the active inputs drive gene expression that further tune their biophysics and the resultant activity. The broad shape of the immature action potential can therefore be thought not as an unfortunate consequence of an immature network, but as the most sensible starting point for a developing neuron, where both Hebbian and spike-time-dependent plasticity are aided by the highest probability of spike coincidence between it and its neighbours (Egger, Feldmeyer et al. 1999, Connors 2017).

This work also presents an improved method of optimising the parameters of simple conductance-based Hodgkin-Huxley models (Hodgkin and Huxley 1952, Morse, Davison et al. 2001, Lepora, Overton et al. 2012), resulting in models that can be more finely tuned to the changing biophysical properties of the maturing neuron, whilst resisting vulnerability to experimental noise. This improvement was achieved by the application of previously reported current-comparison methods (Lepora, Overton et al. 2012) in place of more traditional voltage-comparison methods, and expanded upon by improving the computational efficiency through the derivation of algebraic expressions for the ion-channel gating variables. Combined with established matrix-algebra methods, this allowed target parameters from artificial data sets to be found with high accuracy and speed.

Hodgkin-Huxley models were optimised against realistic synthetic data not to provide a complete phenomenological description of a single cell, but to provide predictions of broad dynamical trends that could be tested against data from real regular-spiking cortical neurons. Whilst the computational work presented here aimed for simplicity in all models, comparison with real experimental data illuminated the necessity of a minimum of two compartments in Hodgkin-Huxley models, as the gross simplifications inherent in single compartment models

strayed too far from realism, making experimental predictions impossible. Though complicated combinations of ion channels were avoided, the necessity of at least three voltage-gated ion channels was demonstrated, as without an initiating sodium current, a fast hyperpolarising potassium current, and a modifying slow potassium current, the diversity of spiking behaviours couldn't hope to be replicated.

Quite by accident, the widely used tracer molecule Neurobiotin was noticed to have an adverse dose-dependent effect on the biophysics of the neurons studied, evident in the effects it had on the action potential waveform. Such a result has been reported, both anecdotally and in the literature (Xi and Xu 1996, Schlösser, ten Bruggencate et al. 1998), but has, to the best of our knowledge, never been investigated for dose dependency. To researchers, the attraction of Neurobiotin over other similar tracer molecules has been its ability to traverse gap-junctions and illuminate gap-junction coupled networks of cells (Rörig, Klausa et al. 1996, Montoro and Yuste 2004, Todd, Kristan et al. 2010); it has been asserted previously that for such networks to be robustly detected, relatively large quantities of Neurobiotin are needed, of concentrations of 5mg/ml or more (Káradóttir and Attwell 2006). Contravening this, we find that low doses of Neurobiotin (1mg/ml) can robustly detect gap junction-coupled cells, without detrimental effect to the active dynamics. We hope that this finding will inform future experimentalists who may also wish to collect concurrent electrophysiological and morphological data.

There are weaknesses in the approach presented in this thesis to be considered and improved upon, if possible, in future work. Within this experimental approach, the discretisation of the age and therefore implied development of the mouse pups used set a limitation on the precision of the results that can be asserted: each age reported comes with an error bar of ±24 hours. This uncertainty can be assuaged in future experiments by not only considering the age of the pups, but also their weight and brain size, and using these additional factors to inform our measure of 'postnatal development'. An additional consideration is that it may be that the age of the cell, rather than the age of the animal that is important. Though these different measures are correlated, they are not necessarily the same. Meanwhile, the ongoing migration of cells, particularly in younger ages, provided a complicating factor; should cells be considered 'barrel cortex cells' if they are merely passing through to more external cortical layers? To address this, the lower limit of development for these studies could be set to the period at which neuronal migration to the barrel cortex is thought to be complete, but this may exclude the first two postnatal weeks that are so dynamic, and so interesting (Osterheld-Haas and Hornung 1996).

The experimental methodology of ex-vivo slice work is unfortunately no more than a proxy for true neuronal action. The damage done to the cortex can be minimised through fast and careful dissection of the brain, but ex-vivo slice electrophysiology will fundamentally sever and disrupt functional networks. For this reason, in vivo electrophysiology, in either awake or anesthetised animals will always be preferable, though it does introduce a great many other challenges, for example, ensuring consistent levels of sedation (Margrie, Brecht et al. 2002, Miquelajauregui, Kribakaran et al. 2015) and parsing intrinsic and passive dynamics from active dynamics under the effects of constant synaptic activity.

It is a large and rather obvious caveat of this thesis that synaptic events are not considered. The synaptic inputs to developing neurons can be presumed to increase in strength and frequency over maturation, as cortical networks form, and sensory experiences rise in number and complexity. Synaptic plasticity studies are numerous (Harris-Warrick and Marder 1991, Nadim and Bucher 2014, Leighton and Lohmann 2016), and indicate critical periods of accelerated synaptic input, shifting the parameter state-space that limits the other biophysical parameters, such as action potential waveform. Moreover, the geometrical effects of synapses on neuronal biophysics has not been touched upon, despite the established knowledge that plasticity drives the growth of axonal boutons and dendritic spines in a great diversity of shapes; this diversity of geometries at even the smallest levels has consequences for the electric signals sent, and hence the information encoded (Major, Larkman et al. 1994, Biess, Korkotian et al. 2007, Rowan, DelCanto et al. 2016).

This thesis considers only one species and does not explore how the patterns of maturation are replicated across mammals. Certainly, it would be interesting to see what features of neuronal maturation are conserved, what aspects are prioritised in animals that reach maturity quickly, and which lead to the biggest cognitive deficits when disrupted. From this, intra-species homeostatic limits could be inferred, and related to both environment and evolution.

Regarding more attainable future work, the barrel cortex lends itself to studies of sensory deprivation, since whiskers can be trimmed, and tactile somatosensory input removed without great distress to the animal (Sun 2009, Ashby and Isaac 2011, Barrera, Chu et al. 2013). Whether the neurons within the barrels of trimmed whiskers remain in their immature state, firing low-amplitude and broad action potentials, or they mature into hyperexcitable cells that compensate for the lack of thalamocortical afferent connections with increased activity, could be investigated in future experiments.

The biophysical development of cortical neurons could be further investigated via comparison of the data presented here with mouse models of disrupted development. Indeed, such work has already been done by examining development in autistic spectrum disorder subtype Fragile-X syndrome in genetic knock-out mice (Domanski 2013). The comparison of development under the influence of Fragile-X, versus wild-type, may enlighten the particular mechanisms that decide regular spiking behaviour, and therefore effective and efficient neuronal communication. Paired with a computational approach, such investigations could elucidate which ion channels may be particularly affected by this disorder, or other conditions.

The above suggestions for future work address specific perturbations in development that could be investigated, but further work could delve into the present data and examine the subtleties of action potential waveform phase-plots in more depth, particularly if computational methods were included. Such analysis could illuminate how the waveform of the AP is influenced not only by the type and proportion of ion channels, but also by the coherence of their dynamics and their synchronisation, as has been previously suggested (Naundorf, Wolf et al. 2006). The cooperative dependency of voltage-gated ion channels is an interesting problem for computational and experimental neuroscientists alike to consider. It could lead to investigations of the electrostatic interplay between ion channels and other features of neurons over development, and address suggestions that the initiation and propagation of the action potential is determined not by simplistic input-output circuitry, but by geometrically defined electrical dipoles (Telenczuk, Fontaine et al. 2017).

From the work presented in this thesis and the literature referenced, how are we to describe the developing neocortex in simplistic terms? One could imagine the functional networks of neurons, like those found within the barrel cortex, as musicians in an orchestra that have never played together before. Starting with spontaneous and short bursts of activity, they gradually tune their frequencies. They begin simple coherent rhythms, before moving onto complex synchronised patterns of communication. The information does not come from one individual alone, though each individual's contribution is crucial. Rather, the collective determines the output of the individual, and vice versa. They learn and grow by listening to one another.

9. Bibliography

Agmon, A. and B. W. Connors (1991). "Thalamocortical responses of mouse somatosensory (barrel) cortex in vitro." Neuroscience **41**(2-3): 365-379.

Amsalem, O., W. Geit, E. Muller, H. Markram and I. Segev (2016). "From Neuron Biophysics to Orientation Selectivity in Electrically Coupled Networks of Neocortical L2/3 Large Basket Cells." Cerebral Cortex (New York, N.Y. : 1991) **26**(8): 3655-3668.

Andersen, S., A. D. Jackson and T. Heimburg (2009). "Towards a thermodynamic theory of nerve pulse propagation." Progress in Neurobiology **88**(2): 104-113.

Arakawa, H. and R. S. Erzurumlu (2015). "Role of whiskers in sensorimotor development of C57BL/6 mice." Behavioural Brain Research **287**: 146-155.

Ashby, M. C. and J. T. Isaac (2011). "Maturation of a recurrent excitatory neocortical circuit by experience-dependent unsilencing of newly formed dendritic spines." Neuron **70**(3): 510-521.

Bahrey, H. L. and W. J. Moody (2002). "Early development of voltage-gated ion currents and firing properties in neurons of the mouse cerebral cortex." Journal of Neurophysiology **89**(4): 1761-1773.

Bahrey, H. L. and W. J. Moody (2003). "Voltage-gated currents, dye and electrical coupling in the embryonic mouse neocortex." Cerebral Cortex (New York, N.Y. : 1991) **13**(3): 239-251.

Baranauskas, G. (2007). "Ionic Channel Function in Action Potential Generation: Current Perspective." Molecular Neurobiology **35**(2): 129-150.

Barbour, B. (2014). "Electronics for electrophysiologists."

Barkley, M. S. and R. FitzGerald (1990). "Influence of embryonic and maternal genotype on gestational events in the mouse." Journal of Reproduction and Fertility **89**(1): 285-291.

Barrera, K., P. Chu, J. Abramowitz, R. Steger, R. L. Ramos and J. C. Brumberg (2013). "Organization of myelin in the mouse somatosensory barrel cortex and the effects of sensory deprivation." Developmental Neurobiology **73**(4): 297-314.

Barry, P. H. (1994). "JPCalc, a software package for calculating liquid junction potential corrections in patch-clamp, intracellular, epithelial and bilayer measurements and for correcting junction potential measurements." Journal of Neuroscience Methods **51**(1): 107-116.

Bean, B. P. (2007). "The action potential in mammalian central neurons." Nature Reviews. Neuroscience **8**(6): 451-465.

Begum, R., Y. Bakiri, K. E. Volynski and D. M. Kullmann (2016). "Action potential broadening in a presynaptic channelopathy." Nature Communications **7**: 12102.

Belousov, A. B. and J. D. Fontes (2013). "Neuronal gap junctions: making and breaking connections during development and injury." Trends in Neurosciences **36**(4): 227-236.

Belousov, A. B., J. D. Fontes, M. Freitas-Andrade and C. C. Naus (2017). "Gap junctions and hemichannels: communicating cell death in neurodevelopment and disease." BMC Cell Biology **18**(1): 4.

Ben-Ari, Y., E. Cherubini, R. Corradetti and J. L. Gaiarsa (1989). "Giant synaptic potentials in immature rat CA3 hippocampal neurones." The Journal of Physiology **416**: 303-325.

Bi, G. Q. and M. M. Poo (1998). "Synaptic modifications in cultured hippocampal neurons: dependence on spike timing, synaptic strength, and postsynaptic cell type." The Journal of Neuroscience : the official journal of the Society for Neuroscience **18**(24): 10464-10472.

Biess, A., E. Korkotian and D. Holcman (2007). "Diffusion in a dendritic spine: The role of geometry." Physical Review E **76**(2).

Bigiani, A., R. Cristiani, F. Fieni, V. Ghiaroni, P. Bagnoli and P. Pietra (2002). "Postnatal development of membrane excitability in taste cells of the mouse vallate papilla." The Journal of Neuroscience : the official journal of the Society for Neuroscience **22**(2): 493-504.

Boudkkazi, S., L. Fronzaroli-Molinieres and D. Debanne (2011). "Presynaptic action potential waveform determines cortical synaptic latency." The Journal of physiology **589**(Pt 5): 1117-1131.
Box, G. E. P. D., Norman R (1987). Empirical model-building and response surfaces, John Wiley and Sons.
Bretscher, M. S. (1972). "Asymmetrical lipid bilayer structure for biological membranes." Nature: New biology **236**(61): 11-12.
Brookings, T., M. L. Goeritz and E. Marder (2014). "Automatic parameter estimation of multicompartmental neuron models via minimization of trace error with control adjustment." Journal of Neurophysiology **112**(9): 2332-2348.
Buhry, L., M. Pace and S. Saïghi (2012). "Global parameter estimation of an Hodgkin–Huxley formalism using membrane voltage recordings: Application to neuro-mimetic analog integrated circuits.", Neurocomputing **81**:75-85
Callaway, E. M. and V. Borrell (2011). "Developmental sculpting of dendritic morphology of layer 4 neurons in visual cortex: influence of retinal input." The Journal of Neuroscience : the official journal of the Society for Neuroscience **31**(20): 7456-7470.
Campbell, R. E., E. Ducret, R. Porteous, X. Liu, M. K. Herde, K. Wellerhaus, S. Sonntag, K. Willecke and A. E. Herbison (2011). "Gap Junctions between Neuronal Inputs But Not Gonadotropin-Releasing Hormone Neurons Control Estrous Cycles in the Mouse." Endocrinology **152**(6): 2290-2301.
Catterall, W. A. (2000). "From ionic currents to molecular mechanisms: the structure and function of voltage-gated sodium channels." Neuron **26**(1): 13-25.
Ciarleglio, C. M., A. S. Khakhalin, A. F. Wang, A. C. Constantino, S. P. Yip and C. D. Aizenman (2015). "Multivariate analysis of electrophysiological diversity of Xenopus visual neurons during development and plasticity." eLife **4**.
Cina, C., J. F. Bechberger, M. A. Ozog and C. Naus (2007). "Expression of connexins in embryonic mouse neocortical development." Journal of Comparative Neurology **504**(3): 298-313.
Connors, B. W. (2017). "Synchrony and so much more: Diverse roles for electrical synapses in neural circuits." Developmental Neurobiology **77**(5): 610-624.
Connors, B. W., L. S. Benardo and D. A. Prince (1983). "Coupling between neurons of the developing rat neocortex." Journal of Neuroscience **3**(4): 773-782.
Connors, B. W. and M. J. Gutnick (1990). "Intrinsic firing patterns of diverse neocortical neurons." Trends in Neurosciences **13**(3): 99-104.
Connors, B. W., M. J. Gutnick and D. A. Prince (1982). "Electrophysiological properties of neocortical neurons in vitro." Journal of Neurophysiology **48**(6): 1302-1320.
Curti, S., G. Hoge, J. I. Nagy and A. E. Pereda (2012). "Synergy between Electrical Coupling and Membrane Properties Promotes Strong Synchronization of Neurons of the Mesencephalic Trigeminal Nucleus." The Journal of Neuroscience **32**(13): 4341-4359.
D'Aguanno, A., B. L. Bardakjian and P. L. Carlen (1986). "Passive neuronal membrane parameters: comparison of optimization and peeling methods." IEEE transactions on bio-medical engineering **33**(12): 1188-1196.
Daou, A., M. T. Ross, F. Johnson, R. L. Hyson and R. Bertram (2013). "Electrophysiological characterization and computational models of HVC neurons in the zebra finch." Journal of Neurophysiology **110**(5): 1227-1245.
Dehorter, N., F. J. Michel, T. Marissal, Y. Rotrou, B. Matrot, C. Lopez, M. D. Humphries and C. Hammond (2011). "Onset of Pup Locomotion Coincides with Loss of NR2C/D-Mediated Cortico-Striatal EPSCs and Dampening of Striatal Network Immature Activity." Frontiers in Cellular Neuroscience **5**: 24.
Deng, P.-Y., Z. Rotman, J. A. Blundon, Y. Cho, J. Cui, V. Cavalli, S. S. Zakharenko and V. A. Klyachko (2013). "FMRP Regulates Neurotransmitter Release and Synaptic Information Transmission by Modulating Action Potential Duration via BK Channels." Neuron **77**(4): 696-711.

Domanski, A. P. F. (2013). A Functional Dissection of Abnormal Signal Processing Performed by the Somatosensory Cortex of young Fmr1-KO mice. Doctor of Philosophy, University of Edinburgh.
Durand, D. (1984). "The somatic shunt cable model for neurons." Biophysical Journal **46**(5): 645-653.
Durand, D., P. L. Carlen, N. Gurevich, A. Ho and H. Kunov (1983). "Electrotonic parameters of rat dentate granule cells measured using short current pulses and HRP staining." Journal of Neurophysiology **50**(5): 1080-1097.
Egger, V., D. Feldmeyer and B. Sakmann (1999). "Coincidence detection and changes of synaptic efficacy in spiny stellate neurons in rat barrel cortex." Nature Neuroscience **2**(12): 1098-1105.
Elias, L. and A. R. Kriegstein (2008). "Gap junctions: multifaceted regulators of embryonic cortical development." Trends in Neurosciences **31**(5): 243-250.
Ermentrout, G. B. and D. H. Terman (2010). The Hodgkin–Huxley Equations. Mathematical Foundations of Neuroscience. New York, NY, Springer New York**:** 1-28.
Feldman, D. E. and M. Brecht (2005). "Map Plasticity in Somatosensory Cortex." Science **310**(5749): 810-815.
Feldmeyer, D., V. Egger, J. Lübke and B. Sakmann (1999). "Reliable synaptic connections between pairs of excitatory layer 4 neurones within a single 'barrel' of developing rat somatosensory cortex." The Journal of Physiology **521**(1): 169-190.
Feldmeyer, D., J. Lübke, R. A. Silver and B. Sakmann (2002). "Synaptic connections between layer 4 spiny neurone-layer 2/3 pyramidal cell pairs in juvenile rat barrel cortex: physiology and anatomy of interlaminar signalling within a cortical column." The Journal of Physiology **538**(Pt 3): 803-822.
Friedrich, P., M. Vella, A. I. Gulyás, T. F. Freund and S. Káli (2014). "A flexible, interactive software tool for fitting the parameters of neuronal models." Frontiers in Neuroinformatics **8**: 63.
Geit, W. V., E. D. Schutter and P. Achard (2008). "Automated neuron model optimization techniques: a review." Biological Cybernetics **99**(4-5): 241-251.
Gentet, L. J., G. J. Stuart and J. D. Clements (2000). "Direct measurement of specific membrane capacitance in neurons." Biophysical Journal **79**(1): 314-320.
Gibson, J. R., M. Beierlein and B. W. Connors (2005). "Functional Properties of Electrical Synapses Between Inhibitory Interneurons of Neocortical Layer 4." Journal of Neurophysiology **93**(1): 467-480.
Gjorgjieva, J., R. A. Mease, W. J. Moody and A. L. Fairhall (2014). "Intrinsic neuronal properties switch the mode of information transmission in networks." PLoS computational biology **10**(12).
Goodenough, D. A. and D. L. Paul (2009). "Gap Junctions." Cold Spring Harbor Perspectives in Biology **1**(1).
Guan, D., W. E. Armstrong and R. C. Foehring (2015). "Electrophysiological properties of genetically identified subtypes of layer 5 neocortical pyramidal neurons: Ca^{2+} dependence and differential modulation by norepinephrine." Journal of Neurophysiology **113**(7): 2014-2032.
Gutman, G. A., K. G. Chandy, S. Grissmer, M. Lazdunski, D. McKinnon, L. A. Pardo, G. A. Robertson, B. Rudy, M. C. Sanguinetti, W. Stühmer and X. Wang (2005). "International Union of Pharmacology. LIII. Nomenclature and molecular relationships of voltage-gated potassium channels." Pharmacological Reviews **57**(4): 473-508.
Haas, J. S. (2015). "A new measure for the strength of electrical synapses." Frontiers in Cellular Neuroscience **9**: 378.
Hady, A. and B. B. Machta (2015). "Mechanical surface waves accompany action potential propagation." Nature Communications **6**: 6697.
Harris-Warrick, R. M. and E. Marder (1991). "Modulation of Neural Networks for Behavior." Annual Review of Neuroscience **14**(1): 39-57.

Hatch, R. J., G. D. C. D. C. Mendis, K. Kaila, C. A. Reid and S. Petrou (2017). "Gap Junctions Link Regular-Spiking and Fast-Spiking Interneurons in Layer 5 Somatosensory Cortex." Frontiers in Cellular Neuroscience **11**: 204.
Hay, E., S. Hill, F. Schürmann, H. Markram and I. Segev (2011). "Models of Neocortical Layer 5b Pyramidal Cells Capturing a Wide Range of Dendritic and Perisomatic Active Properties." PLoS Computational Biology **7**(7).
Hebb, D. (1949). The organization of behavior; a neuropsychological theory. Oxford, England, Wiley.
Heiurg, T. H. O. and A. D. Jackson (2007). "ON THE ACTION POTENTIAL AS A PROPAGATING DENSITY PULSE AND THE ROLE OF ANESTHETICS." Biophysical Reviews and Letters **02**(01): 57-78.
Hille, B. (2001). "Ion Channels of Excitable Membranes, Third Edition.", Sinauer Associates, Inc, Sunderland Massachusettes, USA
Hodgkin, A. L. and A. F. Huxley (1952). "A quantitative description of membrane current and its application to conduction and excitation in nerve." The Journal of Physiology **117**(4): 500-544.
Holcman, D. and R. Yuste (2015). "The new nanophysiology: regulation of ionic flow in neuronal subcompartments." Nature Reviews. Neuroscience **16**(11): 685-692.
Huang, Q., D. Zhou and M. DiFiglia (1992). "Neurobiotin, a useful neuroanatomical tracer for in vivo anterograde, retrograde and transneuronal tract-tracing and for in vitro labeling of neurons." Journal of Neuroscience Methods **41**(1): 31-43.
Huang, S., S. Hong and E. Schutter (2015). "Non-linear leak currents affect mammalian neuron physiology." Frontiers in Cellular Neuroscience **9**: 432.
Ito, M. and T. Oshima (1965). "Electrical behaviour of the motoneurone membrane during intracellularly applied current steps." The Journal of Physiology **180**(3): 607-635.
Jadhav, S. P., J. Wolfe and D. E. Feldman (2009). "Sparse temporal coding of elementary tactile features during active whisker sensation." Nature Neuroscience **12**(6): 792-800.
Kandel, E. R. S., James H.; Jessell, Thomas M.; Siegelbaum, Steven A.; Hudspeth, A.J. (2013). Principles of Neural Science, The McGraw-Hill Companies.
Kandler, K. and L. C. Katz (1995). "Neuronal coupling and uncoupling in the developing nervous system." Current Opinion in Neurobiology **5**(1): 98-105.
Káradóttir, R. and D. Attwell (2006). "Combining patch-clamping of cells in brain slices with immunocytochemical labeling to define cell type and developmental stage." Nature Protocols **1**(4): 1977-1986.
Katz, B. and R. Miledi (1967). "A study of synaptic transmission in the absence of nerve impulses." The Journal of Physiology **192**(2): 407-436.
Katz, L. C. (1995). "Coordination of vertebrate cellular assemblies by gap junctions." Seminars in Developmental Biology **6**(2): 117-125.
Khazipov, R. and H. J. Luhmann (2006). "Early patterns of electrical activity in the developing cerebral cortex of humans and rodents." Trends in Neurosciences **29**(7): 414-418.
Kim, H., L. A. Major and K. E. Jones (2009). "Derivation of cable parameters for a reduced model that retains asymmetric voltage attenuation of reconstructed spinal motor neuron dendrites." Journal of Computational Neuroscience **27**(3): 321-336.
Kimm, T., Z. M. Khaliq and B. P. Bean (2015). "Differential Regulation of Action Potential Shape and Burst-Frequency Firing by BK and Kv2 Channels in Substantia Nigra Dopaminergic Neurons." The Journal of Neuroscience **35**(50): 16404-16417.
Kita, H. and W. Armstrong (1991). "A biotin-containing compound N-(2-aminoethyl)biotinamide for intracellular labeling and neuronal tracing studies: comparison with biocytin." Journal of Neuroscience Methods **37**(2): 141-150.
Kita, T., H. Kita and S. T. Kitai (1984). "Passive electrical membrane properties of rat neostriatal neurons in an in vitro slice preparation." Brain Research **300**(1): 129-139.

Ko, H., L. Cossell, C. Baragli, J. Antolik, C. Clopath, S. B. Hofer and T. D. Mrsic-Flogel (2013). "The emergence of functional microcircuits in visual cortex." Nature **496**(7443): 96-100.
Kole, M. and G. J. Stuart (2012). "Signal Processing in the Axon Initial Segment." Neuron **73**(2): 235-247.
Krouchev, N. I., F. Rattay, M. Sawan and A. Vinet (2015). "From Squid to Mammals with the HH Model through the Nav Channels' Half-Activation-Voltage Parameter." PLoS One **10**(12).
Lankarany, M., W. P. Zhu and M. N. S. Swamy (2014). "Joint estimation of states and parameters of Hodgkin–Huxley neuronal model using Kalman filtering." Neurocomputing **136**: 289-299.
Larsen, D. D. and E. M. Callaway (2006). "Development of layer-specific axonal arborizations in mouse primary somatosensory cortex." The Journal of Comparative Neurology **494**(3): 398-414.
Leighton, A. H. and C. Lohmann (2016). "The Wiring of Developing Sensory Circuits—From Patterned Spontaneous Activity to Synaptic Plasticity Mechanisms." Frontiers in Neural Circuits **10**: 71.
LeMasson, G., E. Marder and L. F. Abbott (1993). "Activity-dependent regulation of conductances in model neurons." Science (New York, N.Y.) **259**(5103): 1915-1917.
Lepora, N. F., C. P. Blomeley, D. Hoyland, E. Bracci, P. G. Overton and K. Gurney (2011). "A simple method for characterizing passive and active neuronal properties: application to striatal neurons." European Journal of Neuroscience **34**(9): 1390-1405.
Lepora, N. F., P. G. Overton and K. Gurney (2012). "Efficient fitting of conductance-based model neurons from somatic current clamp." Journal of Computational Neuroscience **32**(1): 1-24.
Li, H., S. Fertuzinhos, E. Mohns, T. S. Hnasko, M. Verhage, R. Edwards, N. Sestan and M. C. Crair (2013). "Laminar and columnar development of barrel cortex relies on thalamocortical neurotransmission." Neuron **79**(5): 970-986.
Liu, P. W., N. T. Blair and B. P. Bean (2017). "Action Potential Broadening in Capsaicin-Sensitive DRG Neurons from Frequency-Dependent Reduction of Kv3 Current." The Journal of Neuroscience **37**(40): 9705-9714.
Liu, Z., J. Golowasch, E. Marder and L. F. Abbott (1998). "A model neuron with activity-dependent conductances regulated by multiple calcium sensors." The Journal of Neuroscience : the official journal of the Society for Neuroscience **18**(7): 2309-2320.
Llinás, R. R. (2014). "Intrinsic electrical properties of mammalian neurons and CNS function: a historical perspective." Frontiers in Cellular Neuroscience **8**: 320.
Luhmann, H. J., R. A. Reiprich, I. Hanganu and W. Kilb (2000). "Cellular physiology of the neonatal rat cerebral cortex: intrinsic membrane properties, sodium and calcium currents." Journal of Neuroscience Research **62**(4): 574-584.
Luhmann, H. J., D. Schubert, R. Kötter and J. F. Staiger (2011). "Cellular Morphology and Physiology of the Perinatal Rat Cerebral Cortex." Developmental Neuroscience **21**(3-5): 298-309.
Luhmann, H. J., D. Schubert, ouml, R. tter and J. F. Staiger (1999). "Cellular Morphology and Physiology of the Perinatal Rat Cerebral Cortex." Developmental Neuroscience **21**(3-5): 298-309.
Major, G., A. U. Larkman, P. Jonas, B. Sakmann and J. J. Jack (1994). "Detailed passive cable models of whole-cell recorded CA3 pyramidal neurons in rat hippocampal slices." The Journal of Neuroscience : the official journal of the Society for Neuroscience **14**(8): 4613-4638.
Marder, E. and J.-M. Goaillard (2006). "Variability, compensation and homeostasis in neuron and network function." Nature Reviews Neuroscience **7**(7).

Margrie, T. W., M. Brecht and B. Sakmann (2002). "In vivo, low-resistance, whole-cell recordings from neurons in the anaesthetized and awake mammalian brain." Pflugers Archiv : European Journal of Physiology **444**(4): 491-498.
Mason, A. and A. Larkman (1990). "Correlations between morphology and electrophysiology of pyramidal neurons in slices of rat visual cortex. II. Electrophysiology." The Journal of Neuroscience : the official journal of the Society for Neuroscience **10**(5): 1415-1428.
McCormick, D. A. and D. A. Prince (1987). "Post-natal development of electrophysiological properties of rat cerebral cortical pyramidal neurones." The Journal of physiology **393**: 743-762.
Mease, R. A., M. Famulare, J. Gjorgjieva, W. J. Moody and A. L. Fairhall (2013). "Emergence of Adaptive Computation by Single Neurons in the Developing Cortex." The Journal of Neuroscience **33**(30).
Mills, S. L. and S. C. Sey (1998). "The kinetics of tracer movement through homologous gap junctions in the rabbit retina." Visual Neuroscience **15**(4): 765-777.
Miquelajauregui, A., S. Kribakaran, R. Mostany, A. Badaloni, G. G. Consalez and C. Portera-Cailliau (2015). "Layer 4 pyramidal neurons exhibit robust dendritic spine plasticity in vivo after input deprivation." The Journal of Neuroscience : the official journal of the Society for Neuroscience **35**(18): 7287-7294.
Mizuno, H., W. Luo, E. Tarusawa, Y. M. Saito, T. Sato, Y. Yoshimura, S. Itohara and T. Iwasato (2014). "NMDAR-Regulated Dynamics of Layer 4 Neuronal Dendrites during Thalamocortical Reorganization in Neonates." Neuron **82**(2): 365-379.
Montal, M. and P. Mueller (1972). "Formation of bimolecular membranes from lipid monolayers and a study of their electrical properties." Proceedings of the National Academy of Sciences of the United States of America **69**(12): 3561-3566.
Montoro, R. J. and R. Yuste (2004). "Gap junctions in developing neocortex: a review." Brain Research Reviews **47**(1-3): 216-226.
Moody, W. J. and M. M. Bosma (2005). "Ion Channel Development, Spontaneous Activity, and Activity-Dependent Development in Nerve and Muscle Cells." Physiological Reviews **85**(3).
Morse, T., A. Davison and M. Hines (2001). Parameter space reduction in neuron model optimization through minimization of residual voltage clamp current. 31st Annual Meeting of the Society for Neuroscience, San Diego,CA, USA, 10–15 November 2001, Society for Neuroscience Abstracts. **27**.
Murray, L. (2015). Early postnatal development of intrinsic escitability and synaptic input in the mouse barrel cortex, University of Bristol.
Murray, S. A., J. L. Morgan, C. Kane, Y. Sharma, C. S. Heffner, J. Lake and L. Donahue (2010). "Mouse Gestation Length Is Genetically Determined." PLoS One **5**(8).
Nadim, F. and D. Bucher (2014). "Neuromodulation of neurons and synapses." Current Opinion in Neurobiology **29**: 48-56.
Nakamura, Y., H. Harada, N. Kamasawa, K. Matsui, J. S. Rothman, R. Shigemoto, A. R. Silver, D. A. DiGregorio and T. Takahashi (2015). "Nanoscale Distribution of Presynaptic Ca2+ Channels and Its Impact on Vesicular Release during Development." Neuron **85**(1): 145-158.
Naundorf, B., F. Wolf and M. Volgushev (2006). "Unique features of action potential initiation in cortical neurons." Nature **440**(7087).
Neher, E. (1992). Correction for liquid junction potentials in patch clamp experiments. Ion Channels. B. Rudy.
Niday, Z., V. E. Hawkins, H. Soh, D. K. Mulkey and A. V. Tzingounis (2017). "Epilepsy-Associated KCNQ2 Channels Regulate Multiple Intrinsic Properties of Layer 2/3 Pyramidal Neurons." The Journal of Neuroscience : the official journal of the Society for Neuroscience **37**(3): 576-586.
O'Leary, T. and E. Marder (2016). "Temperature-Robust Neural Function from Activity-Dependent Ion Channel Regulation." Current Biology : CB **26**(21): 2935-2941.

O'Leary, T., A. H. Williams, J. S. Caplan and E. Marder (2013). "Correlations in ion channel expression emerge from homeostatic tuning rules." Proceedings of the National Academy of Sciences of the United States of America **110**(28): 54.
O'Leary, T., A. H. Williams, A. Franci and E. Marder (2014). "Cell types, network homeostasis, and pathological compensation from a biologically plausible ion channel expression model." Neuron **82**(4): 809-821.
O'Leary, T. and D. J. A. Wyllie (2011). "Neuronal homeostasis: time for a change?" The Journal of Physiology **589**(20): 4811-4826.
Osterheld-Haas, M. C. and J. P. Hornung (1996). "Laminar development of the mouse barrel cortex: effects of neurotoxins against monoamines." Experimental Brain Research **110**(2): 183-195.
P. Thévenaz, M. U. (2007). "User-Friendly Semiautomated Assembly of Accurate Image Mosaics in Microscopy." Microscopy Research and Technique **70**(2): 135-146.
Palacio, S., V. Chevaleyre, D. H. Brann, K. D. Murray, R. A. Piskorowski and J. S. Trimmer (2017). "Heterogeneity in Kv2 Channel Expression Shapes Action Potential Characteristics and Firing Patterns in CA1 versus CA2 Hippocampal Pyramidal Neurons." eNeuro **4**(4).
Parker, P. R., S. J. Cruikshank and B. W. Connors (2009). "Stability of electrical coupling despite massive developmental changes of intrinsic neuronal physiology." The Journal of Neuroscience : the official journal of the Society for Neuroscience **29**(31): 9761-9770.
Peinado, A., R. Yuste and L. C. Katz (1993). "Extensive dye coupling between rat neocortical neurons during the period of circuit formation." Neuron **10**(1): 103-114.
Penn, A. A., R. O. Wong and C. J. Shatz (1994). "Neuronal coupling in the developing mammalian retina." The Journal of Neuroscience : the official journal of the Society for Neuroscience **14**(6): 3805-3815.
Pereda, A. E. (2016). "The Variable Strength of Electrical Synapses." Neuron **90**(5): 912-914.
Picken Bahrey, H. L. and W. J. Moody (2003). "Early development of voltage-gated ion currents and firing properties in neurons of the mouse cerebral cortex." Journal of Neurophysiology **89**(4): 1761-1773.
Pospischil, M., M. Toledo-Rodriguez, C. Monier, Z. Piwkowska, T. Bal, Y. Frégnac, H. Markram and A. Destexhe (2008). "Minimal Hodgkin–Huxley type models for different classes of cortical and thalamic neurons." Biological Cybernetics **99**(4-5): 427-441.
Rakic, P. (1988). "Specification of cerebral cortical areas." Science (New York, N.Y.) **241**(4862): 170-176.
Rall, W. (1969). "Time constants and electrotonic length of membrane cylinders and neurons." Biophysical Journal **9**(12): 1483-1508.
Richter, L. M. and J. Gjorgjieva (2017). "Understanding neural circuit development through theory and models." Current Opinion in Neurobiology **46**: 39-47.
Rinberg, A., A. L. Taylor and E. Marder (2013). "The Effects of Temperature on the Stability of a Neuronal Oscillator." PLoS Computational Biology **9**(1).
Rörig, B., G. Klausa and B. Sutor (1996). "Intracellular acidification reduced gap junction coupling between immature rat neocortical pyramidal neurones." The Journal of Physiology **490 (Pt 1)**: 31-49.
Rowan, M., G. DelCanto, J. J. Yu, N. Kamasawa and J. M. Christie (2016). "Synapse-Level Determination of Action Potential Duration by K+ Channel Clustering in Axons." Neuron.
Sabatini, B. L. and W. G. Regehr (1997). "Control of neurotransmitter release by presynaptic waveform at the granule cell to Purkinje cell synapse." The Journal of Neuroscience : the official journal of the Society for Neuroscience **17**(10): 3425-3435.
Sabatini, B. L. and K. Svoboda (2000). "Analysis of calcium channels in single spines using optical fluctuation analysis." Nature **408**(6812): 589-593.
Schlösser, B., G. ten Bruggencate and B. Sutor (1998). "The intracellular tracer Neurobiotin alters electrophysiological properties of rat neostriatal neurons." Neuroscience Letters **249**(1): 13-16.

Schulz, D. J., J.-M. M. Goaillard and E. Marder (2006). "Variable channel expression in identified single and electrically coupled neurons in different animals." Nature Neuroscience **9**(3): 356-362.
Schulz, D. J., J.-M. M. Goaillard and E. E. Marder (2007). "Quantitative expression profiling of identified neurons reveals cell-specific constraints on highly variable levels of gene expression." Proceedings of the National Academy of Sciences of the United States of America **104**(32): 13187-13191.
Segev, I., A. Friedman, E. L. White and M. J. Gutnick (1995). "Electrical consequences of spine dimensions in a model of a cortical spiny stellate cell completely reconstructed from serial thin sections." Journal of Computational Neuroscience **2**(2): 117-130.
Shaul, D., B. Yoav, A. G. Albert, S. Felix, M. Henry and S. Idan (2007). "A novel multiple objective optimization framework for constraining conductance-based neuron models by experimental data." Frontiers in Neuroscience **1**: 1.
Shi, W., A. Xianyu, Z. Han, X. Tang, Z. Li, H. Zhong, T. Mao, K. Huang and S.-H. Shi (2017). "Ontogenetic establishment of order-specific nuclear organization in the mammalian thalamus." Nature Neuroscience **20**(4): 516-528.
Shoji, H., K. Takao, S. Hattori and T. Miyakawa (2016). "Age-related changes in behavior in C57BL/6J mice from young adulthood to middle age." Molecular Brain **9**(1): 1-18.
Staiger, J. F., I. Flagmeyer, D. Schubert, K. Zilles, R. Kötter and H. J. Luhmann (2004). "Functional diversity of layer IV spiny neurons in rat somatosensory cortex: quantitative morphology of electrophysiologically characterized and biocytin labeled cells." Cerebral Cortex (New York, N.Y. : 1991) **14**(6): 690-701.
Stemmler, M. and C. Koch (1999). "How voltage-dependent conductances can adapt to maximize the information encoded by neuronal firing rate." Nature Neuroscience **2**(6): 521-527.
Storm, J. F. (1987). "Action potential repolarization and a fast after-hyperpolarization in rat hippocampal pyramidal cells." The Journal of Physiology **385**: 733-759.
Su, X., J.-J. Chen, L.-Y. Liu, Q. Huang, L.-Z. Zhang, X.-Y. Li, X.-N. He, W. Lu, S. Sun, H. Li and Y.-C. Yu (2017). "Neonatal CX26 removal impairs neocortical development and leads to elevated anxiety." Proceedings of the National Academy of Sciences **114**(12): 3228-3233.
Sun, Q.-Q. (2009). "Experience-Dependent Intrinsic Plasticity in Interneurons of Barrel Cortex Layer IV." Journal of Neurophysiology **102**(5): 2955-2973.
Szücs, A. and R. Huerta (2015). "Differential effects of static and dynamic inputs on neuronal excitability." Journal of Neurophysiology **113**(1): 232-243.
Talan, M. (1984). "Body temperature of C57BL/6J mice with age." Experimental Gerontology **19**(1): 25-29.
Taschenberger, H. and H. von Gersdorff (2000). "Fine-tuning an auditory synapse for speed and fidelity: developmental changes in presynaptic waveform, EPSC kinetics, and synaptic plasticity." The Journal of Neuroscience : the official journal of the Society for Neuroscience **20**(24): 9162-9173.
Telenczuk, M., B. Fontaine and R. Brette (2017). "The basis of sharp spike onset in standard biophysical models." PloS One **12**(4).
Tipler, P. A. and G. Mosca (2007). Physics for Scientists and Engineers, W. H. Freeman.
Todd, K. L., W. B. Kristan and K. A. French (2010). "Gap Junction Expression Is Required for Normal Chemical Synapse Formation." The Journal of Neuroscience **30**(45): 15277-15285.
Toledo-Rodriguez, M., B. Blumenfeld, C. Wu, J. Luo, B. Attali, P. Goodman and H. Markram (2004). "Correlation Maps Allow Neuronal Electrical Properties to be Predicted from Single-cell Gene Expression Profiles in Rat Neocortex." Cerebral Cortex **14**(12): 1310-1327.
Torben-Nielsen, B. and E. Schutter (2014). "Context-aware modeling of neuronal morphologies." Frontiers in Neuroanatomy **8**: 92.

Toth, B. A., M. Kostuk, D. C. Meliza, D. Margoliash and H. D. I. Abarbanel (2011). "Dynamical estimation of neuron and network properties I: variational methods." Biological Cybernetics **105**(3-4): 217-237.
Turco, L. J. and A. Kriegstein (1991). "Clusters of coupled neuroblasts in embryonic neocortex." Science **252**(5005): 563-566.
Turrigiano, G. G. and S. B. Nelson (2004). "Homeostatic plasticity in the developing nervous system." Nature Reviews Neuroscience **5**(2).
Valiullina, F., D. Akhmetshina, A. Nasretdinov, M. Mukhtarov, G. Valeeva, R. Khazipov and A. Rozov (2016). "Developmental Changes in Electrophysiological Properties and a Transition from Electrical to Chemical Coupling between Excitatory Layer 4 Neurons in the Rat Barrel Cortex." Frontiers in Neural Circuits **10**: 1.
Vavoulis, D. V., V. A. Straub, J. A. Aston and J. Feng (2012). "A self-organizing state-space-model approach for parameter estimation in hodgkin-huxley-type models of single neurons." PLoS Computational Biology **8**(3).
Venance, L., A. Rozov, M. Blatow, N. Burnashev, D. Feldmeyer and H. Monyer (2000). "Connexin expression in electrically coupled postnatal rat brain neurons." Proceedings of the National Academy of Sciences **97**(18): 10260-10265.
Vivekananda, U., P. Novak, O. D. Bello, Y. E. Korchev, S. S. Krishnakumar, K. E. Volynski and D. M. Kullmann (2017). "Kv1.1 channelopathy abolishes presynaptic spike width modulation by subthreshold somatic depolarization." Proceedings of the National Academy of Sciences **114**(9): 2395-2400.
Wester, J. C. and D. Contreras (2013). "Biophysical mechanism of spike threshold dependence on the rate of rise of the membrane potential by sodium channel inactivation or subthreshold axonal potassium current." Journal of Computational Neuroscience **35**(1): 1-17.
Williams, R. W. (2000). Mapping Genes that Modulate Mouse Brain Development: A Quantitative Genetic Approach. New York, Springer Verlag.
Winnubst, J., J. E. Cheyne, D. Niculescu and C. Lohmann (2015). "Spontaneous Activity Drives Local Synaptic Plasticity In Vivo." Neuron **87**(2): 399410.
Woolsey, T. A. and H. Van der Loos (1970). "The structural organization of layer IV in the somatosensory region (SI) of mouse cerebral cortex. The description of a cortical field composed of discrete cytoarchitectonic units." Brain Research **17**(2): 205-242.
Wright, W. N., B. L. Bardakjian, T. A. Valiante, J. L. Perez-Velazquez and P. L. Carlen (1996). "White noise approach for estimating the passive electrical properties of neurons." Journal of Neurophysiology **76**(5): 3442-3450.
Wu, C. S., C. J. Rosado and H. C. Lu (2011). "What can we get from 'barrels': the rodent barrel cortex as a model for studying the establishment of neural circuits." European Journal of Neuroscience **34**(10): 1663-1676.
Wulfram Gerstner, R. n. (2009). "How Good Are Neuron Models?" Science **326**(16).
Xi, X. Z. and Z. C. Xu (1996). "The effect of neurobiotin on membrane properties and morphology of intracellularly labeled neurons." Journal of Neuroscience Methods **65**(1): 27-32.
Yamada, W. M. K., Christof; Adams, Paul R (1998). Multiple channels and calcium dynamics, Methods in Neuronal Modeling MIT Press Cambridge.
Ye, J., P. J. Rozdeba, U. I. Morone, A. Daou and H. D. I. Abarbanel (2014). "Estimating the biophysical properties of neurons with intracellular calcium dynamics." Physical Review E **89**(6): 62714.
Yu, Y.-C., S. He, S. Chen, Y. Fu, K. N. Brown, X.-H. Yao, J. Ma, K. P. Gao, G. E. Sosinsky, K. Huang and S.-H. Shi (2012). "Preferential electrical coupling regulates neocortical lineage-dependent microcircuit assembly." Nature **486**(7401): 113-117.
Yuste, R., D. A. Nelson, W. W. Rubin and L. C. Katz (1995). "Neuronal domains in developing neocortex: Mechanisms of coactivation." Neuron **14**(1): 7-17.
Zahs, K. R. and E. A. Newman (1997). "Asymmetric gap junctional coupling between glial cells in the rat retina." Glia **20**(1): 10-22.

Zhang, L. I. and M.-m. Poo (2001). "Electrical activity and development of neural circuits." Nature Neuroscience **4**(Supp): 1207-1214.
Zhang, X.-J. J., Z. Li, Z. Han, K. T. Sultan, K. Huang and S.-H. H. Shi (2017). "Precise inhibitory microcircuit assembly of developmentally related neocortical interneurons in clusters." Nature Communications **8**: 16091.
Zolnik, T. A. and B. W. Connors (2016). "Electrical synapses and the development of inhibitory circuits in the thalamus." The Journal of Physiology **594**(10): 2579-2592.